Teleoperation for Steep Country Forestry Harvesting in New Zealand

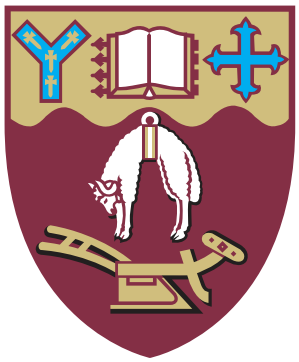

Bartholomew James Estall Milne

Department of Mechanical Engineering

University of Canterbury

A thesis submitted in partial fulfilment of the requirements for the

Doctor of Philosophy

September 2015

I would like to dedicate this thesis to my loving parents ...

Acknowledgements

I would like to express my sincere gratitude to my supervisors Prof. XiaoQi Chen and Dr. Chris Hann, for the continuous support of my PhD study and related research. I would also like to acknowledge the contributions of Scion New Zealand & Future Forests Research, in particular Paul Milliken, Richard Parker, Keith Raymond and Spencer Hill. Acknowledgement must also be given to Trimble Navigation for making their ready-for-excavator equipment available to the program without charge.

I would like to acknowledge the support of the technical team in the Mechanical Engineering Department, especially Julian Murphy, Julian Phillips, Rodney Elliott and Paul Southward. My colleagues have been very helpful during the process, so thanks to Chris Meaclem and Hunter Harrill for their knowledge and expertise.

I would also like to acknowledge my parents, Margaret and Derek. In particular I would like to dedicate this thesis to the memory of Margaret, who passed away on the 29th May 2015 after a sudden illness.

Abstract

New Zealand's forests are commonly planted on steep slopes and include large trees. The research in this thesis contributes to the long term objective of developing a teleoperated mechanised harvester capable of working on slopes of up to 45° steepness and with large trees. The final aim of the project is to create a forestry harvester that provides a comparable improvement to productivity of steep slope harvesting that has been experienced with mechanisation of flat land forestry harvesting in New Zealand. This thesis studies the feasibility and practicability of teleoperation and autonomous control of forestry harvesters, particularly the predominantly excavator-based forestry harvesting machinery in use in New Zealand. The studies were performed on a laboratory scale hydraulic system, but were not able to be tested in the field, but it is considered that the studies presented have made a significant contribution to retrofitting existing forestry harvesters as used in New Zealand. The forestry industry makes a significant contribution to New Zealand's economy. A large amount of steep land was converted to plantation forestry in the 1980s, and these forests are coming to harvesting age. Unfortunately, the forestry industry has high rates of deaths and serious injuries due to the hazardous nature of the work. While mechanised harvesting is used where possible to the improve safety and productivity, much forestry harvesting is carried out on steeply sloped land. Steep slope machinery is available in other countries but the large tree size in New Zealand precludes its use here. New Zealand-specific machines for steep slope harvesting are under development, but most steep slope harvesting is still performed by hand. The specific areas of research this thesis addresses are in teleoperation – autonomous control, visual feedback, haptic feedback, as well as the use of minimal modelling for system identification of the hydraulic machinery.

Trinder Engineering have developed a steep slope harvester using a system of cable anchoring for safety. While this steep slope harvesting machine can perform its task well, the research on teleoperation is aimed at eliminating the hazard to the worker by removing the worker from the machine on the steep slope – "no worker on the slope, no hand on the chainsaw" – without sacrificing the worker's productivity. Teleoperation of forestry machinery is a difficult problem, primarily due to the unstructured and uncontrolled environment in which forestry harvesting takes place. However, improving technology is easing the difficulties of

implementation and is making teleoperation of forestry machines feasible with off-the-shelf computing and networking hardware. The research in this thesis is aimed at maximising the use performance of off-the-shelf computing hardware and software.

The system identification uses minimal modelling to develop the dynamic equations of force and motion. Unlike data driven modelling, which fits the system to the data, minimal modelling is driven by a simplified dynamic model, with inaccuracies being modelled as disturbances. The advantage of minimal modelling is that it is physically derived, so it is easy to see how changes in the machine properties affects the behaviour. This has the potential to allow various types of machinery to be modelled in this way, in particular the minimal modelling was first used to model the dynamic behaviour of a Phantom Omni haptic feedback arm, before being tested on a laboratory scale hydraulic system. This research was used to demonstrate the transferability of minimal modelling between different types of mechanical systems.

The emphasis on retrofitting existing machinery in the forestry industry flows through to a strong emphasis on using control systems suitable for retrofit during the research, including for system identification. The hydraulic test system has been used to test autonomous control, including autonomous obstacle avoidance. The objective is to make teleoperation easier, by removing the requirement of operators to operate all the hydraulic rams themselves. The state of the machine was sensed by measurement of ram lengths, which in combination with a model of the machine joints enabled accurate calculation of joint angles.

In particular, the key novel contribution to the state of the art is in implementation of semi-autonomous teleoperation control using ROS (Robot Operating System), off-the-shelf components and ‘Minimal Modelling’ based system identification. The use of these techniques show it is possible to retrofit autonomous controllers in a modular way, without having detailed design information about the machines or having to design heavily customised control systems.

The research finds that autonomous control using ROS and minimal modelling based system identification techniques are useful for retrofitting excavator based forestry harvesters. In particular, the modularity of the ROS based system and the ability of the minimal modelling to be extended to non-linear systems using linear time variant models of damping to account for the effects of friction and actuator dead zone. The autonomous control tests on the laboratory hydraulic system were successful, showing it is possible to control a hydraulic machine using a ‘conventional’ electrically operated hydraulic retrofit to perform autonomous movements. This, along with the strong industrial nature of this research work, is a significant research step forward to development of safer harvesting machines in New Zealand.

Table of contents

List of figures

[1]Programmable Automation Controller
[2]Pulse Width Modulation
[3]Robot Operating System

[4]Commercial Off-the-Shelf

[5]Pseudo Random Binary Signal

List of tables

[6]Root Mean Square

Glossary

909 Project Project carried out by Cutover Systems Limited in partnership with Scion New Zealand and Future Forests Research LTD. to convert a John Deere 909 to remote control using a ROS and Ethernet based control architecture. 1, 12, 50, 111, 113

Stick Insect A tree traversing machine under development at the University of Canterbury. Like the 909 Project, the Stick Insect uses a ROS and Ethernet based control architecture. 12, 92, 203, 205

Acronyms

ANN Artificial Neural Network. 43

API Application Programming Interface. 66

CAN Controller Area Network. 56, 92, 111

COTS Commercial Off-the-Shelf. xvii, 22, 50, 95, 96

DAC Digital to Analogue Converter. 54, 56

DGPS Differential GPS (Global Positioning System). 25, 27

E-Stop Emergency Stop. 67

GPS Global Positioning System. 27

IMU Inertial Measurement Unit. 56, 57

IP Internet Protocol. 63, 69, 113

ISDN Integrated Services for Digital Network. 34

LHD Load Haul Dump. 29

PAC Programmable Automation Controller. xvi, 53, 54, 56, 64–67, 69, 96, 101, 203

PID Proportional-Integral-Derivative. 64, 120

PRBS Pseudo Random Binary Signal. xviii, xxi, 123, 124, 126, 130–133, 156

PWM Pulse Width Modulation. xvi, 54, 56

RMS Root Mean Square. xxi, 132, 181, 182

ROS Robot Operating System. xvi, xvii, 1, 12, 22, 50, 60, 63–69, 89, 91, 92, 96, 98–100, 102, 110, 112, 113, 116, 117, 203, 205

SIL Safety Integrity Level. 67, 112

SRDF Semantic Robot Description Format. 67, 68

SVD Singular Value Decomposition. 18, 200

TCP/IP Transmission Control Protocol/Internet Protocol. 32, 34, 50, 69

UDP User Datagram Protocol. 69

URDF Unified Robot Description Format. 60, 67, 68, 98, 99

USB Universal Serial Bus. 56

Chapter 1

Introduction

1.1 Overview of Forestry Harvesting

Forestry, or *silviculture* has played a very important role in human civilisation, and will continue to do so for the foreseeable future. Forests are grown in a wide variety of environments and terrains around the world, from flat plains to steep mountains, and from the tropics to sub-arctic climate zones. Commercial plantation forests in New Zealand consist predominantly of fast growing but low value *Pinus Radiata*. In this economic environment, changes in the cost of harvesting have significant effects on the profitability of log extraction. Mechanised harvesting is favoured on flat land because of the lower cost of harvesting. Forestry in New Zealand is predominantly *Pinus Radiata*, a fast growing but low value wood. The forestry machinery is predominantly based on modified excavators, due to their low cost of operation and their ability to handle the physical size of the harvested trees in New Zealand. While steep slope harvesting is common around the world, the steep slope harvesting machines available elsewhere are more specialised and cannot handle such large trees. This exposes a key deficiency in the state of the art: how to make a teleoperated forestry harvesting machine that can operate on steep slopes, has a low manufacturing and running costs, and can handle the harvested tree sizes commonly found in New Zealand.

Scandinavia has one of the most heavily mechanised forestry industries in the world, but the machinery is designed for smaller trees, flat land and a very high level of automation [1]. Japan has forestry on steeply sloped marginal land, but the forestry industry in Japan is in decline due to cheaper wood from overseas (including New Zealand) and is more focused on small scale high value production and environmental management [2–4]. Forestry in North America, in particular the Pacific Northwest (Northern California to South-east Alaska) provides an important example for New Zealand. In particular many items of machinery used in this area such as cable yarders are used in New Zealand with little or no modification.

1.2 The Forestry Industry in New Zealand

The economy of New Zealand is highly dependent on primary industries such as agriculture, fishing and forestry. In the year ending June 2011 primary industries earned NZ$31.5 billion in export receipts (71% of the total) [5]. Forestry contributed NZ$4.5 billion in the same period [5]. Planted forests constitute 1.74 million ha (7%) of New Zealand's total land area, and 90% (1.56 million ha) of the planted area is Radiata Pine (*Pinus Radiata*), with Douglas-fir (*Pseudotsuga menziesii*) plantings the second largest with 110 000 ha (6.3%). The total wood harvest for the year ending 31st March 2010 was 20.7 million m^3. Radiata Pine trees are harvested at an average age of 28.4 years and the average clear fell yield is 473 $m^3\,ha^{-1}$. Each individual tree is on average 2.3 m^3 in volume for sawlogs and 1.6 m^3 for structural timber [6]. Fig. 1.1 shows the typical size and appearance of pine trees just prior to harvest. There are various definitions of the minimum angle that constitutes a "steep slope" as shown in Table 1.1. In this thesis the definition of steep slope is a slope angle greater than 22° with respect to horizontal, as defined in the *Approved Code of Practice for Safety and Health in Forest Operations* [7].

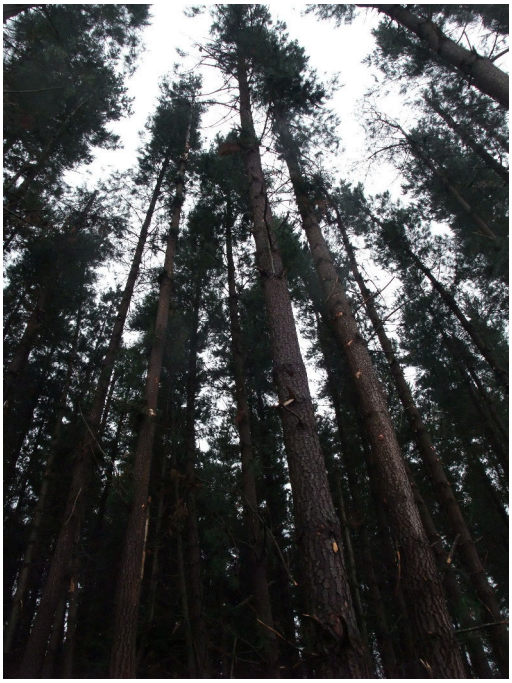

Fig. 1.1 Mature Pine Trees Pre-Harvest.

A large amount of marginal (steep and remote) farm land was converted to forestry in the 1990s, as a result of changes to the economic structure of rural New Zealand during that time (Fig. 1.2). Apart from a period of net deforestation during 2005-2008 for dairy farm

Table 1.1 “Steep Slope” Definitions.

Slope Angle (°)	Slope (%)	Source
19	35	[8]
20	36	[9, 10]
22	40	[7, 11, 12]

conversions, the area of plantation forest has been increasing continually since at least the mid 1980s. Fig. 1.3 shows the distribution of the different ages of plantation pine forestry in New Zealand, with the effect of large areas of tree plantings in the 1990s clearly evident. This has resulted in a large amount of plantation forestry that will be coming to harvest age in the late 2010s and 2020s. A method of harvesting these trees that maximizes profits must be found This is tricky in New Zealand, because mechanisation solutions that rely on high value wood to recover the capital cost of the machinery have limited applicability and usefulness, due to the low value of Radiata Pine wood [13].

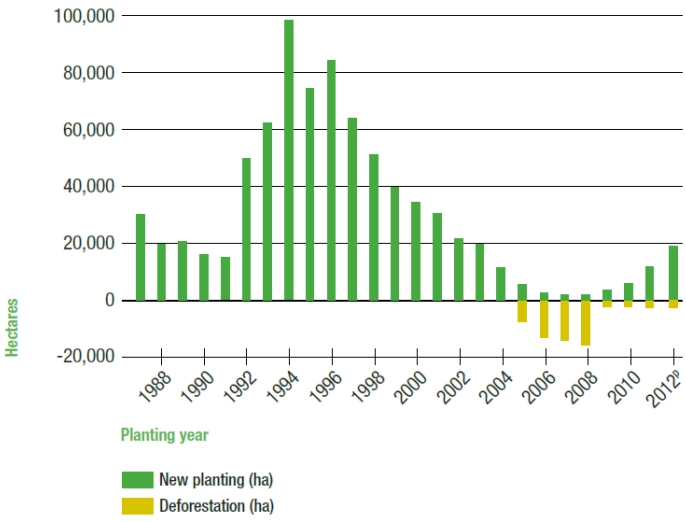

Source: NEFD 2012

Note:
These estimates do not include immature forest cleared for other land uses.
p Provisional

Fig. 1.2 Plantation Forest Plantings 1987-2012 [14].

Mechanised harvesting has been in use in New Zealand for decades for harvesting on flat land and gentle slopes, but large tree harvesters are based on excavators (Fig. 1.4), and are not usable on steep slopes. Specialised steep slope harvesters have been developed overseas, but none of those harvesters are suitable for New Zealand conditions, due to factors such as

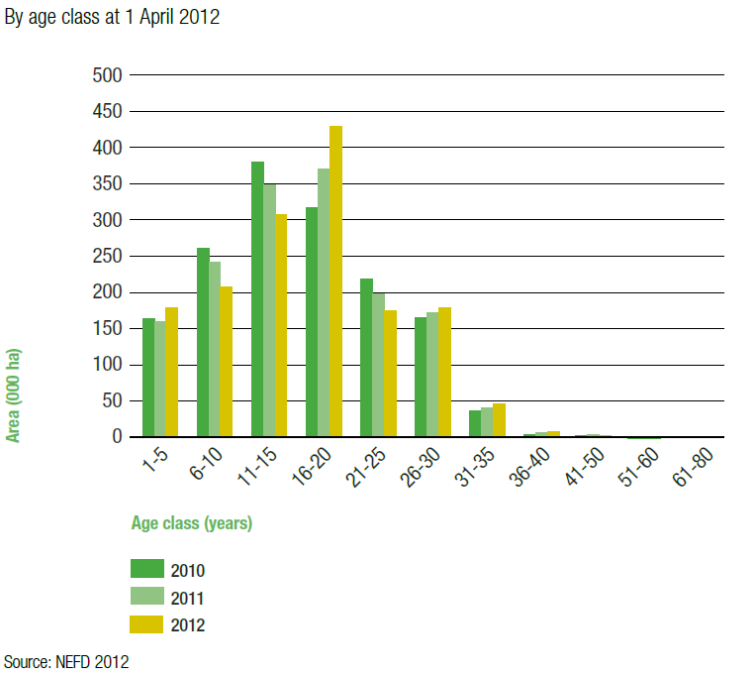

Fig. 1.3 Plantation Pine Age Classes 2013 [14].

soil conditions on steep slopes, large piece sizes and the high capital cost of the machinery relative to the value of the wood being harvested [15, 16].

Fig. 1.4 Excavator Based Harvester (Typical).

In 2009, an estimated 6,000 people were employed in New Zealand's forestry and forestry services industry, including 3,310 people employed in logging. However, manual forest harvest work in New Zealand is perceived as low status, poorly paid, difficult and dangerous, with a fatality rate of 22.4 per 100,000 workers per year. The relatively small number of workers employed means the total number of fatalities is about four per year, but the serious harm injury rate is 18 for every 1000 workers per year, or nearly two serious harm injuries per week. The serious harm injury rate is more than double the rates in mining and utilities, the next most hazardous industries in New Zealand [5, 17]. In summary, mechanical harvesting carries costs of machinery, fuel and maintenance but the productivity improvements reduce the cost of harvesting by up to 50% [13].

1.3 Steep Slope Harvesting in New Zealand

Fig. 1.5 shows a steep slope harvesting site located at Okuku, about 30 km north-west of Christchurch, New Zealand. In the foreground trees have been harvested, and on the slope in the background some the trees are being felled. All the steep slope felling was done manually, with the trees being hauled up the slope whole before having their branches removed and being cut to length for transport.

Fig. 1.5 View of Steep Slope Forestry Harvesting Site.

The logs are held by wire rope strops (chokers) that self-tighten as the logs are pulled up the slope. Fig. 1.6 shows the cable hauler at Okuku Forest extracting a single log, but

multiple logs can be extracted at once (Fig. 1.6). The next step is to sort the logs by size and

Fig. 1.6 Cable hauler extracting a log.

quality at a landing, including cutting to desired lengths Fig. 1.7.

Fig. 1.7 Log cutting and sorting.

In more gently sloping sites, many of the tasks performed by separate machines on steep slopes can be combined. Fig. 1.8 is from a harvesting site in Charteris Bay, on Banks

Peninsula near Christchurch, New Zealand. Mechanised harvesting is in use due to the shallower slopes. The trees were felled and bunched at the harvest site and sent to be sorted and classified in a log forwarder. On steep slopes it is not possible to use a forwarder, so the steep slope harvester's functionality may be limited to felling and bunching, with cutting to length being performed after the log has been delivered to the sorting yard.

Fig. 1.8 Feller, buncher and log forwarder at Charteris Bay, near Christchurch, New Zealand.

1.4 Mechanisation of Steep Slope Harvesting

Trinder, in partnership with Future Forests Research has developed a prototype steep slope harvester called the "ClimbMax" (Fig. 1.9). The ClimbMax system uses a specially designed harvester tethered to an anchor at the top of the slope. For example, this anchor may be another excavator. The tether cable between the two machines is held taut by a retraction mechanism on the harvesting machine. While the tethered arrangement means excavator based harvesters can be used on steep slopes, the operator is still exposed to the hazards of operating heavy machinery on steep slopes, such as disorientation, roll-over and slipping. Moreover, the steep slope also increases the difficulty of rescue in the event of an accident. These hazards are difficult to eliminate, so removing the operator from the machine through teleoperation and autonomous control will be beneficial. The research in this thesis is a laboratory study of the means of teleoperation and autonomous control. The teleoperation research includes studies of visual and haptic feedback, as well as autonomous path planning.

Implementing teleoperation and autonomous path planning requires modelling of machine dynamics and kinematics, which is implemented through identification of the dynamic properties of the Phantom Omni and laboratory scale hydraulic system through minimal modelling.

Fig. 1.9 Trinder ClimbMax Harvester in Operation.

1.5 Robotisation of Steep Slope Tree Harvesting in New Zealand

This project concentrates on hydraulic machinery, but both the John Deere 909 Project and "Stick Insect" tree-to-tree project [18] have significant crossover. The 909 Project has an implementation of remote control using ROS, and the Stick Insect uses ROS and also incorporates real time sensor information. An example path forward would be to use the remote control architecture and visual feedback of the 909 Project with the real time sensing of the Stick Insect.

While Trinder's ClimbMax harvester can operate on slopes of up to 45°, it still requires the presence of an operator in the cab [13, 19]. As teleoperation of a harvesting machine involves the fitting of computer hardware, there are many opportunities for further improvements in productivity such as:

- haptic feedback for the remote operator;

- overlaying orientation information onto the operator's display;
- semi-automation such as using laser-triangulation sensors to autonomously move the felling head to a position where it can grasp a tree;
- using of laser-triangulation sensors for collision avoidance and localised terrain mapping;
- binocular vision for improved depth perception.

The increasing proportion of land planted for forestry will increase the demand for forestry workers. The work is hazardous and has a long training time. Robotisation is being explored to isolate the worker from hazards, increase productivity, and attract more new workers. Many areas of New Zealand are physically suitable for forestry but the lack of infrastructure and high labour costs make harvesting uneconomic [12]. From the point of view of Scion and Future Forests Research, the motivations, research issues and challenges are [20]:

Motivations:

- automation of forest operations: felling, collecting;
- improvements in safety;
- improvements in productivity.

Research issues:

- Machine mobility and stability on steep and soft soil country
- Navigation of harvesting machines
- Sensor fusion and teleoperation

Challenges:

- highly unstructured, obstructive outdoor environment;
- steep and soft soil forestry peculiar to New Zealand;
- big tree sizes in New Zealand.

1.6 Teleoperation

A key difference between teleoperation systems and remote control systems is that teleoperated machines operate solely with a combination of machine sensor information, simulations and models. These features remove the need for direct observation of the machine during operation. Teleoperation systems are more complicated than remote control, but they make it possible to implement more sophisticated control methods that can reduce operator workload.

Teleoperation may be thought of as an extension of remote control. Remote controlled systems are cheaper and easier to implement but are limited to situations where the operator can directly observe the machine. Effective remote control becomes difficult or impossible in conditions like underwater [21–24], nuclear reactors [25, 26], underground mining [27], and where the operator has to be isolated from the machine [28–30].

Effective teleoperation in unstructured and uncontrolled environments requires sensing and modelling combined with a good operator interface. Good feedback and controls are essential for creating telepresence, where an operator can operate a machine as well as if they were controlling it directly. Some types of feedback of interest include haptic (touch-force), orientation, audio, 3D mapping and binocular vision. Other unstructured and uncontrolled environments include mining [31–33], and aircraft control [34, 35].

In summary, some possible benefits of teleoperation of forestry machines based on other field machines are:

- improved comfort for the operator [21, 22, 24, 25, 27, 28, 31, 32, 34, 36–38];
- greater profits by improving operator productivity [28–30, 32, 38];
- implementation of interfaces and control algorithms that enhance operator skills [22–25, 28, 30, 32, 36, 38–48].

As outlined above teleoperation has many significant potential benefits. The main problems that must be addressed in the development of teleoperation are:

- determining the sensors required on the target machine;
- defining the user interface requirements and creating a suitable user interface;
- ensuring the target machine remains safe at all times;
- ensuring the operator has sufficient situational awareness.

1.7 Minimal Modelling & System Identification

Minimal modelling may be considered a form of "grey box" modelling [49]. Minimal models are particularly useful for the modelling of machines with unknown coefficients, especially if it is assumed unknown or unobservable dynamics can be lumped in with observable dynamics. In the case of this thesis the system identification and modelling is aimed at machines for retrofit, where detailed knowledge of the design of the machine is not available. In this case building a "white box" model is impossible, as a white box model implies completely modelling every part of the machine, which is by definition impossible if the way a machine is constructed is not completely known.

The "grey box" model forms the core of a minimal model. Grey box modelling is used as it captures the significant system dynamics. While a minimal model may not capture all behaviours, it is designed so that any known non-linearities can be lumped into the identified parameters. In this sense, if the system identification model is a linear time invariant differential equation, the non-linearities can be accounted for by making the model linear time variant for simulation. While it can be argued that it is meaningless to attempt to identify a linear model on a non-linear system, it must be noted that many systems have regions of operation where they are close to linear, and so a linear model can be meaningfully identified in these operating regions.

Simulation of the minimal model is performed using a standard state space representation. Non-linearities are incorporated by altering the state space model coefficients, resulting in the non-linear system being implemented as a linear time variant system. This technique is useful where some dynamic properties (e.g. damping) are dependent on actuator speed due to non-linear effects such as friction [50]. In general, minimal modelling uses continuous time domain analysis since all the analytical tools of Ordinary Differential Equations (ODEs) are available. For example, minimal modelling allows the capability of directly identifying external loads or disturbance in terms of physical and quantifiable properties. Consider a linear time invariant ordinary differential equation (LTI ODE) with output $y(t)$ and inputs $x(t)$ and $u(t)$ as shown in (1.1). The quantity $x(t)$ represents a control input and $u(t)$ represents external forces and disturbances. The derivatives are written in shorthand notation so that $y^{(n)} = \frac{d^n y}{dt^n}$.

$$\sum_{n=0}^{N} a_n y^{(n)}(t) = \sum_{n=0}^{N} b_n x^{(n)}(t) + c_{\mathrm{u}} u(t) \tag{1.1}$$

Equation (1.1) can be integrated N times to give (1.3). The order of integration is N, so the highest (Nth) order derivative is eliminated. Although the repeated integrations can be written directly, the Cauchy formula for repeated integration allows the repeated time

integrals to be collapsed into single integrations as shown in (1.2). The starting point of the waveform is arbitrary but for convenience is chosen as $\tau = 0$, so the end limit becomes $\tau = t$ (the current time of integration). Application of the Cauchy theorem for repeated integrals (1.2) to (1.1) gives the integrated differential equation (1.3).

$$\int_0^t \frac{(t-\tau)^{N-1}}{(N-1)!} y^{(n)}(\tau)\, d\tau = y^{(n-N)}(t) - \sum_{k=0}^{N-1} y^{(n-N+k)}(0^-)\frac{t^k}{k!} \tag{1.2}$$

$$\begin{aligned} \sum_{n=0}^{N} a_n \int_0^t \frac{(t-\tau)^{N-1}}{(N-1)!} y^{(n)}(\tau)\, d\tau = \ldots \\ \sum_{n=0}^{N} b_n \int_0^t \frac{(t-\tau)^{N-1}}{(N-1)!} x^{(n)}(\tau)\, d\tau + c_{\mathrm{u}} \int_0^t \frac{(t-\tau)^{N-1}}{(N-1)!} u(\tau)\, d\tau \end{aligned} \tag{1.3}$$

Equation (1.3) is close to the final form, but still requires knowledge of the derivatives. While the derivatives could be calculated analytically or numerically, the entire point of the integral method is to avoid calculating derivatives in the first place, as real data is quantised in time and has noise and quantisation errors that are amplified through repeated differentiation. Equation (1.4) represents (1.3) with the derivatives eliminated. The c coefficients represent constants of integration derived from initial conditions on the integrated derivatives. The initial conditions of the integrals (i.e. $y^{(n)}(0^-)$ for $n < 0$) are arbitrary and may be set to zero without loss of generality. The modified formula is shown in (1.4). Note that the a_N and b_N coefficients should actually have the initial values of y and x respectively but the effect of not having the initial conditions is lumped into the c_0 coefficient.

$$\begin{aligned} \sum_{n=0}^{n=N-1} a_n \int_0^t \frac{(t-\tau)^{N-n-1}}{(N-n-1)!} y(\tau)\, d\tau + a_N y(t) = \sum_{n=0}^{n=N-1} b_n \int_0^t \frac{(t-\tau)^{N-n-1}}{(N-n-1)!} x(\tau)\, d\tau + \ldots \\ b_N x(t) + \int_0^t \frac{(t-\tau)^{N-1}}{(N-1)!} u(\tau) d\tau + \ldots \\ c_0 + c_{\mathrm{u}} \sum_{n=1}^{N} c_n t^n \end{aligned} \tag{1.4}$$

Equation (1.4) is ill-conditioned, as all the a_N, b_N and c_N coefficients give the same result up to a multiplicative constant. The main method of making (1.4) well-posed is to fix the value of a single a or b coefficient corresponding to the highest order derivative to 1. This technique is particularly handy if the coefficient of the derivative corresponds to an unknown physical quantity, as it turns all the remaining quantities into ratios that may be easier to identify and give the same system behaviour. The main disadvantage of this method

is numerical instability when the coefficient that is set to 1 should actually be set to zero, as given by the behaviour of the system response. The continuous time final form (1.4) can be modified for discrete time signals by the substitution of an appropriate method of numerical integration. The resulting form may be put in a matrix as shown in (1.5).

$$\begin{bmatrix} Y & X & U & T \end{bmatrix} \begin{bmatrix} \vec{a} \\ \vec{b} \\ c_{\mathrm{u}} \\ \vec{c} \end{bmatrix} = \begin{bmatrix} \vec{0} \end{bmatrix} \tag{1.5}$$

The sub-matrices Y, X, U and T are defined in (1.6), (1.7), (1.8) and (1.9) respectively. The $\vec{a}$, $\vec{b}$ and $\vec{c}$ vectors are defined according to the general form given in (1.10).

$$Y = \begin{bmatrix} \vec{y}^{(-N)} & \vec{y}^{(-N+1)} \cdots \vec{y} \end{bmatrix} \tag{1.6}$$

$$X = \begin{bmatrix} \vec{x}^{(-N)} & \vec{x}^{(-N+1)} \cdots \vec{x} \end{bmatrix} \tag{1.7}$$

$$U = \begin{bmatrix} \vec{u}^{(-N)} \end{bmatrix} \tag{1.8}$$

$$T = \begin{bmatrix} \vec{1} & \vec{t} & \cdots & \frac{\vec{t}^{N-1}}{(N-1)!} \end{bmatrix} \tag{1.9}$$

$$\vec{v} = \begin{bmatrix} v_0 \\ v_1 \\ \vdots \\ v_N \end{bmatrix} \tag{1.10}$$

Once one of the components of the solution vector is assigned a fixed non-zero value, it can be converted to an ordinary least squares problem (1.11).

$$M\vec{x} = \vec{b} \tag{1.11}$$

The simplest methods of solving (1.11) are to either use a pseudo-inverse such as the Moore-Penrose Pseudo-inverse (1.12) or an operator such as backslash division in Matlab (1.13). The Moore-Penrose pseudo-inverse is preferred for general usage, as the Matlab backslash division uses a proprietary algorithm.

$$\vec{x} = M^{+}\vec{b} \tag{1.12}$$

$$\vec{x} = M \backslash \vec{b} \tag{1.13}$$

While the minimal modelling equation can be solved directly, the numerical stability can be significantly enhanced by pre-treating M to eliminate overlaps between its columns, in particular the free variable columns. The least squares solution $\vec{x}$ can be partitioned into "solver" variables and "free" variables. The solver variables are the terms that appear in the differential equation (1.1), and the free variables represent initial values of derivatives and do not appear in (1.1). The free variables are required for the solution, but are discarded because they do not appear in the differential equation. The solver matrix M can be partitioned into two sub-matrices: the solver variables (M_{solv}) and the free variables (M_{free}) (1.14). The T matrix from (1.5) is carried over to (1.14) directly because the initial conditions are always considered unknowns.

$$\begin{bmatrix} M_{\text{solv}} & M_{\text{free}} \end{bmatrix} \begin{bmatrix} \vec{x}_{\text{solv}} \\ \vec{x}_{\text{free}} \end{bmatrix} = \vec{b} \tag{1.14}$$

The T matrix is actually a truncated Vandermonde matrix, and Vandermonde matrices are ill conditioned due to the high cross correlations between different monomials (see Appendix F). The orthogonalisation of the initial conditions is performed using the SVD[1], as shown in (1.15). The type of decomposition used is the "economy" or "reduced" type, as only the singular vectors that correspond to the columns of T are of interest, as all the other singular vectors are associated with singular values of zero. The reason for using the SVD is that it makes it easier to compute the numerical rank of T by examining the singular values directly.

$$M_{\text{free}} = U_{\text{free}} \Sigma_{\text{free}} V_{\text{free}}^{\text{T}} \tag{1.15}$$

The main diagonal of the singular value matrix Σ_{free} consists of a series of decreasing singular values $\sigma_1 \cdots \sigma_n$. A reduced rank SVD is computed by setting all singular values that are less than $\varepsilon\sigma_1$ to zero, where ε is the machine precision ($2.2204 \cdot 10^{-16}$ with double precision arithmetic). The columns of U_{free} that correspond to all zero and "practically zero" ($\sigma_n < \varepsilon\sigma_1$) singular values are discarded and U_{free} is replaced with the reduced set of $\tilde{U}_{\text{free}}$.

$$M = \begin{bmatrix} M_{\text{solv}} & \tilde{U}_{\text{free}} \end{bmatrix} \tag{1.16}$$

The definition of M given in (1.16) then then be used to solve for $\vec{x}$ using (1.12) or (1.13). The free variable solutions resulting from using (1.16) will be "mixed together", but this does not matter, as the values are discarded anyway.

[1] Singular Value Decomposition

1.8 Haptic Feedback

The interface research includes research on usage of Haptic (touch-force) feedback in forestry harvesting, which has not been tried before [15]. Haptic feedback provides information to the operator using force. Some examples of haptic feedback devices are shown in Fig. 1.10 (Phantom Omni) and Fig. 1.11 (Novint Falcon). Haptic feedback is expected to be useful for providing the operator with additional information about the actions they are performing relative to the abilities of the harvester.

While haptic feedback has potential for enhancing situational awareness, haptic devices are mechanical devices with dynamics that contribute to the system's behaviour. Because of this, a system with haptic feedback can become sensitive to time delays and if this is not properly managed the system can become unstable. It is recommended that haptic feedback be controlled by the user so that any instabilities can be eliminated by the user without having to resort to emergency measures.

Fig. 1.10 Phantom Omni.

Fig. 1.11 Novint Falcon.

1.9 Thesis Scope and Objectives

The long term objective of this research program is the development of a harvester for steep slopes suited for New Zealand conditions, to replace the use of manual labour for the felling of trees on steep slopes. The final outcome of the programme is a teleoperated mechanised harvester capable of working on slopes of up to 45° steepness. The desired economic outcome of the project is to create a harvester that provides a comparable improvement to steep slope harvesting to the improvement that has been experienced with mechanisation of flat land forestry harvesting in New Zealand.

The topic area of the research is broad, with multiple paths possible. Since a research setup had to be created from scratch, the scope of the research naturally became coupled with the setup and implementation of a research platform for teleoperation. While the intention was to use the research on Trinder's ClimbMax harvester, the research ended up being focussed on laboratory studies as the ClimbMax became unavailable. The specific areas of research this thesis addresses are teleoperation, control algorithms and most importantly the use of minimal modelling for system identification.

The key research questions are:

- Forestry harvesters used in New Zealand are based on modified excavators. What are the steps required to retrofit these machines for teleoperation?

- How useful are enhanced feedback methods such as haptic feedback for control of the forestry harvester?

- Can minimal modelling be used to identify relevant dynamic parameters of the harvesters without detailed knowledge of the construction of the harvesting machine?
- How robust can the control system be made to noise, measurement error, ill-posed data and component failures? Can this robustness be quantified?

The research contributes to solving the following deficiencies in the state of the art:

- teleoperation of forestry harvesters has been developed but only for short range operation;
- teleoperated harvesters exist, but they are suitable only for flat land and small trees;
- steep slope harvesters exist, but they expose the operator to the hazards of heavy machinery on steep slopes;
- teleoperation of forestry harvesters based on excavators, such as those used in New Zealand has not been attempted before.

1.10 Thesis Layout and Contributions

Chapter 2 contains a review of literature that is relevant to the project. Relevant literature sources include forestry robotics, mining, operator control systems for remote controlled robotics, existing experimental teleoperation platforms, haptic feedback, minimal modelling and stabilisation of bilateral haptic feedback in the presence of time delays. The literature review concentrates on these subjects especially, as they give a good background to; (i) the use of heavy robotics in the uncontrolled and unstructured environments present in forestry and mining; (ii) operator control methods that have been explored in this thesis such as haptic feedback; (iii) autonomous robot control; (iv) setting up experimental teleoperation systems; and (v) stabilising haptic feedback control in the presence of time delay.

Chapter 3 describes the research system setup. The main research systems were the Phantom Omni, and the laboratory scale hydraulic system. The Phantom Omni was available first, so experimental work on minimal modelling and bilateral haptic feedback control was performed on that before the hydraulic test system, which was not operational until approximately 18 months into the research project. The system setup also provides a basis on how the minimal models were developed and used for system identification.

Chapter 4 describes a framework for characterising time delay stabilisation. In particular, it describes the ‘selector function’ method of bilateral haptic feedback that uses a combination of local state, remote state and time delay to determine the haptic feedback that is applied to

the operator. The concept is based on altering the transparency in response to time delay to (i) improve stability, and (ii) take advantage of the ability of the operator to actively stabilise the system if an instability is detected.

Chapter 5 is a study in the use of ROS for teleoperation. ROS is used to teleoperate the hydraulic test system, including the use of haptic feedback, visual feedback and autonomous control. The research contribution of Chapter 5 is that it shows that it is easy to set up a functional teleoperation system using ROS and COTS computer and networking hardware, in particular the ease of setting up wireless teleoperation.

Chapter 6 shows the results of a data driven system identification model on the Phantom Omni. The contribution of Chapter 6 is to compare the minimal modelling method of system identification with the more 'established' data-driven method of system identification, using the Phantom Omni as a small and conveniently available robotic testing platform. Chapter 6 shows that a well-chosen minimal model with sinusoidal steady state responses can get results that are as good as the data driven model, with the notable advantage that sinusoidal steady state responses allow better control of accelerations and forces, and non-linearities are easy to see by inspecting the shape of the output waveform. Chapter 6 also makes the results of the data-driven model easier to interpret, and shows that minimal modelling is indeed a powerful tool for system identification.

Chapter 7 demonstrates a non-linear model based on the kinetic energy of the base joint in the Phantom Omni. The objective is to capture friction as being an energy dependent phenomenon, which makes its estimation in a state space possible. In Chapter 7, a measure of kinetic energy called the "α-invariant" is introduced. The concept of an invariant is used as a properly chosen invariant can make a technique generalisable to any system for which the invariant holds, including non-linear systems. The research in this thesis focused on capturing the non-linearities present in the Phantom Omni at low sine wave frequencies, whose energy was characterised by the α-invariant. The formulation of the α-invariant allowed use of a linear time-variant state space model, that was tested on both sinusoidal steady state and step responses, and was found to improve the model accuracy significantly.

Chapter 8 uses minimal modelling for the system identification of a hydraulic system in a similar way to how it was performed in ch:non_lin_damping. In this case the non-linearities are much more severe than with the Phantom Omni due to the non-linearities and asymmetries of hydraulic valves and rams. In particular, the valve non-linearities were not compensated for, and there is a non-linear relationship between hydraulic ram position and joint angle. While the system as a whole is non-linear, it is still possible to use linear approximations to determine the range in which the system does act linearly. The main contribution is that not only does the minimal model work, it is also possible to identify loads by their effect on

ram behaviour. The fact that meaningful dynamic parameters can be identified on a system where detailed design parameters are now known demonstrates the usefulness of minimal modelling for system identification in the target area of this research, that of machines that have been modified that may lack detailed documentation of their dynamic properties.

Chapter 9 gives the conclusions and discusses future work. Appendix A is a list of publications associated with the research in this thesis.

Chapter 2

Literature Review

2.1 Robotics in Forestry Harvesting

The main challenge of developing teleoperated forestry harvesters is ensuring machine and operator safety in an unstructured and uncontrolled environment. The machine's control system must operate in the presence of uncertainty about tree size and environmental hazards such as wind, weather, sunstrike and soil conditions. In the case of Triton's "Sharc" and "Sawfish", the harvester operates underwater, making it a relevant case study for teleoperation, as it has no facility for having an operator present at all.

Teleoperation and robotisation of forestry harvesting is under active development, especially in Scandinavia [28, 29, 36, 51]. Skogforsk have developed a simulator (see Fig. 2.1) to test the effect of different forestry harvester control methods on operator productivity [41]. Although it is not a teleoperated system, simulators are useful for developing teleoperation user interfaces and testing autonomous functions such as automatic obstacle avoidance. The "Besten & Kuriren" ("Beast & Courier") system (Fig. 2.2) is an example of a remote controlled tree harvester [52]. The Besten is designed for use with multiple log forwarders (the "Couriers"). The Besten is controlled in turn by each log forwarder driver, effectively turning each log forwarder into a harvester. Under certain conditions of tree size and stand density, the Besten can improve productivity by 15% but the productivity improvement is dependent on having enough log forwarders to keep the Besten in operation at all times [52]. While an interesting development, this solution is not suitable for steep slopes in New Zealand as it requires direct forwarder access to the harvester.

The log forwarder's crane arm can be teleoperated using enhanced control methods such as mixed reality and "point and click" interfaces [42]. Fig. 2.3 shows a concept architecture for an autonomous log forwarder [28]. Emde [53] specifies differential DGPS[1] for position

Fig. 2.1 Skogforsk forestry harvesting simulator [41].

Fig. 2.2 “Besten” Remote Controlled Harvester [52]. Forwarder on right.

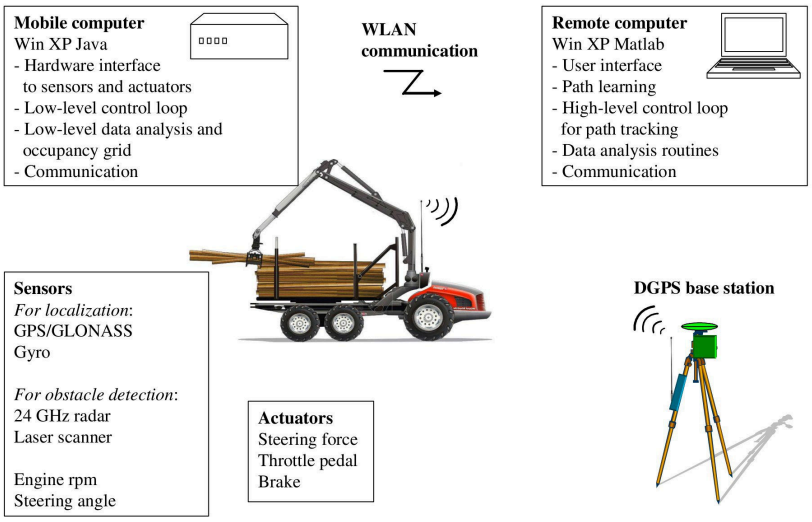

Fig. 2.3 Teleoperation concept architecture for autonomous log forwarders [28].

control of log forwarders, as the accuracy is better than having GPS[2] receivers on the forwarder. In particular, using DGPS overcomes errors caused by signal dropouts when under forest cover, because the DGPS base station is placed in a location optimized for satellite reception. DGPS has been used to remotely control the position and path of a log forwarder [29]. Fig. 2.4 shows the autonomous forwarder and Fig. 2.5 shows its communications architecture. If DGPS coverage is not available, inertial measurements, steering angle and machine speed provide estimates of position and heading. Ringdahl et. al. [29] considered wheel odometry for position estimation but in a forest environment accumulates inaccuracies from wheel slippage too quickly.

Underwater harvesting is a recent innovation in forestry harvesting technology. The interest in underwater harvesting comes from eliminating hazards to shipping and the untapped supply of highly valuable species such as old growth red cedar and tropical hardwoods that were submerged when dams were built. Triton Logging [54] estimates there is US$50 billion worth of wood that can be harvested this way. They have developed two types of underwater harvesters: the “Sharc” harvester that operates from a barge (Fig. 2.6) and the “Sawfish” harvester that operates entirely underwater (Fig. 2.7). The Sharc’s harvesting head is on a specially designed telescopic arm and can work in water depths of up to 37 m. The operator works in the excavator cab and uses cameras and sonar sensors to locate the harvesting head underwater. The “Sawfish” harvester operates entirely underwater. The Sawfish device cuts

[1]Differential GPS (Global Positioning System)
[2]Global Positioning System

Fig. 2.4 Autonomous Forwarder with DGPS navigation [29].

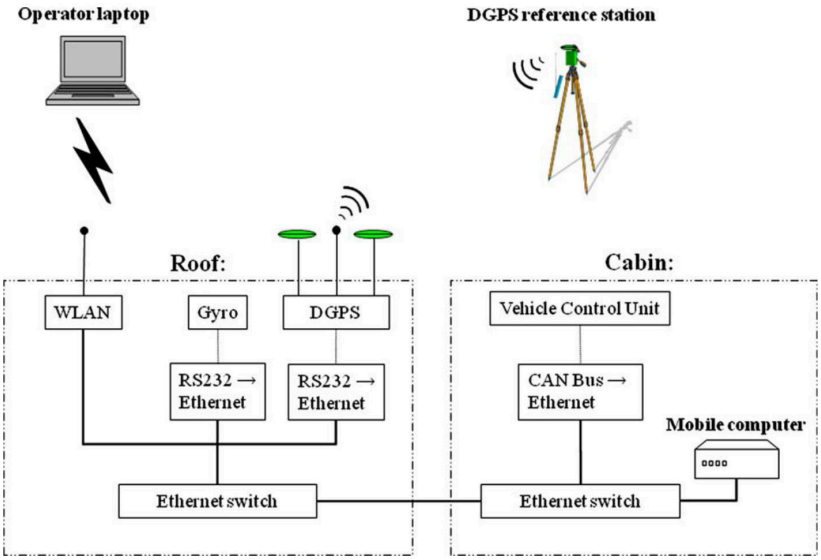

Fig. 2.5 Autonomous log forwarder teleoperation architecture [29].

Fig. 2.6 Triton “Sharc” Underwater Harvester [54].

the logs, which are then floated to the surface using air bags. The use of air bags allows the Sawfish to harvest underwater continuously.

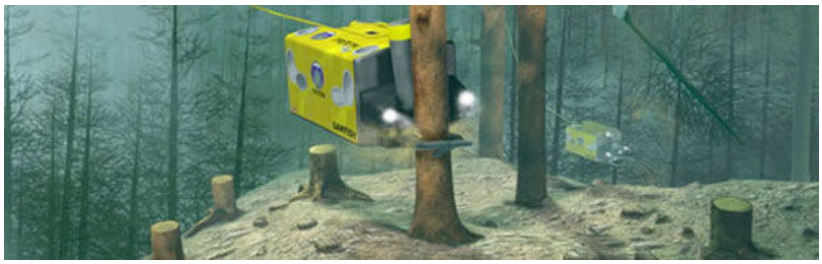

Fig. 2.7 Triton “Sawfish” underwater logging vehicle [54].

2.2 Teleoperation and Semi-Autonomy in Mining

Rio Tinto has several different types of teleoperated machines in use, including LHD[3] trucks and mining plant equipment [27, 30, 37, 45]. Load-haul-dump trucks are suitable for supervisory control as they work on preplanned routes in a structured environment. Fig. 2.8 shows an example if an autonomous LHD truck control system design by Komatsu [30], with a similar control system to the autonomous forwarder control system in Fig. 2.5.

Fig. 2.9 shows an ore crusher at West Angelas mine in Australia that was fitted for teleoperation for a feasibility study [27, 55]. The ore crusher is used to reduce the size of the pieces of iron ore for further processing, and consists of a hydraulic arm with a jackhammer attachment on the end. As part of the study the ore crusher was successfully operated from

[3]Load Haul Dump

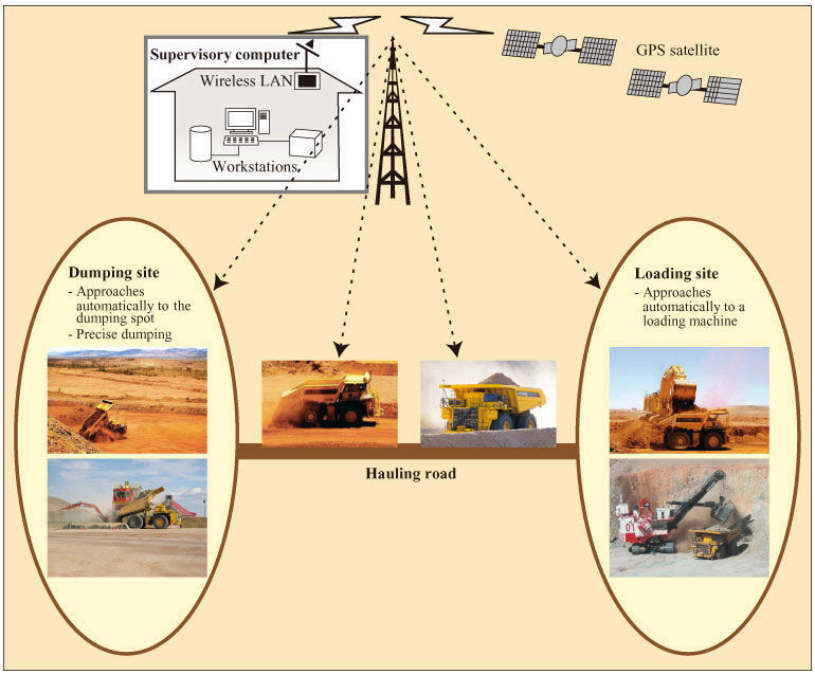

Fig. 2.8 Autonomous Load-Haul-Dump System [30].

1000 km away in Perth. The teleoperation worked as intended but it was thought that haptic feedback would provide a better experience by allowing the operator to feel the behaviour of the tip of the boom [45].

Fig. 2.9 Teleoperated ore crusher [27, 55].

Fig. 2.10 shows a teleoperated machine in use on high wall coal mining [31]. High wall mining allows greater coal recovery but it has a higher risk of cliff collapse. Teleoperated machinery is used to isolate a human operator from the cliff collapse hazard.

Fig. 2.11 shows the “Numbat”. The Numbat is a teleoperated vehicle developed both for mining rescue and research and development [31]. Fig. 2.12 shows the Numbat’s control

Fig. 2.10 Teleoperated high wall coal mining machine [31].

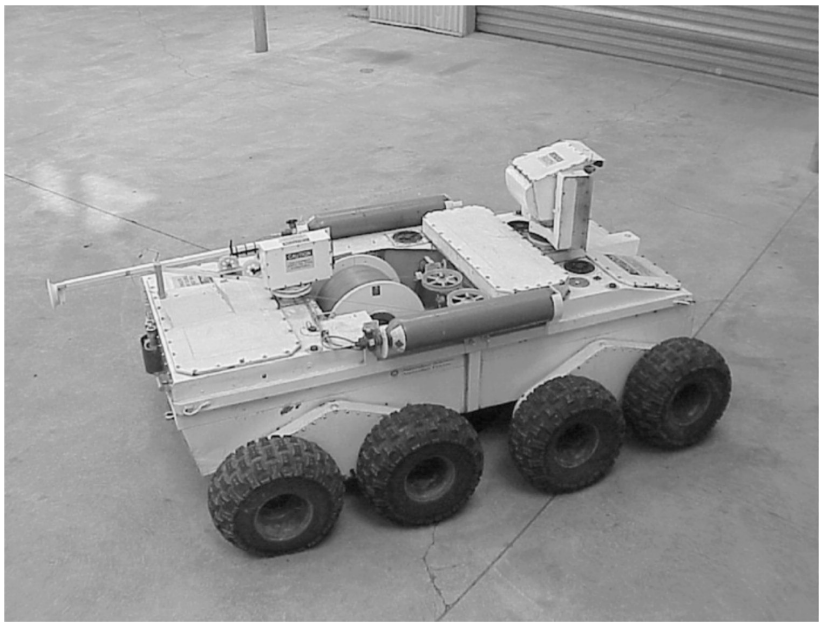

Fig. 2.11 Numbat teleoperated mining vehicle [31].

system architecture. The control system is quite simple, as the Numbat is designed to move slowly enough that the operator could work out the machine dynamics in real time.

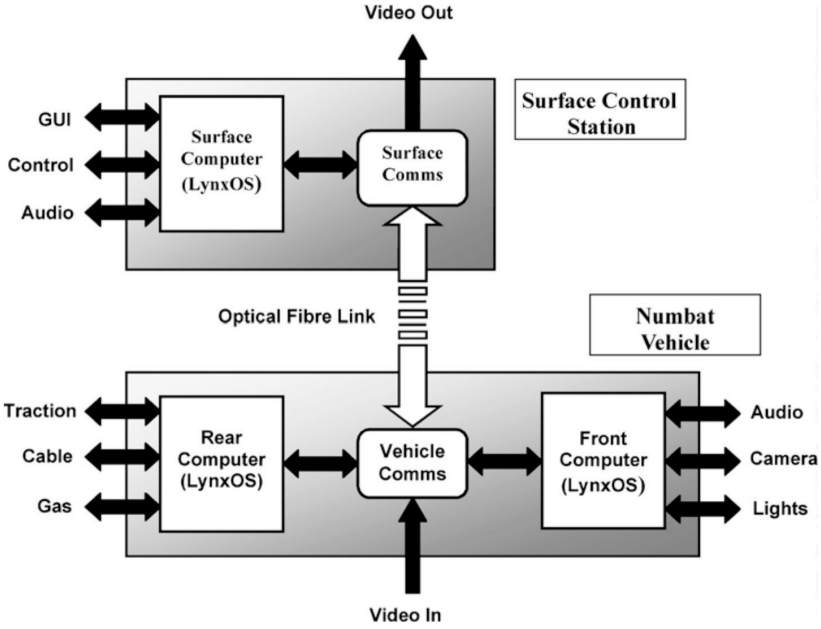

Fig. 2.12 Numbat control architecture [31].

2.3 Teleoperation Control Systems

Fig. 2.13 shows the control system architecture for a Slingsby TA9 underwater manipulator, developed at the Marine Technology Centre at Cranfield during the early 1990s [21]. The Marine Technology Centre were using the manipulator to develop different teleoperation methods, including computer models of operating environments. Internet based teleoperation is not mentioned in [21] because the system was designed in the mid 1990s.

The US Army [34] has developed various communication system architectures (Fig. 2.14) including small UAVs (unmanned aerial vehicles). The US Army has various specialised satellite communication systems but only terrestrial links are being considered for the teleoperated harvester.

There is no fundamental requirement to use the internet or TCP/IP[4] for teleoperation, but the internet is an attractive medium to use due to widespread availability of internet-based communications hardware [37, 56–58]. While the internet is widely available, it has some shortcomings such as unpredictable time delay. For maximum reliability under uncertain time delays, internet-based control systems require delay compensation that can

[4]Transmission Control Protocol/Internet Protocol

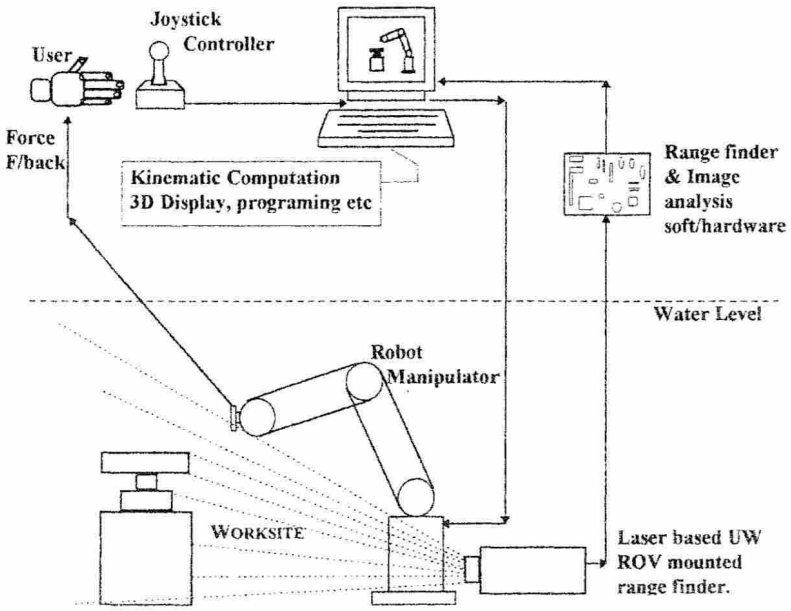

Fig. 2.13 Concept teleoperation for an underwater arm [21].

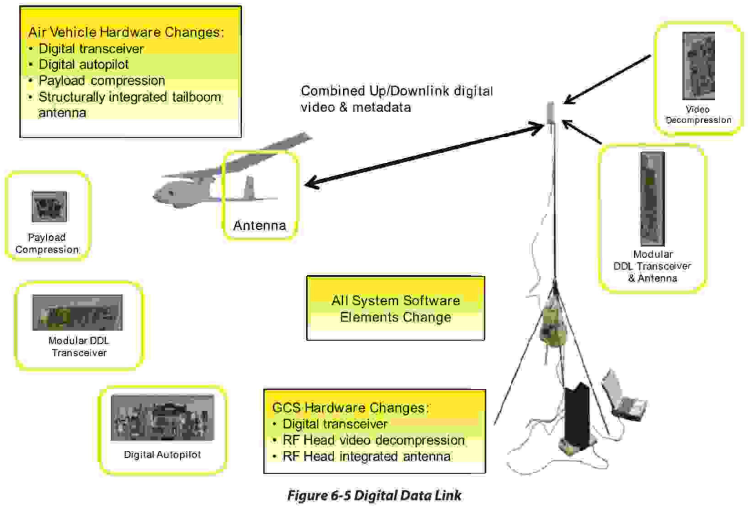

Fig. 2.14 US Army Teleoperation System Overview [34].

accommodate varying time delays and ensure stability and controllability [59–63]. Other communications methods such as ISDN[5] have more predictable communications delays than TCP/IP (Fig. 2.15), but ISDN networks are less widely available than TCP/IP. An alternative approach to immunity from uncertain time delays is to increase the autonomy, so the control system is less dependent on receiving instructions in real time [57]. The main wireless internet (WiFi) standards are 802.11b and 802.11g. 802.11b has longer range but lower data rate, the opposite is true with 802.11g. In [64], two 802.11b adapters were used, as well as an 802.11g adapter and a MeshNetworks WiFi wireless modem. Fig. 2.16 shows the range performance of the different WiFi devices tested, and Fig. 2.17 shows the delay behaviour.

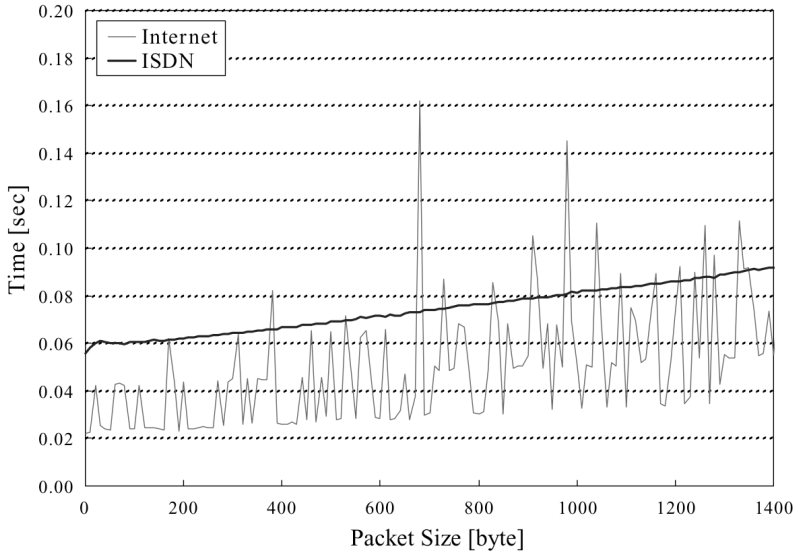

Fig. 2.15 Delay behaviour of ISDN compared to TCP/IP [65].

A shortcoming of using TCP/IP for control is that the transmission delay is not predictable, which is made worse when it is sent over wireless (Fig. 2.17).

Bandwidth is a vital consideration for audio and video transmission. A typical audio bandwidth requirement might be $128\,000\,\mathrm{bit\,s^{-1}}$ for stereo sound. The video bandwidth requirements are dependent on codec but a simple format like M-JPEG (motion JPEG) is preferred for its simplicity and ability to easily recover from dropouts. For ease of control a minimum frame rate of 10 frames per second is desirable [66]. For stereo vision this translates to 20 frames of video per second. A high quality 640×480 pixel JPEG image is about 110 kB, and a medium quality image is about 50 kB. For stereo vision and sound at 10 frames per second the required bandwidths are approximately $18\,\mathrm{Mbit\,s^{-1}}$ for high

[5]Integrated Services for Digital Network

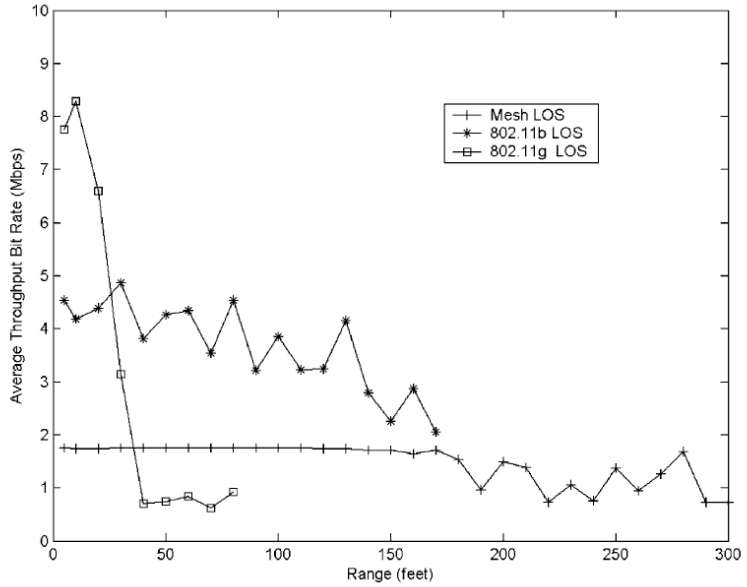

Fig. 2.16 Transmission speed behaviour of different wireless Ethernet devices. 802.11-type device transmit powers are 20 dBm, MeshNetworks 23 dBm [64].

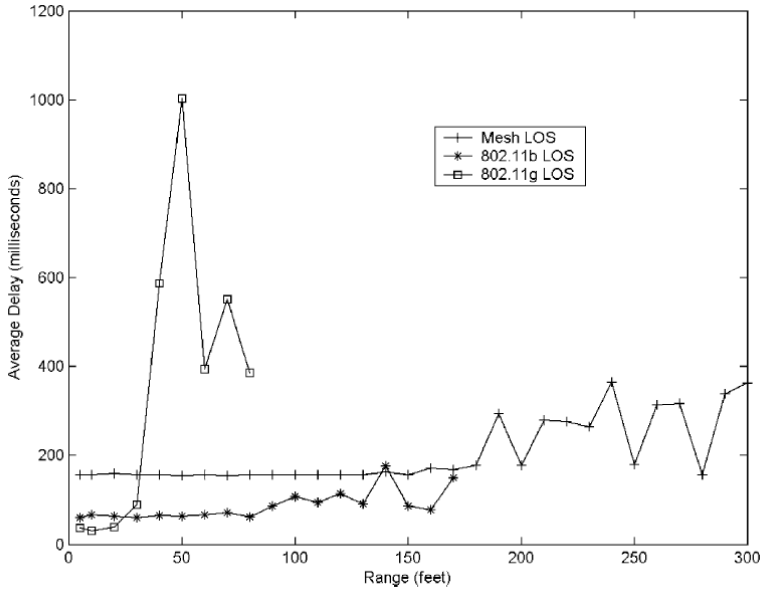

Fig. 2.17 Average delays of various WiFi equipment [64].

quality and 8.3 $\mathrm{Mbit\,s^{-1}}$ for medium quality. The bandwidth may be more than what WiFi equipment can deliver (see Fig. 2.16).

2.4 Operator Interfaces and Control Methods

Fig. 2.18 shows a mining teleoperation interface. The control console is part of a specially made seat, and the feedback is visual via monitors. The control system appears to be a radio control console that has been mounted in front of the seat. Such immersive interfaces are designed to achieve *telepresence*, when the operator is able to control a teleoperated machine as effectively operating it directly [60, 67].

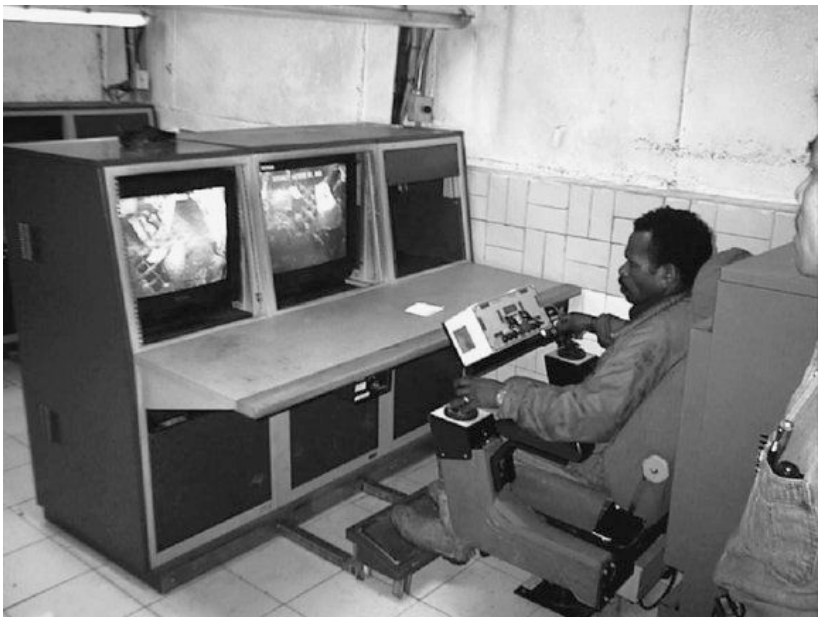

Fig. 2.18 Simple mining teleoperation interface [31].

The high wall coal miner interface is shown in Fig. 2.19. Position information is used with a model of the coal seam to show the approximate position of the drill head. Other information shown includes production amount, depth and explosion hazard.

Simple interfaces are quick to set up, and can often be pieced together from existing off-the-shelf hardware. There is no reason to assume that an advanced interface has to use highly customized and integrated hardware and software. Using carefully selected off-the-shelf hardware and software can reduce development costs substantially, especially for prototypes. Fig. 2.20 shows the status screen for the Numbat. The below absolute zero temperatures in the “Environmental” pane may mean the temperature sensors are disconnected and not

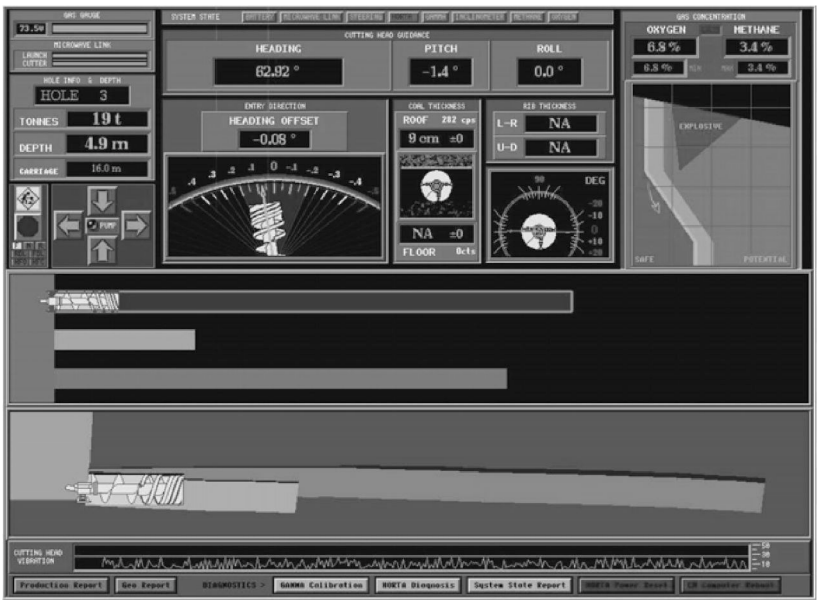

Fig. 2.19 Status Screen for Teleoperated Long Wall Mining Machine [31].

giving readings. If this is the case it is better to have an explicit indication of sensor status to prevent confusing the operator.

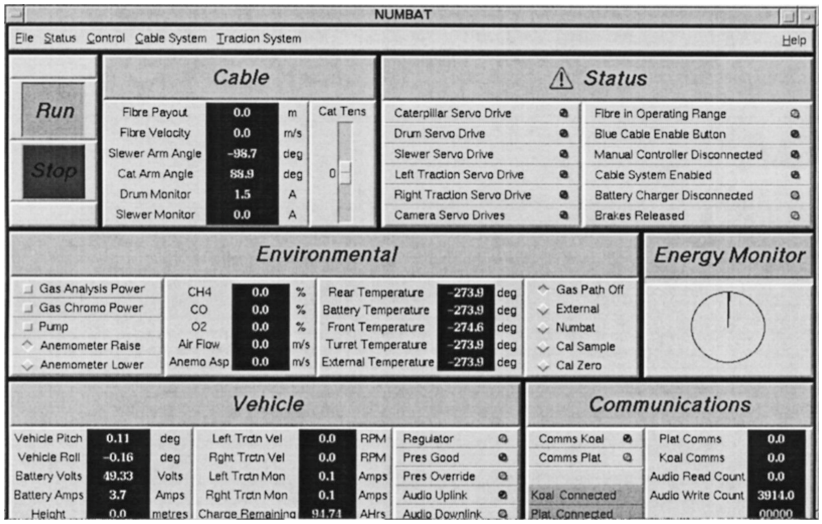

Fig. 2.20 Numbat status display [31].

Argonne National Laboratory has been developing teleoperated equipment for work in nuclear reactors since the 1950s [26, 68]. Fig. 2.21 shows an early system using mechanical feedback. While mechanical feedback allows tactile feedback its range is limited by the mechanical linkages. Fig. 2.22 shows a teleoperated pipe saw for use when performing maintenance on nuclear reactors. During usability testing it was found that the operators had

great trouble keeping the saw blade planar, which resulted in jamming and broken blades [25]. The solution found was to constrain the motion of the saw to a plane perpendicular to the surface of the pipe during cutting. For general movement the operator is able to use the saw with unconstrained movement. When the operator is cutting the pipe they can select the mode to constrain the movement of the saw in one plane only. Fig. 2.23 shows the virtual

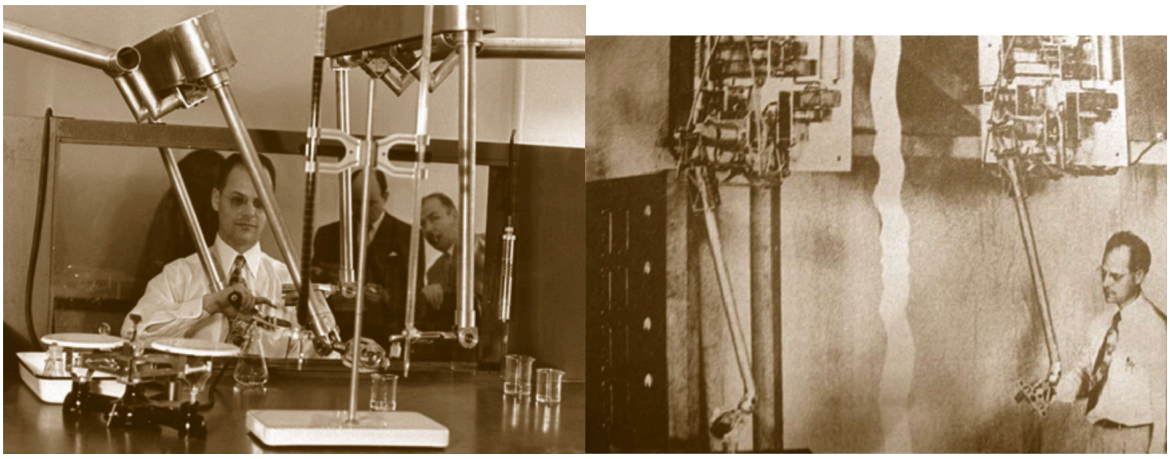

(a) View 1 (b) View 2

Fig. 2.21 Early Teleoperated Machines at Argonne National Laboratory [26].

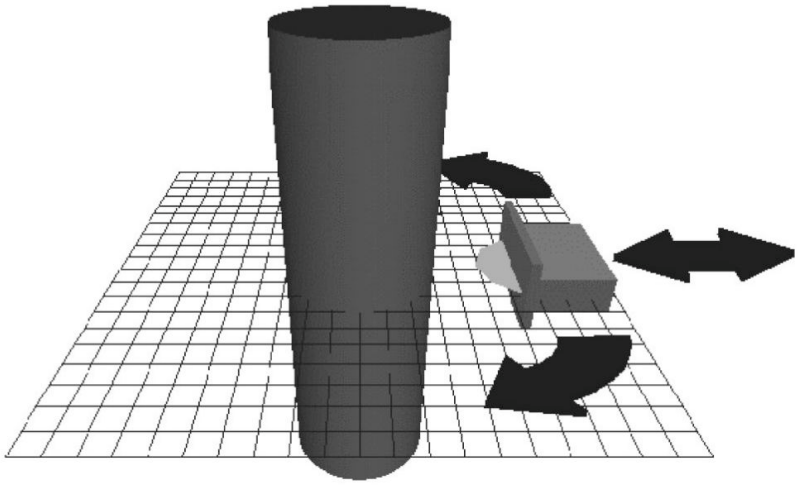

Fig. 2.22 Control Strategy for pipe saw [25].

surfaces imposed on the video feed in the visual interface.

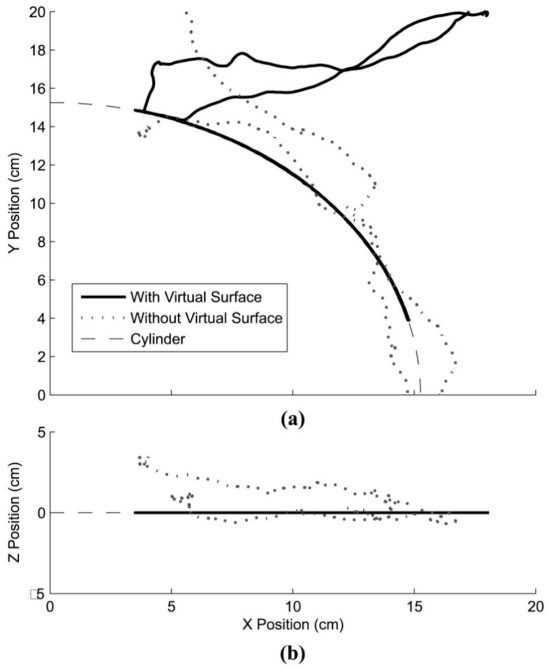

Fig. 2.23 Pipe Saw Virtual Surfaces [25].

2.5 Experimental Platforms for Teleoperation

There is no requirement to use a smaller test system for developing teleoperation. However, using a test system is desirable for the following reasons:

- the machine is too large to fit into available laboratory space [27, 37];
- the machine may be located far away from a suitable location for development [27];
- the machine may be a one-off that cannot be replaced [27];
- it is not necessary to have all of the machine as only a part of the machine's functionality is being teleoperated [46, 48].

Practically any aspect of the behaviour or implementation of the development system is at the discretion of the designer. However, the more closely the test system replicates the behaviour of the field machine the easier it will be to apply results and design features. Example teleoperation development scenarios are:

- Proof of Concept — teleoperation is being developed but without retrofitting a base machine. The control algorithm for a large machine is to be studied or refined. A part of the machine is isolated and used in a test laboratory [46, 65].

- Design for Retrofit – an existing fully functional machine is to be retrofitted for teleoperation. All the mechanical design work has been done and the teleoperation system needs to be designed to accommodate the machines mechanical behaviours [24].

Fig. 2.24 shows the teleoperation system design for a log grabber arm test system [46]. It is notable that it is separated into several distinct layers and modules. Separating the teleoperation system components requires more design effort but makes it easier to transfer components between different systems. Fig. 2.25 shows the log grabber test system in use.

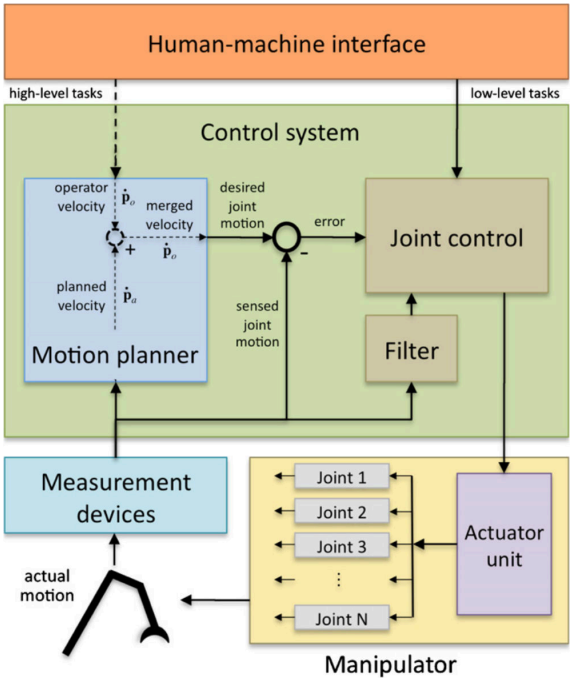

Fig. 2.24 Concept Teleoperation System [46].

Only the log grabber arm has been recreated in the laboratory. The target machine already exists so it makes sense to use the same hardware.

Sometimes the field machine is small enough to be used in the laboratory. The field machine can have work done in the laboratory and outside in more structured and controlled conditions [69]. An example is a small excavator that was fitted out for teleoperation with arm position is shown in Fig. 2.26. The hydraulic control valves have been converted to electrical operation from the original hand levers. Fig. 2.27 shows the arm controlled excavator being tested on a spoil pile.

Fig. 2.28 shows a test system for controlling an excavator arm. The focus of this study was to determine how to make a two-lever control more intuitive [48]. It is important to take into account the effects additional systems have on system pressure and performance.

Fig. 2.25 Log grabber test system [42].

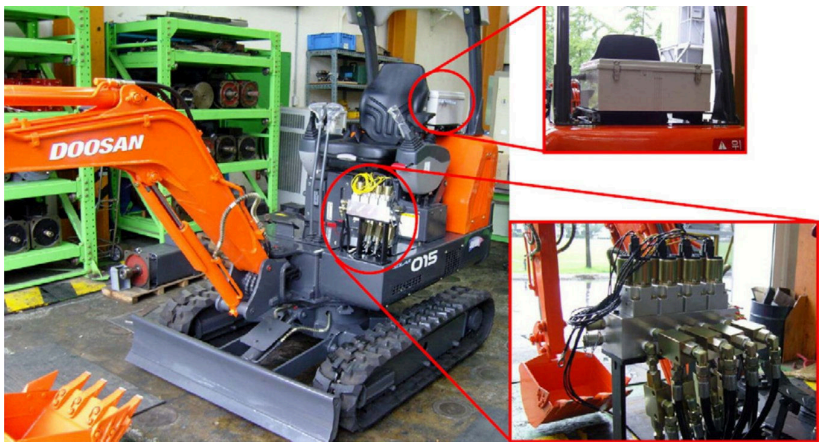

Fig. 2.26 Excavator fitted out for teleoperation [69].

Fig. 2.27 Excavator being field tested [69].

Being able to model and predict these effects is a significant challenge when developing teleoperation on a sub system.

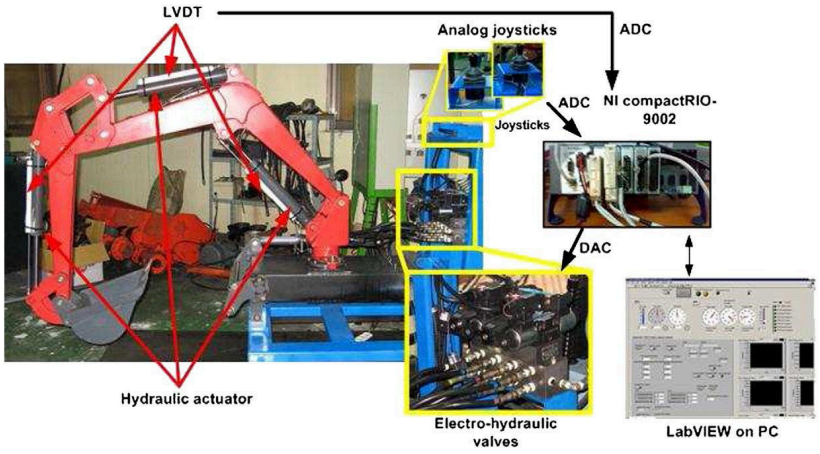

Fig. 2.28 Excavator test system [48].

2.6 Haptic Feedback

Haptic feedback is useful for providing supplementary information to the operator through means such as force reflection or virtual force fields [25, 70]. Haptic feedback devices may be custom built [44], or commercially available systems such as the Phantom Omni. One of the main challenges of haptic feedback is maintaining stability in the presence of time delays. Passivity techniques, like wave variable transforms may help alleviate stability

problems [60, 63, 71, 72]). Haptic feedback has been used to control excavators [43, 47]. Fig. 2.29 shows a mapping of the positions of a Phantom Omni haptic device to the arm on an excavator.

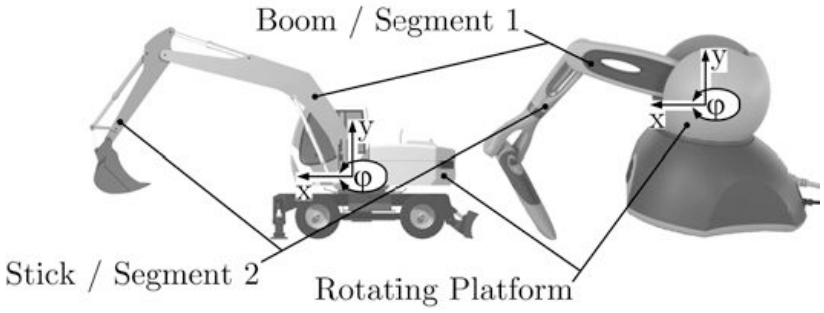

Fig. 2.29 Example mapping of a Phantom Omni haptic device to excavator boom motions [47].

Fig. 2.30 shows a Phantom Omni in use controlling a backhoe [47]. The haptic device was used to evaluate providing trajectory guidance when performing manoeuvres such as shifting soil using the excavator bucket. The Phantom Omni was set up with the arm in the same orientation as the excavator arm. The disadvantage of the setup is that the base of the Phantom Omni gets in the way of the operator's arm. An alternative setup is to have the Phantom Omni arm facing back towards the operator. Appropriate feedback can eliminate any confusion about the movement of the Phantom Omni arm relative to the excavator arm.

Mingde, Dingxuan et. al. [73] describe a method of force feedback control using velocity control. The force feedback is delivered to a special glove worn by the operator. The improved method involves using position-velocity control, where the displacement of the controller from the zero point results in a velocity signal, and the feedback is based on the velocity error [74]. This research was primarily aimed at telesurgery, but the impedance concepts are applicable to forestry harvesting. An important difference is the use of an ANN[6], as opposed to PID controllers. It is claimed that the use of an ANN results in much better tracking performance [75]. Transparent teleoperation without force sensing is very useful because force sensors are often very noisy and difficult to set up, and machine scaling introduces further difficulties [76]. Bilateral teleoperation of two identical devices based on force sensing has been found to be better than force position feedback [77]. However, such a result is only applicable for non-identical machines if adequate scaling is provided.

[6] Artificial Neural Network

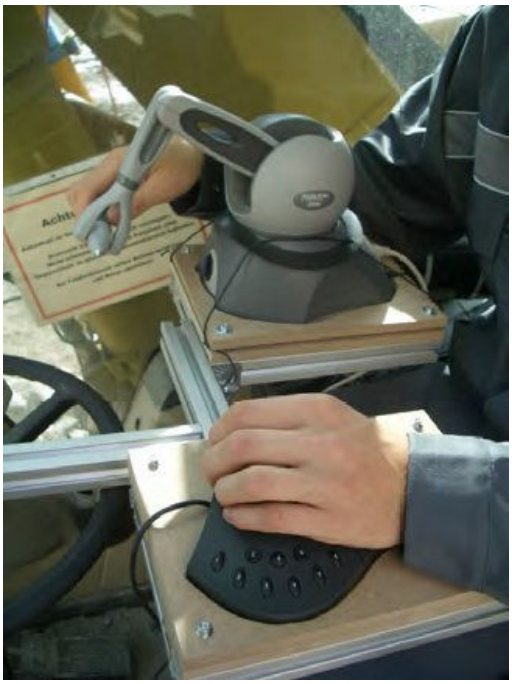

Fig. 2.30 Excavator teleoperation with haptic feedback [47].

2.7 Minimal Modelling for System Identification

This thesis uses identification methods based on physical parameters in a similar way to [78–83]. While [78, 79] state that methods based on measuring individual components are not useful, it is important to have an elementary understanding of how the individual machine components affect the machine behaviour as a whole. Minimal modelling is a framework that is usable in a diverse range of systems including diabetes diagnosis and detection [84], mitral valve modelling [85], rocketry [86] and non-linear modelling in a spring cart [87]. Real-time estimation for system response has been implemented for buildings [88], and minimal modelling based system identification is also capable of doing this. A Phantom Omni provides a good starting point for controlling an excavator as it has a similar kinematic setup [47]. Haptic control is being explored for use in the mining industry [45] and is under development for use in medical applications [70, 89, 90]. A related application is the modelling of friction within the joints of the Phantom Omni such as [91] and [92].

The wavelet method of [91] has the advantage of providing good temporal resolution, but the lack of an attempt to physically justify the meanings of the derived parameters means it is difficult to see the effect of changes in the machine configuration on the model. Naerum [92] is correct in mentioning that unknown parameters can reduce the accuracy of a physical model. However, once again the results leave the question of how changes

in machine parameters affect the identified parameters and the relative contribution each parameter makes to the model accuracy. Minimal modelling can be viewed as an extension to the methods of controlling excavators such as Internal Model Control [93] and Bilateral Matched Impedance Teleoperation [94]. Other modelling methods include Lagrange-Euler and Generalised Newton formulations. One disadvantage with these formulations is they can end up having many parameters and complex mechanisms [95]. There are established methods of identifying excavator parameters such as Generalised Newton, Lagrange-Euler and virtual work formulations [96, 97].

Particular attention is given to papers by Hann et. al. [98], Moorehead et. al. [85] and Wongvanich et. al. [87], that deal with minimal modelling based parameter identification of mechanical systems with non-linearities. Fig. 2.31a and Fig. 2.31b show the step input and response of a spring cart respectively. While the cart exhibits an approximately underdamped linear response, a closer investigation of the step response is required to come up with an accurate minimal model. In particular, frictional damping causes damping to increase at low speeds.

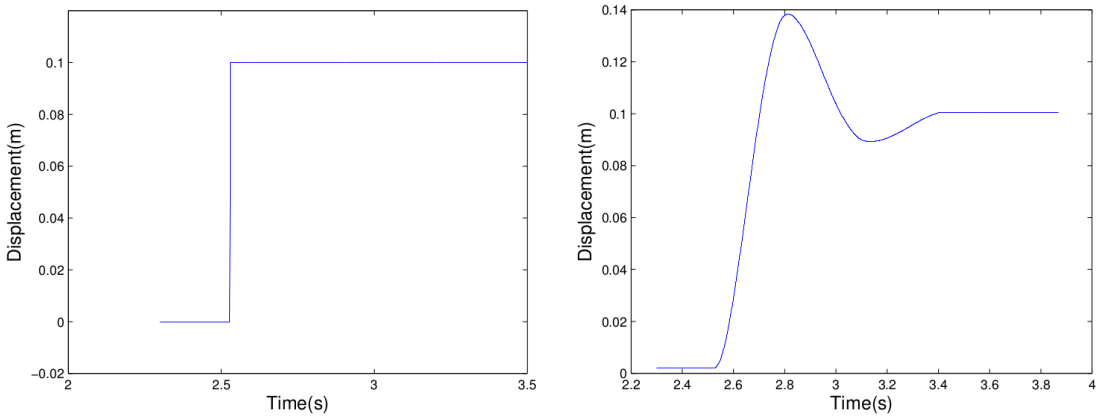

(a) Step Input to Spring Cart.

(b) Actual Spring Cart Response.

Fig. 2.31 Spring Cart Input and Response [87].

Fig. 2.32 shows the true response of the spring cart to a negative step and a linear time variant minimal model. The minimal model is accurate, except for the underestimation of damping at low amplitudes due to friction.

The Laplace Transform approach has been implemented in [99–101] but has issues with accuracy and is highly sensitive to the nature of the function that is being inverted. Non-linear system regression is used in both approaches and is also effective in the time domain. Minimal modelling system identification for the Phantom Omni is not focussed on improving the control response of the Phantom Omni (e.g.[102, 103]), but identifying and modelling its

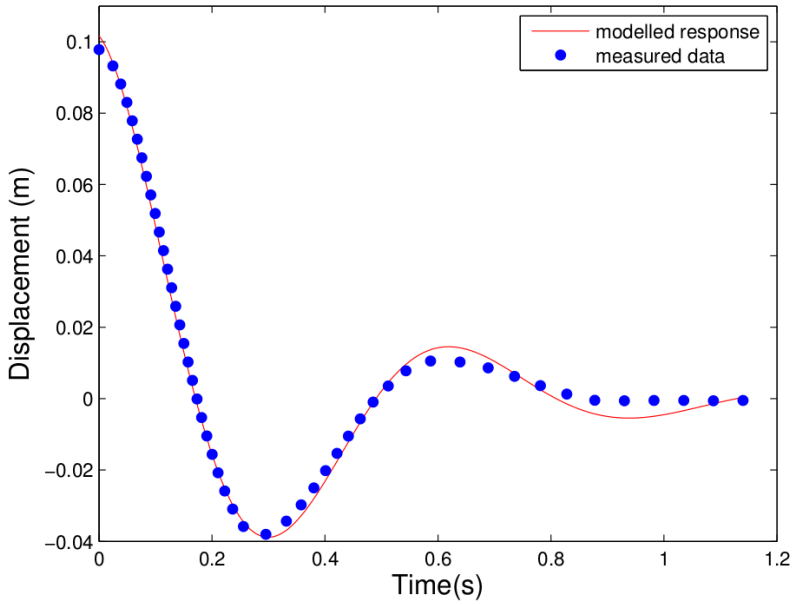

Fig. 2.32 Spring Cart Response with Minimal Model [87].

existing properties as well as developing an algorithm that is generalisable to other systems, for example excavator response. One such study by Cavusoglu et. al. focussed on critically evaluating the control system of a Phantom Premium haptic arm [102, 103].

Energy-based friction models are intended to address a deficiency with the state-of-art of damping and friction modelling. Most models of frictional damping are a function of velocity [81, 83, 104, 105] and there are many forms that get very complex [80, 82, 106, 107]. Often they linearize transfer functions about operating points, use ARX models [108] or just have high order transfer functions [109].

A minimal modelling type method is used to identify parameters in a gravity wave detector [110] but the methods presented in this thesis are intended for identification of non-linearities by examining their effect on the measured amplitude and frequency response of the minimal model. The parameters of the Phantom Omni are identified using sinusoidal steady state analysis. Alternatives such as pseudo-random binary sequences (PRBS) have been used to identify the frequency and phase response of mechanical joints [111]. The advantage of sinusoidal steady state analysis over a PRBS is that non-linearities at a particular frequency are obvious by examining the waveform distortion of the output and there are no intermodulation products to worry about [83].

2.8 Stabilisation of Bilateral Haptic Feedback Under Time Delay

Time delay is inevitable in the process of data transmission on any network, and is a problem as it can destabilize a bilaterally controlled teleoperator. There have been numerous studies that have tried to solve the time-delay problem in the bilateral control of a teleoperator. Anderson and Spong [112] proposed a bilateral control law that maintains stability under the communication time-delay by using transmission line theory (transmission lines have time delay but are resonance free). Niemeyer and Slotine [113] extended this idea and introduced the notion of "wave variable" with the objective of treating the control network as a transmission line, which are inherently passive. Previous teleoperated systems could be made stable with $\sim$0.1 second time delays but passivity was the first method that improved stability by not reducing the control bandwidth [112]. Many papers cover passivity as a solution for compensating time delays in haptic feedback loops, e.g. [24, 60].

The bilateral control based on the scattering theory guarantees the stability of the system for any time delay. However, it loses its stiffness and tends to be sticky as the time delay becomes large [114]. Passive systems can be made stable for a given fixed time delay as well as time varying delays, but the stability condition based on the passivity has been proven to be more conservative [115].

Studies of the operator behaviour by Dyck et. al [116] and Chopra et. al. [117] show that from a control theory point of view, the operator is passive when simply complying with the movement of the controller device, but is active when controlling the position of the haptic feedback device. The working definition of the teleoperation system discussed in this thesis is that the operator *actively* defines and physically maintains the controller in a desired position, and feels what the machine is doing through forces applied to the controller. This situation actually relaxes the stability criteria, as the operator is able to add extra damping when needed to stop oscillations [118, 119].

Hashtrudi-Zaad's PhD thesis [120] addressed stabilising bilateral teleoperation in the presence of time delay, in particular the Bilateral Force/Position Controller [121]. The main motivation for using a position controller is that the robots are used as servomechanisms that take position arguments. In this case, using position feedback is also more versatile, as velocity can always be computed from position numerically. Hashtrudi-Zaad have studied an excavator that is fitted out as a servo position control with impedance control [122]. They take advantage of pre-existing control systems in the excavator to simplify the design of the teleoperation system. This makes the implementation of bilateral haptic feedback much simpler as real time feedback information does not need to be transmitted through the

communication medium. The impedance control helps with scaling the machines, as the controller will always be smaller than the excavator.

The two-port passivity criterion guarantees the stability of teleoperation systems as long as environment, operator, and control network are passive, regardless of the amount of uncertainty in the dynamics of each component; thus resulting in robust stability of the teleoperation system [112, 123]. However, the passivity requirement for each network in a coupled system renders the robust stability condition conservative. For instance, a control network can be active, while the one-port network resulting from the control network termination with a passive environment is passive. Instead, a condition based on the structured singular value (SSV) [124], or absolute stability based on Llewellyn's Absolute Stability Criterion from circuit theory [125], guarantees the passivity of the one-port network caused by terminating the control network with any passive environment (operator). Such passivity condition results in coupled stability for any passive operator and environment.

2.9 Summary

Chapter 2 has reviewed literature from a wide variety of disciplines including forestry, mining, underwater machines and nuclear power plants. The main research gap identified is that nobody has conducted detailed research on the problems relevant to teleoperated forestry harvesting on steep slopes in New Zealand, in particular the problems of retrofitting existing generic machines for teleoperation and haptic feedback. These problems include simplifying the identification of dynamic parameters, stable characterisation of non-linearities such as friction, and implementation of modifications to control systems that are as easy and simple to retrofit to existing machines as possible.

Chapter 3 outlines the setup of the research systems used in the preparation of the thesis.

Chapter 3

System Setup

3.1 Introduction

This chapter describes the research set ups used for performing the research in this thesis. The primary goal was to have laboratory scale versions of the machinery that is used in the field, with similar kinematics and actuation systems. The two main systems used for the laboratory research were a Phantom Omni haptic feedback device, and a laboratory scale hydraulic arm (hydraulic test system). While both systems are different to a full size excavator based tree harvester, they both have similar kinematics, and for the hydraulic test system, the same actuation.

Since the Phantom Omnis were available first, and the general principle of minimal modelling is so transferable between different mechanical devices, the minimal modelling was implemented and tested on a Phantom Omni before the hydraulic test system. The purpose of the laboratory scale hydraulic machine was that (i) a full-size hydraulic machine would have been impractical in the laboratory, and (ii) the use of minimal modelling is intended to produce kinematic models of the hydraulic test system that are transferable between different mechanical systems, so the results obtained from the laboratory scale system can be scaled to a full-size machine.

The Phantom Omni was used to do the first proof of concept of minimal modelling. While the Phantom Omni is primarily designed as a haptic feedback device, its kinematics are similar to an excavator arm, so the minimal modelling results for the movement of the base were applicable to the project as a whole. The minimal modelling done on the Phantom Omni provides a basis for modelling the laboratory scale hydraulic arm, which in turn provides a basis for modelling the full-size excavator. The time delay testing was performed with two Phantom Omnis, as they provided a compact platform for testing response to time delays. In

particular, they would not do too much damage if they became unstable and started moving uncontrollably.

The hydraulic robot controls were implemented using ROS. In particular, Scion New Zealand has experience in using ROS for remote control on a John Deere 909 tree harvester, and given ROS's modular nature many of the design techniques used on the 909 Project were applicable to this research, in particular the kinematics modelling and control. Since ROS runs on Linux and the teleoperation used Ethernet for communications, the laboratory control system used off-the-shelf general purpose PCs for the control computers, and standard wireless Ethernet hardware for the teleoperation. This was intended to demonstrate that expensive, custom-made hardware was not inherently necessary for retrofitting the existing harvester controls for teleoperation.

Early in the project, an assessment was made on whether to buy and modify a commercial off-the-shelf teleoperation system or to develop a teleoperation system in-house from off-the-shelf parts. The closest purpose built teleoperation systems were considered to be for mining. However, the high cost (NZ$180000) and extensive modifications required resulted in the decision to pursue the development of an in-house system using COTS hardware and custom software written to run in ROS [126]. The choice of in-house development was justified due to the much greater flexibility during development, especially in the control components and architecture. Even if a commercial off-the-shelf teleoperation system becomes available, the findings from the in-house development will provide background and guidance of what is required.

3.2 Phantom Omni Matlab Setup

The system identification, time delay and data driven modelling experiments on the Phantom Omni were performed in Simulink, using libraries supplied by Quarc. The Quarc libraries have blocks and functions for Simulink to interact with the Phantom Omni. The Quarc library provides blocks that interface with the Phantom Omni's IEEE 1394/FireWire interface. Quarc also supplies communications blocks that work over TCP/IP, which allows for experiments with bilateral haptic feedback over a network. The Phantom Omni uses encoders for sensing joint positions, which are converted into joint angles using the Quarc libraries. Since the joint encoders are relative, the Phantom Omni requires calibration from time to time. The calibration could not be done from Matlab and was done with specialised software supplied by Sensable, the manufacturers of the Phantom Omni.

3.2.1 System Identification

The system identification was done using Simulink's standard signal generators. The data was gathered in Simulink, then processed using Matlab code. The minimal modelling system identification did not use any specialised system identification toolboxes, and the data driven modelling used the System Identification Toolbox.

3.2.2 Phantom Omni Time Delay Stability Testing

The time delay testing was performed using two Phantom Omnis and two computers connected to each other over an Ethernet link. The intrinsic time delay between the computers was very small, so delay blocks were put into the simulation to simulate a significant delay. Fig. 3.1 shows the setup that was used in the stability testing.

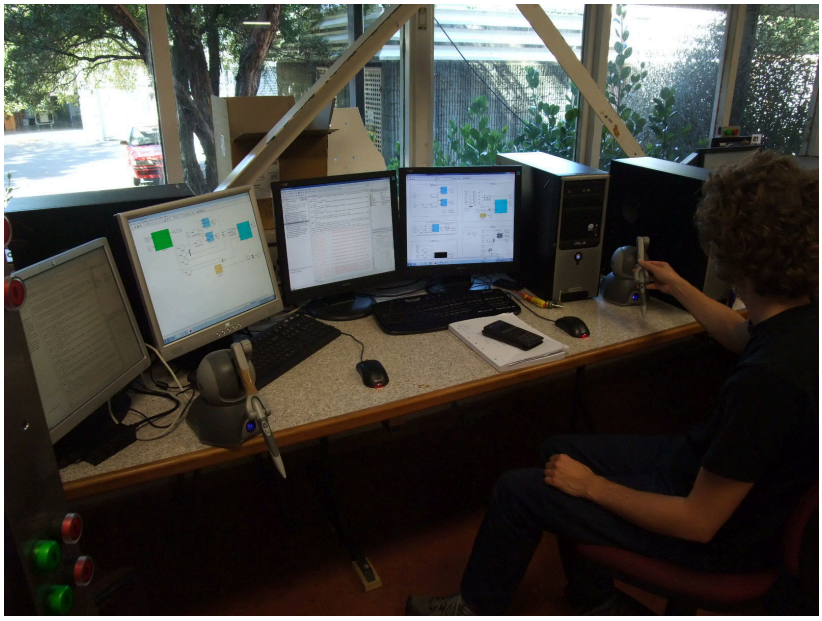

Fig. 3.1 Stability Testing Setup.

3.3 Hydraulic Robot Setup

The research robotic system is a small scale hydraulic arm (Fig. 3.2). The hydraulic arm is similar to a full size excavator, except that only a single joystick is required for control, as there are no controls for the bucket. The machine is immobile so controls for the tracks have not been investigated.

Fig. 3.2 Hydraulic Test System without sensors fitted.

3.3.1 Hydraulics

Fig. 3.3 shows the hydraulics in the hydraulic test system. Each of the three rams is connected to four-way, three-position, closed centre electro-hydraulic proportional valves. The ram load is sensed by the Pressure Compensator valve using a system of sensing lines that detect the highest load pressure on any given ram, then keeps the system pressure at least 110 psi (7.58 bar) higher. Table 3.1 shows the specifications of the hydraulic test system, and Table 3.2 shows the specifications of the hydraulic rams themselves. The maximum forces are based on an operating pressure of 800 psi (5.52 MPa), and the maximum speeds are based on a flow rate of 5.78 L min^{-1}. The exact inner radius of the cylinder was not measured but was calculated from the ratio of maximum extension speed to maximum retraction speed.

Table 3.1 Lab System Hydraulics Specifications.

Part	**Description**
Prime Mover	Electric Motor 4 pole induction, rated output 0.75 kW (1 hp) at 1410 rpm
Pump Flow	5.78 L min^{-1} at 1410 rpm (0.0041 L per revolution)
Pump	Constant Displacement
Valves	Electrically operated proportional valves
Set Point Relief Pressure	800 psi (5.52 MPa)
Maximum Relief Pressure	1130 psi (7.79 MPa) at 5.78 L min^{-1} pump flow and 0.75 kW Prime Mover output
Pressure Compensator Bias Spring	110 psi (0.758 MPa)

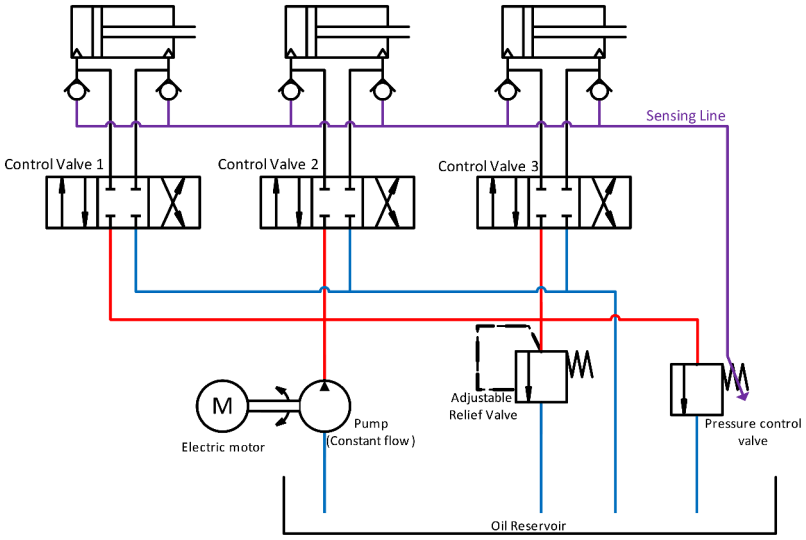

Fig. 3.3 Hydraulic Test System Diagram.

Table 3.2 Hydraulic Ram Specifications.

Quantity	**Ram 1**	**Ram 2**	**Ram 3**
Minimum Length (mm)	395	390	465
Maximum Length (mm)	545	540	720
Cylinder Inner Radius (mm)		26.4	
Cylinder Outer Radius (mm)		31.8	
Ram Shaft Radius (mm)		15.9	
Extension Area (m^2)		$2.190 \cdot 10^{-3}$	
Retraction Area (m^2)		$1.395 \cdot 10^{-3}$	
Maximum Extension Speed (ms^{-1})		0.04398	
Maximum Retraction Speed (ms^{-1})		0.06906	
Maximum Extension Force (N)		12000	
Maximum Retraction Force (N)		7700	

3.3.2 Input and Output

The hydraulic test system uses a PAC and amplifiers to control the valves. The PAC is a SNAP PAC R1 model manufactured by Opto 22. The PAC was chosen because the original target of the teleoperation project was the Trinder ClimbMax. The PAC communicates with the controlling computer through an Ethernet connection. While a computer running PAC Project Basic is required for PAC programming, a different computer can be used for the actual communication of commands. In the laboratory setup the PAC programming computer was a Windows PC, but the general libraries supplied by Opto 22 were used for writing programs in Linux. Fig. 3.4 shows the control cabinet with its associated circuitry.

Fig. 3.4 Hydraulic Arm Control Cabinet. From Top: Power Supply, PAC, Protective Circuit Breaker and Connections, PWM Generators ($\times 3$).

The PAC is programmed from Opto 22's "Pac Control" software. The PAC is programmed using control charts (Fig. 3.5), which are very similar to flow charts, and run simultaneously. The `WatchDog_Timer` and `Control` charts run indefinitely, but the `Powerup` chart runs when first powered to launch the other two charts. The watchdog time has a period of one second and is reset every time a new control packet is received. If the watchdog timer expires, the PAC shuts the valves so the hydraulic arm does not move. The valve commands are sent to the PAC as 32 bit floating point values in the range of -100 to +100, where a command of +100 represents maximum extension, and -100 represents maximum retraction. The valve commands have a dead band, where any valve command with an absolute value less than 1 is rounded to zero.

The `Control` chart sends the received valve commands to DAC[1] modules that output a control voltage from 0 V to 10 V. The DAC outputs are sent to PWM generators (Valves 2 and 3), or valve current controllers (Valve 1). The M171 PWM generators (Fig. 3.4, lower right) for Valves 2 and 3 are motor drivers but are suitable for driving valves. The base ram has controllers that control the valve coil directly, but the other two rams have motor controllers that generate a PWM voltage to drive the valve coils. Tests of the resistance and inductance of the valve coils shows the coils have a fast enough response (time constant

[1] Digital to Analogue Converter

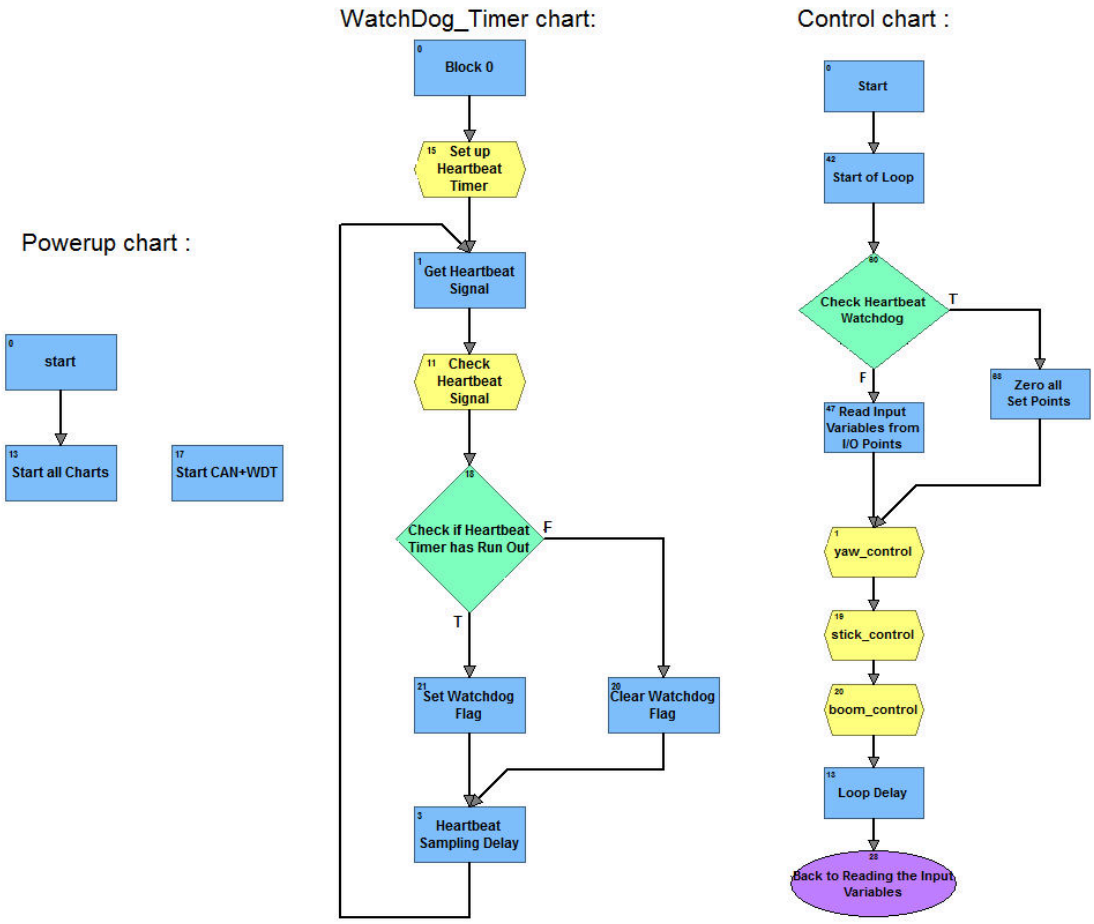

Fig. 3.5 PAC Control Charts.

140 µs) to assume the valve current changes instantaneously at the 100 Hz frequency of PWM operation.

Valve 1 has two valve current controllers. The DAC output is programmed to put out a non-zero voltage to a single valve at a time. Valves 2 and 3 have a single PWM generator each. The PWM output is switched between the valve coils using relays depending on whether the valve command is for the ram to extend or retract. While this arrangement saves on outputs in the PAC, if there are enough output channels this is not necessary and omission simplifies the output hardware.

3.3.3 Robot Sensing

Two types of sensors were used on the hydraulic arm's joint angles: slope sensing and ram length sensing. The slope sensors are IMU[2] based and the ram length sensors use string encoders. The sensor data is received over a USB[3] to CAN[4] bus adapter connected to the "local" control computer and processed for both feedback about the machine state and control. Fig. 3.6 shows the hydraulic test system with the rams and arm links labelled. In Fig. 3.6 Link 1 can be thought of as the boom and Link 2 as the stick.

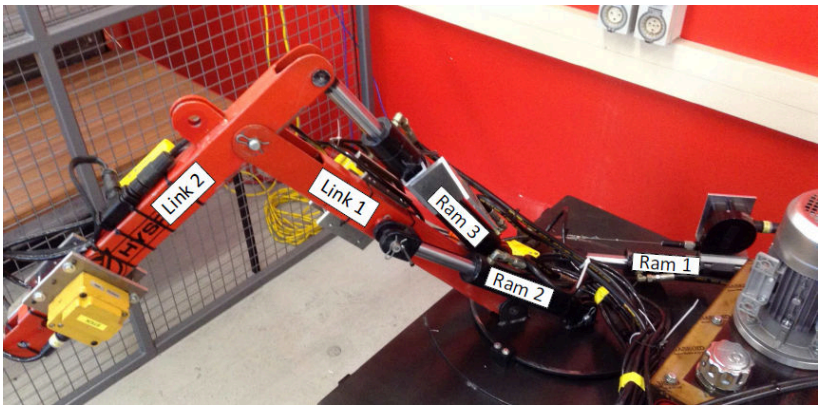

Fig. 3.6 Hydraulic Test System with Links and Rams Labelled.

Joint Encoders

Joint encoders were considered for use, but the joints in the hydraulic robot have not been engineered for inclusion of joint encoders. As a result, slope sensors were favoured, with

[2]Inertial Measurement Unit
[3]Universal Serial Bus
[4]Controller Area Network

calculation of joint angles from ram length measurements. Excavators have a similar problem with joint encoders, as their joints are designed for durability, not precision.

Slope Sensors

Slope sensors (Fig. 3.7) use an IMU to compute the gravity vector, which is then used to calculate the slope angle, roll and pitch. The advantage of using this type of slope sensor is they are self-contained, do not require calibration and can be mounted on the arm at any convenient point. The differences in sensed angles can be used to calculate joint angles between different arm segments.

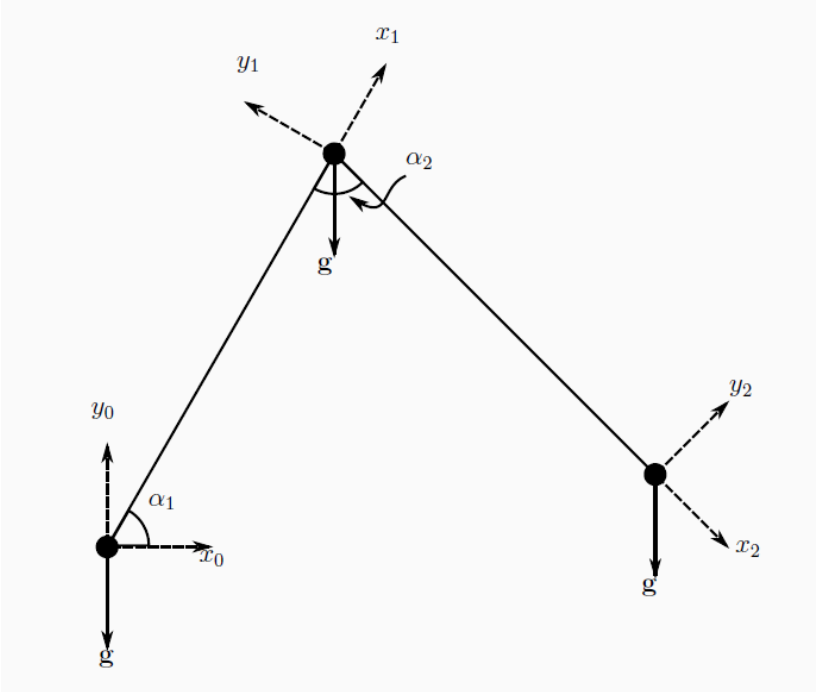

Fig. 3.7 Principle of Gravity Vector Based Joint Angle Measurement.

Fig. 3.8 shows the slope sensors that were supplied by Trimble. Slope sensors were fitted to the base, boom and stick links. The slope sensors are the most sensitive when the joint rotation axis is perpendicular to the gravity vector, and have zero sensitivity when the joint rotation axis is parallel. For this reason, the slope sensors are suitable for measuring the shoulder and elbow joint angles but unsuitable for measuring the waist angle.

The main shortcoming of using slope sensors based on IMUs is that cancellation of the non-gravitational accelerations requires complex algorithms. Any imperfection in the correction causes the joint angles to appear to change when in fact they are not changing. This effect was noticed on the hydraulic arm and caused instability with some control regimes,

Fig. 3.8 Hydraulic Arm Showing Trimble Slope Sensors.

particularly with the haptic feedback. The haptic feedback would respond to movements "seen" by the slope sensors which did not actually happen.

Ram Length Sensing

String encoders were used for the research, because they are non-invasive and easy to set up. The main issues with using string encoders are that the dimensions of the triangle must be measured accurately, and the angle accuracy depends on the initial calibration. The encoders used were Trimble CE21 encoders, and these require calibration after every power cycle. In the lab the string encoders were calibrated by driving all the rams to their shortest lengths and setting that reading as zero. Once the string encoder was calibrated the string encoder reading was added to a "zero length offset" distance to obtain the true length of the ram for calculations.

Fig. 3.9 shows the string encoder setup to measure the length of Ram 2, which measures the angle at the shoulder joint. The situation shown is an example of where the slope sensors give incorrect readings, since the shoulder joint is "leaning back" towards the waist joint. The ram length derived angle measured at $-6°$ ($6°$ clockwise of vertical) but the slope sensor read $6°$.

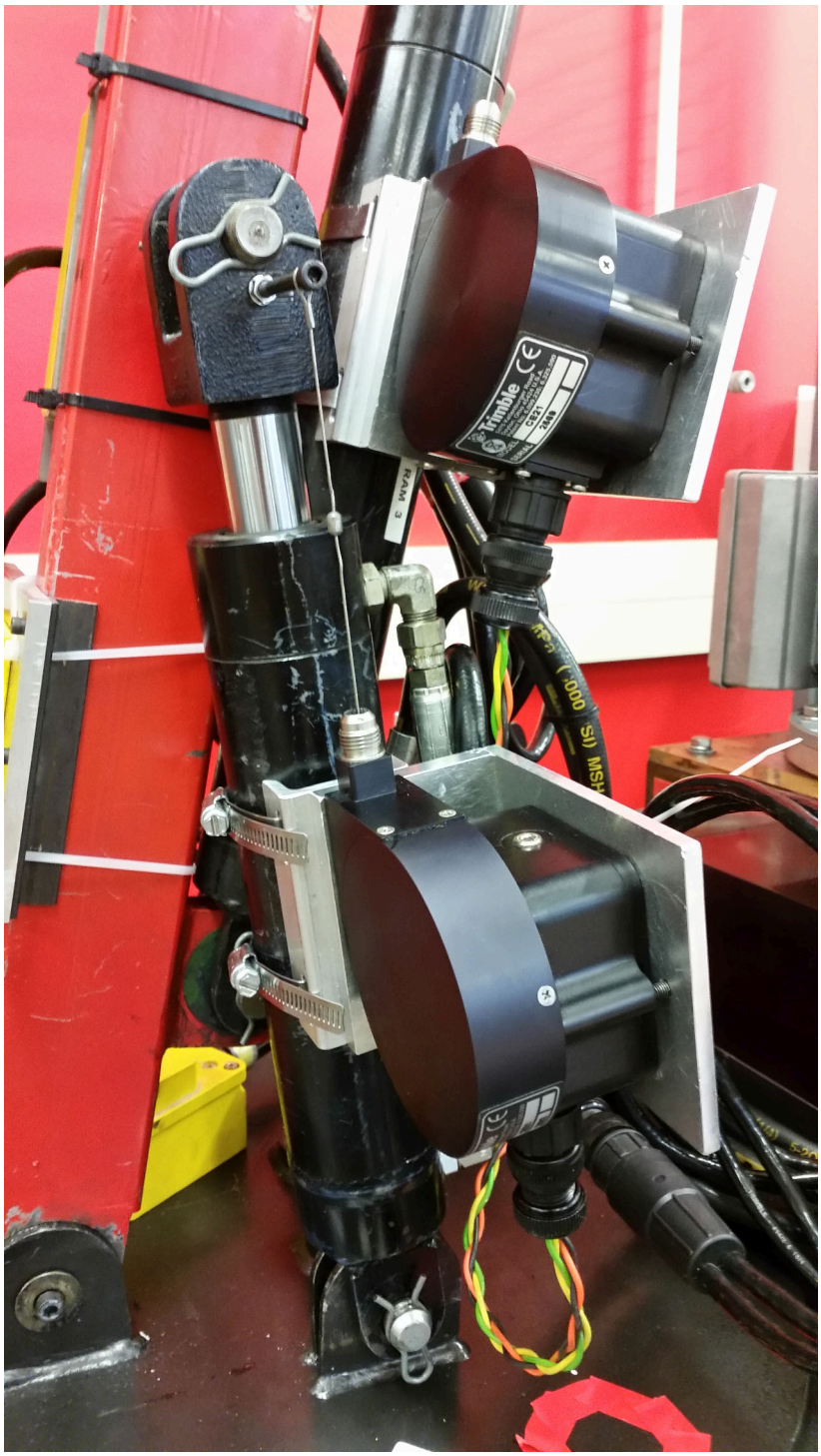

Fig. 3.9 String Encoder Installed to Measure Ram Length.

3.3.4 Kinematics and Joint Torques Model

Appendix B shows drawings of the hydraulic test system with dimensions used to calculate joint angles and ram forces. The drawings are generated from a SolidWorks model of the arm, and the information about the arm's joints is exported as a URDF[5] file for use with ROS's kinematic functions. The URDF file contains information about the joints, their locations, orientations and offset angles. The advantage of using the URDF data export is that all the kinematic properties of the hydraulic test system are directly linked to a single model.

While the URDF model works with joint angles, the actuators that need control are hydraulic rams. The data in the URDF file includes information about the locations of the ends of the rams, so that for a given target set of joint angles a set of ram lengths can be easily generated using the standard kinematic libraries included with ROS (see next section). In practice, the ram lengths were calculated entirely from information in the URDF file, but the equations below give some insight into how the calculations were performed. The method for calculating the joint torques is given in Appendix C.

Ram 1

Page 2 in Appendix B shows the rotating base in its "zero angle" position (3.1). The result in (3.1) is given in radians, so the quantity 0.57648 in (3.1) is 33.03° in radians.

$$\theta_{\text{base}} = \cos^{-1}\left(2.7773 - \left(\frac{x_1}{288.35}\right)^2\right) - 0.57648 \tag{3.1}$$

The ram force is computed using the *torque angle*, given by ϕ_{base} as shown in (3.2).

$$\phi_{\text{base}} = \cos^{-1}\left(\frac{x_1}{176} - \frac{1224.1}{x_1}\right) \tag{3.2}$$

The ram force can then be derived from the torque, moment radius and torque angle, as shown in (3.3).

$$\begin{aligned} F_1 &= \frac{\tau_1}{r_1 \sin(\phi_{\text{base}})} \\ &= \frac{\tau_1}{0.088\sqrt{1 - \left(\frac{x_1}{176} - \frac{1224.1}{x_1}\right)^2}} \end{aligned} \tag{3.3}$$

[5]Unified Robot Description Format

The torque is given in (3.4).

$$\tau_1 = 0.088F_1\sqrt{1-\left(\frac{x_1}{176}-\frac{1224.1}{x_1}\right)^2} \tag{3.4}$$

Table 3.3 gives an overview of Ram 1's torque capabilities at 800 psi (5.52 MPa) system pressure.

Table 3.3 Ram 1 Dynamic Specifications.

	Load Torque (N m)		
Ram Position	**Extension**	**Retraction**	**Ram Displacement** (mm)
Full Retraction	548.3	351.9	395
Full Extension	555.3	356.3	545
Any Position	1056	677.6	464.2

Ram 2

The derivations of joint angles and torque angles is similar to Ram 1. The resulting equation for joint angle is given in (3.5).

$$\theta_{\text{boom}} = \cos^{-1}\left(1.659-\left(\frac{x_2}{354.2}\right)^2\right)-\frac{\pi}{2} \tag{3.5}$$

The ram force is computed using the torque angle, as shown in (3.6).

$$\phi_{\text{boom}} = \cos^{-1}\left(\frac{191.94}{x_2}+\frac{x_2}{865}\right) \tag{3.6}$$

The ram force is given in (3.7).

$$F_2 = \frac{\tau_2}{0.145\sqrt{1-\left(\frac{191.94}{x_2}+\frac{x_2}{865}\right)^2}} \tag{3.7}$$

The torque is given in (3.8).

$$\tau_2 = 0.145F_2\sqrt{1-\left(\frac{191.94}{x_2}+\frac{x_2}{865}\right)^2} \tag{3.8}$$

Table 3.4 gives an overview of Ram 2's torque capabilities at 800 psi (5.52 MPa) system pressure.

Table 3.4 Ram 2 Dynamic Specifications.

	Load Torque (N m)		
Ram Position	**Extension**	**Retraction**	**Ram Displacement** (mm)
Full Retraction	1727	1108	390
Full Extension	1040	667.1	540
Any Position	1740	1117	464.2

Ram 3

The derivations of joint angles and torque angles is similar to Ram 1. The resulting equation for joint angle is given in (3.9). The offset of -1.4802 rad radians represents an angle offset of $6.6 - 1.41 - 90 = -84.81$ degrees.

$$\theta_{\text{stick}} = \cos^{-1}\left(2.1533 - \left(\frac{x_3}{427.45}\right)^2\right) - 1.4802 \tag{3.9}$$

The ram force is computed using the torque angle, as shown in (3.10).

$$\phi_{\text{stick}} = \cos^{-1}\left(-\frac{1161}{x_3} + \frac{x_3}{300}\right) \tag{3.10}$$

The ram force is computed using the joint angle directly (3.11).

$$F_3 = \frac{\tau_3}{0.15\sqrt{1 - \left(-\frac{1161}{x_3} + \frac{x_3}{300}\right)^2}} \tag{3.11}$$

The torque is given in (3.12).

$$\tau_3 = 0.15F_3\sqrt{1 - \left(-\frac{1161}{x_3} + \frac{x_3}{300}\right)^2} \tag{3.12}$$

Table 3.5 gives an overview of Ram 3's torque capabilities at 800 psi (5.52 MPa) system pressure.

Table 3.5 Ram 3 Dynamic Specifications.

	Load Torque (N m)		
Ram Position	**Extension**	**Retraction**	**Ram Displacement** (mm)
Full Retraction	233.9	150.1	460
Full Extension	1111	712.7	720
Any Position	1800	1155	590.3

3.3.5 Visual Feedback

Visual feedback comes from an Axis M2014 IP[6] camera mounted on the turntable, as shown in Fig. 3.10. The IP cameras can stream directly to an Internet Browser window, so ROS is not strictly required. However, it is good to integrate the camera with the rest of ROS as the browser interface provides no direct means of integrating extra information, such as camera status. ROS uses a modified version of the Axis camera drivers.

Fig. 3.10 Turntable Camera Location.

The camera data is streamed over Ethernet, received by the computer, and converted into a ROS camera image message. The mounting of the camera (Fig. 3.11) is close to the view an operator would see if they were operating a full sized harvester. If no signal from the camera is received for one second, an annotation "`Stream is not Live`" appears on the display to warn the operator that the picture being seen is not being updated.

The turntable camera is mounted on a special pole to give it a field of view approximately the same as what an operator in a full size excavator would see. Fig. 3.10 shows the operator's camera position. On a full sized harvester there are two main positions for mounting the operator's camera: mounting the camera inside the cab in the approximate position of the operator's head, or mounting it outside the cab just above the front windscreen. The main advantage of having the camera in the operator's cab is that the camera requires less protection from the weather and the viewpoint is more similar to an operator's. The main advantage of mounting above the front window is the camera is always out of the way and the picture is less affected by a dirty windscreen and protective bars.

[6]Internet Protocol

Fig. 3.11 Turntable Camera View.

3.3.6 Controller Setup

The controller runs on a PC using ROS. The valve commands from the ROS PC are sent over an Ethernet link to the PAC, which generates the drive voltages for the coil controllers. Fig. 3.12 shows the fundamental structure of the control architecture used for the hydraulic test system. An explanation of the quantities in Fig. 3.12 is given in Table 3.6. The quantities in Fig. 3.12 are linked by transfer functions, some of which (e.g. the PID[7] controller) are linear, but others (e.g. Non-Linearity Compensator and length sensor) are non-linear. The overall goal is to provide a linear response of the system as a whole, from r to $x^\star$.

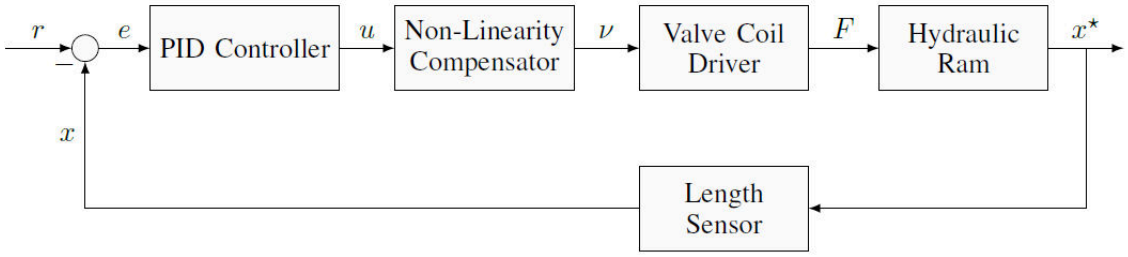

Fig. 3.12 Low Level Control Loop Architecture.

[7]Proportional-Integral-Derivative

Table 3.6 Explanation of Quantities in Fig. 3.12.

Quantity	Description (unit)
x	Input position (m)
e	Error (m)
u	PID Command, normalised so that $\|u\| \leq 1$ (no unit)
v	Converted Valve Command, normalised so that $\|v\| \leq 100$ (no unit)
F	Force on the ram (N)
x	Position of the ram as measured by the sensors (m)
$x^\star$	Actual position of the ram (m)

3.4 Robot Operating System (ROS) Setup

ROS is used to implement the control system, including receiving sensor data, calculating control commands and sending control commands to the PAC. ROS has been selected and used because it is specifically designed for robotics development. In particular, ROS includes event queueing and message handling libraries, which means development can concentrate on the control algorithms themselves rather than data handling. A full description of the capabilities of ROS is beyond the scope of this thesis, but more information may be found at the ROS Website (`http://ros.org`). ROS is designed to run on Ubuntu Linux. The control computers in the laboratory run ROS Hydro on Ubuntu Linux 12.04 "Precise Pangolin".

ROS works by separating the data handling from the data processing. A ROS control system will work with a large number of small programs (nodes). The nodes communicate with each other using messages. A sending node publishes a message with a named topic (e.g. `/node/position`) and another node can receive this data by subscribing to the topic. At the highest level, teleoperation is implemented in ROS by splitting the programs it runs between a "local" machine (the machine connected to the robot) and a "remote" machine (the machine the controller interacts with). In reality, with the exception of hardware inputs and outputs there is no fundamental boundary between the two machines. In fact, the "local" and "remote" machine can be the same! The flexibility of the machine arrangements is useful for testing the teleoperation against running the teleoperation program on a single machine.

The ROS computers in the laboratory interact with each other over Ethernet, though the existing control system can easily be extended to interactions using the internet. The ROS computer connected directly to the PAC is designated the "local" computer. The local computer is designated the master, and is the control computer that interacts with the hydraulic test system directly. The present control system is set up as a "single-master" system. The primary advantage of a single master system is its ease of setup. The main

drawback of the single master system is that if the master computer fails the entire control system stops working.

3.4.1 Software Interface with the Robot

The design philosophy in this research is to maintain ROS's goal of having small nodes that do a small number of things well and keep coupling between different nodes to a minimum. It is also useful to maintain a hierarchy of different software functions in line with the ROS Control architecture diagram given in Fig. 3.13. Doing this allows decoupling the design of the ROS control system from the design of the sensors, and reduces the interdependency between different algorithms, which may have been written by different people at different times. The PAC is accessed from ROS through a node that uses library code supplied by Opto 22. The ROS interface takes data in ROS topics, translates it into the form used by the PAC, and then despatches it to the PAC over Ethernet using Opto 22's own API[8] functions.

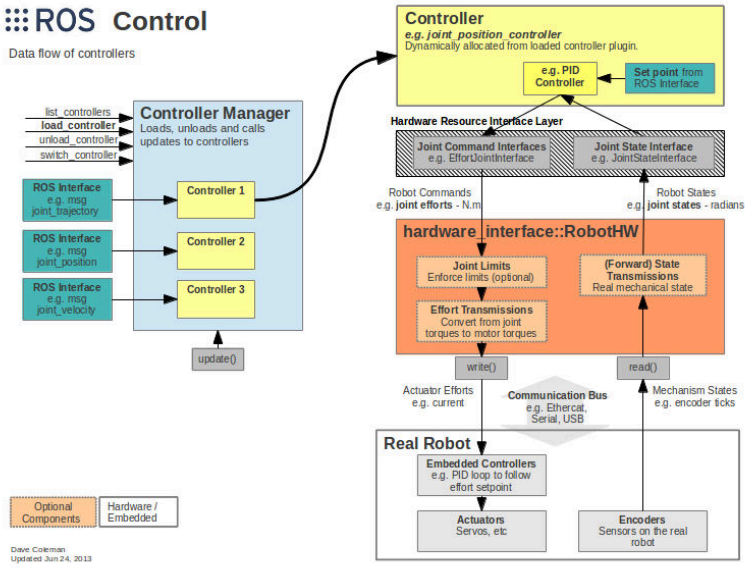

Fig. 3.13 High Level ROS Control Architecture.

[8] Application Programming Interface

3.4.2 Control System Safety

The main safety features in the hydraulic test system are a SIL[9] 3 rated E-Stop[10], and a watchdog timer that is programmed into the PAC. The E-Stop disables the pump if the button is pressed. The button may be pressed at any time and must be reset before attempting to start or restart the pump.

The PAC itself is not turned off if the E-Stop is activated, so it will continue to issue the same command to the valve. While the hydraulic pump will no longer be providing power, the valves may still be open to some degree. This scenario can still cause ram movement, but any problems with this can be eliminated by providing an input to the PAC from the emergency stop and cutting off the circuit to the valve coils.

Another important influence on safety is the computer and network security. Security issues that are important include authenticating commands and making sure that a given harvester or robot is only controlled by a single computer. In the laboratory only one controller computer was used at a given time. Scenarios in which more than one computer is trying to communicate with it simultaneously have not been tested.

3.4.3 Kinematics Model

Although it is possible to derive the kinematics directly from the drawings in Appendix B, an add-in to SolidWorks was used to generate a kinematics solver plug-in directly from the SolidWorks model of the robot. The kinematics architecture uses ROS's `MoveIt!` libraries to perform kinematics (forward and inverse) and path planning. `MoveIt!` has the advantage of having complete integration with ROS with a wide range of kinematics and motion planning libraries, and once the robot model has been created all of these libraries are available. The robot model is based on a URDF files and SRDF[11] files. The URDF file has information about the joint locations and axes in the robot, and does not require detailed information about the size and shape of the robot or its parts; this is a beneficial feature for existing equipment that lacks a detailed solid model.

The SolidWorks model was created from direct measurement of the robot and includes the arm, table and legs. In particular, the solid model allows the derivation of a model of arm inertia that is useful for path planning. The extra information about moments of inertia is included in the SRDF file and is used along with the URDF file by `MoveIt!`. In the case of the hydraulic test system, the solid model, and the assumption it was constructed from

[9] Safety Integrity Level
[10] Emergency Stop
[11] Semantic Robot Description Format

mild steel was also used to calculate the mass and rotational inertia of each arm segment. Achievable path plans are provided by using the rotational inertia from the SRDF file, joint limits from the URDF file, and using them to limit acceleration, speed and joint angles to what the robot is physically capable of.

The coordinate systems specified in the URDF are generated from SolidWorks by specifying reference coordinate systems. Ram lengths in the solid model are calculated by placing reference coordinates at each end of the rams. The ram length can then be calculated from the distance to the two coordinate system origins. This feature is used to measure ram lengths, which otherwise would not be directly possible with a URDF model as URDF models do not allow closed paths in a kinematic chain. A more advanced robot format SRDF is used by `MoveIt!`, as it is able to store extra information such as end effectors and closed kinematic chains.

3.4.4 Open Loop Joystick

The Open Loop joystick is the simplest of the interfaces. The joystick controls the hydraulic valves directly, with no sensor feedback. While it is not autonomous, its main use is for sensor calibration and testing if the rams are controllable or not. For example, the hydraulic test system requires the rams to be driven to their shortest length before calibration. The open loop joystick interface is the only way to do this, as any other one that uses sensor feedback will not work because the sensors are not calibrated or are not working. The open loop joystick setup is also the most similar in principle to the way an excavator is conventionally operated. Note that in the laboratory setup only a single joystick is required, as the joystick used has three degrees of freedom and the robot has three degrees of freedom.

3.4.5 Phantom Omni

The Phantom Omni is operated in ROS using a third party library written by Dane Powell [127]. The library creates a ROS node that provides an interface between the Phantom Omni hardware and ROS. The Phantom Omni is connected using IEEE 1394/FireWire, so a FireWire driver is required in Linux, which in this setup was the Juju driver. A suite of Linux utilities are provided by Sensable/Geomagic for calibrating the Phantom Omni, and these are used for checking the state of Phantom Omni before usage in ROS. Once the Phantom Omni is set up and running, conventional ROS programming can be used to read in the joint positions and issue joint commands.

3.4.6 Implementation of Teleoperation

Teleoperation is one of the primary goals of the project, and justification needs to be given for why it is not mentioned more specifically in conjunction with the different interfaces and controls. The reason is that ROS is extremely flexible with respect to the layout of the control system, so apart from any changes due to the properties of the communication medium itself (delay etc.) no specific changes are required to the source code.

In ROS, implementation of teleoperation is a matter of determining which programs should run on the local computer and which should run on the remote computer, by setting the `ROS_MASTER_URI` environment variable appropriately. The lab implementation has identical code bases on both computers, with different launcher files for the local and remote machines. Some programs must run on the remote computer e.g. user interface and input. Others must run on the remote computer e.g. sensor and machine control interfaces. For example, the autonomous robot control has the trajectory generator running on the remote computer, and the real time feedback controllers run on the remote computer. Single computer operation is possible by running both the local and remote programs together, with `ROS_MASTER_URI` set to the IP address of the single computer.

All of ROS's communications run over TCP/IP or UDP[12], so it never actually sees the medium over which it is transmitted. The only effects that are seen in ROS are the latency and data rate. As long as the latency and data rate are within requirements the system will work. As a consequence of using TCP/IP and UDP the teleoperation can be extended to operations over the internet quite easily. The key to easy teleoperation with ROS is to separate out the different software components to run on the local computer and the remote computer. Ideally, the remote computer should generate the high level commands, and the local computer should generate all the low level real time control signals. Autonomy works extremely well with this type of teleoperation due to its ability to separate high level and low level commands. Implementing teleoperation in this way allows the same code base to be used on both the local and remote computers. While in the longer term specific code bases can be developed, the use of identical code bases eases research and development significantly.

3.5 Summary

Chapter 3 has outlined the setup of the research systems, including the Phantom Omni and the hydraulic test system. In particular, it has described the overall system architecture and the means of control using ROS and the PAC. Special attention has been paid to the

[12] User Datagram Protocol

ability to ease the transition from a laboratory system to a full size machine, particularly the transferability of the minimal model and similar actuation systems. This is a distinguishing feature from many development systems that use a highly specialised laboratory system, but then face the problem of converting the laboratory control system to something suitable for use on a full sized machine.

Chapter 4 is a study of time delay compensation of haptic feedback using two Phantom Omnis.

Chapter 4

Delay Compensation for Haptic Feedback

4.1 Introduction

This chapter presents an investigation of the stability of a teleoperation system, where the host and client machines are controlled using individual PD controllers. The investigation has been performed with two Phantom Omnis connected together over an Ethernet network link, with a similar architecture to the teleoperation system as a whole. The purpose of this research is to study how haptic feedback interfaces could be used for forestry teleoperation, most particularly maximising resistance of a haptic feedback control system to instability. The goal of using haptic feedback is to enhance the operator's perception of the state of the machine. In an ordinary manned machine the operator is able to use cues such as actuation force on the controls and the feel of the position of the machine (the "arse-o-meter") to judge machine position, load and safety. While controllers such as keyboards, mice and joysticks are perfectly useful as input devices, the actuator feel an operator inside the machine receives during machine operation is lost, meaning the operator can lose awareness of the behaviour of the machine. The goal of the haptic feedback is to restore some of this feeling by being able to feel the machine. Since the haptic feedback device is being used both as a control input and a force output, the haptic feedback arm and the machine can end up 'controlling each other' and oscillating, a problem made worse by time delays. Internet links have uncertain time delay, which makes the problem more difficult and the implementation of fixed delay compensation impractical.

The special feature of the haptic feedback architecture outlined in this chapter is that both the controlled signals and the 'round trip' delayed signals are presented to a given host or

client machine - meaning there are two possible paths for haptic feedback with known delays. While PD controllers are simple to implement, they are affected by time delays, resulting in control system instability. This chapter analyses the stable area of a bilateral teleoperation system with independent PD controllers, including the standard PD control method, and the method based on switching between two standard controllers using a 'selector function', that selects the haptic feedback to use based on the local (controlling device) and remote (device being controlled over the network) positions, speeds and time delays. Small time delays and low speeds mean the position of the local device is reflected entirely in the local device, whereas at high speeds and long time delays the haptic feedback is based on the delayed position of the local device.

The objective is to create a teleoperation system where the host and the client machines are tuned to individually optimise their own responsiveness and stability, then use the resulting system with teleoperation over the internet. Unfortunately, the internet has unpredictable (and possibly unsymmetrical) time delay. To get around this while preserving transparency, a 'selector function' is used to determine how to do the position feedback. For short delays, the client machine uses the host machine's position directly. For long delays, the host machine uses the round-trip delayed host signal. This is designed to give the operator a feel of how quickly the machine can react to a user input. The end goal is to pick an amount of 'selection' of the haptic feedback signal that keeps both systems stable while simultaneously maximising transparency and minimising perceived delay.

4.2 Stability and Performance Evaluation

4.2.1 Stability

Due to the presence of delays in the communication channel and uncertainties in operator and especially environmental dynamics, the stability robustness and performance of teleoperation system will degrade. In fact, the stability and performance are often contradictory, and a compromise must be found between these two elements. If all the teleoperation system components are LTI, one can take advantage of linear system stability analysis tools such as the Nyquist criterion or root locus method to make sure that all the closed-loop system poles are in the right-half-plane [128]. Energy-based stability analysis such as Lyapunov and passivity theories are often used [129] for this purpose too. For the analysis of teleoperation system stability, passivity-based analysis tools are mainly employed, but Llewellyn's Absolute Stability Criterion is less conservative.

4.2.2 Passivity-Based Methods

Passivity theory, which applies equally well to linear and non-linear systems, is a powerful method to analyse stability of teleoperation systems. If the energy injected to the system is not negative (i.e. the system dissipates energy), the system is passive [130]. The mathematical description of a passive single port device is shown in (4.1) for force f and velocity v.

$$\int_0^t f(\tau)v(\tau)d\tau + E(0) \geq 0, \forall t \geq 0 \tag{4.1}$$

Equation (4.1) holds for admissible forces and velocities, where the product is defined to be positive when power enters the system port. Equation (4.1) states that the energy supplied to a passive network must be positive for all time. For the Master-client two-port network block of Fig. 4.1(b), the passivity condition is expressed as (4.2).

$$\int_0^t f_1(\tau)v_1(\tau) - f_2(\tau)v_2(\tau)d\tau + E(0) \geq 0, \forall t \geq 0 \tag{4.2}$$

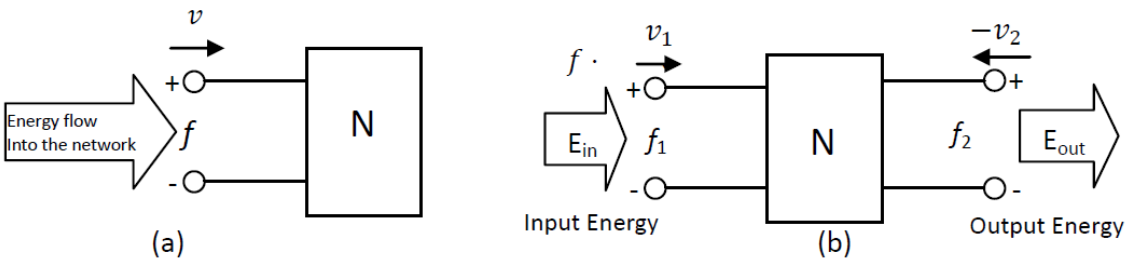

Fig. 4.1 Energy Flow Diagrams for One- and Two-port Networks.

The idea of passivity can be used to guarantee stable operation without exact knowledge of model information.

4.2.3 Llewellyn's Absolute Stability Criterion

Llewellyn's Absolute Stability Criterion [120] is derived from the properties of electrical networks, but can be applied to mechanical devices by substituting force for voltage and speed for current. An N-port electric network can be characterized by the relationship between voltage $u(t)$ and current $i(t)$. For a linear time invariant (LTI) one-port network in the frequency domain, this relationship is specified by its impedance $Z(s)$ according to

$$U(s) = Z(s)I(s) \tag{4.3}$$

where $U(s)$, $I(s)$ are the Laplace transforms of $u(t)$ and $i(t)$ respectively. For an LTI two-port, this relationship is conveniently specified by $Z(s)$ in matrix form, according to

$$\begin{bmatrix} U_1(s) \\ U_2(s) \end{bmatrix} = \begin{bmatrix} Z_{11} & Z_{22} \\ Z_{21} & Z_{22} \end{bmatrix} \begin{bmatrix} I_1(s) \\ I_2(s) \end{bmatrix} = Z(s) \begin{bmatrix} I_1(s) \\ I_2(s) \end{bmatrix} \tag{4.4}$$

where $U_1(s)$, $U_2(s)$, $I_1(s)$, $I_2(s)$ are the Laplace transforms of the respective input voltage and current from different ports. Llewellyn's Absolute Stability Criterion states that an LTI two-port impedance network $Z = \begin{bmatrix} Z_{11} & Z_{22} \\ Z_{21} & Z_{22} \end{bmatrix}$ is absolutely stable if and only if the conditions listed below hold.

1. $Z_{11}(s)$ and $Z_{22}(s)$ have no poles in the right half of the complex plane.
2. Any pole of the $Z_{11}(s)$ and $Z_{22}(s)$ is on the imaginary axis is simple with real and positive residue.
3. $\Re(Z_{11}) > 0$, $\Re(Z_{22}) > 0$, $\frac{2\Re(Z_{11})\Re(Z_{22}) - \Re(Z_{12}Z_{21})}{|Z_{12}Z_{21}|} > 1$

Llewellyn's Absolute Stability Criterion results in a less conservative robust stability condition compared to the two-port passivity criterion. If it can be ensured that the host-client two-port network corresponding to a teleoperation system meets the absolute stability criterion, then the teleoperation system is stable.

4.2.4 Transparency

Considering the teleoperation system in Fig. 4.2, the host and client forces and positions can be written in terms of the exogenous input forces F_{u}^* (user) and F_{e}^* (environment) as (4.5) and (4.6) where α_{ij}, β_{ij} for $i, j = 1, 2$ are rational transfer functions.

$$\begin{aligned} v_{\mathrm{u}} &= \alpha_{11} F_{\mathrm{u}}^* + \alpha_{12} F_{\mathrm{e}}^* \\ v_{\mathrm{e}} &= \alpha_{21} F_{\mathrm{u}}^* + \alpha_{22} F_{\mathrm{e}}^* \end{aligned} \tag{4.5}$$

$$\begin{aligned} F_{\mathrm{u}} &= \beta_{11} F_{\mathrm{u}}^* + \beta_{12} F_{\mathrm{e}}^* \\ F_{\mathrm{e}} &= \beta_{21} F_{\mathrm{u}}^* + \beta_{22} F_{\mathrm{e}}^* \end{aligned} \tag{4.6}$$

The system provides position matching, or kinematic correspondence, if and only if the following conditions hold.

1. Kinematic Correspondence Condition:

$$\frac{\alpha_{11}}{\alpha_{21}} = \frac{\alpha_{12}}{\alpha_{22}} = \gamma_{\mathrm{v}} \tag{4.7}$$

holds, where γ_v is the position scaling factor. In the same way, force matching is providing if and only if

2. Force Matching Condition:

$$\frac{\beta_{11}}{\beta_{21}} = \frac{\beta_{12}}{\beta_{22}} = \gamma_f \tag{4.8}$$

holds, where γ_f is the force scaling factor.

For the two Phantom Omni situation γ_v and γ_f are chosen as unity since the machines are identical. For other scenarios (e.g. haptic control of an excavator) however these quantities will not in general be unity because the host and client devices may have different position and force capabilities. The impedances transmitted to the operator and environment, as shown in Fig. 4.2, are defined and derived in term of the α and β parameters according to (4.9).

$$Z_{to} = \left.\frac{F_u}{V_u}\right|_{F_e^*=0} = \frac{\beta_{11}}{\alpha_{11}} \tag{4.9}$$

$$Z_{te} = \left.\frac{F_e}{V_e}\right|_{F_u^*=0} = \frac{\beta_{22}}{\alpha_{22}} \tag{4.10}$$

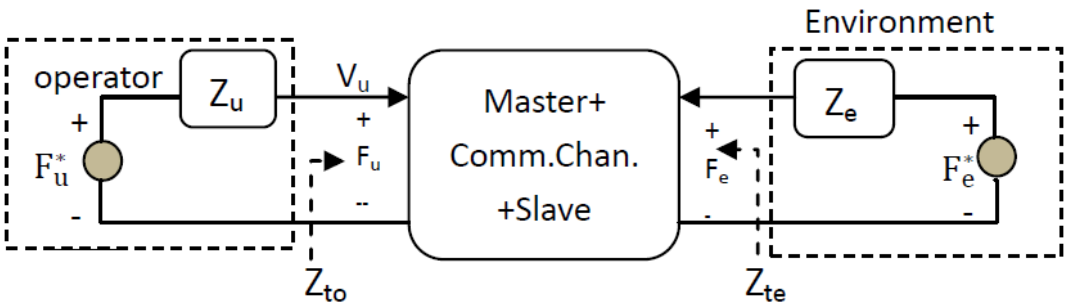

Fig. 4.2 Network Block Diagram of a Teleoperation System.

Bilateral impedance matching is defined as a condition in which the transmitted impedance to the operator and environment match the environment and the operator impedances, respectively, that is Equations (4.11) and (4.12) must hold.

$$Z_{to} = Z_e \equiv \left.\frac{F_e}{v_e}\right|_{F_e^*=0} \tag{4.11}$$

$$Z_{te} = Z_u \equiv \left.\frac{F_u}{v_u}\right|_{F_u^*=0} \tag{4.12}$$

In fact, bilateral impedance matching is composed of two unilateral impedance matching conditions, namely operator impedance matching (4.13) and environment impedance matching (4.14). From (4.5)-(4.6), (4.9)-(4.10) and (4.11)-(4.12), one can express the two matching conditions in terms of α and β as

- Operator impedance matching:

$$\frac{\beta_{11}}{\alpha_{11}} = Z_{\text{to}} = Z_{\text{e}} = \frac{\beta_{21}}{\alpha_{21}} \rightarrow \frac{\beta_{11}}{\beta_{21}} = \frac{\alpha_{11}}{\alpha_{21}} \tag{4.13}$$

- Environment impedance matching:

$$-\frac{\beta_{22}}{\alpha_{22}} = Z_{\text{te}} = Z_{\text{e}} = -\frac{\beta_{12}}{\alpha_{12}} \rightarrow \frac{\beta_{12}}{\beta_{22}} = \frac{\alpha_{12}}{\alpha_{22}} \tag{4.14}$$

4.3 Robot Setup and Results

The system is set up as described in Section 3.2.2, and consists of two Phantom Omni haptic devices: a 'host' and a 'client' (sometimes described as 'master' and 'slave'). The host device is used by the operator for haptic feedback, and the client device responds to the operator's command and environmental disturbances. It is important to note the Phantom Omnis are being used as *servomechanisms*, so the internal dynamics are abstracted away from the haptic feedback implementation. The control system is set up in Matlab, and consists of the server that is used by the operator, and the client, which is the robot being controlled. Fig. 4.3 and Fig. 4.4 show the architectures for the server and client respectively. As well as the signalling, the client and server also incorporate detection of connection status, and the option to turn off the haptic feedback. If haptic feedback is turned off, the client will simply follow the server, and no haptic feedback will be given to the operator. This feature is useful for stabilising the machines if a stability problem occurs.

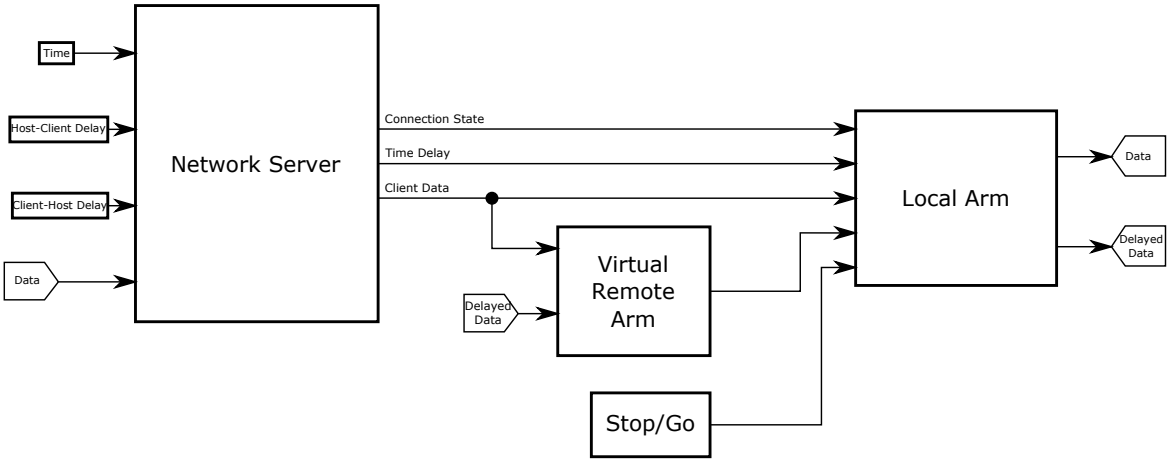

Fig. 4.3 Phantom Omni Server Architecture.

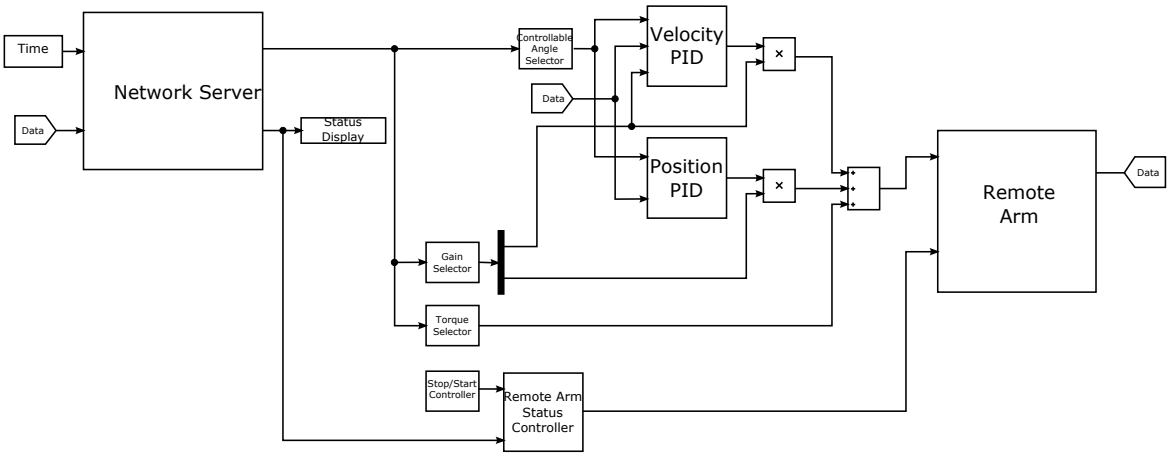

Fig. 4.4 Phantom Omni Client Architecture.

The control system takes a vector of joint position commands and uses conventional PD controllers. While the Phantom Omni has well-known non-linearities [78] the PD control is considered to provide acceptable performance for the purpose of the stability proof. Fig. 4.5 shows the implementation of the Phantom Omni interface for the haptic feedback. The Phantom Omni block is supplied by Quarc/Quanser, and takes an input torque and outputs the joint angles and stylus buttons. The stylus buttons are used to control the haptic feedback, and the angles from the Phantom Omni are converted to Denavit-Hartenberg angles. Conversion to Denavit-Hartenberg angles is used as they entirely separate the joint angles from each other, whereas the raw angles have cross coupling due to the construction of the Phantom Omni's internal mechanisms.

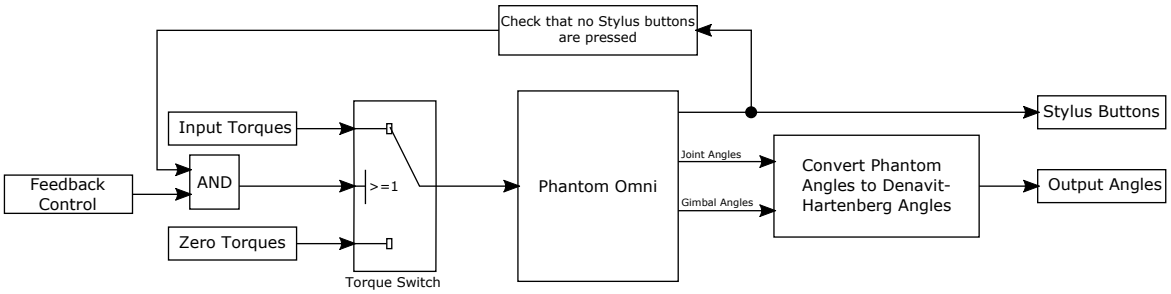

Fig. 4.5 Server Phantom Omni Setup.

Fig. 4.6 shows the architecture of the delay compensator. The delay compensator implements the haptic feedback stabilisation, and uses the measured delay to determine the delay to apply to the server position data. The delay data comes from measurements of a time stamp embedded in the data sent between the server and client. The experimentally derived selector function uses the following inputs:

- Delay time.
- Local and remote positions and speeds and Forces.

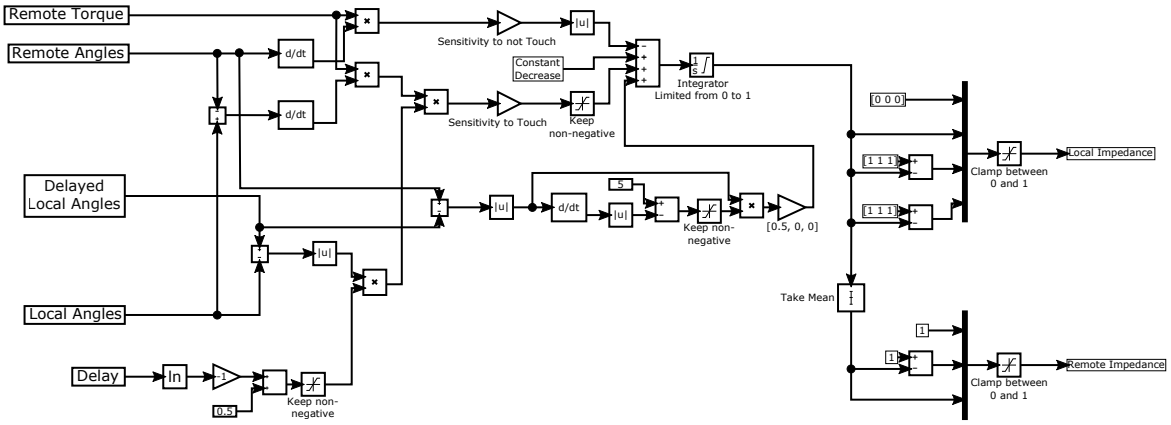

Fig. 4.6 Delay Compensation Architecture.

The proportional and derivative gains (k_p and k_d) are chosen to be the same in both the host and client, to provide symmetry in operation and to ensure there is no complex non-linear coupling between the controllers. For example, if one controller had a much higher proportional gain, a natural resonance could be potentially set up between the client and host even without time delay. The controller is a displacement-displacement method, where the force from the user produces a given displacement, which is copied by the client. Unlike a velocity-velocity method, this approach results in a bounded steady state error even with the presence of numerical rounding. The actuation forces F_h and F_c are defined in (4.15) and (4.16).

$$F_\mathrm{h} = S(t)(k_\mathrm{p}e_\mathrm{hc} + k_\mathrm{d}\dot{e}_\mathrm{hc}) + (1 - S(t))(k_\mathrm{p}e_\mathrm{hh} + k_\mathrm{d}\dot{e}_\mathrm{hh}) \tag{4.15}$$

$$F_c = (1 - S(t))(k_\mathrm{p}e_\mathrm{cc} + k_\mathrm{d}\dot{e}_\mathrm{cc}) + S(t)(k_\mathrm{p}e_\mathrm{ch} + k_\mathrm{d}\dot{e}_\mathrm{ch}) \tag{4.16}$$

The error values as used in (4.15) and (4.16) are calculated as in (4.17), (4.18), (4.19) and (4.20).

$$e_\mathrm{hc} = x_\mathrm{c}(t - \tau_\mathrm{ch}) - x_\mathrm{h}(t) \tag{4.17}$$

$$e_\mathrm{hh} = x_\mathrm{c}(t - \tau_\mathrm{ch}) - x_\mathrm{h}(t - \tau_\mathrm{hh}) \tag{4.18}$$

$$e_\mathrm{ch} = x_\mathrm{h}(t - \tau_\mathrm{hc}) - x_\mathrm{c}(t - \tau_\mathrm{cc}) \tag{4.19}$$

$$e_\mathrm{cc} = x_\mathrm{h}(t - \tau_\mathrm{hc}) - x_\mathrm{c}(t) \tag{4.20}$$

The τ terms represent the different system delays. The quantities τ_{hh} and τ_{cc} are round trip delay times for the host and client, and τ_{hc} and τ_{ch} are the one-way delays from host to client and client to host. For example, if the host moves forward it will create an error e_{cc} in the frame of reference for the client. This error will move the client forward based on the gains k_p and k_d in (4.16), and this error will be reflected back to the host as e_{hh}. The same set of gains are applied on the host in (4.15) to generate a force F_h that "feels" the same as the force on the client, thus providing transparency. The function $S(t)$ (selector) is bounded between 0 and 1, and functions as an automatic continuous switch which selects which controller to use for haptic feedback. The formula for $S(t)$ is given in (4.21).

An experimentally defined formula for $S(t)$ is given in (4.21), where $A(t)$, $B(t)$ and $C(t)$ are defined in (4.22), (4.23) and (4.24) respectively. Since there is no direct measurement of force, the force is modelled from the output of the PD controllers for each robot. The sat int function is an integral, but the value is limited to between 0 and 1.

$$S(t) = \text{sat int}\,(bB(\lambda)C(\lambda) + c - aA(\lambda)d\,\lambda, 0, t, 1, 0) \tag{4.21}$$

$$A(t) = |\dot{x}_c(t-\tau_{ch})F_c(t-\tau_{ch})| \tag{4.22}$$

$$B(t) = F_c(t-\tau_{ch})\frac{d}{dt}|x_c(t-\tau_{ch}) - x_h(t)| = F_c(t-\tau_{ch})\cdot(\dot{x}_c(t-\tau_{ch}) - \dot{x}_h(t))\cdot \text{sgn}(x_c(t-\tau_{ch}) - x_h(t)) \tag{4.23}$$

$$C(t) = (0.5 - \ln(\tau_{hh}(t)))|x_h(t-\tau_{hh}) - x_h(t)| \tag{4.24}$$

The gains a and b in (4.21) determine how sensitive the controller is to external forces. A higher value of a makes the controller more transparent, and a higher value of b makes the controller more sensitive to external forces. The constant c is used to slowly return the controller to transparent bilateral teleoperation when not under actuation. The function $A(t)$ in (4.22) decreases $S(t)$ when the client does work and takes energy out of the system, based on the idea of passivity. There are two main causes of error between the client and host. The first cause of error is when the host arm is moved and the client arm is yet to catch up, and the second is when there is an obstruction, stopping the client arm. The function $B(t)$ distinguishes between these two cases via the derivative in (4.23).

The purpose of the function $C(t)$ in (4.24) is to take the delay into consideration by looking at how much the host has moved over the delay time. For example, with a large time delay, when the host is moved rapidly there will be a noticeable reflected force applied to

the host. In order to maintain stability, the parameter $C(t)$ anticipates this large movement and decreases the reflected force. Coefficients for a, b and c were determined experimentally, and are shown in Table 4.1.

Table 4.1 Assigned a, b and c parameters in (4.21).

	Joint 1	**Joint 2**	**Joint 3**
a	7	5	6
b	5	6	5
c	-0.02	-0.01	-0.01

Two case studies are given to further explain (4.21), (4.22), (4.23) and (4.24).

Case Study 1: Client is moved against barrier.

When the client first touches the barrier, it will try to move through it as it is following the path of the host. The reflected force will be felt on the host as $-F_{\mathrm{c}}(t-\tau_{\mathrm{ch}})$. Since $\dot{x}_{\mathrm{c}}(t-\tau_{\mathrm{ch}})$ is small compared to $\frac{d}{dt}|x_{\mathrm{c}}(t-\tau_{\mathrm{ch}})-x_{\mathrm{h}}(t)|$ in (4.23), $S(t)$ in (4.21) will increase and the host will begin to match the position of the (stopped) client.

Case study 2: Client receives a sharp disturbance or impulse from a stationary position.

At the instant the impulse is first applied, $A(t)$ and $B(t)$ in (4.22) and (4.23) will be 0 since the client is stationary. As the impulse takes effect $A(t)$ and $B(t)$ will both increase and the PD controller in the first term of (4.16) will act to return the client arm to the neutral position. The host will receive the reflected force, delayed by τ_{ch}. If the client instead receives a step input, the situation resembles that in case study 1.

The parameter $C(t)$ is used to take the delay into consideration by looking at how much the host has moved over the communications delay time. For example, if there is a large time delay, a rapid movement of the host will cause a large force on the host due to the amount the client will be expected to move over that time. The extra push back acts as a deterrent to the host moving the host arm so rapidly, as their movement will cause instability. It is interesting to note that the only delay time which is important is the round time delay (the time taken for information to get from the host to the client and back). For example, for a time delay t_{d0}, there is no difference between the cases $\tau_{\mathrm{ch}}=t_{\mathrm{d0}}$,$\tau_{\mathrm{hc}}=0$ and $\tau_{\mathrm{ch}}=0$, $\tau_{\mathrm{hc}}=t_{\mathrm{d0}}$.

To demonstrate the method, an experimental test was performed where the client was moved into a solid object and then pulled off again. An artificial latency of 1 s was added,

since the actual latency in the TCP/IP link was only 0.01 s. Fig. 4.7 shows the displacements of the host (dashed) and client (solid). Initially, the host is moved a distance significantly further than the distance from the client to the object. The client tracks closely the movement of the host, then stops when it hits the object. A force is then pushed back on the client, which brings the host back to a similar relative position to the client. At 5.5 s, the host is moved back to the start position with a further movement back and forward at the end. Overall, the motion of the host and client are closely matched thus providing an initial proof-of-concept of this approach.

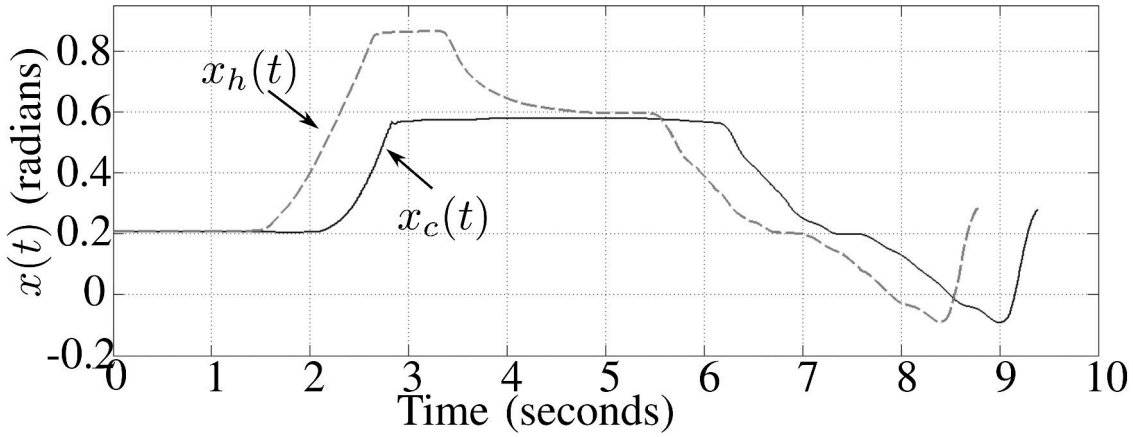

Fig. 4.7 Phantom Omni Client Architecture.

Further tests gave similar results from near-zero to two second time delays as well as time-varying delays suggesting this simplified controller of (4.15) and (4.16) is suitable for haptic feedback in this application.

4.4 Stability Analysis of Teleoperation System using Llewellyn's Stability Criterion

Teleoperators are designed to enable humans to manipulate dangerous, remote or delicate tasks via robotic manipulators with enhanced safety, at lower cost or better accuracy. As shown in Fig. 4.8, a teleoperation system generally has five components, such as those determined by Hashtrudi-Zaad in his PhD thesis [120]:

- The *operator* who wishes to operate the remote task.
- The *host* (or *master*) controller that is used by the operator.

- A communication-channel through which the control commands are transmitted.
- The *client* (or *slave*) manipulator that performs the task.
- The *remote environment* on which the task is conducted by the client machine

The final application of this research is to haptically control a large hydraulic machine from a hand held controller, which is different to the scenario of a host machine controlling a near identical client. The advantage of position-position teleoperation is that it eliminates steady state error when neither machine is moving.

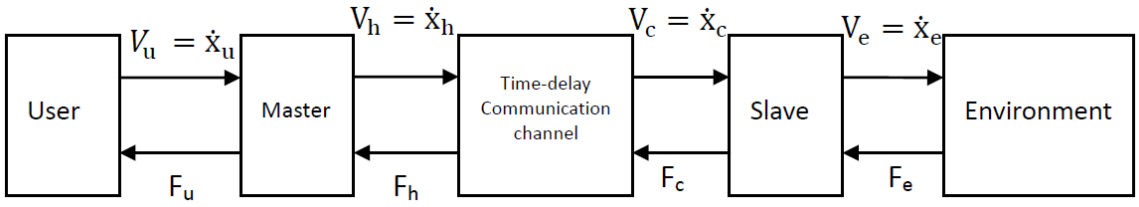

Fig. 4.8 Block Diagram of a Complete Teleoperation System.

Consider the block diagram of a teleoperation system as shown in Fig. 4.8, where the host, client and communication channel are lumped into a linear-time-invariant (LTI) host-client two-port network (MSN) model [112]. The operator and environment are assumed to be in contact with the host and client, and are modelled around their contact operating point by lumped LTI dynamics as (4.25) where x_h and x_c denote respective positions of the host and client arms, and F_h and F_c are the actuator driving forces.

$$\begin{aligned} F_u - F_h &= m_h \ddot{x}_h - b_h \dot{x}_h \\ F_c - F_e &= m_c \ddot{x}_c - b_c \dot{x}_c \end{aligned} \tag{4.25}$$

The quantities b_h and b_c represent the viscous coefficients of the driving mechanism for the client and host respectively. F_u is the force that the operator applies to the host, and F_e denotes the force that the client arm exerts on the environment.

Fig. 4.9 shows the two-channel bilateral haptic feedback teleoperation system with the location of the PD controllers highlighted. PD controllers are easy to set up and implement, but with this approach it is well known that time delays cause instabilities. The objective is to find the stability condition or area of this teleoperation system. The actuation forces F_h and F_c are defined in (4.26).

$$\begin{aligned} F_h &= K_h \cdot (x_h(t) - x_c(t - \tau_{ch})) + D_h \dot{x}_h \\ F_c &= K_c \cdot (x_h(t - \tau_{hc}) - x_c(t)) + D_c \dot{x}_c \end{aligned} \tag{4.26}$$

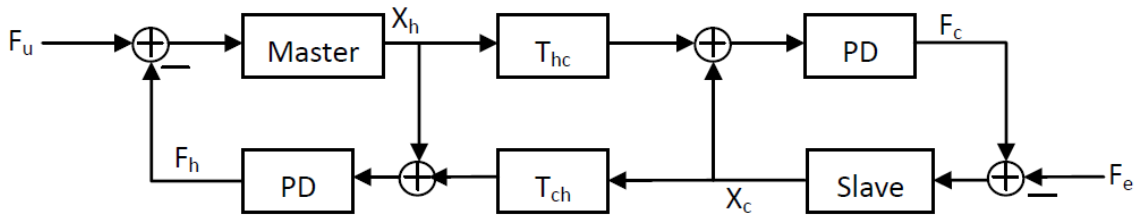

Fig. 4.9 Block Diagram of Independent PD Controllers for Delayed Teleoperation System.

where K_h and K_c are proportional gains, and D_h and D_c are derivative gains. The quantities τ_{hc} and τ_{ch} are the time delays from the host to the client, and from the client to the host, respectively. By applying (4.26) to the dynamics of two-channel teleoperation system, the matrix describing the bilateral delayed teleoperator shown in Fig. 4.9 is given by

$$\begin{bmatrix} F_u \\ F_e \end{bmatrix} = \begin{bmatrix} sm_h + b_h + D_h + \frac{K_h}{s} & \frac{K_h}{s} e^{-s\tau_{ch}} \\ \frac{K_c}{s} e^{-s\tau_{hc}} & sm_c + b_c + D_c + \frac{K_c}{s} \end{bmatrix} \begin{bmatrix} V_h \\ -V_c \end{bmatrix} = \begin{bmatrix} Z_{11} & Z_{12} \\ Z_{21} & Z_{22} \end{bmatrix} \begin{bmatrix} V_h \\ -V_c \end{bmatrix} \tag{4.27}$$

Applying Llewellyn's stability criterion to (4.27), we can find that the teleoperator is stable if the three conditions (4.28)-(4.30) are satisfied at all frequencies $s = j\omega$.

$$\Re(Z_{11}) = b_h + D_h > 0 \tag{4.28}$$

$$\Re(Z_{22}) = b_c + D_c > 0 \tag{4.29}$$

$$\frac{2\Re(Z_{11})\Re(Z_{22}) - \Re(Z_{12}Z_{21})}{|Z_{12}Z_{21}|} = \frac{2(b_h + D_h)(b_c + D_c) - \Re\left(\frac{K_h K_c}{-\omega^2} e^{-j\omega(\tau_{ch}+\tau_{hc})}\right)}{\left|\frac{K_h K_c}{(j\omega)^2} e^{-j\omega(\tau_{ch}+\tau_{hc})}\right|} \geq 1 \tag{4.30}$$

Equation (4.30) holds because of the inequality (4.31).

$$K_h K_c \frac{\sin^2\left(\frac{\omega(\tau_{hc}+\tau_{ch})}{2}\right)}{\omega^2} \leq K_h K_c \frac{(\tau_{ch} + \tau_{hc})^2}{4} \tag{4.31}$$

Considering inequality (4.29), the stability condition (4.28) can be further simplified to (4.32).

$$(b_{\mathrm{h}}+D_{\mathrm{h}})(b_{\mathrm{c}}+D_{\mathrm{c}}) \geq K_{\mathrm{h}}K_{\mathrm{c}}\frac{(\tau_{\mathrm{hc}}+\tau_{\mathrm{ch}})^2}{4} \tag{4.32}$$

When knowing the delayed teleoperator parameters of b_{h}, b_{c}, τ_{ch},and τ_{hc}, we choose suitable PD controller parameters K_{h}, K_{c}, D_{h}, and D_{c} that the stability conditions (4.30), (4.31), (4.32) are satisfied, then the teleoperation system is absolutely stable.

An experiment was set up using two Phantom Omnis, where the host Phantom Omni controlled the position of the client Phantom Omni and vice versa over an Ethernet link. For round trip time delays up to around 0.5-2 seconds (the target time delays for stability), a number of difficulties were experienced in obtaining consistent stability on the teleoperation system with existing controllers. The approach used utilized a simplified control approach based on switching between standard two PD controllers to provide the best combination of stability and transparency. Using PD controllers, it was found to be considerably easier to set up and experimentally tune the system. The stability analysis of the improved control approach is given as follows. For a selector function $S(t) \in [0,1]$ the control laws are set up as follows in (4.33).

$$\begin{aligned} F_{\mathrm{h}} &= S(t)\cdot(K_{\mathrm{h}}e_{\mathrm{hc}}+D_{\mathrm{h}}\dot{e}_{\mathrm{hc}})+(1-S(t))\cdot(K_{\mathrm{h}}e_{\mathrm{hh}}+D_{\mathrm{h}}\dot{e}_{\mathrm{hh}}) \\ F_{\mathrm{c}} &= S(t)\cdot(K_{\mathrm{c}}e_{\mathrm{ch}}+D_{\mathrm{c}}\dot{e}_{\mathrm{ch}})+(1-S(t))\cdot(K_{\mathrm{c}}e_{\mathrm{cc}}+D_{\mathrm{c}}\dot{e}_{\mathrm{cc}}) \end{aligned} \tag{4.33}$$

The error values in (4.33) are calculated as shown in (4.34)-(4.37).

$$e_{\mathrm{hc}}(t) = x_{\mathrm{h}}(t) - x_{\mathrm{c}}(t-\tau_{\mathrm{ch}}) \tag{4.34}$$

$$e_{\mathrm{hh}}(t) = x_{\mathrm{h}}(t) - x_{\mathrm{h}}(t-\tau_{\mathrm{hh}}) \tag{4.35}$$

$$e_{\mathrm{ch}}(t) = x_{\mathrm{c}}(t) - x_{\mathrm{h}}(t-\tau_{\mathrm{hc}}) \tag{4.36}$$

$$e_{\mathrm{cc}}(t) = x_{\mathrm{c}}(t) - x_{\mathrm{c}}(t-\tau_{\mathrm{cc}}) \tag{4.37}$$

These errors are shown in the frequency domain in terms of the frequency domain representation of the speed in (4.38)-(4.41).

$$E_{\mathrm{hc}}(s) = \frac{1}{s}(V_{\mathrm{h}}(s) - e^{-s\tau_{\mathrm{ch}}}V_{\mathrm{c}}(s)) \tag{4.38}$$

$$E_{\mathrm{hh}}(s) = \frac{V_{\mathrm{h}}(s)}{s}(1-e^{-s\tau_{\mathrm{hh}}}) \tag{4.39}$$

$$E_{\mathrm{ch}}(s) = \frac{1}{s}(V_{\mathrm{c}}(s) - e^{-s\tau_{\mathrm{hc}}}V_{\mathrm{h}}(s)) \tag{4.40}$$

$$E_{\mathrm{cc}}(s) = \frac{V_{\mathrm{c}}(s)}{s}(1 - e^{-s\tau_{\mathrm{cc}}}) \tag{4.41}$$

The τ terms represent the different system delays. The quantities τ_{hh} and τ_{cc} are round trip delay times for the host and client, and τ_{hc} and τ_{ch} are the one-way delays from host to client and client to host respectively. Note that the round trip delays τ_{hh} and τ_{cc} are kept separate because if the time delay is variable they will not have the same values.

For example, if the host moves forward it will create an error e_{ch} in the frame of reference for the client. This error will move the client forward based on the gains K_{c} and D_{c} in Equation (4.33) and this error will be reflected back to the host as e_{hc}. The gains K_{h} and D_{h} are applied on the host in (4.33) to generate a force F_{h} that "feels" the same as the force on the client, thus providing transparency.

4.5 Selector Function Analysis

The function $S(t)$ (selector) is bounded between 0 and 1 and functions as an automatic continuous switch that selects which controller to use for haptic feedback. The primary objective of the selector function is to make the haptic feedback as transparent as possible while still preserving stability.

4.5.1 $S(t) = 1$

When $S(t) = 1$, the stability conditions are analysed as below. Applying (4.33) to (4.25), the two-port network model of the delayed teleoperator becomes

$$\begin{bmatrix} F_{\mathrm{u}} \\ F_{\mathrm{c}} \end{bmatrix} = \begin{bmatrix} sm_{\mathrm{h}} + b_{\mathrm{h}} + D_{\mathrm{h}} + \frac{K_{\mathrm{h}}}{s} & \left(\frac{K_{\mathrm{h}}}{s} + D_{\mathrm{h}}\right) e^{-s\tau_{\mathrm{ch}}} \\ \left(\frac{K_{\mathrm{c}}}{s} + D_{\mathrm{c}}\right) e^{-s\tau_{\mathrm{hc}}} & sm_{\mathrm{c}} + b_{\mathrm{c}} + \left(\frac{K_{\mathrm{c}}}{s} + D_{\mathrm{c}}\right) e^{-s(\tau_{\mathrm{ch}}+\tau_{\mathrm{hc}})} \end{bmatrix} \begin{bmatrix} V_{\mathrm{h}} \\ V_{\mathrm{c}} \end{bmatrix} = \begin{bmatrix} Z_{11} & Z_{12} \\ Z_{21} & Z_{22} \end{bmatrix} \begin{bmatrix} V_{\mathrm{h}} \\ V_{\mathrm{c}} \end{bmatrix} \tag{4.42}$$

Applying Llewellyn's stability criterion to the impedance matrix of (4.42), we can find that the teleoperator is stable if the following three conditions (4.43)-(4.45) are satisfied at all frequencies:

$$\Re(Z_{11}) = b_{\mathrm{h}} + D_{\mathrm{h}} > 0 \tag{4.43}$$

$$\Re(Z_{22}) = b_c + D_c \cos(\omega(\tau_{ch} + \tau_{hc})) - \frac{K_c \sin(\omega(\tau_{ch} + \tau_{hc}))}{\omega} > 0 \tag{4.44}$$

where we set $y_1 = \frac{K_c \sin(\omega(\tau_{ch}+\tau_{hc}))}{\omega} - D_c \cos(\omega(\tau_{ch} + \tau_{hc})$, $K_c = 1$, $\tau_{ch} = \tau_{hc} = 3$ s and $D_c = 0.5$, we can check the value of y_1 for all frequencies. Fig. 4.10 illustrates that y_1 variations with frequency tend to a limit when K_c and D_c are fixed. If we choose suitable K_c and D_c, the stability condition 2 will be satisfied.

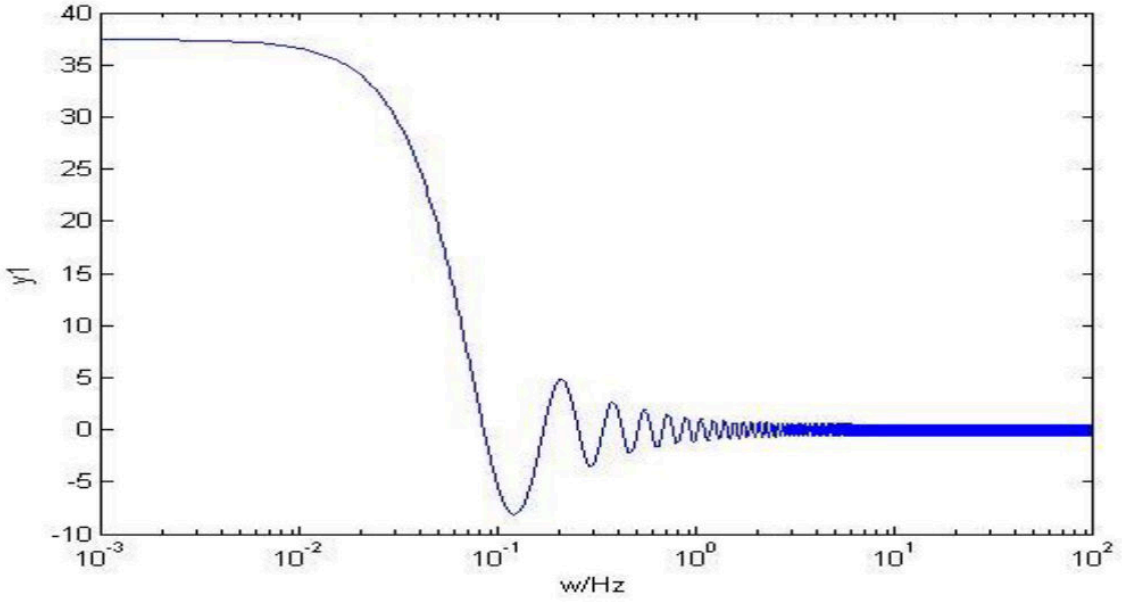

Fig. 4.10 Curve of y_1 with respect to ω.

The stability condition 3 is evaluated as follows:

$$\frac{2(b_h+D_h)b_c+\left(2b_hD_c+D_hD_c-\frac{K_hK_c}{\omega^2}\right)\cdot\cos(\omega(\tau_{ch}+\tau_{hc})-\frac{\sin(\omega(\tau_{ch}+\tau_{hc}))}{\omega}\cdot(2b_hK_c+D_hK_c-D_cK_h)}{\sqrt{\left(D_hD_c-\frac{K_hK_c}{\omega^2}\right)^2+\frac{(K_cD_h+K_hD_c)^2}{\omega^2}}} \geq 1 \tag{4.45}$$

Rewriting (4.45), we get the following inequality:

$$2(b_h + D_h)b_c \geq \sqrt{\left(D_hD_c - \frac{K_hK_c}{\omega^2}\right)^2 + \frac{(K_cD_h+K_hD_c)^2}{\omega^2}} - \left(2b_hD_c + D_hD_c - \frac{K_hK_c}{\omega^2}\right)\cos(\omega(\tau_{ch} + \tau_{hc}) + \frac{\sin(\omega(\tau_{ch}+\tau_{hc}))}{\omega} \cdot (2b_hK_c + D_hK_c - D_cK_h) \tag{4.46}$$

If we define a function $y_2(\omega)$ as the right hand side of (4.46), and $K_c = K_h = 1$, $\tau_{ch} = \tau_{hc} = 3$ s, $D_c = D_h = 0.5$ and $b_h = 1$, we get the variation of y_2 with frequency. Fig. 4.11

illustrates that y_2 variations with frequency tend to a limit when K_c, K_h, D_c and D_h are fixed. If suitable values are picked then stability condition 3 can be satisfied.

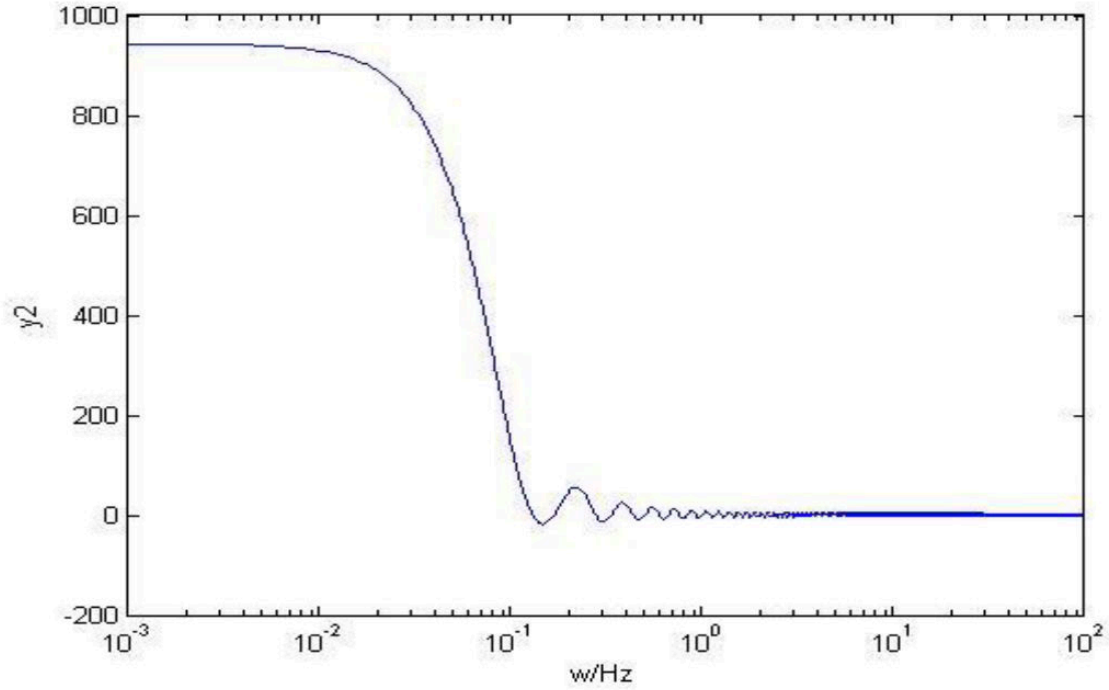

Fig. 4.11 Curve of y_2 with respect to ω.

4.5.2 $S(t) = 0$

When $S(t) = 0$, applying (4.33) to (4.25), the two-port model describing the delayed teleoperator becomes

$$\begin{aligned} Z_{11} &= sm_h + b_h + e^{-s(\tau_{ch}+\tau_{ch})}\left(D_h + \frac{K_h}{s}\right) \\ Z_{12} &= e^{-s\tau_{ch}} \cdot \left(\frac{K_h}{s} + D_h\right) \\ Z_{21} &= e^{-s\tau_{hc}} \cdot \left(\frac{K_c}{s} + D_c\right) \\ Z_{22} &= sm_c + b_c + D_c + \frac{K_c}{s} \end{aligned} \tag{4.47}$$

$$\Re(Z_{11}) = b_h + D_h\cos(\omega(\tau_{hc}+\tau_{ch})) - \frac{K_h}{\omega}\sin(\omega(\tau_{hc}+\tau_{ch})) > 0 \tag{4.48}$$

$$\Re(Z_{22}) = b_c + D_c > 0 \tag{4.49}$$

$$\frac{2(b_{\mathrm{h}}+D_{\mathrm{h}})b_{\mathrm{c}}+\left(2b_{\mathrm{h}}D_{\mathrm{c}}+D_{\mathrm{h}}D_{\mathrm{c}}-\frac{K_{\mathrm{h}}K_{\mathrm{c}}}{\omega^2}\right)\cdot\cos(\omega(\tau_{\mathrm{ch}}+\tau_{\mathrm{hc}})-\frac{\sin(\omega(\tau_{\mathrm{ch}}+\tau_{\mathrm{hc}})}{\omega}\cdot(2b_{\mathrm{h}}K_{\mathrm{c}}+D_{\mathrm{h}}K_{\mathrm{c}}-D_{\mathrm{c}}K_{\mathrm{h}})}{\sqrt{\left(D_{\mathrm{h}}D_{\mathrm{c}}-\frac{K_{\mathrm{h}}K_{\mathrm{c}}}{\omega^2}\right)^2+\frac{(K_{\mathrm{c}}D_{\mathrm{h}}+K_{\mathrm{h}}D_{\mathrm{c}})^2}{\omega^2}}}\geq 1 \tag{4.50}$$

Rewriting (4.50), we get the following inequality:

$$2(b_{\mathrm{c}}+D_{\mathrm{c}})b_{\mathrm{h}}\geq\sqrt{\left(D_{\mathrm{h}}D_{\mathrm{c}}-\frac{K_{\mathrm{h}}K_{\mathrm{c}}}{\omega^2}\right)^2+\frac{(K_{\mathrm{c}}D_{\mathrm{h}}+K_{\mathrm{h}}D_{\mathrm{c}})^2}{\omega^2}}-\left(2b_{\mathrm{c}}D_{\mathrm{h}}+D_{\mathrm{h}}D_{\mathrm{c}}-\frac{K_{\mathrm{h}}K_{\mathrm{c}}}{\omega^2}\right)\cos(\omega(\tau_{\mathrm{ch}}+\tau_{\mathrm{hc}})+\frac{\sin(\omega(\tau_{\mathrm{ch}}+\tau_{\mathrm{hc}})}{\omega}\cdot(D_{\mathrm{h}}K_{\mathrm{c}}-2b_{\mathrm{c}}K_{\mathrm{h}}-D_{\mathrm{c}}K_{\mathrm{h}}) \tag{4.51}$$

As with $S(t)=1$, we also come to the conclusion that the three stability conditions will be satisfied when we choose the appropriate K_{c}, K_{h}, D_{c} and D_{h}.

4.6 Summary

This chapter introduces the notion of a selector function for stabilising bidirectional haptic feedback, in the context of unpredictable time delay, as found on a communication system that uses Ethernet, such as the hardware used for the teleoperation. The haptic feedback stabilisation method uses a 'selector function' that selects the source of the haptic feedback force to apply to the operator. While the selector function is intended to improve stability, the practical system developed also includes a mechanism for turning off haptic feedback, in case the operator does not desire to have haptic feedback present. The feature can also be used to stop oscillations, though the user is also capable of actively damping out the oscillations as well if desired. The Matlab implementation worked well, though a ROS version will need to be developed for deployment on the hydraulic test system.

A further investigation was performed for haptic feedback devices using Llewellyn's Stability Criterion. This is based on finding a basis for determining what PD controller gain coefficients will result in haptic feedback. A theorem for this is derived, and the results explored for a time delay. It is of note that the derivation is for a fully passive system, but future work includes extending the mathematics to a system in which the human operator actively attempts to stabilise the system.

Chapter 5 describes the experiments on the hydraulic test system on teleoperation and autonomous control.

Chapter 5

Hydraulic Machine Teleoperation using ROS

5.1 Introduction

This chapter covers the implementation of teleoperation and semi-autonomous control of the hydraulic test system using ROS. The chapter covers the implementation of the ROS control system, including the detailed implementation of the kinematic model. The hydraulic test system was supplied as is without measurements, so the measurements for the kinematic model were gathered directly from the hydraulic test system. However, developing kinematic models from direct measurements is an important step for the research project, as the teleoperation project is focused on retrofitting existing machinery, for which detailed design information may not be available.

The kinematic model is used to develop the autonomous control. Autonomous control is part of the teleoperation research, as it contributes to the research goals of reducing the cognitive load on the operator, and optimising machine movements for safety and efficiency. While autonomous control on its own is important, a further enhancement is the use of obstacle avoidance. ROS uses a 'scene graph', that is a digital representation of the physical contents of the area the machine is operating in. The data source for the scene graph can either be from sensor data, or models. In this research the data source was a model of the obstacle data, but the scene model can be upgraded to use real time sensor data. However, for the purposes of path planning the data source does not matter – as long as the obstacle position in the scene graph matches the obstacle position relative to the robot in real life the concept of autonomous path planning is proven.

Wherever possible the ROS based control system has been implemented “asynchronously” - messages are generated and received as and when they are generated, as opposed to being part of a central clock domain. The main area in which data is synchronised is when multiple data streams must be merged together, such as CAN bus data from multiple sources. The control system outlined in this chapter is very general purpose, and has been used for system identification of the hydraulic test system as outlined in Chapter 8. The key applicability of the system in this chapter to the research is that the system is the same type as the one that would be used on a full sized harvester. While the hydraulic test system is not a servo mechanism, this research shows that autonomous path planning can be performed even on a non-servo system.

5.2 Initial Concepts

5.2.1 Robots and Kinematics

The initial investigation of the kinematics used an electrically operated robot (Fig. 5.1). The electrically robot was developed in 2011 as an investigation into tree-to-tree forestry movement (the “Stick Insect” [18]). The electrically operated robot was used for kinematics investigation as the kinematic setup was similar to an excavator.

The electrically operated arm’s end effector position has no redundant degrees of freedom, as the end effector moves in a single plane with two degrees of freedom. Fig. 5.2 shows a map of the workspace of the electrically operated arm for 10 mm actuator intervals. The lack of intersection of contour lines implies the solutions are unique. The closer the contours are, the more precision that can be obtained in a particular position.

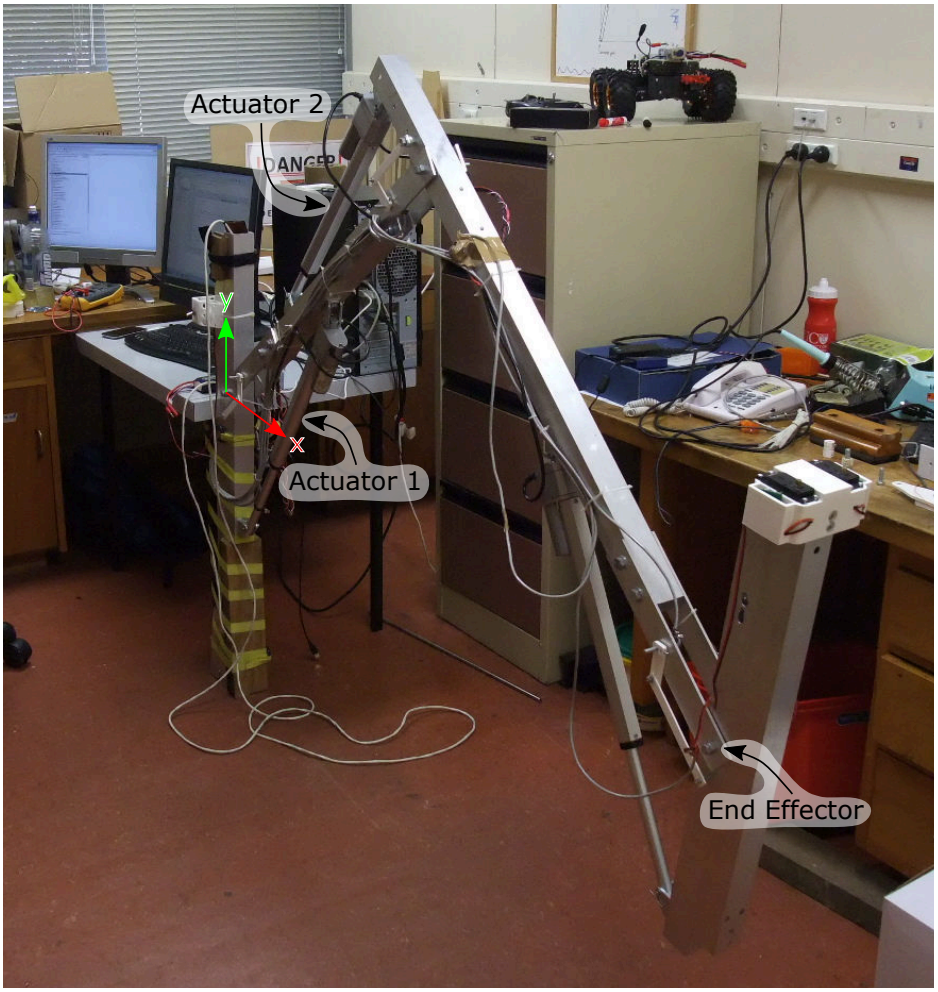

Fig. 5.1 Electrically Operated Robot.

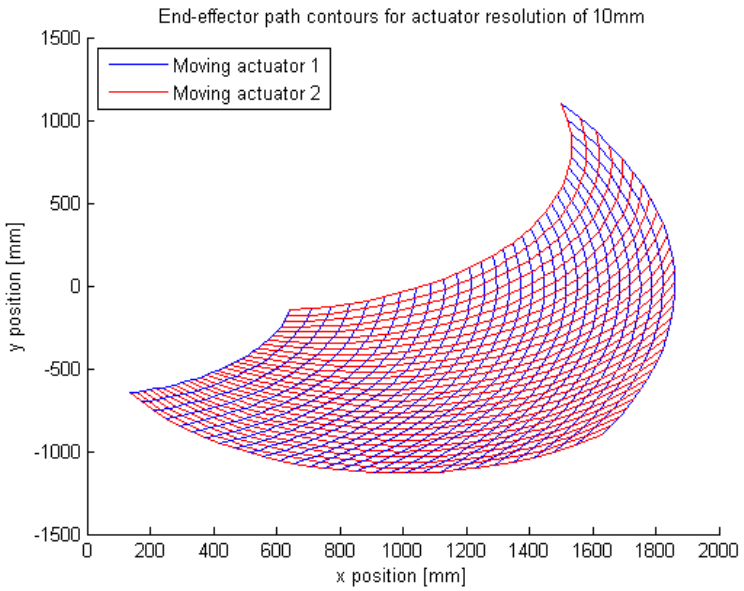

Fig. 5.2 Electrically Operated Robot – Contour Map.

Fig. 5.3 shows the contour map shaded by the angle of intersection between the contour lines. While the spacing between the contour lines gives the positioning resolution, the angle of intersection between the contour lines gives the numerical stability of the inverse kinematic solution. Perpendicular contour lines have minimal numerical instability, and parallel contour lines show a singularity in the actuator length to position mapping. Apart from the numerical stability, the angle is useful for determining the relative overlap between the actions of the different actuators – if the contour intersection is 90°, the robot at that point moves in a rotated Cartesian Coordinate system. If the contours are parallel, the actuators both have the same effect, so the actuator positions for a position in this situation are indeterminate.

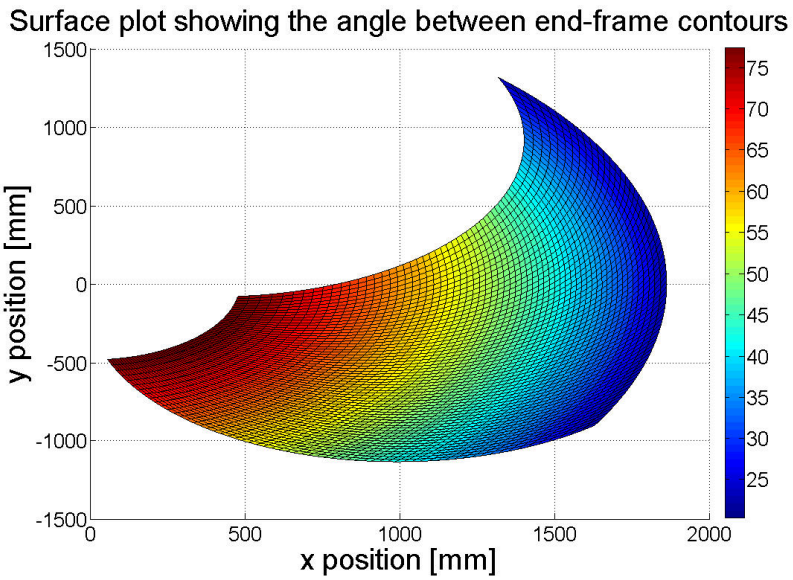

Fig. 5.3 Electrically Operated Robot – Singularity Map.

Fig. 5.4 shows a numerical inverse kinematics solver. The concept behind the figure is that for a given actuator position it was cheaper to store the contours in a lookup table than try to calculate the inverse kinematics directly. In particular, the end effector was capable of being rotated which would have made the kinematic system overdetermined, and this research was intended to provide a basis for how overdetermined kinematic systems would be solved.

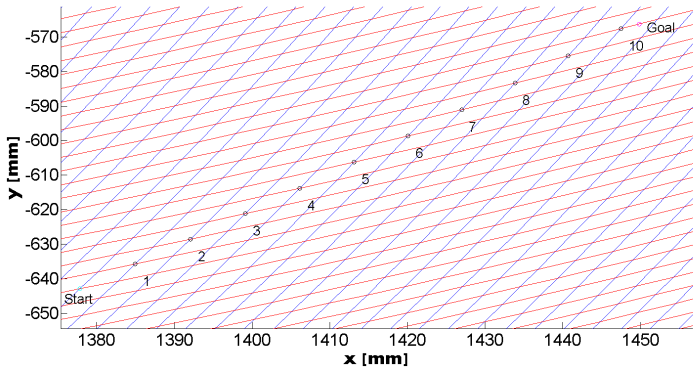

Fig. 5.4 Electrically Operated Robot – Numerical Inverse Kinematics Greedy Search.

5.2.2 Harvester Teleoperation

Initial studies were also performed on whether an in-house or COTS would be used for the research. Fig. 5.5 shows the high-level concept architecture using off-the-shelf components.

It is assumed the COTS extends from the user interface to the valve controller on the harvester. This architecture was rejected for teleoperation, because of the cost and the constraints it would have imposed on the research system.

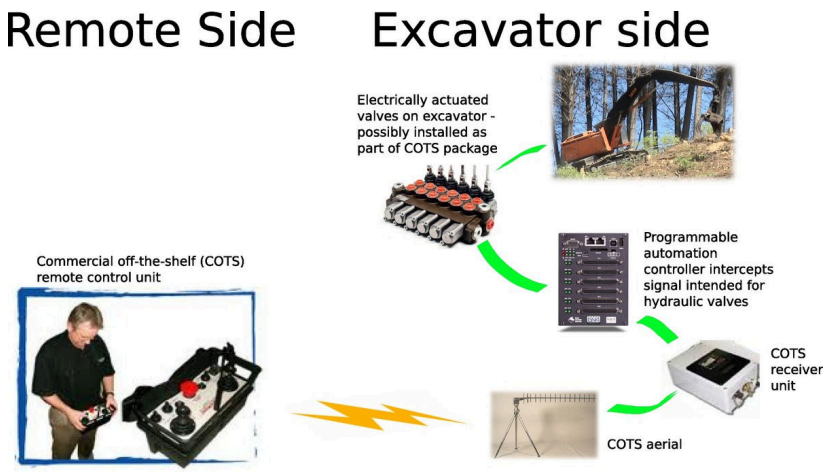

Fig. 5.5 Wireless Teleoperation – Initial Concept Architecture with COTS Components.

The research implementation shifted to an architecture that used COTS radio transceiver systems, but had an in-house user and controller interface (Fig. 5.6). The primary advantage of this system architecture was its flexibility for research. In particular, it allowed the use of ROS on the computer as an operating system for implementing control and path planning. The operator's controls can be a joystick, and the computer is used to generate the control systems to be sent over the wireless link. The wireless link is connected to the PAC, which has the interface that drives the hydraulic valves. The hydraulic valves are electrically operated proportional valves, using signals supplied by the PAC.

Fig. 5.7 shows an early router test setup. The final architecture was changed to have a computer on both the local and remote sides, as it was a good use of ROS's capabilities and allowed the splitting of the remote control into "local" and "remote" tasks.

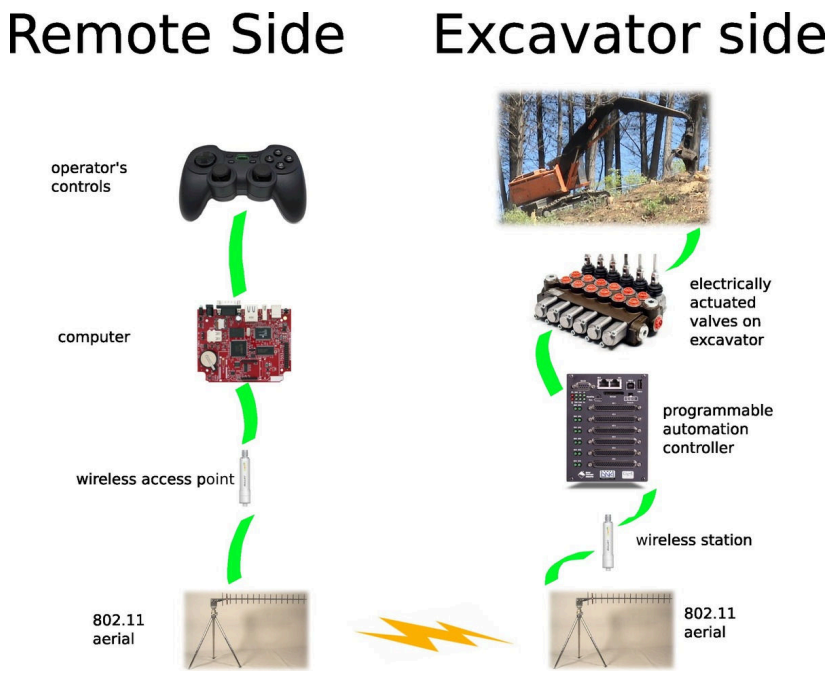

Fig. 5.6 Wireless Teleoperation – Research Implementation.

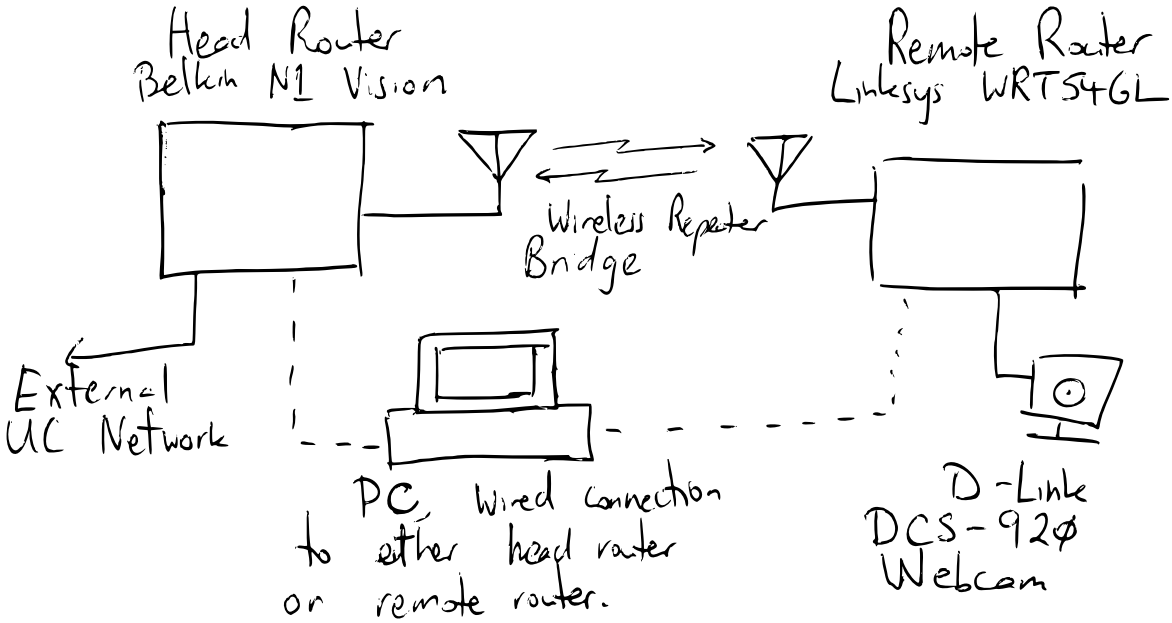

Fig. 5.7 Initial Router Setup – With Webcam.

5.3 Model and Kinematics Setup in ROS

Original design drawings of the hydraulic test system were not available, so a SolidWorks model of the hydraulic test system was developed from direct measurements. The solid model had enough detail to capture all the major dynamics, in particular the ram lengths and end effector position. Appendix B shows drawings of the SolidWorks model of the hydraulic test system. ROS and `MoveIt!` only support open kinematic loops, so the hydraulic rams cannot be modelled directly as the ram, base and arm form a closed triangle. The workaround was to convert the ram lengths to joint angles and vice versa for actual control, but leave the rams themselves out of the model. Fig. 5.8 shows ROS's joint model, and the hydraulic test system's coordinates were designed to align with the ROS definitions.

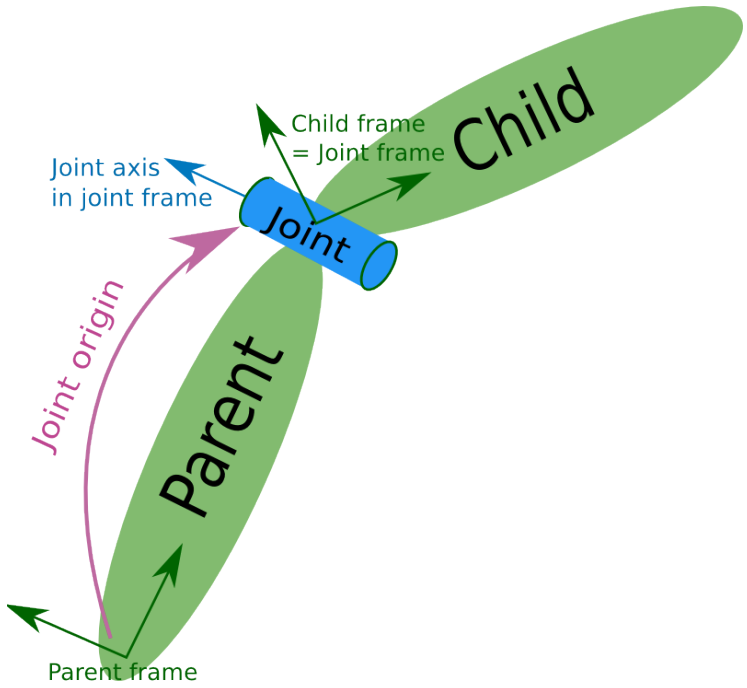

Fig. 5.8 ROS Joint Kinematics Diagram.

The inverse kinematics can be solved analytically, since the arm has a three dimensional range of movement and movement ability in each of the three dimensions. It was decided to use ROS's `IKFast` package for forward and inverse kinematics in all cases, since the resulting output integrates better with the other ROS tools (e.g. `MoveIt!`), and an updated kinematics solver can be automatically created from the altered URDF model.

The kinematic information for the robot was generated from the SolidWorks model directly, using the `SW2URDF` plug-in [131]. The `SW2URDF` plug-in uses SolidWorks's reference geometry feature to define axis sets, and their relationships in terms of offset, roll, pitch and

yaw. While there are no mandatory guidelines for defining axes and angles, it is better to use ROS's angle and orientation conventions and convert them at the edges of the system, rather than make the ROS model fit the non-ROS angles. Therefore, the following axis/angle conventions were used:

- the x axis was aligned along the length of a given arm segment, and the y axis was pointing left as per the ROS convention;
- y axes in joints in the same plane are parallel (i.e. an angle change causes rotation in the same direction);
- as many joint axis offset components are set to zero as possible;
- as many joint roll, pitch and yaw angles were set to zero or multiples of 90° as possible;
- the "zero joint angle" position corresponds to a position the machine can physically reach.

Since great care was taken to ensure reference geometry was aligned exactly along x, y or z axes or was at exact angles, the URDF output had to be carefully checked and edited for correctness, in particular against "flipping", where an axis and angle that should be positive in a particular direction would appear as negative and rotated 180°. Table 5.1 shows all the coordinate systems used in the kinematic model of the hydraulic arm, and Fig. 5.9 shows drawings of the coordinate systems defined in Table 5.1.

Table 5.1 Kinematic Coordinate Systems.

Reference Geometry	**Location**	**Comment**
`Axis_World`	`Coord_World` z axis	Reference vertical axis.
`Axis_Waist`	Axis that base rotates about	
`Axis_Shoulder`	Axis that boom rotates about	
`Axis_Elbow`	Axis that stick rotates about	
`Coord_World`	Corner of table	World "datum" reference system.
`Coord_Table`	Table location directly under rotating base	
`Coord_Base`	Coordinate system for rotating base	Reference for path planning.
`Coord_Boom`	Coordinate system for boom	
`Coord_Stick`	Coordinate system for stick	
`Coord_end_effector`	End Effector	Reference for End Effector
`Coord_ram1_end1`	Table end of Ram 1	Coordinate system for measuring length of Ram 1
`Coord_ram1_end2`	Base end of Ram 1	Coordinate system for measuring length of Ram 1
`Coord_ram2_end1`	Base end of Ram 2	Coordinate system for measuring length of Ram 2
`Coord_ram2_end2`	Boom end of Ram 2	Coordinate system for measuring length of Ram 2
`Coord_ram3_end1`	Boom end of Ram 3	Coordinate system for measuring length of Ram 3
`Coord_ram3_end2`	Stick end of Ram 3	Coordinate system for measuring length of Ram 3

The ram coordinate systems in Table 5.1 (`Coord_ram`□`_end`□) are in the same plane for a given ram, so the ram length is computed by computing the norm of the coordinate

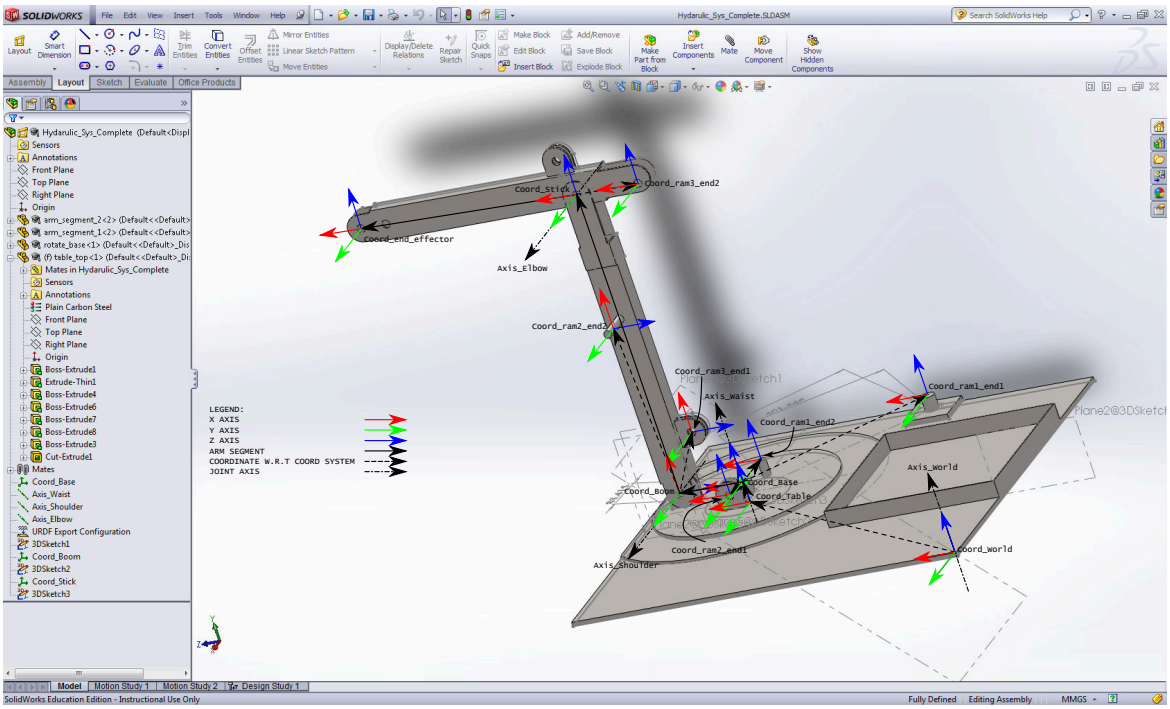

Fig. 5.9 SolidWorks Model with Coordinate Systems Highlighted.

transformation vector between the ram coordinate systems extracted from the ROS topic `/tf`. Table 5.2 is a summary of the different joints in the hydraulic arm and how they map to each other. All distances are given in metres and angles in radians.

Table 5.2 Hydraulic Arm Joints.

Joint		**Links**		**Origin**						**Axis**		
Name	**Type**	**Parent**	**Child(ren)**	x	y	z	r	p	y	x	y	z
table_joint	fixed	world	table	0.715	-0.57	0.01666	0	0	0		N/A	
waist	revolute	table	base	0	0	0	0	0	0	0	0	1
shoulder	revolute	base	boom	0.145	0	0.0325	0	$-\frac{\pi}{2}$	0	0	1	0
elbow	revolute	boom	stick	0.74	0	0	0	$\frac{\pi}{2}$	0	0	1	0
end_effector_joint	fixed	stick	end_effector	0.53	0	0.0115	0	0	0		N/A	
ram1_end1_joint	fixed	table	ram1_end1	-0.34	-0.328	0.02934	0	0	0		N/A	
ram1_end2_joint	fixed	base	ram1_end2	-0.019796	-0.085745	0.02934	0	0	-0.22689		N/A	
ram2_end1_joint	fixed	base	ram2_end1	0	0.075	0.0325	0	0	0		N/A	
ram2_end2_joint	fixed	boom	ram2_end2	0.4325	0.075	0	0	$\frac{\pi}{4}$	0		N/A	
ram3_end1_joint	fixed	boom	ram3_end1	0.4325	0	0.07	0	0.11519	0		N/A	
ram3_end2_joint	fixed	stick	ram3_end2	-0.15	0	0	0	0	0		N/A	

5.4 Autonomous Path Planning

Teleoperation, path planning and obstacle avoidance are treated together as ROS does not explicitly distinguish between them. The teleoperation was implemented with the local

machine controlling the robot and communicating with the PAC and sensors, and the remote machine being used to generate the planned path. Fig. 5.10 shows the physical setup of the obstacle test for the hydraulic test system. The obstacle is a fence post with a diameter of 175 mm. The planning scene model has a 175 mm buffer zone has been added all around it, as the path planner assumes the robot can touch the obstacle on a planned path.

Fig. 5.10 Obstacle Avoidance Physical Setup.

The path is planned taking into account the limits of the joint angles and speeds. There are also velocity and acceleration limits, but these are less meaningful as the actual velocity and acceleration limitations depend on the rams, not the joint. But there is an non-linear relationship between the ram speed and the angular speed, so the minimum joint speed was used for the extension of the ram.

Sometimes a particular state is not allowed due to a collision with a scene object (Fig. 5.11 with post actual size). If this is the case the colliding part will turn red. Collisions can occur between any two solid bodies, but the `MoveIt!` Setup Assistant is normally set to ignore collisions between adjacent machine segments. Ignoring these collisions is useful because model and sensor inaccuracies can cause the machine to seem to collide with itself even though it is not physically. This is especially noticeable at shallow joint angles - the solid model of the robot arm appears to have a collision between the boom and the stick at shallow joint angles despite it being physically impossible in real life. If collisions between adjacent machine segments was taken into account the path planning can be unreliable because the

machine might appear to be colliding with itself even though such a position is physically impossible and only represents an error in the solid model.

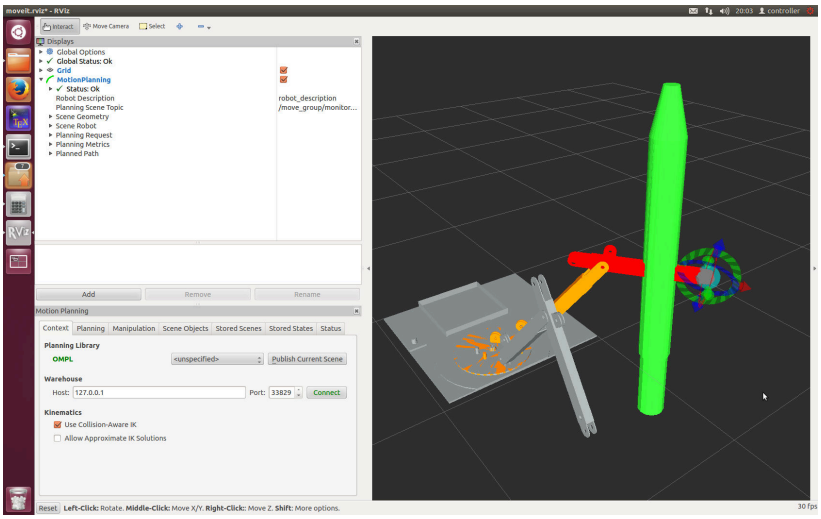

Fig. 5.11 `MoveIt!` Trajectory Plan – Disallowed Position with Colliding Part Shown in Red.

The `MoveIt!` based trajectory planner uses inverse kinematics, joint dynamic limits (speed, acceleration, etc.) and knowledge about obstacles to plan a trajectory that gets to the desired point while meeting all of the aforementioned constraints. The planning works with a planning scene consisting of a computer model of the robot and its surroundings. In the case of the hydraulic test system, a computer model of a post was made and this was placed in the planning scene to reflect the setup shown in Fig. 5.10. The robot is moved around by dragging the model to a different point then executing the path.

Fig. 5.12 shows a planned path for a scene with no obstructions. The starting point is on the right and the end point is on the left at the location where the orange arm and the blue ball with marked coordinates is. The path planner shows a “straightforward” path between the start and end points, as would be reasonably expected from a human operator. This operation is an important “sanity check” to ensure the path planner is working properly.

Fig. 5.13 shows the planned path with the post model loaded, but without the planning scene published to ROS’s path planner. Since the planning scene has not been published, the path planner does not yet “know” the post is there. The post model in the planning scene has been made larger than the real post by adding a 150 mm “buffer zone”, to prevent the robot unintentionally contacting the post during a planned path. An allowance of this type is important because sensor and model errors will cause the arm to not conform exactly to its planned path, both in the laboratory and in the forest.

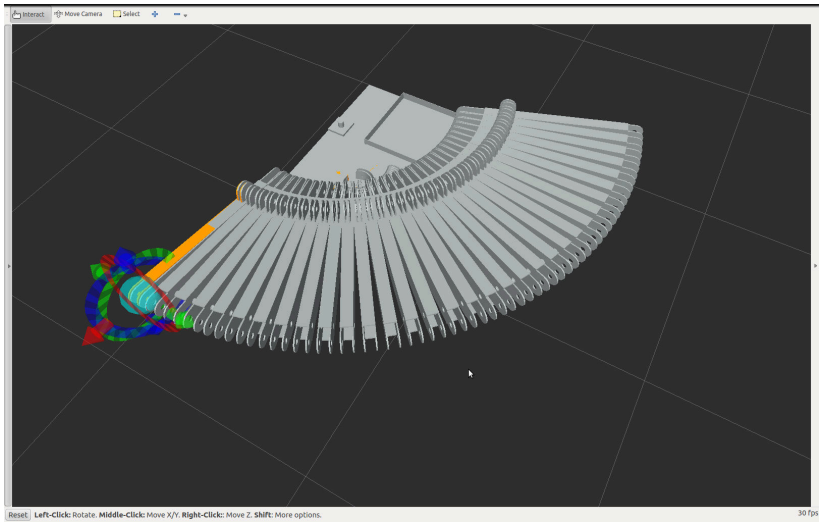

Fig. 5.12 Planned Path – No Obstructions.

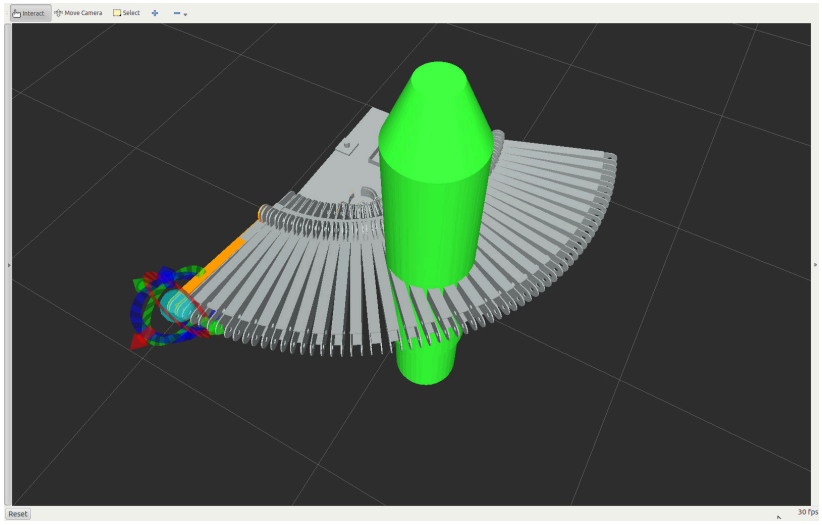

Fig. 5.13 Planned Path – With Collision.

The planned path shown in Fig. 5.13 is clearly unsuitable due to the collision with the post. However, once the planning scene has been published any subsequently planned paths will be devised to avoid the post. Fig. 5.14 and Fig. 5.15 show the planned path to avoid the post.

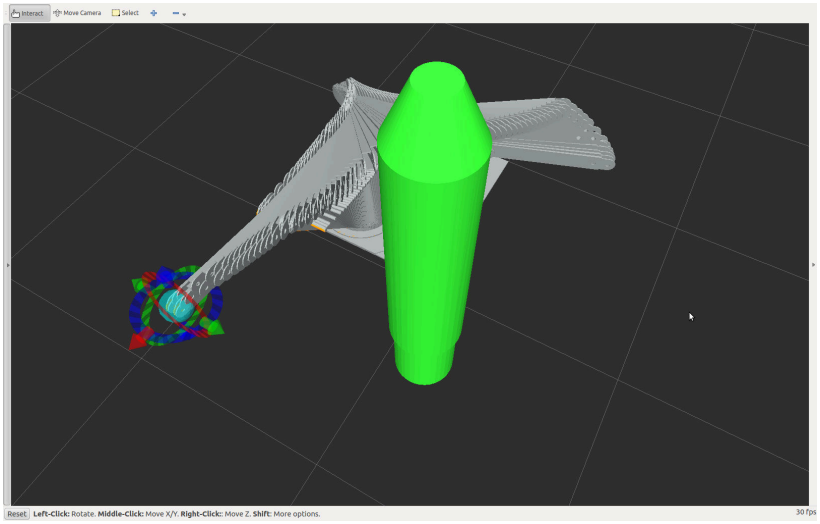

Fig. 5.14 Planned Path – View from Front of Hydraulic Test System.

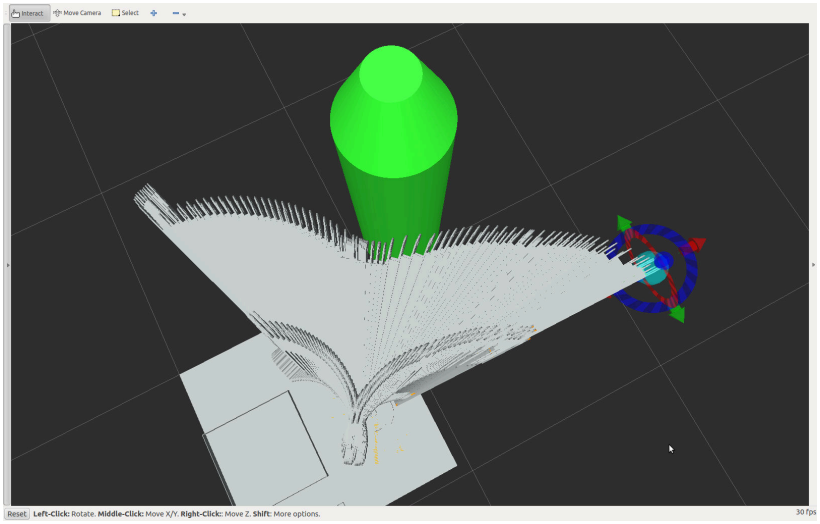

Fig. 5.15 Planned Path – View from Rear of Hydraulic Test System.

The autonomous path planning successfully avoided the post, under both local control and teleoperation. Fig. 5.16 shows a plan view of the planned path and the actual path. The path is from the lower right to the upper left. The plan view is the most important, as it directly shows the hydraulic test system avoiding the post. Fig. 5.16 shows the hydraulic test system is not acting as a ‘perfect’ servo system, but is still able to avoid the obstacle.

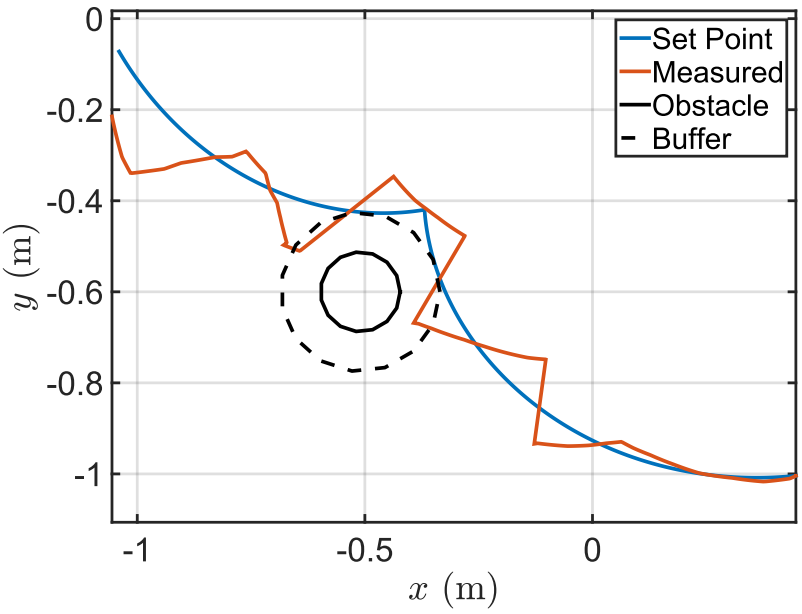

Fig. 5.16 Autonomous Path – Plan View.

Fig. 5.17, Fig. 5.18, Fig. 5.19 are frame grabs from an autonomous path plan at the start, in the middle, and at the end of the planned path respectively.

Fig. 5.17 Autonomous Path – Beginning.

Fig. 5.18 Autonomous Path – During Obstacle Avoidance.

Fig. 5.19 Autonomous Path – End.

`MoveIt!` is designed to work with servo mechanisms that control the joint angle directly. However, the hydraulic test system is controlled with the rams, so the inputs to the control system are ram lengths. The ram lengths were converted from the planned path joint angles using a joint angle to ram converter service. Fig. 5.20, Fig. 5.21, Fig. 5.22 shows the set point and controlled ram lengths respectively.

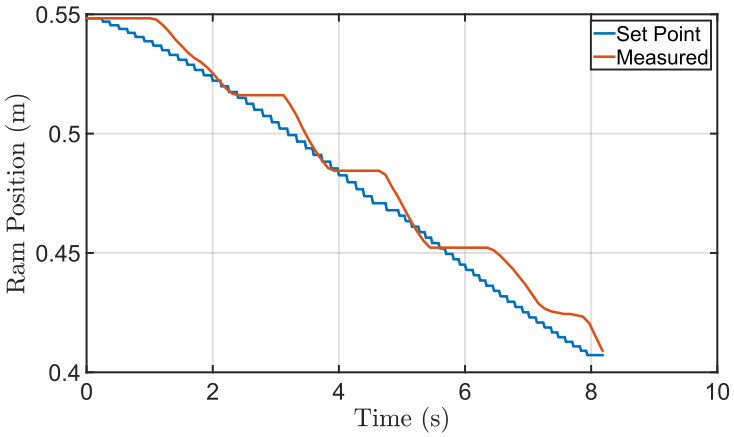

Fig. 5.20 Autonomous Path – Ram 1 Length.

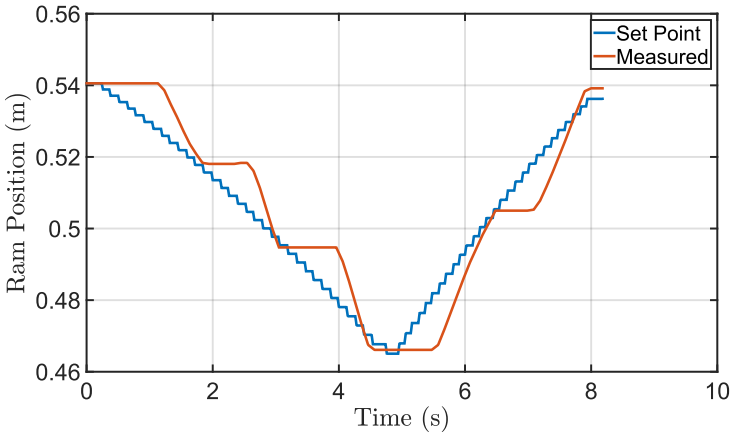

Fig. 5.21 Autonomous Path – Ram 2 Length.

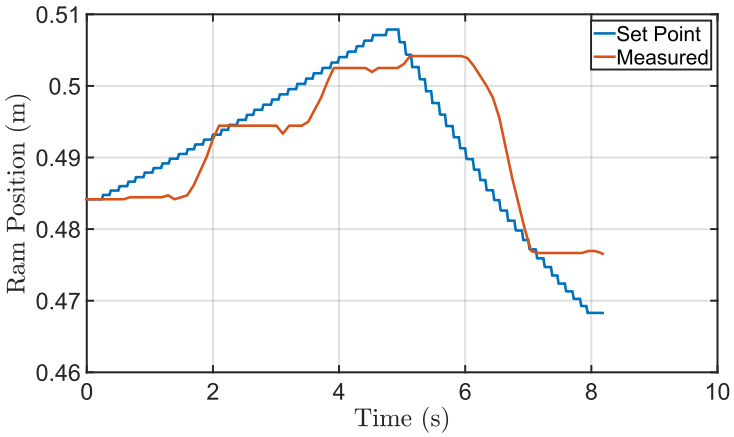

Fig. 5.22 Autonomous Path – Ram 3 Length.

Ram 3 conforms less closely to the set point than the other two rams – this is an effect that needs further investigation, but in this case it was not a problem, as the end effector still avoided the post successfully. A possible cause is that there was not enough available hydraulic pressure in the hydraulic test system to move the ram. Cylindrical coordinates are a useful means of characterising the motion of the hydraulic test system, as the arm itself moves in a plane, and the angle of that plane is controlled by the base angle. Fig. 5.23, Fig. 5.24 and Fig. 5.25 show the planned and measured ρ, θ and z respectively. The only constraint in cylindrical coordinates is that $\rho < 0.777$ – the radial distance of the post from the rotating base of the arm. The behaviour of ρ around $t = 9$ is due to the command trying to make the arm 'bend backward'. This did not happen in the measured behaviour, and was not necessary to avoid the obstacle. The minimum in z around $t = 9$ is also unnecessary – z could have been a smooth path and the obstacle avoidance would have been successful. The behaviour is confirmed by Fig. 5.22 – the ram movement could have been identical to the measured one without loss of avoidance of the obstacle.

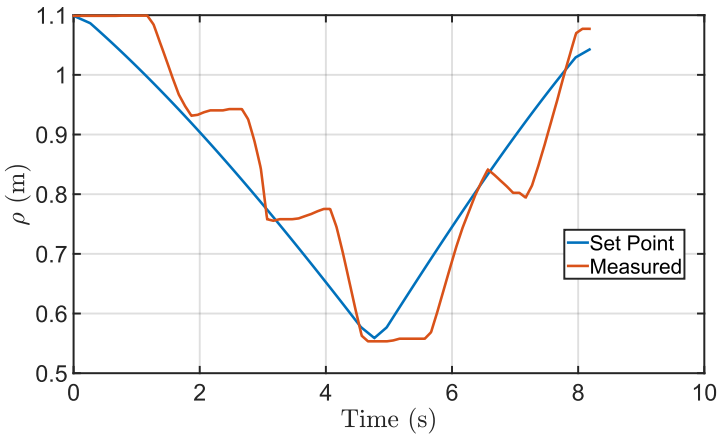

Fig. 5.23 Autonomous Path Cylindrical Coordinates – ρ.

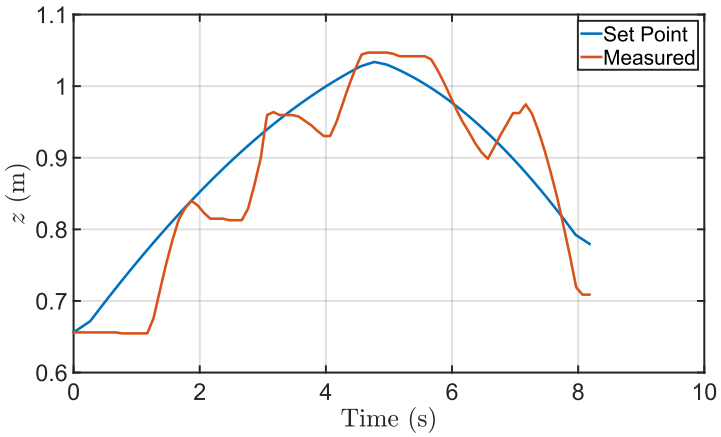

Fig. 5.24 Autonomous Path Cylindrical Coordinates – z.

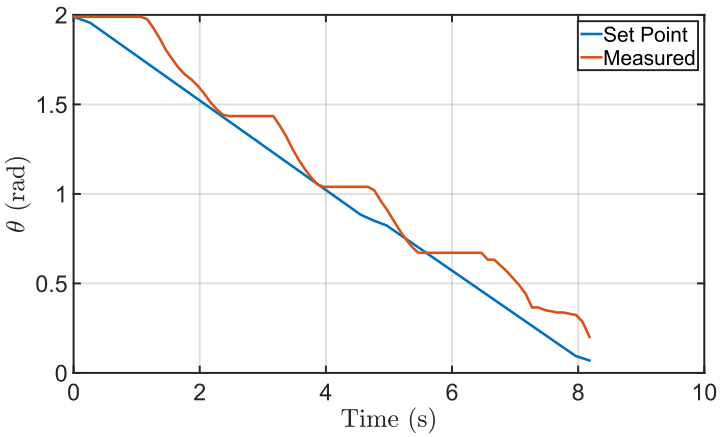

Fig. 5.25 Autonomous Path Cylindrical Coordinates – θ.

The post was manually inserted into the scene, but the posts can be detected by other means such as laser scanning or other means of detection. The ram joints are not servomechanisms, so the motion does not conform to the path, and the timeouts in ROS are not compatible with the arm's motion. Further research is required to overcome this limitation, as it will make the implementation with a full sized harvester more difficult.

An example situation for semi-autonomy would be automatic grabbing of a tree from a point and click style interface. All path planning and obstacle detection would be handled by the machine, with the operator providing safety oversight and telling the machine where to go next. There are two main areas that are important to semi-autonomy in the forestry machine: autonomous path planning and autonomous obstacle avoidance. The two are closely linked but the data sources are different. The obstacle avoidance testing used a model of an object whose size and location were both known in advance. In a forest this is not the case, but related research in identifying trees using a laser scanner would be suitable for application to an excavator based machine.

5.5 Haptic Feedback

Haptic feedback has been trialled using a Sensable/Geomagic Phantom Omni haptic feedback arm. The Phantom Omni is designed to be held in the hand, so the operator controls the arm by holding the stylus of the Phantom Omni and changing its position. In this usage scenario the Phantom Omni will give resistance to movement in proportion to the error in joint angles between the hydraulic test system and the Phantom Omni. As the hydraulic arm starts to move towards the Phantom Omni's position the force will decrease. The operator will feel this as a decrease in resistance and the feeling that the hydraulic arm has moved to the desired position. The Phantom Omni is also able to operate in non-haptic feedback mode. In this mode, the joint angles of the Phantom Omni are used to control the joint angles of the arm, but there is no force feedback to the Phantom Omni. The modes are switched between by pressing the two grey buttons on the stylus.

Fig. 5.26 shows the Phantom Omni arm mirroring the joint angles on the hydraulic arm. The image of the hydraulic arm also emphasises that an accurate solid model is not a prerequisite. The model has joints in the same locations and with the same axes as the real hydraulic arm, but the links were modelled as simple boxes.

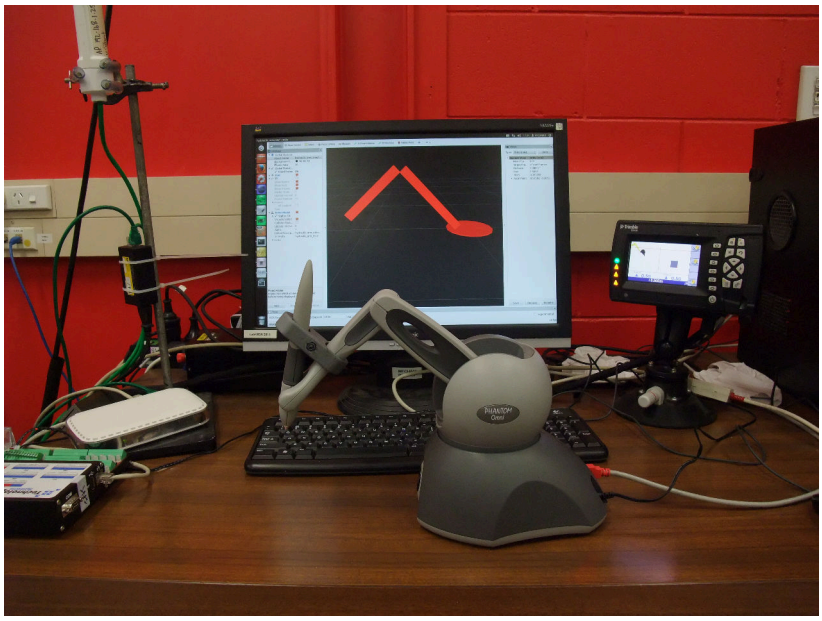

Fig. 5.26 Phantom Omni Mirroring Arm Position.

5.6 Discussion and Recommendations

5.6.1 Related Projects

A related project is being pursued to teleoperate a John Deere 909 harvester (909 Project). The scope of this research is different from the 909 Project as it deals directly with hydraulics, whereas the controls for the John Deere are done using CAN bus commands. While the work on cameras and semi-autonomy has been done on the hydraulic test system, with a suitable interface it can be transferred to a CAN bus controlled machine such as the John Deere. The obstacle avoidance scenarios shown are not based on real time sensor data. However, work is being done in the on using laser scanners to detect trees in real time. An example of tree detection from a laser scanner point cloud is shown in Fig. 5.27.

The final application of the research is to implement semi-autonomy on a full sized excavator. There are different levels of semi-autonomy, the greater the level of semi-autonomy the more must be known about the target machine's construction and materials. Direct coordinate control requires just knowledge of joint locations and angles, whereas autonomous path planning requires knowledge of the construction of the machine so a path can be planned and executed which is within the physical capabilities of the machine.

Extending this research to a machine in the field requires Training and Integration into Worksite Special plans, especially if it the first such machine in use. Operators need to be made aware that workers in surrounding areas may not always be aware of what the machine

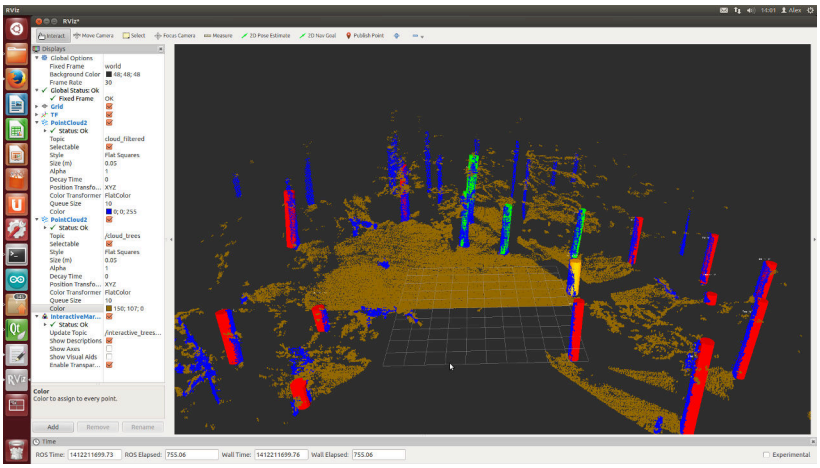

Fig. 5.27 Example of Automatic Tree Detection from Stick Insect Project.

is doing, and should be careful to ensure that workers in the surrounding area are able to get out of the way of the machine if required. Conversely, personnel working near a teleoperated machine need to ensure they have a plan for avoiding hazards. These plans should include escape routes in case control is lost to a teleoperated machine. It is recommended that personnel never approach a teleoperated machine unless under instruction of the operator. At a minimum, operators need the following knowledge about the machine and teleoperation system:

- Starting and stopping the engine.
- Determination of when the machine is in teleoperation mode.
- Emergency stops, their operation and how to reset them.
- Start of work day, end of work day and other “Make Safe” procedures.

5.6.2 Safety and Emergency Stops

It is recommended that all life safety emergency stops are rated to a minimum of IEC61508 SIL 2 or PLd. While the ROS control system does not have a SIL rating, a separate emergency stop system can be integrated into the control system. The ROS Control system is not designed or intended to provide life safety in the event of a malfunction or failure of the machine or control system. It is recommended that the design of the Emergency stop be totally separated from the ROS based control system. The role of ROS is primarily as a control system, not a safety system, and emergency stop systems can be built from standard off the shelf parts.

5.6.3 Worksite Safety and Hazards from Semi-Autonomy

The most significant new hazard from semi-autonomy is that the machine can now move in ways that are not directly predictable by personnel in the surroundings. In an excavator this should be covered by the standard safe work practice of never being inside the radius of the boom and stick. At present this should be enough for the machine as autonomous movement of the tracks has not been covered. A machine moving semi-autonomously may also knock over an object it encounters in its path and this needs to be taken into account when planning out work sites.

While the machine can move semi-autonomously, and can avoid obstacles there are still limitations on how quickly and accurately the machine can avoid the obstacles, due to the positioning accuracy. The semi-autonomous obstacle avoidance should never be depended on to protect life and property. It is also noted that the remote operator will not be able to see the surroundings as well as an operator in the cab so care needs to be taken to avoid any blind spots. Good communication will be essential to ensuring that no dangerous situations arise.

5.6.4 Visual Feedback

Cameras on the outside of the machine will be exposed to very harsh operating conditions. Cameras designed for excavators are generally low profile, well sealed against moisture and condensation and have hardened glass lenses to resist scratching. It is recommended that any camera system mounted on an excavator have an International Protection rating of IP69K, so it is dust tight and can withstand water blasting.

Visual feedback is recommended on all sides of the machine. In particular it should never be assumed the only direction the machine may move is where the operator's cab camera is pointing (i.e. the same direction as the boom). In some applications such as a tail-hold/backline, the normal direction of movement will be at 90° to the boom. It must also not be forgotten that the cameras are not just for machine control – they are also useful for detecting hazards in the environment around the machine.

ROS has libraries such as OpenCV which have machine vision capabilities that could be used to perform tasks like automatic tree recognition. The 909 Project is using IP cameras integrated with a ROS based control system. It is recommended that this course be pursued as using IP cameras gives much more flexibility in system design than proprietary designs.

5.6.5 Autonomy

An example situation for semi-autonomy would be automatic grabbing of a tree from a point and click style interface. All path planning and obstacle detection would be handled by the machine, with the operator providing safety oversight and telling the machine where to go next. There are two main areas that are important to semi-autonomy in the forestry machine: autonomous path planning and autonomous obstacle avoidance. The two are closely linked, but the data sources are different. The obstacle avoidance testing used a model of an object with known size and location. In a forest this is not the case, but related research in identifying trees using a laser scanner would be suitable for application to an excavator based machine.

Some different implementations of semi-autonomy along with their pros and cons are shown in Table 5.3. The main points to consider are the sort of operator interface required and the sort of sensing required. All types of autonomy require sensors of machine state but not all types require sensors for the surrounding environment and this is an important point to consider, as a control system that does not require environmental sensing will be cheaper and possibly more robust than a control system that does.

Table 5.3 Summary of Different Types of Semi-Autonomous Control.

Type	**Description**	**Pros**	**Cons**
Cylindrical Coordinate Control	Excavator controls work on arm in cylindrical coordinates (radius, slew angle, height)	Sensors only required on machine and not for environment	No obstacle avoidance
"Point and Click" Interface with Autonomous Obstacle Avoidance	Operator specifies end point of manoeuvre, obstacles are automatically avoided	Less input required from operator	Requires accurate physical model of machine and environment which can be difficult to acquire, cumbersome for small manoeuvres
Real-time Haptic Feedback	Operator "feels" machine movements in real time with haptic (touch-force) feedback	Helps restore feeling lost with teleoperation, does not require environmental sensing	Performance and stability heavily dependent on time delay
Workspace Haptic Feedback	Similar to "Point and Click" interface except operator can use haptic feedback to feel where the machine is physically capable of going	Less dependent on network latency than real-time haptic feedback	No feel for machine movement during manoeuvres, has same sensing requirements as "Point and Click" interface

5.6.6 Haptic Feedback

Haptic feedback has many possibilities for control. The haptic feedback that was tested was position control. There are other possibilities, such as giving the boundaries of a workspace including obstructions. The Phantom Omni is a research tool only and is not considered durable enough for daily use in a forestry environment. However, the project has possession of a Novint Falcon haptic feedback device, which can be used for further research on haptic feedback. The kinematics of the Novint Falcon are quite different to the Phantom Omni and an excavator but ROS has the kinematic libraries to make the two devices useful together. One of the advantages of the Novint Falcon is that it is designed for daily use as a gaming machine, whereas the Phantom Omni is designed as a research and development machine.

5.7 Summary

The research in this chapter shows that it is possible to implement autonomous path planning over a wireless link on the hydraulic test system. This is an important goal for teleoperation, as it shows the ROS-based architecture used is capable of delivering the teleoperation-based research goals. The hydraulic test system did not have any design drawings available, and the hydraulics controls were not optimised for linearised control, so future research includes reducing the jerkiness of the robot motion by using specialised valve controllers, such as servo valves.

Initially there was some uncertainty about whether to use a modified off-the-shelf system or develop a system in-house. There is certainly justification for such uncertainty as it is essential to ensure that one does not attempt to “reinvent the wheel”. However, in this case the in-house development route has been well chosen. It has provided a measure of flexibility in development that would be very difficult to obtain from a full commercial off the shelf teleoperation system that would have needed to be adapted to forestry harvesting anyway.

The choice of using ROS for teleoperation development was inspired, and has allowed a degree of development that would have been much more difficult any other way. The most important issue is scaling the performance from the laboratory system to a full sized excavator. However, the similar setup of the laboratory system and a proper understanding of the physical properties of the excavator should ease this task.

The greatest potential for applications of semi-autonomy in a logging operation include modification of the excavator control style (e.g. cylindrical coordinate control) and autonomous path planning. The reason is that control in cylindrical coordinates reduces the cognitive load on the operator and is extensible to steep country harvesting because the coordinate calculations can be compensated for machine slope automatically. Autonomous

path planning with obstacle avoidance means an operator does not have to control a machine all the time, even when there are obstacles in the environment that would normally require manual intervention from an operator.

Future research includes developing the ROS-based wireless teleoperation for deployment in the field on a full sized harvester. This will require field testing of the wireless communications and ensuring the harvester's hydraulics are retrofitted with suitable servo controls. Other future research includes integrating real time sensing into the scene graph generation, so that a harvester in the forest could avoid a tree obstacle in real time. At present the path planner is designed around the motion of the joint angles themselves, however further future research includes developing path planners that work in terms of the hydraulic rams, so all joint speed and acceleration limitations are specified in terms of the rams themselves, rather than the joint angle. Doing this will ensure the performance of the path planner is always fully optimised.

Chapter 6 describes a data-driven system identification of the Phantom Omni, which is used to compare with the minimal model based system identification.

Chapter 6

Data Driven System Identification of a Phantom Omni's Yaw Response

6.1 Introduction

The research objective of this chapter is to compare the accuracy of data driven modelling against a physically derived minimal model of the Phantom Omni's yaw response. The yaw (base angle) response is used because it is independent of gravitational disturbances, and gravity compensating springs that are present in some of the actuated joints of the Phantom Omni. This means that while the Phantom Omni has three degrees of freedom, the arm angles are held in fixed positions.

The desire to compare data driven modelling to minimal modelling comes from testing the accuracy of the minimal model against the 'well known and established' technique of data driven modelling. The comparison is not just for accuracy, but also for the simplicity of the data driven model, and how well it can be approximated by the minimal model. It is expected that the lack of constraints on the form of the data driven model will make it more accurate than the minimal model, but on the other hand the goal of making the error output white noise (i.e. uncorrelated with any signal but itself) means the data driven model is at risk of over fitting, especially where the measurement error of the response becomes on the order of the response amplitude. In the Phantom Omni this occurs at frequencies above its resonance and cut off, so any predictions of the data driven model at high frequencies needs to be carefully scrutinised as to whether it gives any useful information over the minimal model.

6.2 Experimental Setup

The Phantom Omni haptic device can be modelled as a multiple input, multiple output (MIMO) system that describes the motion of all six joints. The model is reduced to a 3-input by 3-output system since three of the joints in the stylus are physically held in fixed positions. The reduced system for the actuated joints consists of three input torques and three joint angle outputs, which means that in the absence of any further simplifications a total of nine transfer functions is needed in order to obtain a complete system description.

6.2.1 Phantom Omni Dynamics Model

Fig. 6.1 shows a Phantom Omni with the joint angles labelled. This chapter covers the modelling of the response of the base joint angle θ_1, while keeping the joint angles θ_2, θ_3 and all joints on the "stylus" fixed. The joints on the stylus are held in fixed positions by a cuff, and θ_2 and θ_3 are controlled by a PID controller integrated into the Phantom Omni Simulink control environment.

Fig. 6.1 Phantom Omni with labelled joint angles (Courtesy Sensable/GeoMagic).

The behaviour of the Phantom Omni can be described by the general differential equations of motion and torque given in (6.1). The process of developing the dynamic model for the Phantom Omni is very similar to the process for the Phantom Premium haptic device as outlined in [78, 102, 132].

$$M(\vec{\theta})\ddot{\vec{\theta}} + C(\dot{\vec{\theta}}, \vec{\theta})\dot{\vec{\theta}} + g(\vec{\theta})) = \vec{u} \tag{6.1}$$

Equation (6.1) describes the device dynamics with $\vec{\theta} \in \mathbb{R}^{3\times1}$ as the joint angles, $\vec{u} \in \mathbb{R}^{3\times1}$ the torques acting on the joints, $M \in \mathbb{R}^{3\times3}$ the inertia matrix, $C \in \mathbb{R}^{3\times3}$ the Coriolis and centrifugal torque matrix and $\vec{g} \in \mathbb{R}^{3\times1}$ the vector describing other torques acting on the joints due to effects such as gravity. In the rest of the paper the torque $\vec{u}$ is replaced by the command voltage $\vec{v}$ such that $\vec{u} = \overline{B}\vec{v}$, for a matrix $\overline{B} \in \mathbb{R}^{3\times3}$ of coupling constants between the input command voltage and the joint torque. This is done as the command voltage is known directly, whereas the joint torques are not directly measured.

The Phantom Omni is being actuated about the yaw (θ_1) axis with all other joint angles held constant. It is assumed the controllers for joint angles θ_2 and θ_3 are "stiff" enough that θ_2 and θ_3 are constant even though they are not kept physically restrained in fixed positions like the stylus angles. Equation (6.1) can therefore be simplified to the scalar equation (6.2). Since θ_2 and θ_3 are assumed constant it follows that $\dot{\theta}_2$, $\dot{\theta}_3$, $\ddot{\theta}_2$ and $\ddot{\theta}_3$ are all zero. It is also assumed there is no cross coupling between one actuator command and another, so $\overline{\beta}_{12}$ and $\overline{\beta}_{13}$ are set to zero.

$$\begin{bmatrix} m_{11} & m_{12} & m_{13} \end{bmatrix} \begin{bmatrix} \ddot{\theta}_1 \\ \ddot{\theta}_2 \\ \ddot{\theta}_3 \end{bmatrix} + \begin{bmatrix} c_{11} & c_{12} & c_{13} \end{bmatrix} \begin{bmatrix} \dot{\theta}_1 \\ \dot{\theta}_2 \\ \dot{\theta}_3 \end{bmatrix} + g_1 = \begin{bmatrix} \overline{\beta}_{11} & \overline{\beta}_{12} & \overline{\beta}_{13} \end{bmatrix} \begin{bmatrix} v_1 \\ v_2 \\ v_3 \end{bmatrix} \tag{6.2}$$

Simplification of the system (6.2) to eliminate fixed angles gives (6.3). The gravitational term g_1 is set to zero as per [132], as the motion of θ_1 is in a horizontal plane.

$$m_{11}\ddot{\theta}_1 + c_{11}\dot{\theta}_1 = \overline{\beta}_{11}v_1 \tag{6.3}$$

Identification of the haptic device is performed using a closed loop system with the control law $v_1(t) = k_{\mathrm{p}}(r(t) - \theta_1(t))$ in (6.3). This results in the closed loop characteristics of the system described by (6.4). The reference input is described by $r(t)$. Closing the loop eliminates the open loop pole present at the origin which means the step response now has a bounded value as $t \to \infty$. Moreover, the closed loop system yields a dimensionless transfer function.

$$m_{11}\ddot{\theta}_1 + c_{11}\dot{\theta}_1 = \overline{\beta}_{11}k_p(r - \theta_1) \tag{6.4}$$

The input signal $r(t)$ is chosen for the experiment. The input signal can be of any form but this paper limits the waveform to sine waves and pseudo-random binary sequences. The model parameters of the Phantom arm are identified and simulated for different amplitudes to see changes in response for identification of non linearities.

6.2.2 Sinusoidal Steady State Model

Sinusoidal steady state modelling uses the response of the differential system described by (6.4) to a sine wave input $r(t) = A_\mathrm{r}\sin(\omega t)$, with A_r being the angle amplitude in radians.

$$m_{11}\ddot{\theta}_1 + c_{11}\dot{\theta}_1 + \overline{\beta}_{11}k_\mathrm{p}\theta_1 = \overline{\beta}_{11}k_\mathrm{p}A_\mathrm{r}\sin(\omega t) \tag{6.5}$$

The parameters of (6.5) are not identifiable as all coefficients contain unknowns. Dividing both sides of (6.5) by m_{11} and making the substitutions $C = \frac{c_{11}}{m_{11}}$ and $\beta = \frac{\overline{\beta}_{11}k_p}{m_{11}}$ yields the identifiable equation (6.6).

$$\ddot{\theta}_1 + C\dot{\theta}_1 + \beta\theta_1 = \beta A_\mathrm{r}\sin(\omega t) \tag{6.6}$$

The value of m_{11} may be found by forming a model of the arm inertia in terms of masses of the arm segments and joint angles. The inertia model allows (6.6) to model the arm at any combination of joint angles, including joint angles that change over time. If the system is approximated as linear, θ_1 can be modelled as a sinusoid in the fundamental frequency (6.7).

$$\theta_{1\mathrm{m}} = A_1\sin(\omega t) + A_2\cos(\omega t) \tag{6.7}$$

Substituting (6.7) into (6.6) results in a set of simultaneous equations to solve for β and C (6.8).

$$\begin{bmatrix} A_1 - A_\mathrm{r} & -\omega A_2 \\ A_2 & \omega A_1 \end{bmatrix}\begin{bmatrix}\beta \\ C\end{bmatrix} = \begin{bmatrix}\omega^2 A_1 \\ \omega^2 A_2\end{bmatrix} \tag{6.8}$$

For a single frequency ω, β and C can be solved analytically. A single frequency is adequate to identify β and C since both frequency and phase information can be used. If the system is truly linear β and C will be correct regardless of ω or A_r. In reality the accuracy of

β and C is affected by choice of ω, so using a variety of frequencies is used, resulting in the system of simultaneous equations (6.9).

$$\begin{bmatrix} A_{11}-A_{\mathrm{r}} & -\omega_1 A_{21} \\ A_{21} & \omega_1 A_{11} \\ A_{12}-A_{\mathrm{r}} & -\omega_2 A_{22} \\ A_{22} & \omega_2 A_{12} \\ \vdots & \vdots \\ A_{1N}-A_{\mathrm{r}} & -\omega_2 A_{2N} \\ A_{2N} & \omega_N A_{1N} \end{bmatrix} \begin{bmatrix} \beta \\ C \end{bmatrix} = \begin{bmatrix} \omega_1^2 A_{11} \\ \omega_1^2 A_{21} \\ \omega_2^2 A_{12} \\ \omega_2^2 A_{22} \\ \vdots \\ \omega_N^2 A_{1N} \\ \omega_N^2 A_{2N} \end{bmatrix} \tag{6.9}$$

Equation (6.9) is solved using ordinary least squares to yield β and C at a given set of θ_2 and θ_3 angles. The transfer function describing the dynamic equations model is given in (6.10).

$$H(s) = \frac{\beta}{s^2 + sC + \beta} \tag{6.10}$$

The identified value of C in (6.10) consists of the component for the internal damping coefficient of the Phantom Omni software and a physical damping coefficient (ζ_{phys}) with respect to non-linear physical friction (e.g. stiction).

6.2.3 Data Driven Model

The parametric system estimation can be used once the overall characteristics of the system are determined by the spectral estimation of the PRBS response. The system configuration shown in Fig. 6.2 is used for the parametric estimation. In this configuration the real system is described by (6.11), where $u(t) = k_{\mathrm{p}} \cdot (r(t) - y(t))$ is the input signal, $y(t)$ is the output signal and $e(t)$ is the error signal. The real system is described by $G_0(q)$ and the noise is shaped by $H_0(q)$. This real system is estimated by the model $G(q)$ and the noise is modelled as $H(q)$. In these descriptions q is a shift operator, such that q^{-n} denotes a time delay of n samples.

$$y(t) = G_0(q)u(t) + H_0(q)e(t) \tag{6.11}$$

The real system (6.11) is estimated by optimizing the model coefficients so that the residual signal $e(t)$ is maximally decorrelated with itself as well as with the input signal $u(t)$. Minimal cross correlation between the input signal and the residual signal indicates that $G(q)$ describes the real system $G_0(q)$ accurately. If $H(q)$ accurately describes the real noise

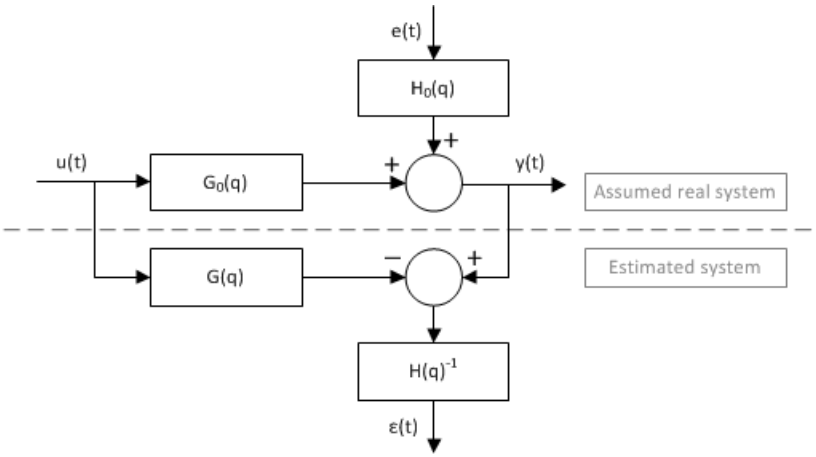

Fig. 6.2 Configuration for Data Driven Modelling Parametric Estimation.

shaping $H_0(q)$, the residual signal should be close to white noise. Unlike the minimal model the input is a PRBS. The flip time of the PRBS is optimised to ensure that most of the energy in the PRBS is concentrated at the frequencies of interest. In the case of the Phantom Omni the frequencies of interest are below 10 Hz.

6.3 Results

6.3.1 Spectral estimation

Fig. 6.3 shows the spectral estimates for A_{r} =0.07 rad and A_{r} =0.14 rad. The amplitudes of 0.07 rad and 0.14 rad were chosen as it is observed that neither value of A_{r} drives the base of the arm beyond its range of rotation. The phase response goes from 0° to −180° up to 5 Hz. There are extra poles and zeros at higher frequencies but these are not considered of interest as the arm has very low response at these frequencies, so these poles and zeros will not have a noticeable effect on the arm dynamics. The spectral estimation implies that a linear system model with two more poles than zeros is a suitable starting point for the data driven modelling and confirms the validity of the dynamic system modelling in the frequencies of interest.

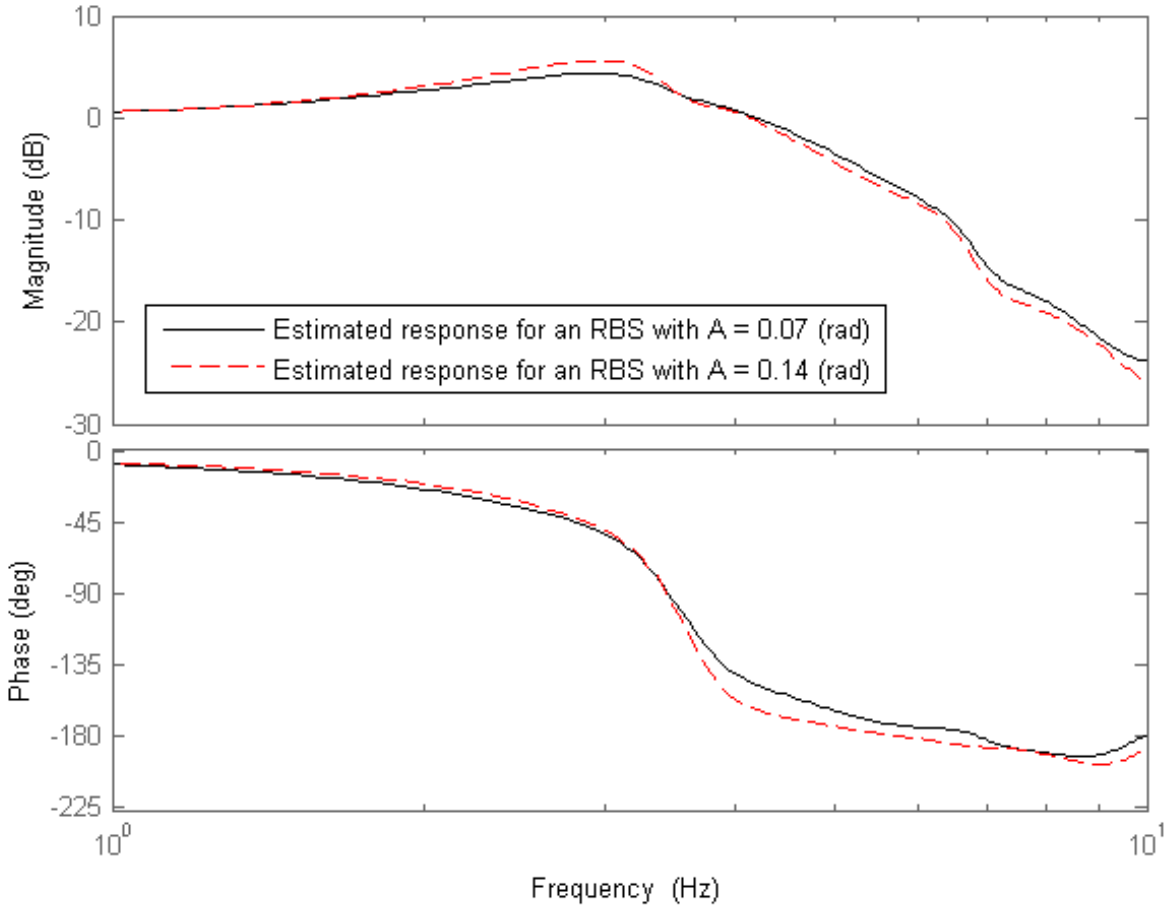

Fig. 6.3 Spectral Estimation Results.

6.3.2 Data Driven Parametric estimation

The output has very low levels of noise, so the data driven modelling results are focused on output error (6.12). Simulation results show adding extra poles and zeros gives significantly better accuracy. Introducing extra complexity increases the accuracy of the model for higher frequencies, which are attenuated by the system. The data driven model describes the real system accurately when looking at various simulation results.

The spectral estimate implies that the model of (6.4) is accurate at the frequencies of interest. Initial measurements showed the Phantom arm significantly attenuates frequencies above 10 Hz, so the data driven model was optimised for maximum accuracy for frequencies below 10 Hz. The Phantom Omni driver uses a sampling frequency of 1000 Hz which is sufficiently high to measure all relevant dynamics. Since the frequencies of interest are so small relative to the sampling frequency, it is also reasonable to approximate the Phantom arm as a continuous time system.

A measurement duration of 100 s was chosen as sufficient to accurately estimate the system using the data driven model. The actual identification used a PRBS. A PRBS with a flip time of 0.3 s ($N_c = 300$) was chosen to keep the frequencies of interest below ≈10 Hz. The PRBS was performed using two amplitudes, $A_r = 0.07$ and $A_r = 0.14$ rad, to compare the parameter identification results at different amplitudes. Equation (6.12) shows the data driven model.

$$\theta_1(t) = \frac{B(q)}{F(q)} r(t) + e(t) \tag{6.12}$$

With parametric estimation it is necessary to determine the system delay and the order of both polynomials (N_b and N_f). A system delay of four samples has been estimated from step response data ($N_k = 4$). The results of the spectral estimate indicate the model should be a system with two more poles than zeros. This information, in combination with the definition of the polynomials, indicates that: $N_B = N_F - 1$. An output error model with $N_B = 1, N_F = 2$ (two poles and no zeros) and $N_k = 4$ has been chosen. While increasing the order of the model reduces the cross correlation between the residual signal and the input signal, the lowest order has been chosen because the difference in model accuracy was not noticeable in simulation.

The observations about frequency response and phase shift motivate the use of a continuous-time formulation for identification of the system coefficients. The shift operator formulation (6.11) may be converted to the continuous-time transfer function (6.13) by observing that the

frequencies of interest are very low relative to the control system sampling frequency (10 Hz vs. 1000 Hz).

$$H(s) = \frac{b_0}{s^2 + sf_1 + f_0} \tag{6.13}$$

Various parameters (e.g. N_c and the amplitude of the input signal) were varied and signal processing (e.g. down sampling and filtering) had been introduced to determine the robustness of the data driven identification method. Results remained nearly identical for any investigated setting; this includes noise shaping and increasing the model order.

6.3.3 Dynamic equations model

By calculation the parameter c_{11} is found to be zero when θ_2 and θ_3 are chosen constant. However, c_{11} is considered a damping parameter and simulations show that a zero value for c_{11} does not give usable results since no damping is incorporated. Based on the physical properties of the Phantom Omni device and the fact that the Phantom Omni software internally incorporates a fixed damping coefficient of $k_{\text{int}} = 0.02$ a damping coefficient should be included in the model.

$$c_{11,\text{new}} = c_{11,\text{old}} + k_{\text{int}} + k_{\text{phys}} \tag{6.14}$$

6.3.4 Comparison between modelling methods

Fig. 6.4 shows Bode plots for the spectral estimate, data driven model and dynamic equations model at an input amplitude of A_r =0.07 rad, and Fig. 6.5 the same data for A_r =0.14 rad. Since the spectral estimate provides a rough estimate of the frequency characteristics it can only give a rough indication of the accuracy of the data driven model and the dynamic equations model. Nevertheless, it can be seen from the plots that substantial differences exist between the data driven modelling method and the dynamic equations modelling method with respect to the spectral estimate.

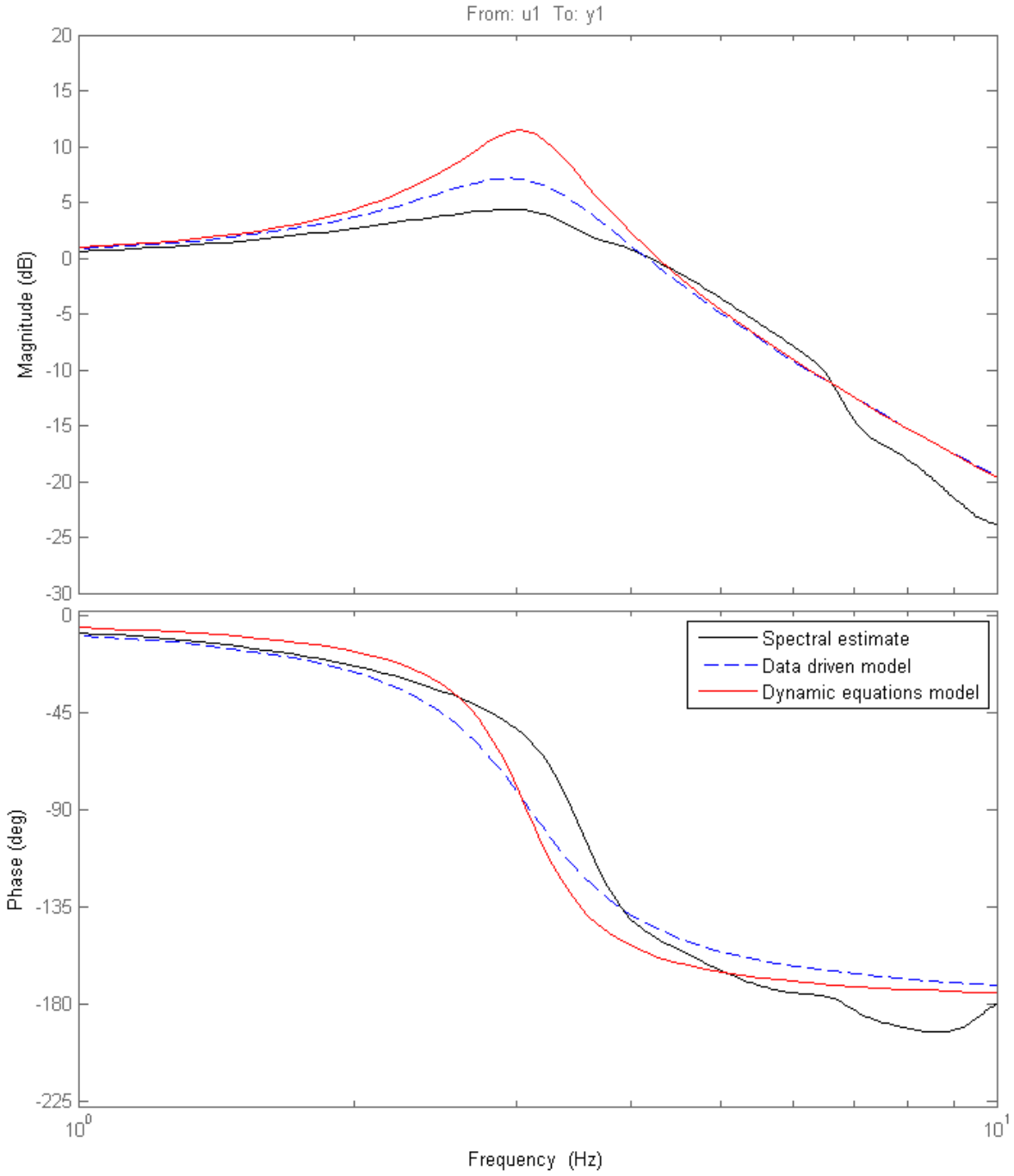

Fig. 6.4 Bode plots for spectral estimate and system models at A_r =0.07 rad.

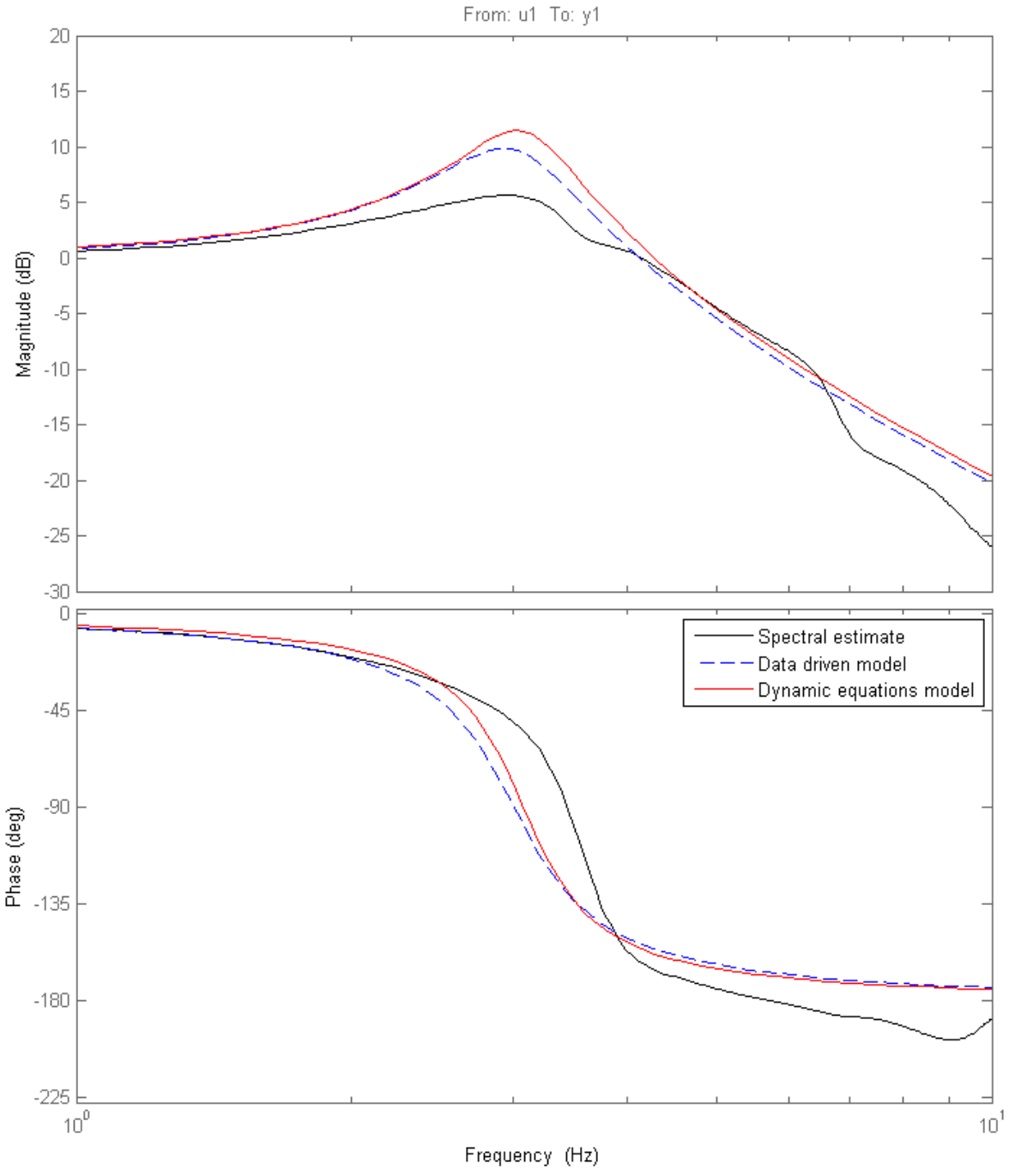

Fig. 6.5 Bode plots for spectral estimate and system models at $A_r = 0.14$ rad.

For A_r =0.07 rad and A_r =0.14 rad, the peak frequency and resonance frequency for the dynamic equations model are higher than for the data driven model. Due to the fact that the dynamic equations model does not depend on the input signal (for constant θ_2 and θ_3) there is no change in the resonance frequency. For data driven modelling, a new model is identified for every new dataset, making the resonance frequency subject to small changes, as can be noticed from the results. Nevertheless, a noticeable difference in the estimation of the resonance frequency can be seen when comparing the data driven model to the dynamic equations model.

Table 6.1 shows the coefficients of (6.13). It can be seen that the assumption of the dynamic model (6.10) that the constant coefficients are identical in both the numerator and denominator are valid, especially when $A_r = 0.07$. Note also that the damping decreases at higher amplitudes. This is possibly due to the increased effect of stiction at lower amplitudes. The dynamic model coefficients were identified at $A = 0.07$ and are assumed identical for all amplitudes, so the entries for $A_r = 0.14$ are identified with a '$\star$'. Table 6.2 shows the calculated peak response and resonance frequencies from the data in Table 6.1.

Table 6.1 Identified Model coefficients at θ_1 =45°, θ_2 =90°.

A (rad)	0.07	0.14
b_0 (s^{-2})	380.1	350.9
f_0 (s^{-2})	380.7	357.1
f_1 (s^{-1})	8.781	6.082
β (s^{-2})	374.5	$\star$
C (s^{-1})	5.216	$\star$

Table 6.2 Comparison of model properties.

Model	**Data Driven**		**Dynamics**	
A_r (rad)	0.07	0.14	0.07	0.14
Peak (Hz)	2.94	2.93	3.45	3.69
Resonance (Hz)	3.11	3.01	3.94	3.94

Further analysis can be performed by observing the outcome from simulations (i.e. a comparison in time domain) of the models found through both modelling approaches. All input signals for simulations, as well as the initial conditions for the models have been set at zero for t =0 s. In Fig. 6.6 a typical part of a simulation with a PRBS as an input signal is shown for both models at A_r =0.07 rad. For reference, the measured response is depicted. Fig. 6.7 depicts the error between the models and the measured response. The data driven model has a smaller error, but the only difference between the data driven model and the

dynamic model is that the constant coefficients on the numerator and denominator of the transfer function are allowed to be different from each other.

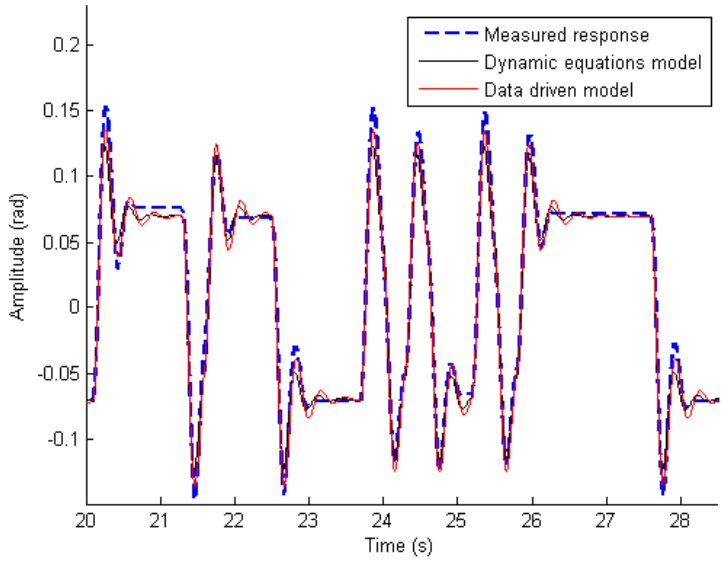

Fig. 6.6 Comparison of simulation results using a PRBS as input signal with A_{r} =0.07 rad as input.

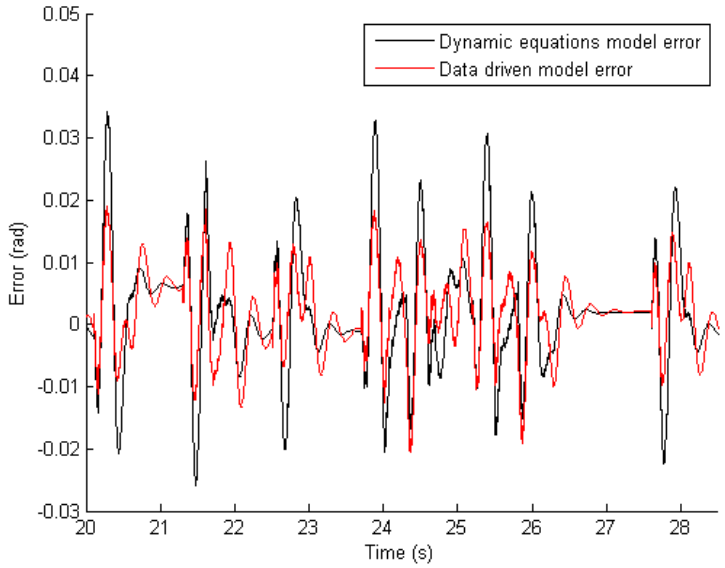

Fig. 6.7 Error for comparison of simulation results using a PRBS as input signal with A_{r} =0.07 rad as input.

Table 6.3 shows the relative RMS errors of both models with respect to the real response for PRBS and Chirp input signals. The chirp signal went from 1 Hz to 10 Hz at the rate of $0.1\,\mathrm{Hz\,s^{-1}}$. The relative RMS errors for the data driven model are found to be smaller for both input signals and both amplitudes. For A_r =0.07 rad, an error ratio of 1.33 and 1.34 is found for a Chirp input and a PRBS respectively. For A_r =0.14 rad, these ratios are found to be 1.33 and 1.79 respectively. Note that these ratios are based on the estimated upper bound regarding the accuracy of the dynamic equations model and therefore represent the "best case" scenario.

Table 6.3 Relative RMS errors evaluated for the dynamic equations and data driven method for PRBS and Chirp.

Model	**Data Driven**		**Dynamics**	
A_r (rad)	0.07	0.14	0.07	0.14
RMS error PRBS (rad)	0.10	0.10	0.13	0.17
RMS error Chirp (rad)	0.41	0.54	0.54	0.72

Concluding the comparison between the two modelling methods, it is found that although both methods cannot accurately describe all non-linear behaviour (e.g. friction) a noteworthy difference exists regarding the estimation of the resonance frequency. The dynamic equations modelling approach estimates the resonance frequency of the system better than the data driven modelling approach.

6.4 Summary

The system describing the motion of the base/yaw (θ_1) axis of a Phantom Omni haptic feedback arm has been estimated using data driven modelling. The purpose of this was to determine whether an increase in useful accuracy can be achieved compared to the minimal model derived from the dynamical system representing the physical properties of the Phantom Omni. It has been found that while the data driven model captures more behaviours, the extra behaviours occur at high frequencies where the response is highly damped in any case. It was found that the data driven model could be simplified to the same form as the minimal model, and the extra complexity in the form of extra poles and zeros did not show any evidence of a useful increase in accuracy.

Simulations for the motion of the yaw of the Phantom Omni show that the data driven model is more accurate than the dynamic equations model. This implies that data driven modelling could produce a more accurate model of the system as a whole. However, the source of extra accuracy, compared to the dynamic equation model is easily identifiable

and can be incorporated into the dynamic equation model. Note that the dynamic equations model used for the comparison reflects the upper bound case with respect to its accuracy. Results have shown that the accuracy of the (linear) data driven model is limited by some non-linear behaviours of the system. The closed loop measurements on the haptic device are conducted with a proportional gain and no derivative gain. A damping coefficient is added to the dynamic equations model which is justified by the fact that the Phantom Omni device physically experiences a certain damping and it incorporates an additional damping coefficient in its software as well.

The research output of this chapter is that minimal modelling is capable of producing an accurate physical model when compared to the data driven model. It shows that if the dynamics of the system is known in advance, a data driven model can also be simplified by constraining the form of the data driven model to the dynamic model. However, this is effectively the same as the minimal model, so any accuracy increase comes down to the difference of the response of the non-linearities between the sinusoidal inputs of the minimal model control input and the PRBS of the data driven model. Another advantage of the minimal model is that it is much easier to control machine speeds and accelerations with sinusoidal inputs, and the smoother transitions put less strain on the actuators. This feature is particularly important for field testing of machines, where failure during testing is an outcome to be avoided at all costs.

Chapter 6 has covered the data-driven modelling of the Phantom Omni. Chapter 7 outlines the derivation and implementation of a non-linear damping model that enables real-time estimation of damping from the output waveform.

Chapter 7

Non-Linear Damping Characterisation of a Phantom Omni Haptic Feedback Device

7.1 Introduction

This chapter presents a novel minimal modelling methodology for identifying and simulating non-linear behaviour in the steady state yaw response of a Phantom Omni haptic feedback arm. The research objective is to capture non-linear damping behaviour by interactions and correlations of parameters from simplified linear models with physical quantities. A formulation based on the total energy of sine wave has been explored, as it provides a convenient way of bootstrapping the non-linear model in this case, but the non-linearities could be other properties like hysteresis or dead-space behaviour which worked well for the hydraulic arm.

The research in this chapter explores the formulation of an invariant for characterising the non-linearity. The objective of using an invariant is to generalise a non-linear systems to a given locally linear behaviour. The advantage of this approach is that the nature of the non-linearity becomes unimportant, if a suitable invariant can be found, the system will act the same. For a steady state periodic system the internal energy (excluding inputs and losses) should not vary over each cycle, so internal energy is a good candidate for an invariant. The non-linear model was characterised from sinusoidal steady state responses. While energy can be used as an invariant, it is desirable the invariant formulation does not depend on the wave shape in itself. In other words, an energy invariant using the position, speed and acceleration

is better than an invariant dependent on attributes such as sine wave amplitude, frequency and phase.

The rationale for using the invariant formulation in this research is to make the control algorithms as scalable as possible between different machine sizes. The research in this chapter was performed on Phantom Omni. However, the formulation is such that it could be implemented on any other type of machine with minimal changes. This is where the power of the invariant formulation comes in: the ability to use the same type of system model with many different types and sizes of machines. This is an important contribution to the goal of being able to retrofit existing forestry machines for teleoperated harvesting.

The dynamic model uses information from experimental observations of sinusoidal steady state frequency responses and the mean energy of the input to characterise non-linear damping and torque constants. The non-linear damping model relates a number of linear model representations of the torque constant and damping parameters to the energy of the arm using an "α-invariant" formulation. The α-invariant formulation takes a snap shot of the effective energy in the system at an instant of time, which allows the transferral of steady state modelling into transient modelling. An advantage of the α-invariant over control methods such as sliding mode control [133] is that it is continuous and does not require membership functions.

The α-invariant model is used to characterise the dynamic response of the Phantom Omni arm with respect to the base. While the Phantom Omni is produced primarily as a haptic feedback device, it has its own dynamic properties that make it a useful research platform for system identification and modelling. Standard friction models such as Coulomb friction can be used, but the objective of this research is to characterise the relationship between input energy and damping. The energy approach is explored because during parameter identification of the Phantom Omni using sinusoidal steady state analysis, there was an observed increase of damping at low frequencies. The measure used for energy was based on the squared angular speed, angular position and angular acceleration. This measure is derived from the algebraic properties of a sine wave, and is intended to capture non-linear damping behaviour by interactions and correlations of parameters from simplified linear models with physical quantities. In other systems, such as the hydraulic test system, the α-invariant could be derived from non-linear properties such hysteresis or dead-space behaviour.

A minimal model of inertia is included to incorporate dependencies of the torque constant and damping on combinations of arm joint angles in the pitch axis of motion. The inertia model is derived from the linearised response of the arm and has the important feature that it does not require detailed knowledge of the masses of the Phantom Omni's arm components or their distribution. The results show the α-invariant non-linear model significantly outperforms

the linear model, demonstrating that this energy formulation is an accurate representation of the physical mechanisms in the Phantom Omni. Overall the invariant provides a very efficient way of capturing highly non-linear dynamics with a small number of parameters and experiments and has a physically justifiable mechanism.

The Phantom Omni dynamics are modelled by a physically derived second order ODE with time varying coefficients, similar to the methods outlined in [134, 135]. Unlike those papers, the non-linear characteristics of the input actuation are modelled as a function of energy dissipation of the input waveform in each cycle and utilising a method similar to equating coefficients for fast and accurate system identification. The system identification method uses sinusoidal test inputs over a small number of robotic arm positions and a minimal model of inertia to characterise the arm's behaviour at all other positions. Our scenario with closed loop PD control is similar to [82, 136], although in our case any springiness in the base response comes solely from the feedback loop setup.

7.2 α-Invariant Energy Characterisation

7.2.1 Derivation from Sinusoidal Waves

For any sinusoidal wave $v = A\sin(\omega t + \phi)$, the phase portrait $(v, \dot{v})$ is an ellipse, as shown in Fig. 7.1. The ellipse conforms to the standard equation which is shown in terms of v and $\dot{v}$ in (7.1).

$$\frac{v^2}{a^2} + \frac{\dot{v}^2}{b^2} = 1 \tag{7.1}$$

For an under-damped second order system such as the Phantom Omni, the area of the ellipse increases up to resonance then begins to shrink as the frequency increases. The α-invariant is derived from the idea that the area of the ellipse represents the energy dissipated by the input. Differentiating (7.1) with respect to t and solving for a^2 yields (7.2).

$$\frac{2v}{a^2} + \frac{1}{b^2} \cdot 2\dot{v}\frac{d\dot{v}}{dv} = 0 \tag{7.2}$$

Solving Equation (7.2) for the ratio $\frac{b^2}{a^2}$ gives Equation (7.3).

$$\frac{b^2}{a^2} = -\frac{\dot{v}}{v}\frac{d\dot{v}}{dv} \tag{7.3}$$

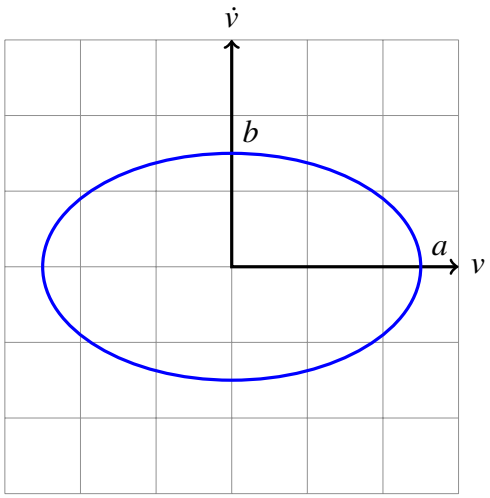

Fig. 7.1 Phase portrait of a sinusoid.

The quantity $\frac{d\dot{v}}{dv}$ is eliminated by substituting $\frac{d\dot{v}}{dv} = \frac{d\dot{v}}{dt} \div \frac{dv}{dt}$, giving (7.4).

$$a^2 = -\frac{v}{\ddot{v}}b^2 \tag{7.4}$$

Substituting (7.4) into (7.1) gives a formula for b^2 (7.5), by multiplying both sides by b^2 and substituting Equation (7.4).

$$\frac{b^2}{a^2}v^2 + \dot{v}^2 = b^2 \tag{7.5}$$

The result is Equation (7.6), which is constant for any given ellipse.

$$b^2 = \dot{v}^2 - v\ddot{v} \tag{7.6}$$

Due to the properties of derivatives of a sinusoid, the ellipse undergoes a pure scaling transformation, so its dimensions may be characterised solely by the b parameter. Equation (7.6) motivates the definition of the α-invariant as b^2, as shown in (7.7).

$$\alpha = \dot{v}^2 - v\ddot{v} \tag{7.7}$$

The α-invariant as defined in (7.7) is valid for any waveform with at least $\mathbb{C}^2$ continuity, as the validity criterion requires the α-invariant in (7.7) to always have a real value. For a

sine wave of the form $v(t) = A\sin(\omega t + \phi)$ the expression in Equation (7.7) reduces to (7.8). A sine wave has a well defined α-invariant, since it is $\mathbb{C}^\infty$, meeting the $\mathbb{C}^2$ constraint.

$$\begin{aligned}\alpha &= \dot{v}^2 + \omega^2 v^2 \\ &= (A\omega\cos(\omega t + \phi))^2 + \omega^2 \cdot (A\sin(\omega t + \phi))^2 \\ &= \omega^2 A^2\end{aligned} \tag{7.8}$$

The α-invariant in (7.7) is geometrically equivalent to the square of the vertical distance of the ellipse of (7.1), which is proportional to the area of the ellipse as frequency increases. Thus, for a sinusoidal response α represents the energy supplied as the frequency increases and is an invariant of the curve $v(t)$. In other words, for any sinusoidal input $v(t)$, the value of α is constant at all times.

7.2.2 α-Invariant for Non-Sinusoidal Periodic Waveforms

In practise, the output response of a system to a sine wave input is never perfectly sinusoidal so the α quantity is approximated using an average over a complete cycle, as shown in (7.9). In particular, while the α-invariant is constant for sinusoidal waveforms. The advantage of the average α-invariant formulation is that it is the same value no matter where in the cycle it is taken from. Due to the integration, the continuity requirement for v is relaxed from $\mathbb{C}^2$ for (7.8) to $\mathbb{C}^1$, so $\mathbb{C}^1$, waveforms such as triangle waves can also have a valid average α-invariant when taken over an entire cycle.

$$\alpha \approx \frac{1}{T}\int_{t-T}^{t} \dot{v}^2 - v\ddot{v}\, d\tau \tag{7.9}$$

Equation (7.9) is an important property of any input actuator response as it is related to the energy dissipated during each cycle, so the α invariant can be used to characterise damping and torque constant changes for different frequencies using only the values of the input and its derivatives. For example, if the damping is made a function of angular frequency it is only suitable for predicting steady state responses to a sine wave input. However, writing the damping as a function of α has the capability of describing damping changes for any input including transient step responses.

7.2.3 Convergence Properties

Attention must be given to the convergence properties of the α-invariant. Consider a periodic waveform of the type shown in (7.10). The first and second derivatives are given in (7.11) and (7.12) respectively.

$$v = \sum_{n=0}^{\infty} c_n \cos(n\omega_0 t + \phi_n) \tag{7.10}$$

$$\dot{v} = -\omega_0 \sum_{n=0}^{\infty} n c_n \sin(n\omega_0 t + \phi_n) \tag{7.11}$$

$$\ddot{v} = -\omega_0^2 \sum_{n=0}^{\infty} n^2 c_n \cos(n\omega_0 t + \phi_n) \tag{7.12}$$

The α-invariant for a periodic waveform is calculated using (7.9) from the definitions of v, $\dot{v}$ and $\ddot{v}$ given in (7.10)-(7.12). The mean α invariant sum is shown in (7.13).

$$\begin{aligned} \alpha &= \frac{1}{T}\int_0^T \dot{v}^2 - v\ddot{v}\,dt \\ &= \omega_0^2 \sum_{n=0}^{\infty} n^2 c_n^2 \end{aligned} \tag{7.13}$$

The value of α from (7.13) is considered "well behaved" if it stays a non-negative real number at all times. Since α is the sum of squares of real numbers, it will always be non-negative. Equation (7.14) shows the requirements for the α-invariant to be finite.

$$\omega_0^2 \sum_{n=0}^{\infty} n^2 c_n^2 < \infty \tag{7.14}$$

Equation (7.14) does not have a general solution. However, in general for periodic waveforms the c_n coefficients are often less than the inverse of a monomial function of n multiplied by a constant as shown in (7.15).

$$c_n^2 = \frac{k_0^2}{n^p} \tag{7.15}$$

If the sum of c_n^2 for all n is finite then the α invariant itself will be finite.

$$\begin{aligned} \sum_{n=0}^{\infty} n^2 \cdot \frac{k_0^2}{n^p} &< \infty \\ \sum_{n=0}^{\infty} n^{2-p} &< \infty \end{aligned} \tag{7.16}$$

Equation (7.16) gives the result $p > 3$, since the sum in (7.16) will always converge if $2 - p < -1$. Since (7.16) is for the squared value of c_n, the actual value of c_n is given in (7.17).

$$|c_n| < \frac{|k_0|}{n^{\frac{3}{2}}} \tag{7.17}$$

Some waveforms, such as square waves and sawtooth waves have an n^{-1} amplitude dependency in their Fourier series coefficients, and therefore do not have a rigorously defined α-invariant according to either (7.7) or (7.9). Triangle waves have a well defined average α invariant since the amplitudes for a triangle wave are proportional to n^{-2}. For example, triangle waves, which are $\mathbb{C}^1$, have a well-defined average α-invariant according to (7.9) but not a well defined α-invariant according to (7.7).

7.3 Phantom Omni Experimental Setup

The Phantom Omni is driven from Matlab/Simulink using the QuaRC block libraries provided by Quanser as outlined in Section 3.2. Fig. 7.2 shows a Sensable/Geomagic Phantom Omni with the actuated joints labelled. The arm consists of three actuated joints J_1, J_2 and J_3 and several non-actuated joints that allow freedom of movement of the "stylus" attached to link L_2. In all the experiments of this paper the angle of joint J_1 is varied while angles of joints J_2 and J_3 are held constant.

7.3.1 Model Structure and Derivation

Fig. 7.3 shows a kinematic diagram of the Phantom Omni, with the controlled angles annotated. The joints J_2 and J_3 are held at fixed angles γ_1 and γ_2 during each experimental run, and the un-actuated joints and stylus are constrained to fixed positions by a special cuff that is placed on Link 2. The physical model of the Phantom Omni is derived in a broadly similar to the way Tahmesbi identified parameters for the Phantom Premium 1.5 [78]. The main difference is that in this paper it is assumed the angular velocities and accelerations on all Joints 2 and 3 are zero. The torque $u(t)$ corresponding to motion in the yaw axis is defined in (7.18) for a command voltage $v(t)$ applied to the internal motor to generate torque and $\theta(t)$ as the angle about J_1.

$$u(t) = \overline{\beta} v(t) - \overline{C}\dot{\theta}(t) \tag{7.18}$$

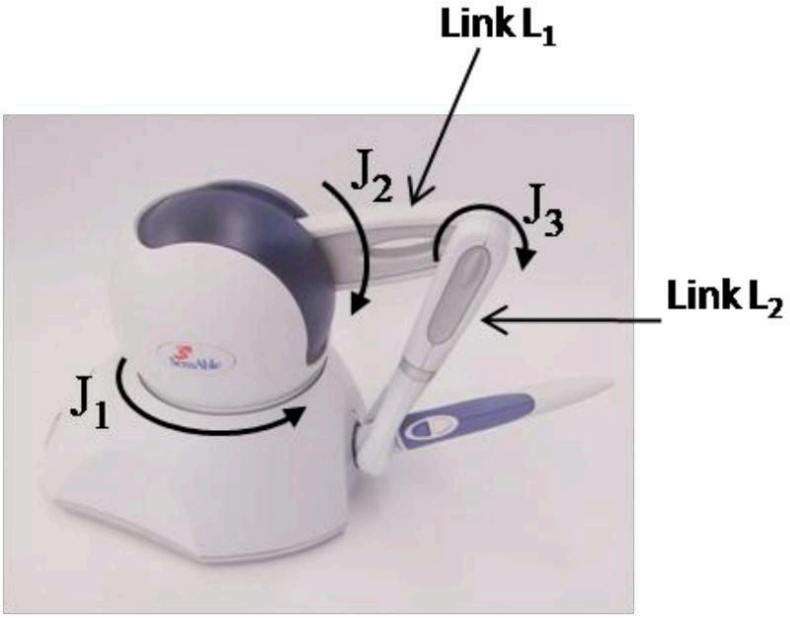

Fig. 7.2 Phantom Omni (Courtesy SenSable/Geomagic).

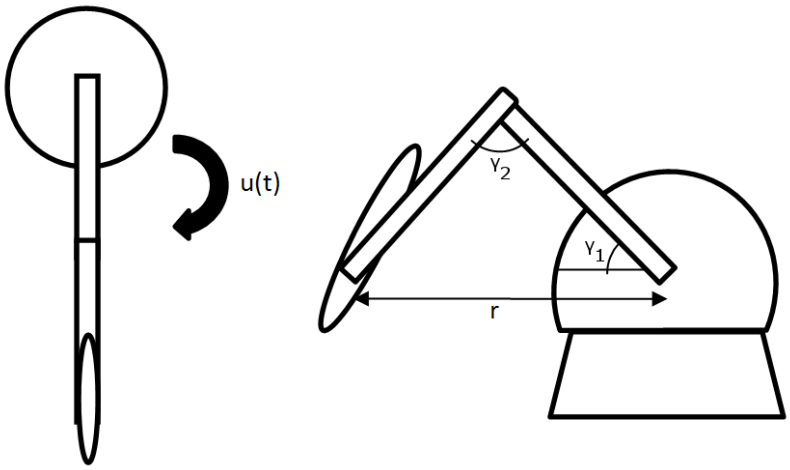

Fig. 7.3 Phantom Omni top and side views.

The quantities $\overline{\beta}$ and $\overline{C}$ in (7.18) are the torque proportionality constant and the viscous damping constant of the joint itself and its actuator. In the experiments there was no external load applied to the Phantom Omni, so it is assumed all the torque generated is used to accelerate the rotating mass of the arm. The arm torque balance is defined in (7.19) where I is the moment of inertia of the arm about the yaw axis for a given γ_1 and γ_2.

$$u(t) = I\ddot{\theta} \tag{7.19}$$

Substituting (7.19) into (7.18) produces the kinematic-dynamic model (7.20).

$$I\ddot{\theta} + \overline{C}\dot{\theta} = \overline{\beta}v(t) \tag{7.20}$$

The quantities $\overline{C}$ and $\overline{\beta}$ come from the intrinsic physical properties of joint J_1 and its actuator, including damping forces and actuator gain. Since $\overline{C}$ and $\overline{\beta}$ are defined as properties of the joint itself they do not depend on inertia, but they do depend on the kinetic energy in the joint represented by α. They are independent of the joint angle because the yaw axis has no torsional spring and the axis is vertical and so not affected by gravity.

An important insight about (7.20) is that its behaviour is not dependent on the actual values of I, $\overline{C}$ and $\overline{\beta}$ themselves, but their ratios. Therefore an inertia model can be derived by setting $\overline{\beta}$ to $1\,\mathrm{kg\,m^2\,rad\,s^{-2}\,V^{-1}}$ and allowing the inertia model alone to capture the changes in C and $\tilde{\beta}$. With this in mind, dividing through by the inertia and using substitutions $C = \frac{\overline{C}}{I}$ and $\tilde{\beta} = \frac{1}{I}$ gives the simplified model (7.21) for constant γ_1 and γ_2 angles in Fig. 7.3. The inertia is thus lumped into C and $\tilde{\beta}$ in (7.21) and direct knowledge of the physical properties of the arm (e.g. masses) is *not* required to model its behaviour. However, a model that works for all arm angles requires a model of inertia, that is shown later in the Chapter.

$$\ddot{\theta} + C\dot{\theta} = \tilde{\beta}v(t) \tag{7.21}$$

7.3.2 Controller Implementation

A proportional (P) controller is used to eliminate the control voltage from (7.21). Using a P-controller makes direct comparison of amplitude and phase of input and output angle possible, by changing the transfer function from voltage→angle to angle→angle. The control voltage $v(t)$ is defined in (7.22) where $r(t)$ is the driving reference function, and $\theta(t)$ is the measured base angle corresponding to yaw movement of the Phantom Omni.

$$v(t) = k_\mathrm{p} \cdot (r(t) - \theta(t)) \tag{7.22}$$

Substituting (7.22) into (7.21) and setting $\beta = \tilde{\beta} k_{\mathrm{p}}$ yields (7.23).

$$\ddot{\theta} + C\dot{\theta}(t) + \beta\theta(t) = \beta r(t) \tag{7.23}$$

During the system identification stage the Phantom Omni is being driven with a sinusoidal input wave, so $r(t)$ in (7.23) is defined as a sine wave given in (7.24).

$$r(t) = A_{\mathrm{r}} \sin(\omega t) \tag{7.24}$$

The goal is to use (7.23) and (7.24) to find the resonant frequency β and the damping constant C from the output time domain sinusoidal response. The constants A_{r} and k_{p} are chosen to ensure a sufficiently high voltage so that the arm has enough response that overcomes stiction and the common dead space present in most physical systems.

7.3.3 Step Response

Step response data is obtained by driving the base with a square wave with a frequency of 0.25 Hz and amplitude of 0.07 rad for a set of fixed γ_1 and γ_2 joint angles. The frequency of the square wave is low enough so that the Phantom Omni has sufficient time to get to its "final" position during each half cycle, turning the square wave response into a series of step responses. The square wave response is used to validate the α-invariant formulation on non-sinusoidal inputs and to test responses to arm joint angle combinations not used to tune parameters. The numerical simulation of the square wave is done for a two second (half cycle) from just after the input transition. The avoidance of any time right on the transition avoids any numerical problems caused by square waves not being $\mathbb{C}^1$.

7.3.4 α-Invariant for Phantom Omni

In practice, the response to a sine wave input will not be a perfect sine wave. However, the differences with the Phantom Omni are small, so that a response to a single frequency sine wave input is locally linear and can thus be approximated accurately by a linear sum of $\cos(\omega t)$ and $\sin(\omega t)$. This approximation is mathematically equivalent to an expression of the form $A_1 \cos(\omega t) + A_2 \sin(\omega t)$, which preserves the invariant property of alpha as shown by the analysis of (7.1)-(7.7). In addition, the approximation smooths out noise in the data and so avoids the computation of second order derivatives in (7.7). Substituting

$\theta = A_1\cos(\omega t) + A_2\sin(\omega t)$ and $r(t)$ from (7.24) into (7.22) yields the input voltage defined by (7.25).

$$v(t) = k_\mathrm{p}\cdot(-A_1\cos(\omega t) + (A_r - A_2)\sin(\omega t)) \tag{7.25}$$

The parameters A_1 and A_2 are frequency and inertia dependent, but constant for each sinusoidal steady state response. The input voltage $v(t)$ in (7.25) is substituted into (7.7) and simplified to give an analytical expression for the α-invariant defined in (7.26).

$$\alpha = k_\mathrm{p}^2\omega^2(A_1^2 + (A_r - A_2)^2) \tag{7.26}$$

Since α is a function of ω, it can automatically account for frequency changes which is very useful for characterising the values of C and β across a range of frequencies for a given set of arm joint angles. Specifically, for a given arm inertia I, the parameters C and β in (7.23) are written as functions of α, which correspond to the model in (7.27).

$$\ddot{\theta} + C(\alpha, I)\cdot\dot{\theta}(t) = \tilde{\beta}(\alpha, I)\cdot v(t) \tag{7.27}$$

The quantities C and $\tilde{\beta}$ in (7.27) will change for different arm angles, since the inertia will change, but by fixing the angles γ_1 and γ_2 the models of $C(\alpha, I)$ and $\tilde{\beta}(\alpha, I)$ can be separated into an inertia dependent part.

7.3.5 Inertia Modelling

The simplified inertia model about the yaw axis is derived using the thin rod approximation and Parallel Axis Theorem on each arm segment. The reference axis for the parallel axis theorem is the z axis and the radial distance is the distance along the ρ axis from the origin in the base of the arm to the arm component's centre of mass. Fig. 7.4 shows the approximate centres of masses of the respective arm segments and central shell, including the combined centre of mass of Link 2 and the Stylus. The centre of mass of the combined Link 2 and stylus was found experimentally to be quite close to the centre of mass of Link 2 alone, so Link 2 and Link 3 are combined as a single link with an offset centre of mass.

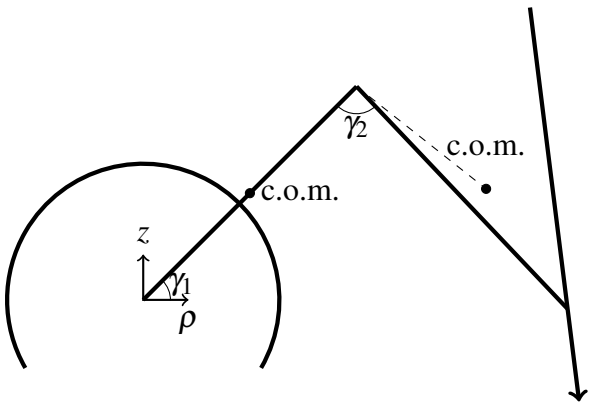

Fig. 7.4 Simplified diagram of Phantom Omni showing centre of masses.

Equation (7.28) shows the approximate inertia of the arm based on the arm lengths and masses, where I_{base} is the inertia of the base and m_n and L_n are the respective masses and lengths of Link n.

$$I = I_{\text{base}} + \frac{1}{3}m_1 L_1^2 \cos^2(\gamma_1) + m_2 \cdot \left(L_1 \cos(\gamma_1) + \frac{1}{2}L_2 \cos(\pi - \gamma_1 - \gamma_2 - \gamma_{\text{offs}})\right)^2 + \frac{1}{12}m_2 L_2^2 \cos^2(\pi - \gamma_1 - \gamma_2 - \gamma_{\text{offs}}) \tag{7.28}$$

While the simplified inertia model (7.28) has a physical derivation, it assumes the arm segments are thin rods, their masses and lengths are known and the centre of mass is exactly at the midpoint. A modified inertia model (7.29) is proposed that uses the basic form of the simplified inertia model, but does not make any assumptions about the relationship between the physical attributes of the arm and the inertia model coefficients. The modified inertia model is similar to the simplified model except the trigonometric coefficients are not fixed in terms of masses and lengths. This feature allows more flexibility in the inertia model with respect to unknown distributions of masses. The more flexible inertia model is shown in (7.29). It is developed by expanding (7.28), grouping the coefficients and allowing the values to "float" rather than fixing their form in terms of the masses and lengths.

The $I_{\square}$ coefficients in (7.28) represent the total effects of each arm segment on the different trigonometric quantities. Unless $I_{\text{base}} = 0$ it is not possible to "reverse engineer" the masses and lengths, as for two segments there are four unknowns but five quantities that must be derived from them. However, unless the assumptions that underlie (7.28) are exactly correct, (7.29) will provide a more accurate inertia model as it includes more flexibility for

accommodating non-uniform distributions of mass. The modified inertia model is deemed physically valid if I_{base}, I_1, I_2 and I_3 are non-negative.

$$\begin{aligned} I =& I_{\text{base}} + I_1 \cos^2(\gamma_1) + I_2 \cos^2(\pi - \gamma_1 - \gamma_2 - \gamma_{\text{offs}}) + \\ & I_3 \cos(\gamma_1) \cos(\pi - \gamma_1 - \gamma_2 - \gamma_{\text{offs}}) \end{aligned} \tag{7.29}$$

The final models (7.30) and (7.31) show the final inertia model for the linear coefficients. A damping ratio $\overline{C}_0$ is introduced in (7.31), with $\overline{C}_0 = \frac{\overline{\beta}}{\overline{C}} \equiv \frac{\tilde{\beta}_{\text{linear}}}{C_{\text{linear}}}$. This transformation is valid because it is derived from the property that $\overline{\beta}$, $\overline{C}$ and $\overline{C}_0$ are solely functions of the intrinsic physical properties of Joint 1, and are therefore independent of the states of Joints 2 and 3.

$$\tilde{\beta}_{\text{linear}} \triangleq \frac{1}{I} \tag{7.30}$$

$$C_{\text{linear}} \triangleq \frac{1}{\overline{C}_0 I} \tag{7.31}$$

The I_{base}, I_1, I_2, I_3, γ_{offs} and $\overline{C}_0$ coefficients are found in Matlab using its standard non-linear least squares solver (`lsqnonlin`) and a test function derived by combining (7.29), (7.30) and (7.31). The input data consists of the arm angles γ_1, γ_2 and $\tilde{\beta}_{\text{linear}}$, C_{linear} calculated at each arm angle from the fitted sine wave sweeps. The full regression equations are shown in (7.32)-(7.34), with vector forms representing the complete sets of γ_1, γ_2 and $\tilde{\beta}_{\text{linear}}$, C_{linear} for all arm angles tested.

$$\begin{aligned} \vec{I} =& I_{\text{base}} + I_1 \cos^2(\vec{\gamma}_1) + I_2 \cos^2(\pi - \vec{\gamma}_1 - \vec{\gamma}_2 - \gamma_{\text{offs}}) \\ & + I_3 \cos(\vec{\gamma}_1) \cos(\pi - \vec{\gamma}_1 - \vec{\gamma}_2 - \gamma_{\text{offs}}) \end{aligned} \tag{7.32}$$

$$\vec{\tilde{\beta}}_{\text{linear}} = \frac{1}{\vec{I}} \tag{7.33}$$

$$\vec{C}_{\text{linear}} = \frac{1}{\overline{C}_0 \vec{I}} \tag{7.34}$$

The non-linear regression result from Matlab gives the best set of parameters I_{base}, I_1, I_2, I_3, γ_{offs} and $\overline{C}_0$ that minimises the sum squared error between the left hand side and right hand side of Equations (7.33) and (7.34). Once the inertia model coefficients are identified, a model for the damping can proceed as described in the next section.

7.4 Mathematical Modelling and Analysis Description

7.4.1 Non-Linear Damping Model

A plot of experimentally determined damping against the α-invariant (Fig. 7.12) shows damping increases rapidly with decreasing α. Since α is related to energy, this behaviour is not surprising as at low energy stiction effects dominate, producing a high damping coefficient. The friction properties are dependent on intrinsic physical properties of the joint itself and so the inertia of the arm is not relevant to their formulation. At higher input energies stiction disappears and the only damping is viscous damping. For a given inertia I this behaviour is captured by a tri-linear piecewise model (7.35) where $\Pi_{\alpha_m,\alpha_n}(\alpha) = \mathrm{H}(\alpha-\alpha_m) - \mathrm{H}(\alpha-\alpha_n)$ is the Boxcar function. The quantities $C_0,\ldots,C_3$ are defined in (7.36) and $\alpha_0,\ldots,\alpha_3$ are a monotonically increasing series of break points between the different models.

$$\begin{aligned} C(\alpha,I) = &\left[C_0(I) + \frac{C_1(I)-C_0(I)}{\alpha_1-\alpha_0}(\alpha-\alpha_0)\right]\cdot\Pi_{\alpha_0,\alpha_1}(\alpha) \\ &+ \left[C_1(I) + \frac{C_2(I)-C_1(I)}{\alpha_2-\alpha_1}(\alpha-\alpha_1)\right]\cdot\Pi_{\alpha_1,\alpha_2}(\alpha) \\ &+ \left[C_2(I) + \frac{C_3(I)-C_2(I)}{\alpha_3-\alpha_2}(\alpha-\alpha_2)\right]\cdot\Pi_{\alpha_2,\alpha_3}(\alpha) \end{aligned} \tag{7.35}$$

$$\begin{aligned} C_0(I) &= C(\alpha_0,I) \\ C_1(I) &= C(\alpha_1,I) \\ C_2(I) &= C(\alpha_2,I) \\ C_3(I) &= C(\alpha_3,I) \end{aligned} \tag{7.36}$$

The break points are found by a grid search with the goal of minimising the error between the model and the true data at each inertia. In other words, for each inertia I, four damping values $C_0(I),\ldots,C_3(I)$ uniquely characterise the tri-linear approximation to the non-linear damping curve. The values of $\alpha_0,\ldots,\alpha_3$ in (7.36) are chosen in a grid search to minimize the least squares error. Fig. 7.5 shows a typical example of $C(\alpha,I)$ curves for three monotonically increasing values of inertia, $I_\mathrm{a} < I_\mathrm{b} < I_\mathrm{c}$.

The damping curve in Fig. 7.6 drops as inertia increases from I_a to I_c. This behaviour makes physical sense since a high inertia corresponds to more mass being further away from the axis of rotation. The higher inertia results in more energy storage at a given rotational velocity and more torque for a given change in angular velocity. Hence, with higher inertia viscous friction effects dominate thus giving lower damping values.

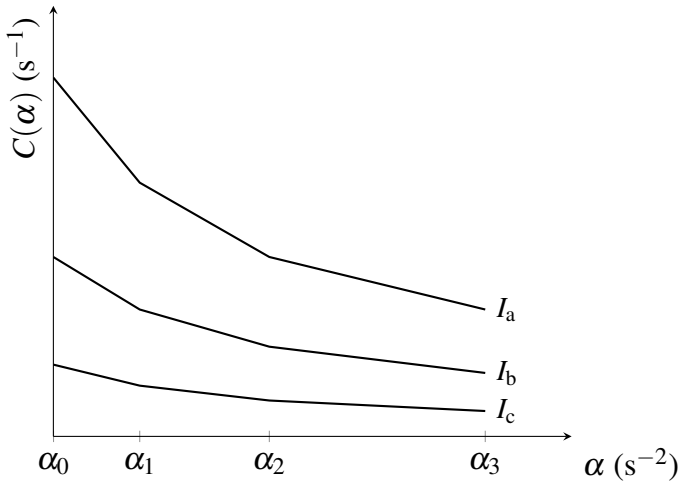

Fig. 7.5 Illustrative non-linear damping curves as a function of α for various values of inertia.

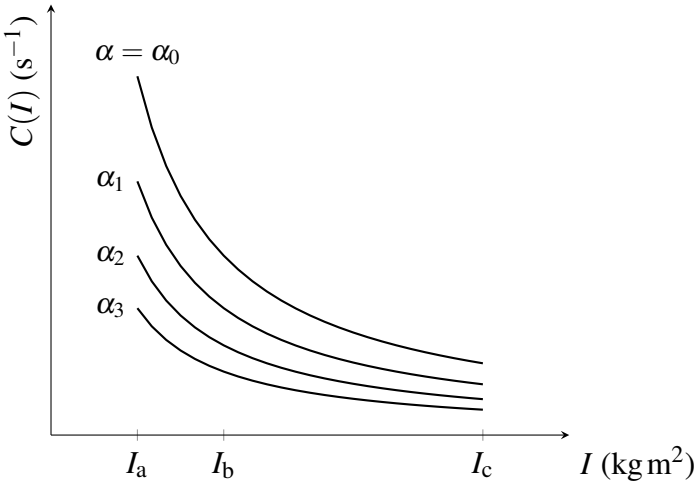

Fig. 7.6 Illustrative non linear damping model as a function of inertia for different values of α.

Fig. 7.5 and Fig. 7.6 represent vertical slices of the $C(I,\alpha)$ surface in (7.27) that correspond to constant I and constant α respectively. The slices at constant I give sharply decreasing curves where the slices of constant α are more slowly decreasing. The curves are defined by (7.37).

$$\begin{aligned} C_0(I) &= \frac{1}{C_{01}I} \\ C_1(I) &= \frac{1}{C_{11}I} \\ C_2(I) &= \frac{1}{C_{21}I} \\ C_3(I) &= \frac{1}{C_{31}I} \end{aligned} \tag{7.37}$$

7.4.2 Non-Linear Torque Constant Model

A plot of experimentally determined damping against the α invariant (Fig. 7.13) suggests the torque constant $\tilde{\beta}$ can be modelled by a decreasing linear line. For a given inertia I, the model is defined in (7.38) where $\tilde{\beta}_0$ and $\tilde{\beta}_1$ are the torque constant values at the predefined α values $\overline{\alpha}_0$ and $\overline{\alpha}_1$ respectively. Fig. 7.7 shows a family of different $\tilde{\beta}$ lines for monotonically increasing inertias I_1, I_2 and I_3.

$$\tilde{\beta}(\alpha,I) = \tilde{\beta}_0(I) + \frac{\tilde{\beta}_1(I) - \tilde{\beta}_0(I)}{\overline{\alpha}_1 - \overline{\alpha}_0}(\alpha - \overline{\alpha}_0) \tag{7.38}$$

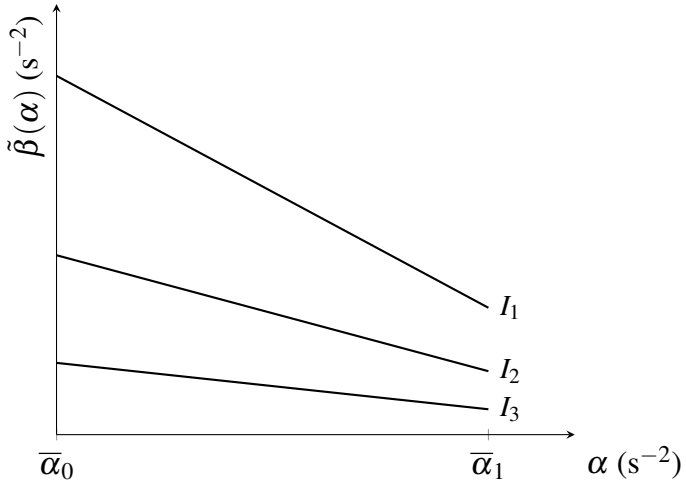

Fig. 7.7 Torque Constant as a function of α for various values of inertia.

Therefore, in a similar way to the damping in (7.37), for a given inertia two torque constant values uniquely characterise the torque constant curve. The final model for $\beta(\alpha,I)$

includes models of inertia defined by (7.39), where I is the inertia from measured data and the curves are defined so that $\beta_0'(I), \beta_1'(I) < 0$ and $\beta_0(\overline{\alpha}_0, I), \beta_1(\overline{\alpha}_1, I) > 0$.

$$\begin{aligned} \tilde{\beta}_0(I) &= \frac{1}{\tilde{\beta}_{01} I} \\ \tilde{\beta}_1(I) &= \frac{1}{\tilde{\beta}_{11} I} \end{aligned} \tag{7.39}$$

Fig. 7.8 gives an example of the $\beta_0(I)$ and $\beta_1(I)$ curves. Fig. 7.8 shows a typical example of modelled $\beta(\alpha, I)$ curves for different values of α.

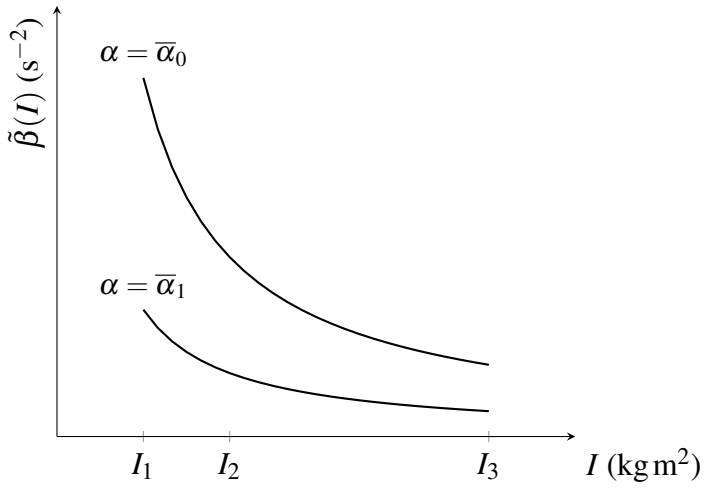

Fig. 7.8 Torque Constant Model as a function of inertia for different values of α.

7.4.3 Algorithm for Determination of Coefficients

The next step is to include the asymptotic inertia models of the damping and torque constants given by (7.37) and (7.39). In other words, the non-linear parameter models of (7.35) - (7.39) are fitted to the measured $C_{\text{data}}(\omega)$ and $\beta_{\text{data}}(\omega)$. The unknown parameters to identify are $C_{01}, C_{11}, C_{21}, C_{31}, \tilde{\beta}_{01}$ and $\tilde{\beta}_{11}$. However, these parameters cannot be optimised directly with linear least squares since (7.37) and (7.39) are non-linear. Therefore, the values of $C_0, \ldots, C_3, \tilde{\beta}_0$ and $\tilde{\beta}_1$ are first optimised for each arm angle to create intermediate "data". The models of (7.37) and (7.39) are then inverted, and fitted to the inverted independent damping and torque constant "data" values by linear least squares. The procedure is summarised in list of steps in Fig. 7.9.

Step 1: For a given set i of arm angles ${}^{i}\gamma_1$ and ${}^{i}\gamma_2$, treat $C_0 = C_0(I), \cdots, C_3(I)$ and $\tilde{\beta}_0 = \tilde{\beta}_0(I), \tilde{\beta}_1 = \tilde{\beta}_1(I)$ as global constants. Fit these to the measured $C_{\text{data}}(\omega)$ and $\tilde{\beta}_{\text{data}}(\omega)$ for each arm position.
Step 2: Define the resulting values of Step 1 by $\overline{C}_{j,i} \equiv \{C_j(I)$ corresponding to ith arm angle combination and $j = 0,1,2,3\}$ and $\overline{\beta}_{j,i} \equiv \{\beta_j(I)$ corresponding to ith arm angle combination and $j = 0,1\}$.
Step 3: Using the values from Step 2, define: $C_{0,\text{data}} \equiv \left\{\overline{C}_{0,i}, i = 1,\ldots,9\right\}, \ldots, C_{3,\text{data}} \equiv \left\{\overline{C}_{3,i}, i = 1,\ldots,9\right\}$ and $\tilde{\beta}_{0,\text{data}} \equiv \left\{\overline{\tilde{\beta}}_{0,i}, i = 1,\ldots,9\right\}, \tilde{\beta}_{1,\text{data}} \equiv \left\{\overline{\tilde{\beta}}_{1,i}, i \equiv 1,\ldots,9\right\}$.
Step 4: Fit $C_{01}I, \cdots, C_{31}I$ and $\tilde{\beta}_{01}I, \tilde{\beta}_{11}I$ from the inverse of (7.37) and (7.39) to the inverse of $C_{0,data}$ and $\beta_{0,data}$ from Step 3 by linear least squares. For example, $C_{01}I$ would be fitted to 9 intermediate "data" values $\frac{1}{\overline{C}_{0,1}}, \frac{1}{\overline{C}_{0,2}}, \cdots, \frac{1}{\overline{C}_{0,9}}$, which ensures that the resulting optimisation is linear.
Step 5: Output $C_{01}, C_{11}, C_{21}, C_{31}, \tilde{\beta}_{01}, \tilde{\beta}_{11}$.

Fig. 7.9 Algorithm for identifying damping and torque constant models of (7.37) and (7.39) for a three-segment piecewise C model and linear $\tilde{\beta}$ model.

7.4.4 Sinusoidal Steady State Analysis

Sinusoidal steady state analysis is used to derive the amplitudes A_1 and A_2 at a particular frequency for calculation of the α invariant using (7.26). For each fixed arm position corresponding to a constant inertia, the Phantom Omni is driven with a sine wave input and allowed to reach steady state. In general the response $\theta(t)$ will not be perfectly sinusoidal due to noise, un-modelled disturbances and non linearities. The magnitude difference and phase shift between the steady state response and the input wave is calculated by approximating the output waveform as a sine wave with the same frequency as the input as defined in (7.40).

$$\tilde{\theta}(t) = A_1 \cos(\omega t) + A_2 \sin(\omega t) \tag{7.40}$$

For each ω, the A_1 and A_2 coefficients are obtained by solving the matrix equation (7.41), where $\vec{t}$ is the vector of time values and $\vec{\theta}$ is the vector of measured angle values in the experiment.

$$\begin{bmatrix}\cos(\omega\vec{t}) & \sin(\omega\vec{t})\end{bmatrix}\begin{bmatrix}A_1\\A_2\end{bmatrix} = \begin{bmatrix}\vec{\theta}\end{bmatrix} \tag{7.41}$$

Equation (7.41) is solved by linear least squares and the resulting A_1 and A_2 are used to find C and β at a particular sine wave input frequency by (7.42) and (7.43).

$$C_{\text{data}}(\omega) = -\frac{\omega A_{\text{r}} A_1}{A_1^2 - (A_{\text{r}} - A_2)A_2} \tag{7.42}$$

$$\beta_{\text{data}}(\omega) = \frac{\omega^2 (A_1^2 + A_2^2)}{A_1^2 - (A_{\text{r}} - A_2)A_2} \tag{7.43}$$

Equations (7.42) and (7.43) are derived by solving (7.27) with $v(t)$ given by (7.25) for the steady state solution equal to $A_1 \cos(\omega t) + A_2 \sin(\omega t)$, equating coefficients and solving analytically. The values of $C_{\text{data}}(\omega)$ and $\beta_{\text{data}}(\omega)$ are subsequently used to calculate the non-linear C and β models along with the invariant formulation. For a given Phantom Omni position γ_1 and γ_2 the calculation of C and β over all frequencies is performed by first substituting $\theta = \tilde{\theta}(t)$ from (7.40) into (7.23) and equating coefficients of $\cos(\omega t)$ and $\sin(\omega t)$ yields (7.44).

$$\begin{aligned} -\omega^2 A_1 + \omega A_2 C + A_1 \beta = 0 \\ -\omega^2 A_2 + \omega A_1 C + (A_2 - A_{\text{r}})\beta = 0 \end{aligned} \tag{7.44}$$

Equation (7.44) is written in the matrix form as shown in (7.45).

$$\begin{bmatrix} \vec{\omega} \circ \vec{A}_2 & \vec{A}_1 \\ \vec{\omega} \circ \vec{A}_1 & \vec{A}_2 - A_{\text{r}} \vec{1}_{n\times 1} \end{bmatrix} \begin{bmatrix} C \\ \beta \end{bmatrix} = \begin{bmatrix} \vec{A}_1 \circ \vec{\omega}^2 \\ \vec{A}_2 \circ \vec{\omega}^2 \end{bmatrix} \tag{7.45}$$

The quantities $\vec{\omega}$, $\vec{\omega}^2$, $\vec{A}_1$ and $\vec{A}_2$ are defined in (7.46), and the symbol $\circ$ represents the Hadamard (element wise) product of two vectors or matrices (c.f. $.*$ operator in Matlab).

$$\begin{aligned} \vec{\omega} &= [\omega_1, \omega_2, \cdots, \omega_n]^{\text{T}} \\ \vec{\omega}^2 &= \vec{\omega} \circ \vec{\omega} = \left[\omega_1^2, \omega_2^2, \cdots, \omega_n^2\right]^{\text{T}} \\ \vec{A}_1 &= [A_1(\omega_1), A_1(\omega_2), \cdots, A_1(\omega_n)]^{\text{T}} \\ \vec{A}_2 &= [A_2(\omega_1), A_2(\omega_2), \cdots, A_2(\omega_n)]^{\text{T}} \end{aligned} \tag{7.46}$$

In a similar way to (7.37) and (7.39), the effects of inertia are modelled by the following asymptotic curves given in (7.47) and (7.48), where the inertia I is the modified inertia model (7.29).

$$C_{\text{linear}}(I) = \frac{1}{\overline{C}_0 I} \tag{7.47}$$

$$\beta_{\text{linear}}(I) \triangleq \frac{1}{I} \tag{7.48}$$

The resulting model is defined in (7.49).

$$\begin{aligned} \ddot{\theta} + C_{\text{linear}}(I)\dot{\theta} &= \tilde{\beta}_{\text{linear}}(I)v(t) \\ \tilde{\beta}_{\text{linear}}(I) &= \frac{\beta_{\text{linear}}(I)}{k_{\text{p}}} \end{aligned} \tag{7.49}$$

The model of (7.49) is non-linear with respect to inertia. However, for any fixed inertia or equivalent arm position the yaw response is linear, hence (7.49) is still referred to as "global linear" for comparative purposes.

7.4.5 Numerical Solution method

The numerical solution uses a state space formulation which treats the differential equation (7.27) as linear time invariant for the duration of a particular time step. The treatment is similar to the "quasilinearisation" technique of identifying unknown state parameters in real time as described by Kagiwada [137]. The actual coefficient values of C and $\tilde{\beta}$ are calculated from the estimated invariant and the estimated second derivative of the input and output. The second derivatives and α value are determined by iterating through the governing equations of the system until all three quantities converge to the larger of either an absolute tolerance or a relative tolerance.

The numerical solution method is implemented using Matlab's `ode45` solver to evaluate a linear time variant ordinary differential equation. The `ODEFUN` argument to `ode45` is given as a function that calculates the C and $\tilde{\beta}$ values to use at the given point in time using α and any other parameters relevant to the implementation. Equation (7.21) is used with `ode45` in state space form as Equation (7.50).

$$\begin{aligned} \dot{\theta} &= \Phi \\ \dot{\Phi} &= -C(\alpha(t), I)\Phi + \tilde{\beta}(\alpha(t), I)v(t) \\ \alpha(t) &= \dot{v}^2 - v\ddot{v} \\ v(t) &= k_{\text{p}}(r(t) - \theta(t)) \end{aligned} \tag{7.50}$$

For a sinusoidal input, $v(t)$ is given by (7.25). However, (7.50) cannot be solved directly for θ and Φ since α is dependent on $\ddot{v}$ which is dependent on $\ddot{\theta}$. Let C_{linear} and $\tilde{\beta}_{\text{linear}}$ be

the global linear model parameters for the given inertia I from (7.47) and (7.48). The ith approximation to α at $t = t_0$ is defined by (7.51).

$$\begin{aligned}
\alpha^{(i)}_{\text{approx}}(t_0) &= \dot{v}^2(t_0) - v(t_0)\ddot{v}^{(i-1)}_{\text{approx}}(t_0) \\
C^{(i)}_{\text{approx}}(t_0) &= C(\alpha^{(i)}_{\text{approx}}(t_0), I) \\
\tilde{\beta}^{(i)}_{\text{approx}}(t_0) &= \tilde{\beta}(\alpha^{(i)}_{\text{approx}}(t_0), I) \\
\dot{\Phi}^{(i)}_{\text{approx}}(t_0) &= -C^{(i)}_{\text{approx}}(t_0)\Phi(t_0) + \tilde{\beta}^{(i)}_{\text{approx}}(t_0)v(t_0) \\
\ddot{v}^{(i)}_{\text{approx}}(t_0) &= k_{\text{p}} \cdot (\ddot{r}(t_0) - \dot{\Phi}^{(i)}_{\text{approx}}(t_0)), \quad i = 1, 2, \ldots, N
\end{aligned} \tag{7.51}$$

$$\ddot{v}^{(0)}_{\text{approx}}(t_0) = -C_{\text{linear}}\Phi + \tilde{\beta}_{\text{linear}}v(t_0) \tag{7.52}$$

For the given initial starting approximation of (7.52), $\alpha^{(i)}_{\text{approx}}$ is updated at each iteration $i = 1, 2, \ldots, N$ until the stopping rule condition defined in (7.53) is met.

$$|\alpha^{(i)}_{\text{approx}} - \alpha^{(i-1)}_{\text{approx}}| < \max\left(10^{-6}, 10^{-3}|\alpha^{(i)}_{\text{approx}}|\right) \tag{7.53}$$

Equation (7.53) ensures the iterative algorithm stops when α_{approx} has converged to within 10^{-6} or 0.1 %, whichever is the larger change. The modified form of the standard relative error equation is used, to ensure the stopping condition calculation remains numerically stable when $|\alpha_{\text{approx}}| \to 0$. The tolerances for (7.53) were chosen empirically and in all cases gave rapid convergence with only a few iterations required.

7.5 Results

Two main experiments were performed on the Phantom Omni. The experiments consisted of a sinusoidal steady state frequency response for identifying model parameters, and step responses for testing the parameters on data the model was not tuned on. The frequency response experiments were performed in nine different joint angle positions corresponding to the combinations of angles given in Table 7.1. To verify the sine wave derived non-linear model a 0.25 Hz square wave input was used with the 25 joint angle positions given in Table 7.2.

Table 7.1 Phantom Arm Joint Angles for Frequency Response.

Experiment 1 - Frequency Response	
γ_1 **Angle**	γ_2 **Angles**
25°	70°, 90°, 115°
45°	70°, 90°, 115°
65°	70°, 90°, 115°

Table 7.2 Phantom Arm Joint Angles for Step Response.

Experiment 2 - Step Response	
γ_1 **Angle**	γ_2 **Angles**
25°	60°, 70°, 90°, 110°, 115°
35°	60°, 70°, 90°, 110°, 115°
45°	60°, 70°, 90°, 110°, 115°
55°	60°, 70°, 90°, 110°, 115°
65°	60°, 70°, 90°, 110°, 115°

7.5.1 Modified Inertia and Damping Model

Table 7.3 is a summary of the input and output data from the inertia modelling. It is pleasing to see the fitted and modified inertias all match closely, as well as the damping ratio. This shows the simplified inertia and damping model (7.29)-(7.31) is capable of accurately capturing the linear dynamics of the Phantom Omni. The $\overline{C}_0$ ratio is calculated by a simple linear regression between the fitted C_{linear} and $\tilde{\beta}_{\text{linear}}$. The identified data in Columns 5 and 6 implies the $\frac{C_{\text{linear}}}{\tilde{\beta}_{\text{linear}}}$ ratio ($\overline{C}_0$) is approximately 36.727, which is corroborated by the identified ratio of 36.693. The results at γ_1 =45° and γ_2 =90° compare well with the data driven model results of $\tilde{\beta} = 172.3$ and $C = 5.216$ for the PRBS input, although they are also close to the results for γ_1 =25° and γ_2 =90°. This is expected, as the modelled $\tilde{\beta}$ and C from the sinusoidal steady state responses are also close together in value. Table 7.4 shows the matched coefficients of the modified inertia model, offset angle and damping ratio from matching the fitted $\tilde{\beta}_{\text{linear}}$ and C_{linear} in Table 7.3 using the non-linear regression (7.33) and (7.34).

Table 7.3 Frequency Response Calculated from Global Linear Model of C_{linear} and $\tilde{\beta}_{\text{linear}}$.

Set Angle (°)		**Mean True Angle** (°)		**Fitted**		**Modelled**	
γ_1	γ_2	γ_1	γ_2	C_{linear} (s^{-1})	$\tilde{\beta}_{\text{linear}}$ (s^{-2})	C_{linear} (s^{-1})	$\tilde{\beta}_{\text{linear}}$ (s^{-2})
25	70	21.54	69.54	5.890	231.53	6.061	222.41
25	90	20.55	88.54	4.728	177.35	4.876	178.90
25	115	19.31	112.44	4.288	149.43	3.955	145.12
45	70	40.68	68.52	5.998	226.42	6.122	224.65
45	90	39.83	87.63	4.901	176.06	5.048	185.23
45	115	39.16	111.98	4.612	154.47	4.329	158.86
65	70	60.68	67.62	7.185	275.32	7.229	265.26
65	90	60.08	87.00	6.275	222.82	6.242	229.04
65	115	59.56	111.45	5.915	207.83	5.821	213.59
		$\overline{C}_0$ Ratio		36.727		36.693	

Table 7.4 Experimentally Determined Inertia Model Parameters for (7.29) and Damping.

Quantity	**Value**
I_{base}	$1.063 \cdot 10^{-3}\,\text{kg m}^2$
I_1	$1.401 \cdot 10^{-3}\,\text{kg m}^2$
I_2	$2.889 \cdot 10^{-3}\,\text{kg m}^2$
I_3	$9.392 \cdot 10^{-3}\,\text{kg m}^2$
γ_{offs}	9.931°
$\overline{C}_0$	36.693

7.5.2 Non-Linear Resonance and Damping

Fig. 7.10 and Fig. 7.11 show the resulting model fits of (7.37) and (7.39) to this intermediate damping and torque constant data.

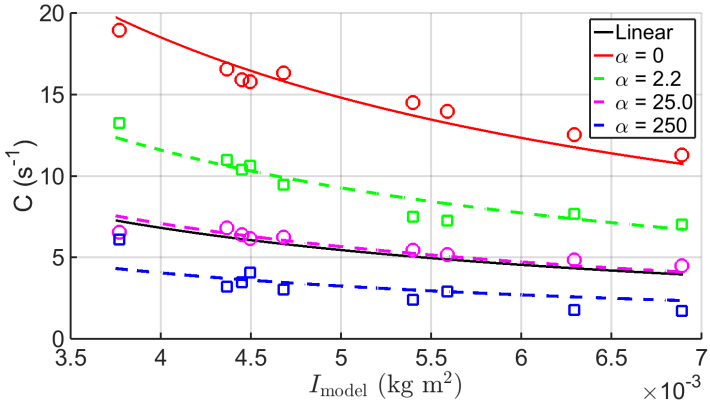

Fig. 7.10 Non-linear C model as a function of inertia I with Global Linear Model for comparison.

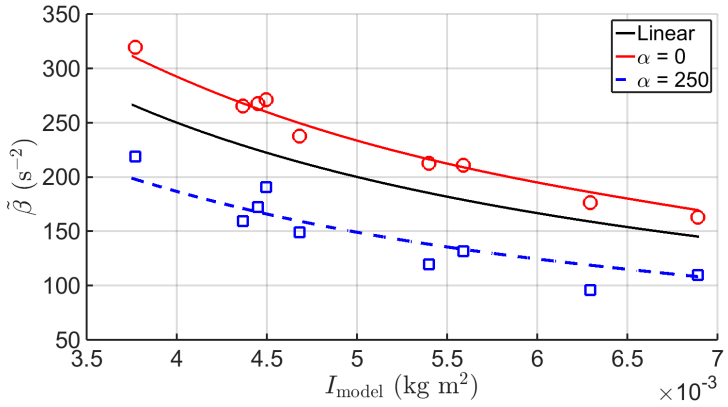

Fig. 7.11 Non-linear $\tilde{\beta}$ model as a function of inertia I with Global Linear Model for comparison.

The final non-linear model parameters that describe $C(\alpha, I)$ and $\tilde{\beta}(\alpha, I)$ in (7.37) and (7.39) derived from data gathered at the set point angles in Table 7.1 are given in Table 7.5 and Table 7.6.

Table 7.5 Non-linear $\tilde{\beta}$ model parameters.

Quantity	α value	Value
$\tilde{\beta}_{01}$	0	1.3405
$\tilde{\beta}_{11}$	250	0.8558

Table 7.6 Non-linear C model parameters.

Quantity	Value	α value	Ratio to Identified $\overline{C}_0$
C_{01}	61.733	0	1.68238
C_{11}	35.316	2.2	0.96245
C_{21}	21.570	25	0.58783
C_{31}	13.509	250	0.36816

Table 7.3 gives the numerical comparison between the measured and modelled damping and torque constant data. A similar approach to Fig. 7.9 is now applied to the global linear model to identify the unknown parameters C_{L0}, C_{L1}, β_{L0} and β_{L1} in (7.47) and (7.48). As a comparison the parameters of Table 7.5 and (7.37) and (7.39) are used to simulate the non-linear model defined by (7.22), (7.24) and (7.27). The results of this modelling are summarised in Table 7.7.

Table 7.7 Comparison of 90th Percentile Absolute Errors on Magnitude and Phase Angle for Linear and Non-Linear Models.

Setpoint		**90th Percentile Linear**		**90th Percentile Non-Linear**	
γ_1	γ_2	Magnitude	Phase (°)	Magnitude	Phase (°)
25	70	0.6410	12.1902	0.4146	6.3605
25	90	0.4776	19.4772	0.2756	2.7394
25	115	0.4737	10.6066	0.1935	3.4813
45	70	0.5002	13.2881	0.2202	2.1805
45	90	0.3675	25.3134	0.5202	7.3346
45	115	0.5762	15.0195	0.5173	4.3214
65	70	0.3939	14.0549	0.3714	13.9204
65	90	0.4312	16.2316	0.2028	2.7323
65	115	0.3403	14.3577	0.2968	5.9665
Average		0.4668	15.6155	0.3347	5.4485

7.5.3 Frequency Response

To see the impact of the α-invariant energy approach of (7.27), a frequency response experiment is performed with the robot arm in the $\gamma_1 = 65°$, $\gamma_2 = 90°$ position, which is one of the positions in Table 7.1. For this experiment the driving frequencies are $f = [1.5, 2, 2.5, 3, 3.5, 4, 5, 6, 7]$Hz. The parameters $C_{\text{data}}(\omega)$ and $\beta_{\text{data}}(\omega)$ are determined from (7.42) and (7.43) and represent the damping and torque constants derived from the data, and are referred to as "measured data". The effective mean α-invariant is also computed for each frequency using (7.26) and is referred to as $\alpha_{\text{data}}(\omega)$. The global linear model parameters C_{linear} and β_{linear} are computed by solving (7.45) by linear least squares which yields the results shown in Table 7.8.

Table 7.8 Linear Model Parameters for $\gamma_1 = 65°, \gamma_2 = 90°$.

Quantity	**Fitted**	**Modelled**	
C_{linear}	6.275	6.242	s^{-1}
β_{linear}	445.6	458.0	s^{-2}
$\tilde{\beta}_{\text{linear}}$	222.8	229.0	s^{-2}

The functions $C(\alpha, I)$ and $\tilde{\beta}(\alpha, I)$ in (7.37) and (7.39) are fitted by linear least squares to the damping and torque constant data $C_{\text{data}}(\omega)$ and $\beta_{\text{data}}(\omega)$. The quantities $C_0 = C_0(I), \ldots, C_3 = C_3(I)$ and $\tilde{\beta}_0 = \tilde{\beta}_0(I), \tilde{\beta}_1 = \tilde{\beta}_1(I)$ are treated as global constants, since I is fixed in this case. For the case of β, this process involves fitting a linear line to β_{data}. The resulting values of $C_0, \ldots, C_3$, $\tilde{\beta}_0$, $\tilde{\beta}_1$ and the predefined α values are given in Table 7.9. Fig. 7.12 and Fig. 7.13 show the resulting damping and torque constant models versus the measured data as well as the data for the global linear approximation in Table 7.8.

Table 7.9 Model parameters for $\gamma_1 = 65°, \gamma_2 = 90°$.

Quantity	**Value**
I	$0.004\,366\,\mathrm{kg\,m^2}$
C_0	$16.955\,\mathrm{s^{-1}}$
C_1	$10.619\,\mathrm{s^{-1}}$
C_2	$6.486\,\mathrm{s^{-1}}$
C_3	$3.710\,\mathrm{s^{-1}}$
$\tilde{\beta}_0$	$267.6\,\mathrm{s^{-2}}$
$\tilde{\beta}_1$	$170.9\,\mathrm{s^{-2}}$

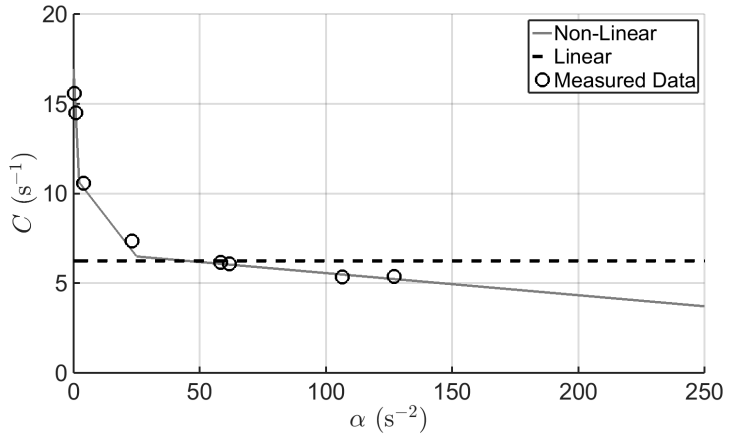

Fig. 7.12 C as a function of α-invariant at $\gamma_1 = 65°$, $\gamma_2 = 90°$.

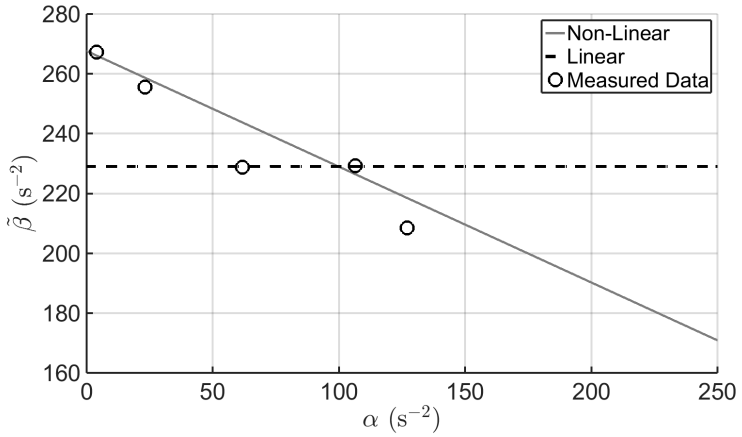

Fig. 7.13 $\tilde{\beta}$ as a function of α-invariant at $\gamma_1 = 65°$, $\gamma_2 = 90°$.

The non-linear damping model of (7.27) is now simulated with the technique described in (7.50) - (7.52). The equivalent non-linear model magnitude and phase values for each frequency are computed by fitting sine waves to the resulting output waveforms using (7.40), and comparing to the input $r(t)$ wave defined in (7.24). Fig. 7.14 and Fig. 7.15 show the magnitude and phase responses of the non-linear model of (7.27) and global linear model of (7.23) plotted against the measured data. Fig. 7.16 shows an example of the time domain outputs. All these figures demonstrate a significant improvement in modelling accuracy with the α-invariant formulation.

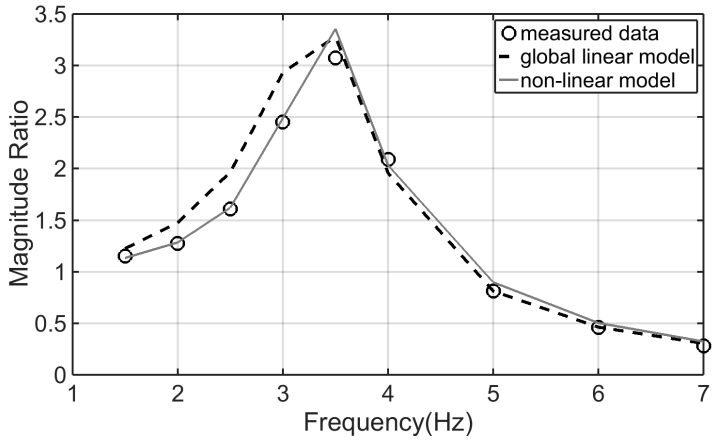

Fig. 7.14 Fundamental Frequency magnitude response for $\gamma_1 = 65°$, $\gamma_2 = 90°$.

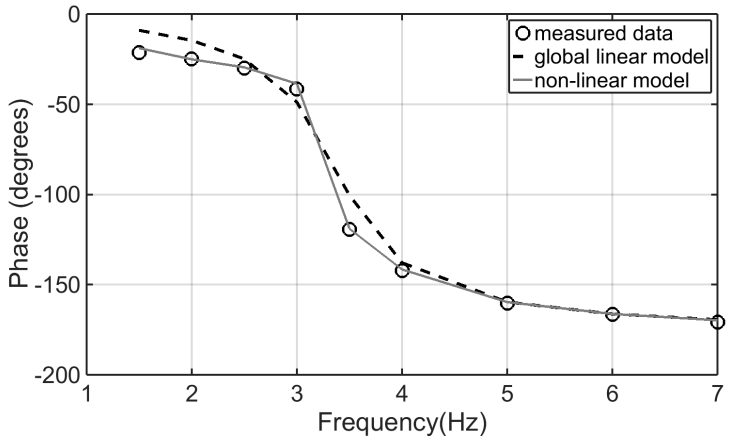

Fig. 7.15 Fundamental Frequency phase response for $\gamma_1 = 65°$, $\gamma_2 = 90°$.

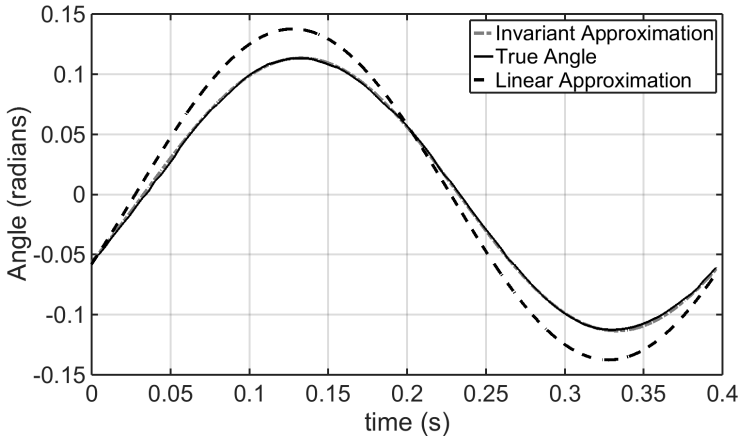

Fig. 7.16 Time domain response comparison for $\gamma_1 = 65°$, $\gamma_2 = 90°$ at $f = 2.5$Hz.

Fig. 7.17 shows that modelling damping acceleration solely as a function of velocity doesn't work for the Phantom Omni yaw response. The response does exhibit the Stribeck Effect but the curve has loops which suggests that the damping acceleration is not a function of velocity alone. Velocity is also not an invariant for a sinusoidal wave, which makes it difficult or impossible to generalise non-linear behaviour based on velocity to other scenarios. The advantage of the α-invariant method over the other methods is that it can utilize steady state experiments to predict non-linear transient responses.

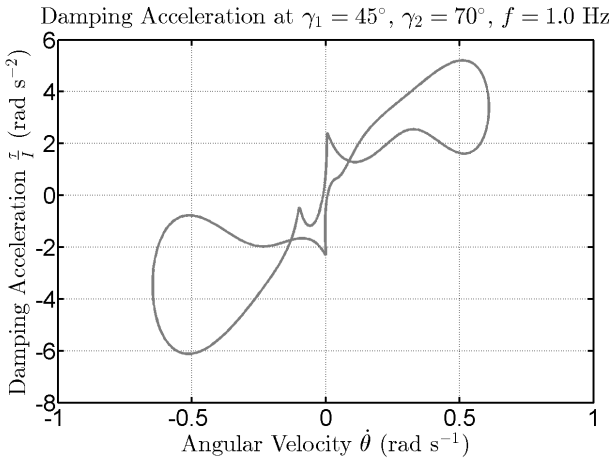

Fig. 7.17 Damping-Angular Velocity Characteristic for $\gamma_1 = 45°$, $\gamma_2 = 70°$ at $f = 1$ Hz.

7.5.4 Step Response Validation

To further validate the non-linear modelling approach, a second set of step responses was performed as summarised in Table 7.2. These step responses include a number of unique

arm positions that were not used in the tuning of parameters from the sinusoidal responses of Table 7.1, so the results are a good test of the predictive capabilities of the models. The Phantom Omni was driven with a 0.25 Hz square wave with an amplitude of $A_\mathrm{r} = 0.07$rad. The square wave may be considered a step response since the Phantom Omni settles to its final position significantly faster than the period of the square wave. In this analysis the underlying differential equation is defined in (7.54) where $\mathrm{H}(t)$ is the Heaviside step function, with $\theta(0^-) = -0.07$ and $\theta'(0^-) = 0$. The Phantom Omni response is from a step input from an initial starting point of -0.07 rad to a final required yaw angle of 0.07 rad. Fig. 7.18 shows the first 1 s of the response of the Phantom Omni to the negative-to-positive transition of a 0.25 Hz square wave, which is described by (7.54).

$$\begin{aligned} \ddot{\theta} + C\dot{\theta} &= \tilde{\beta} v(t) \\ v(t) &= k_\mathrm{p} A_\mathrm{r} \cdot (2\,\mathrm{H}(t) - 1) \end{aligned} \tag{7.54}$$

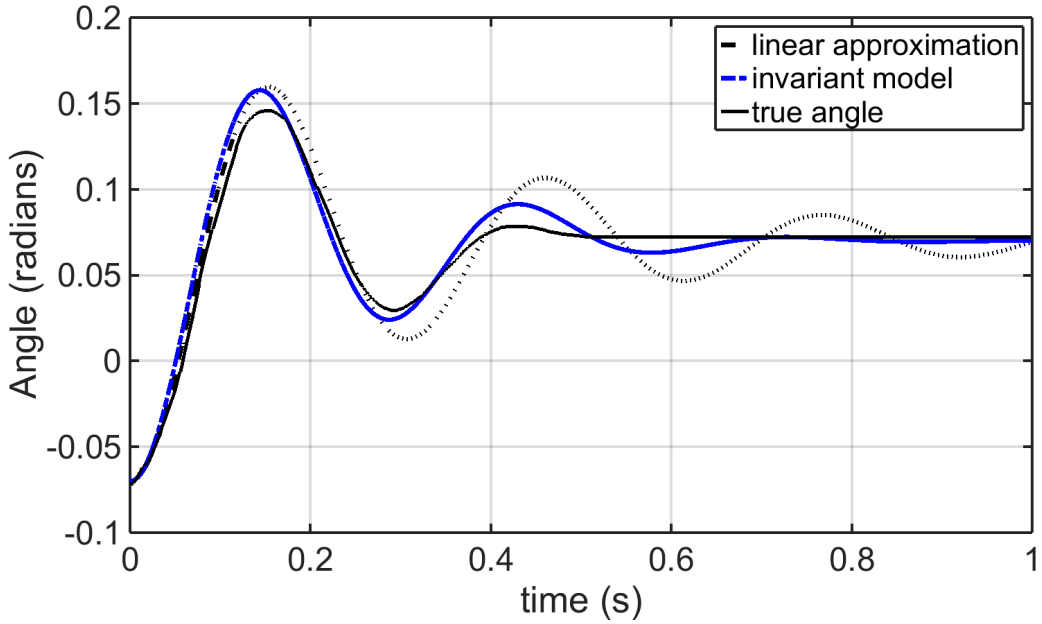

Fig. 7.18 Comparison of time domain responses to a step input for $\gamma_1 = 65°$, $\gamma_2 = 90°$.

The non-linear model captures transient behaviour much more accurately than the linear model. For example the non-linear model reaches steady state significantly faster than the linear model and captures the time periods and amplitudes of the measured data peaks more accurately as well. Table 7.10 shows the median and 90th percentile for absolute angle error figures for all the step response experiments of Table 7.2. The increasing errors with increasing γ_2 are due to the larger effect of inaccuracies in the inertia model approximation

Table 7.10 Absolute Error Percentile Results for Step Response.

		Absolute Angle Errors (rad)			
		Lin Abs Error		**Invariant Abs Error**	
γ_1	γ_2	**Median**	**90th %ile**	**Median**	**90th %ile**
25	60	0.0083	0.0207	0.0036	0.0123
25	70	0.0098	0.0230	0.0045	0.0138
25	90	0.0120	0.0276	0.0067	0.0157
25	110	0.0138	0.0314	0.0082	0.0160
25	115	0.0145	0.0320	0.0087	0.0167
35	60	0.0075	0.0217	0.0021	0.0068
35	70	0.0099	0.0230	0.0029	0.0078
35	90	0.0140	0.0270	0.0036	0.0088
35	110	0.0167	0.0293	0.0041	0.0100
35	115	0.0175	0.0298	0.0043	0.0096
45	60	0.0087	0.0206	0.0030	0.0109
45	70	0.0097	0.0230	0.0036	0.0119
45	90	0.0118	0.0270	0.0058	0.0138
45	110	0.0133	0.0298	0.0073	0.0150
45	115	0.0137	0.0303	0.0076	0.0156
55	60	0.0070	0.0265	0.0020	0.0092
55	70	0.0088	0.0259	0.0025	0.0093
55	90	0.0120	0.0256	0.0037	0.0090
55	110	0.0137	0.0270	0.0037	0.0091
55	115	0.0139	0.0271	0.0036	0.0093
65	60	0.0066	0.0192	0.0023	0.0089
65	70	0.0078	0.0209	0.0024	0.0111
65	90	0.0097	0.0231	0.0034	0.0118
65	110	0.0108	0.0235	0.0037	0.0126
65	115	0.0112	0.0238	0.0041	0.0129
Medians		0.0113	0.0256	0.0043	0.0115

of Link 2 and the Stylus have on the inertia as a whole. While putting the centre of mass of the combined Link 2 and Stylus on the axis of Link 2 does contribute the errors seen in Table 7.10 the errors are reduced from when the centre of mass is put in the "true" location as shown in Fig. 7.4. The median absolute error of each non-linear model response is 2.6 times lower than the linear model response. Out of the 25 experiments, there are 16 joint arm angle combinations that had no sine wave generated data. Hence these results validate that this modelling approach is applicable to capturing all yaw dynamics across the full range of arm angle combinations of the Phantom Omni.

7.6 Summary

This chapter introduces the α-invariant based energy formulation on the input waveform as a means of characterising non-linear damping and torque constant changes over time and as a function of inertia. The energy α is an invariant of any pure sine wave input and is proportional to the area of the ellipse in phase space, or equivalently the energy dissipated during one cycle. The output response of the Phantom Omni yaw angle for a number of frequency response experiments was accurately fitted by sine waves showing that it is locally behaving like a linear system. However a linear system with constant damping and resonant frequency was not adequate to capture the global response over all frequencies.

The results obtained show that the mean energy as described by the α invariant of the input to the Phantom Omni's base actuator is a useful way of characterising the behaviour of the resonant frequency and damping. The damping is heavily dependent on the α invariant which can be explained by the effects of stiction. The work is a good starting point for proving the α invariant concept as it is used in a scenario that experiences the compounded effects of non-linearities from the arm segments and other driven parts of the arm attached to the base.

The effects of inertia were included using an asymptotic curve. The overall non-linear model could not be solved directly using standard non-linear ODE solvers and required an iterative procedure inside the state derivative. The non-linear model accurately captured Phantom Omni yaw dynamics across a full range of arm joint angle combinations and gave significant improvements in magnitude, phase and time domain response compared to a global linear model that did not use the α parameter.

The proposed energy based modelling method is very useful for revealing non-linear dynamics in oscillating systems with a relatively small number of experiments. It is extendible to the identification of model parameters directly from any transient response data, though steady state experiments were chosen since they maximise the signal to noise ratio and

allow the fitting of sine waves to approximate the average response. Deviations between the time domain shape of the fitted sine waves to the measured response is also a good way of revealing if any non-linear dynamics are present.

Finally, with sine waves the α parameter has a unique invariant geometrical property that more clearly separates out damping and torque constant behaviour at various input energy levels in the Phantom Omni. For example, at low energy inputs, or low values of α, the damping is very high, which captures stiction, but as α increases the damping falls exponentially representing viscous friction.

The yaw axis was used as a proof-of-concept of the invariant methodology since it was the most difficult with non-linear effects of inertia and much higher damping. The invariant method shows promise due to its ability to synthesise an accurate non-linear model from a simple set of experiments, and its ability to apply these in real time using a simple ODE or state space model without needing to characterise all the dynamics of the Phantom Omni. The presented non-linear modelling methodology uses simple inertia formulations, which are easily scalable to larger machines such as excavators. Apart from scaling the algorithm, the main challenge of transferring the knowledge from the Phantom Omni to a full sized excavator is taking into account the different actuation systems used in an excavator. In particular, the hydraulic rams in an excavator produce a non-linear relationship between actuator speed and joint speed and the α invariant algorithm will need to take this into account when performing sinusoidal steady state analysis.

The α-invariant model of damping was critical for linking the local linear models for a better result without the complexity that a full friction model would entail. While the energy measure was used for the Phantom arm, any other measure of a system's state or intrinsic physical properties can be used to generate an α-invariant measure as a means of linking local linear models into a global model. This reduces the complexity of the modelling by making the dynamic parameters time-varying then correlating them with physical quantities.

Chapter 8

Hydraulic Ram System Identification

8.1 Introduction

This chapter outlines the process of developing a minimal model for a hydraulic machine from first principles, and the identification process of the resulting minimal model. The research objective is to demonstrate that the same minimal modelling principles that were used for modelling the Phantom Omni are applicable to the hydraulic machine. The research in this chapter uses first principles to create a locally linear minimal model of the hydraulic arm. The hydraulic arm has non-linearities that are known in advance, such as the asymmetry in response of the hydraulic rams between extension and retraction. This phenomenon is accounted for by identifying two models, which are for the ram extending and the ram retracting. While the linearised minimal model may seem to have limited applicability, it can actually be used to identify the linear region of the rams and actuators, and it can be used to devise a linear time variant state space form for simulation.

The research in this chapter on the hydraulic test system extends the minimal modelling approach used for the Phantom Omni. The model is derived from the properties of the rams and valves along with approximations to the behaviour of the hydraulic system in its linear region. The hydraulic system components are designed to be approximately linear, but the objective of this chapter is to identify the extent of the linearity. Given the significant non-linearities, the minimal model results are inspected to determine when the linearised minimal model is giving physically meaningful results. A proof of the ability to identify physically meaningful parameters is presented.

The chapter focuses on two tests for identifying the dynamic parameters using the minimal model: sinusoidal steady state, and square wave steady state. The square wave response is used to compare the ease and accuracy of the dynamic parameter identification between the sine wave response and the square wave response. The sinusoidal steady state

model is used to gather response data at individual frequencies for aggregation into a 'global' model. The square wave steady state response is used to record the step response. Although a square wave is not the same as a step, the square wave frequency is set low enough that each half cycle of square response is effectively the same as a step response. The main advantage of the square wave response is that the sinusoidal steady state response is quite time consuming to run, whereas the square wave response enables the testing of many different frequencies simultaneously. It is important to note that the friction behaviour exhibits stochastic characteristics, so the parameter identification from the square wave response is performed using the entire waveform, the last cycle and the mean of all response cycles.

8.2 Hydraulic System Model

8.2.1 Controller Setup

The controller architecture (Fig. 3.12) uses proportional controllers with programmable compensation for valve dead zones. Proportional controllers are used because of their simplicity and suitability for identifying parameters when the hydraulic system is in its linear region. Each ram has its own P controller. The P controller gains have been set (see Table 8.1) to give satisfactory responses without causing instabilities. All the P-controllers are designed to output a "normalised" command $u \in [-1,1]$, where $u = +1$ means maximum effort to extend the ram and $u = -1$ means maximum effort to retract the ram. The P-controller output u is sent to the non-linearity compensator, which normalises the resulting valve command v to the range $[-100,100]$ for use by the PAC. While the non-linearity compensator can compensate for dead zones, it has been set up as a linear amplifier with a gain of 100.

Table 8.1 P Controller Gains.

Ram	$\bar{k}_\mathrm{p}$ (m^{-1})	k_p (m^{-1})
Ram 1	40	4000
Ram 2	20	2000
Ram 3	20	2000

The ram length is measured using a string encoder which communicates with the controller using CAN bus. The string encoder has a resolution of $\frac{5}{9}$ (0.5556) mm and a reporting time of 100 ms. The control bandwidth is limited by the string encoder to 5 Hz, but the control bandwidth is not expected to be a problem as the test frequencies used are all significantly below 5 Hz.

8.2.2 Hydraulic Circuit

A physical model of the hydraulic system is derived by examining the datasheets of the hydraulic system components and the interactions between them. The pressure compensator valve causes a dependence between supply pressure P_S on pump flow Q_0, pressure compensator flow Q_h and load pressure P_L as shown in (8.1).

$$P_s = P_s(Q_0, Q_h, P_L) \tag{8.1}$$

The Chain rule is used to find the complete time derivative of P_s (8.2). The pump flow Q_0 is assumed constant so it does not appear in (8.2). The supply pressure is simply load pressure with a variable offset from the valve so $\frac{\partial P_s}{\partial P_L} \equiv 1$.

$$\dot{P}_s = \dot{P}_L + \frac{\partial P_s}{\partial Q_h}\dot{Q}_h \tag{8.2}$$

8.2.3 Electro-Hydraulic Proportional Valve Characteristics

Fig. 8.1 shows the valves exhibit a dead zone non-linearity with respect to coil current, and Fig. 8.2 shows how the valve flow varies with pressure at a given coil current. In the experiments v is exactly 100 times the current shown on the curves. Measurement of the electrical properties of the valve coils (time constant $\approx 140\,\mu s$) shows the electrical properties of the valve coils will make a negligible contribution to the system dynamics and is ignored. The valve is designed as a constant flow device, but it is notable the valve exhibits negative incremental admittance $\frac{\partial Q_v}{\partial P_S}$ above approximately 250 psi (1.8 MPa) pressure. The control model is derived by algebraically expressing the slopes and spacing of the lines in Fig. 8.1 and Fig. 8.2 for a normalised valve command v.

$$Q_v = Q_v(P_s, v) \tag{8.3}$$

Equation (8.3) can be formed into its own time derivative in the same manner as (8.2).

$$\dot{Q}_v = \frac{\partial Q_v}{\partial P_s}\dot{P}_s + \frac{\partial Q_v}{\partial v}\dot{v} \tag{8.4}$$

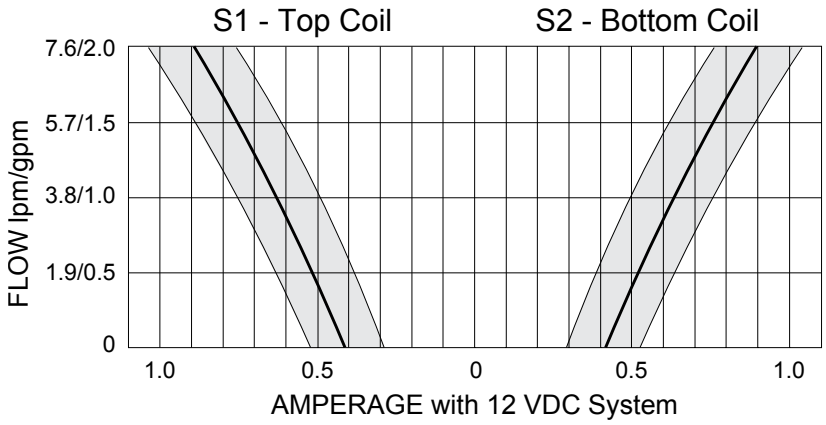

Fig. 8.1 Valve Flow Characteristics as a Function of Current [138].

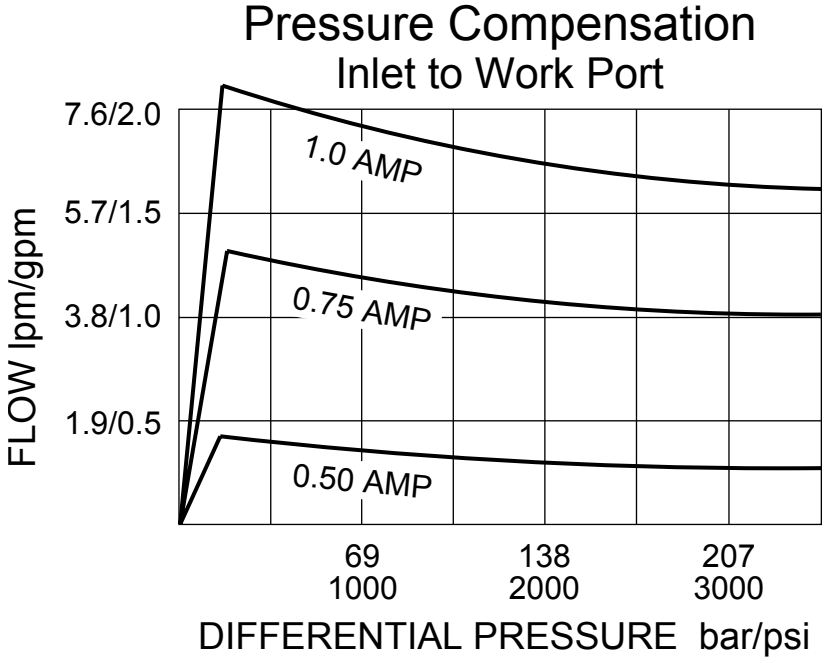

Fig. 8.2 Valve Flow Characteristics as a Function of Pressure [138].

8.2.4 Pressure Compensator Characteristics

Fig. 8.3 shows the characteristics of the pressure compensator valve. The pressure compensator valve fitted has a 110 psi "bias" spring fitted, meaning the minimum supply pressure is 110 psi even at load pressure and/or when the valves are closed. The load pressure on the sensing line acts to increase the pressure drop, so for example the fitted 110 psi pressure compensator with a 120 psi ram load will have the same pressure drop behaviour as a pressure compensator with a 230 psi bias spring.

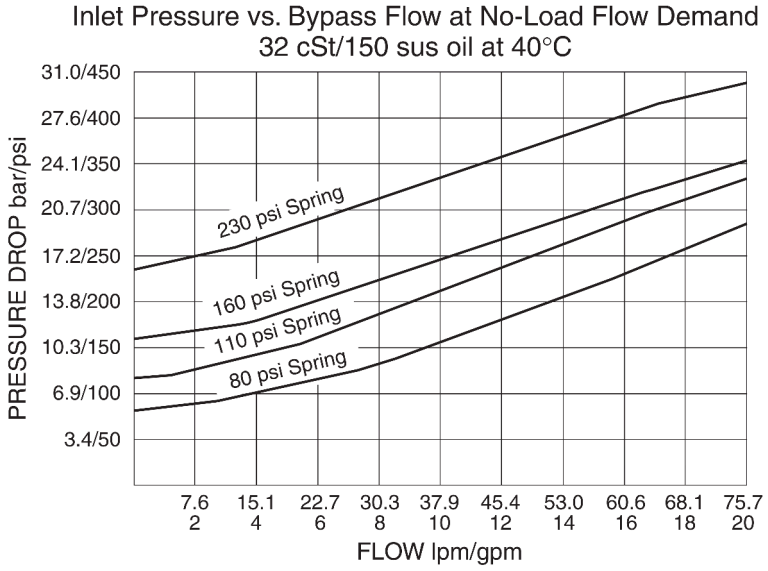

Fig. 8.3 Pressure Compensator Valve Characteristics as a Function of Pressure [139].

8.2.5 End Effector Load Model

The end effector gravity load is modelled using the lengths and angles as shown in Fig. 8.4. The gravity load is modelled as an extra disturbance, as the inertial load will be identified as part of (8.15). Since the base of the machine is horizontal, the general equation for the gravity torque is $\tau_{gn} = mgr_{gn}$, where r_{gn} is the horizontal distance from the rotation axis of the arm base to the centre of mass of the end effector. The equations for end effector radial distance and torque are shown in (8.5), (8.6), (8.7) and (8.8) respectively.

$$r_{g2} = 0.46864\cos(\theta_2 + \theta_3 - 0.024609) + 0.74\sin(\theta_2) \tag{8.5}$$

$$r_{g3} = 0.46864\cos(\theta_2 + \theta_3 - 0.024609) \tag{8.6}$$

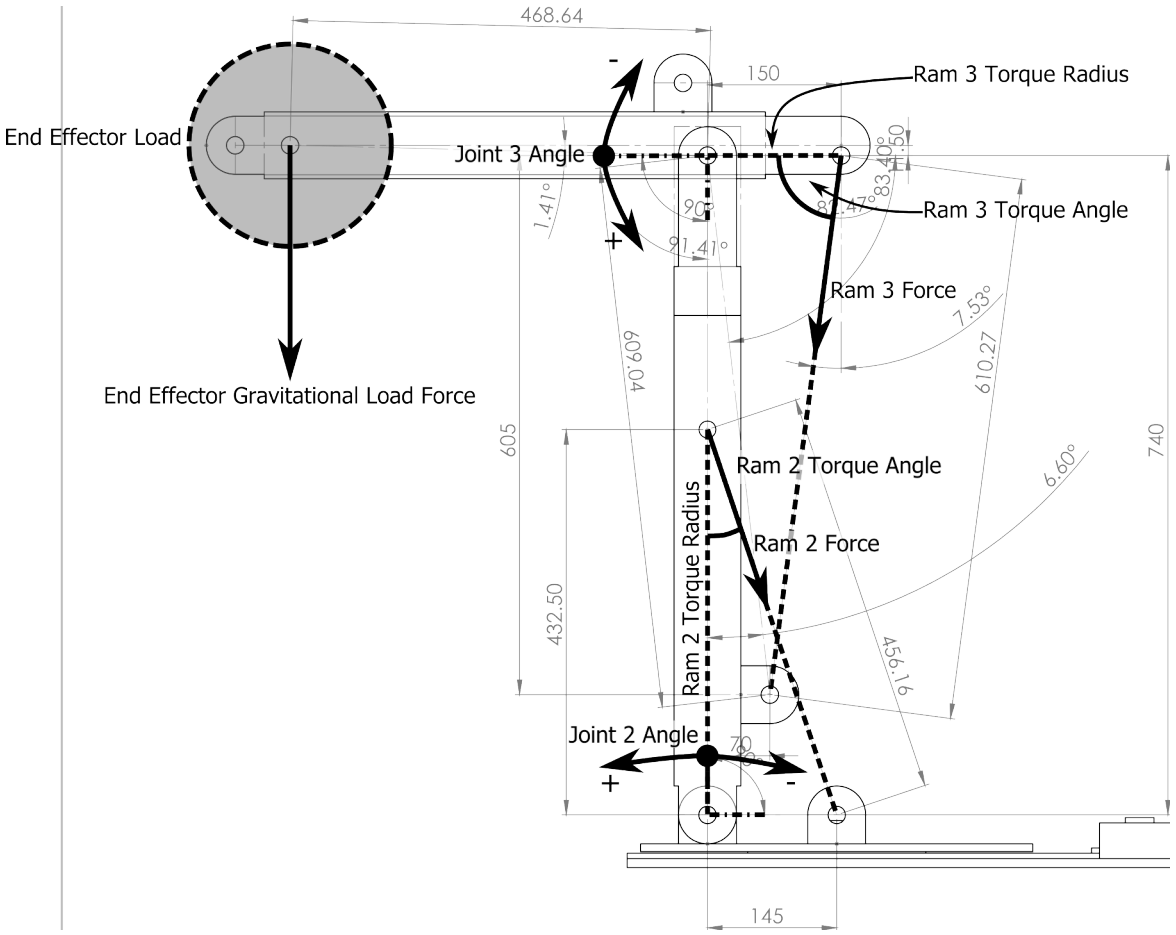

Fig. 8.4 Hydraulic Machine at Zero Angle Arm Positions Showing Load and Ram Forces and Torques.

$$\tau_{g2} = m_{load} g r_{g2} \tag{8.7}$$

$$\tau_{g3} = m_{load} g r_{g3} \tag{8.8}$$

8.3 System Model

The complete system model is created by noting that P_s is the same pressure in both (8.4) and (8.9). If fluid compressibility is ignored the pressure compensator flow and the valve flow adds up to the pump flow at all times, giving the conservation law $\dot{Q}_h = -\dot{Q}_v$. Incompressible fluid also means the flow $\dot{Q}_v$ can be calculated directly from measurements of ram speed and area. The resulting supply pressure derivative is shown in (8.9).

$$\dot{P}_s = \dot{P}_L - \frac{\partial P_s}{\partial Q_h} \dot{Q}_v \tag{8.9}$$

The partial derivatives are condensed into hydraulic admittances g ($\mathrm{m^3\,s^{-1}\,Pa^{-1}}$), resistances r ($\mathrm{Pa\,s\,m^{-3}}$) and transfer ratio μ ($\mathrm{m^3\,s^{-1}}$). For (8.9) we will define $\tilde{r}_{vh} = \frac{\partial P_s}{\partial Q_h}$. For (8.4) we will define $\tilde{g}_v = \frac{\partial Q_v}{\partial P_s}$ and $\tilde{\mu} = \frac{\partial Q_v}{\partial v}$. The result is shown in (8.10).

$$(1 + \tilde{g}_v \tilde{r}_{vh}) \dot{Q}_v - \tilde{g}_v \dot{P}_L = \tilde{\mu} \dot{v} \tag{8.10}$$

Equation (8.10) is used to develop a "small signal" linear model by setting $\tilde{g}_v$, $\tilde{r}_{vh}$ and $\tilde{\mu}$ constant. If the hydraulic fluid is assumed incompressible, the ram speed and flow rate are related directly by $Q_v = \dot{x}A$ where A is the area of the ram and $\dot{x}$ is the ram speed. The pressure P_L can be modelled as $P_L = -\frac{m\ddot{x} + b\dot{x} + F_0}{A}$, where m is the mass of the piston, b is the viscous damping coefficient and F_0 represents any extra forces not accounted for by the viscous friction term. If the small signal parameters $\tilde{r}_{vh}$, $\tilde{g}_v$ and $\tilde{\mu}$ are assumed constant (8.10) can be integrated with respect to time to give (8.11).

$$(1 + \tilde{g}_v \tilde{r}_{vh}) Q_v - \tilde{g}_v P_L = \tilde{\mu} v \tag{8.11}$$

Equation (8.12) is formed by substituting the expressions for pressure and flow into (8.11).

$$(1 + \tilde{g}_v \tilde{r}_{vh}) \dot{x}A + \tilde{g}_v \cdot \frac{m\ddot{x} + b\dot{x} + F_0}{A} = \tilde{\mu} v \tag{8.12}$$

Multiplying both sides by A gives (8.13).

$$\tilde{g}_{\mathrm{v}} m\ddot{x} + \left(\tilde{g}_{\mathrm{v}} b + (1 + \tilde{g}_{\mathrm{v}}\tilde{r}_{\mathrm{vh}})A^2\right)\dot{x} + \tilde{g}_{\mathrm{v}} F_0 = \tilde{\mu} A \nu \tag{8.13}$$

Equation (8.13) has units of $\mathrm{m}^5\,\mathrm{s}^{-1}$, which are considered unwieldy. Dividing both sides by $\tilde{g}_{\mathrm{v}} m$ gives (8.14) in metre$/\mathrm{s}^2$.

$$\ddot{x} + \frac{\tilde{g}_{\mathrm{v}} b + (1 + \tilde{g}_{\mathrm{v}}\tilde{r}_{\mathrm{vh}})A^2}{\tilde{g}_{\mathrm{v}} m}\dot{x} + \frac{F_0}{m} = \frac{\tilde{\mu} A}{\tilde{g}_{\mathrm{v}} m}\nu \tag{8.14}$$

Collecting terms, defining $\tilde{\beta} = \frac{\tilde{\mu} A}{\tilde{g}_{\mathrm{v}} m}$, $C = \frac{b}{m} + \frac{(1+\tilde{g}_{\mathrm{v}}\tilde{r}_{\mathrm{vh}})A^2}{\tilde{g}_{\mathrm{v}} m}$ and $a_0 = \frac{F_0}{m}$ gives (8.15).

$$\ddot{x} + C\dot{x} + a_0 = \tilde{\beta}\nu \tag{8.15}$$

If (8.15) is being treated as a LTI ODE (linear time invariant ordinary differential equation), it can be integrated directly to give the integral equation (8.16). The integral formulation is used because it reduces inaccuracies caused by numerical differentiation of the relatively low resolution ram length measurements. The terms c_0 and c_1 represent initial conditions in the integral equation.

$$C\int_0^t x(\tau)\,d\tau - \tilde{\beta}\int_0^t (t-\tau)\nu(\tau)\,d\tau + \frac{1}{2}a_0 t^2 + c_0 + c_1 t = -x \tag{8.16}$$

8.3.1 Parameter Identification with Dead Zones

The system identification is divided into three main regions of operation as given in Table 8.2. The regions are for positive valve command, negative valve commands and dead zone. The dead zone may be further divided by ram speed into positive dead zone (ram speed > 0) and negative dead zone (ram speed < 0).

Table 8.2 Operating Region Descriptions.

Description	Subscript	Command Range
Positive	$\square_{\mathrm{p}}$	$\nu \geq \nu_{\mathrm{dzp}}$
Negative	$\square_{\mathrm{n}}$	$\nu \leq \nu_{\mathrm{dzn}}$
Dead Zone	$\square_{\mathrm{dz}}$	$\nu_{\mathrm{dzn}} < \nu < \nu_{\mathrm{dzp}}$

The dynamic parameters and dead zones are identified first, then the dynamic parameters within the dead zone. The dead zone command values ν_{dzp} and ν_{dzn} are generated from $a_{0\mathrm{p}}$ and $a_{0\mathrm{n}}$ using $\nu_{\mathrm{dzn}} = \frac{a_{0\mathrm{n}}}{\tilde{\beta}_{\mathrm{n}}}$ and $\nu_{\mathrm{dzp}} = \frac{a_{0\mathrm{p}}}{\tilde{\beta}_{\mathrm{p}}}$ respectively. The positive and negative parameter identification starts from (8.15). It can then be double integrated to form an equation similar to (8.16), but with a different set of initial conditions for each region. The positive valve

command parameters are identified directly, and the negative valve command parameters are identified as offsets to the positive parameters. Note that for any negative parameter z_n, $z_n = z_{0p} + z_{0pn}$. The negative parameters are identified this way as it produces better numerical stability than identifying the positive and negative parameters separately. Models with a restricted subset of dynamic parameters are identified by constraining the values of the unwanted parameters to zero using `lsqlin` in Matlab.

$$C_p\dot{x} - \tilde{\beta}_p v + a_{0p} = -\ddot{x} \tag{8.17}$$

$$(C_p + C_{pn})\dot{x} - (\tilde{\beta}_p + \tilde{\beta}_{pn})v + (a_{0p} + a_{0pn}) = -\ddot{x} \tag{8.18}$$

Once the dead zones a_{0p} and a_{0n} are known, the parameter identification within the dead zones can be carried out. The input and a_0 are both constrained to zero, so the only parameter identified is damping. The damping can be identified either in the dead zone as a whole, or for positive and negative ram speeds. The square wave response has separate dead zone dampings for positive and negative speeds, and the sine wave has a single dead zone. The single dead zone is solved using a dual dead zone model and `lsqlin` by constraining the two identified dead zones to have the same value.

The positive dead zone parameters are identified in regions where $v_{dzp} > v > 0$, and the negative dead zone parameters are identified in regions where $v_{dzn} < v < 0$. The regression is performed using (8.16) with constrained least squares with constraints $C_{dzp} \geq 0$, $C_{dzn} \geq 0$ and $a_{0p} = a_{0n} = \tilde{\beta}_p = \tilde{\beta}_n = 0$. The constraints are put in place to ensure the model within the dead zone is passive.

Given the nature of frictional damping it is expected the identified damping in the dead zone is greater than the identified damping outside the dead zone. If this is not the case, the appropriate out of dead zone damping may be substituted for the dead zone damping. For example, if the identified $C_{dzp} < C_p$ then C_{dzp} may be set equal to C_p.

8.3.2 Sine Wave Modelling

The sine wave model is done with an offset and a sinusoidal wave. The offset is not required for the sinusoidal modelling, but is used for calculating the dead zone. The sine wave models are shown in (8.19) and (8.20). The offset x_0 is used for calculating the positive and negative dead zone. Although $r(t)$ has an offset (0.46 m), only the offset *difference* affects the valve command because the controller is a proportional controller.

$$r(t) = A_r \sin(\omega t) \tag{8.19}$$

$$x(t) = x_0 + A_r|H|\sin(\omega t + \phi) \tag{8.20}$$

Single Frequency Model

The sine wave response is derived by fitting sinusoidal waves to the input and output, and calculating β and C from the amplitude and phase of the output sinusoid relative to the input. The calculations are done with the amplitude of the input normalised to 1. Equation (8.21) is the complex representation of the transfer function, where $|H|$ is the transfer function magnitude and ϕ is the phase shift angle. Equation (8.22) shows the model in terms of β and C.

$$H = |H|\exp(j\phi) \tag{8.21}$$

$$|H| = \frac{\beta}{\beta - \omega^2 + j\omega C} \tag{8.22}$$

The values of β and C are calculated using (7.42) and (7.43) with the substitutions $|H|^2 = A_1^2 + A_2^2$ and $A_2 = |H|\cos\phi$.

$$C(\omega) = -\frac{\omega|H|\sin\phi}{|H| - \cos\phi} \tag{8.23}$$

$$\beta(\omega) = \frac{\omega^2|H|}{|H| - \cos\phi} \tag{8.24}$$

The model is considered to give a *prima facie* valid result when $\beta > 0$ and $C > 0$. The model at low frequencies is still useful for deriving a global sine wave model, but data at high frequencies where $\beta > 0$ and $C < 0$ is not used, as it implies a high phase shift that is impossible for a second order system with non negative β and C. The resonant frequency $\beta > 0$ if at a given frequency, $\cos\phi < |H|$, or $|\phi| < \cos^{-1}|H|$. The damping is non-negative when $-\sin\phi < 0$, or when $0 < \phi < -180$.

At low frequencies the dead zone causes a fixed phase lag, because the error needs to reach a minimum threshold before movement will occur (Fig. 8.5) [140]. The lag then needs to be such that the error is at least that threshold to maintain movement. Suppose the actuator dead zone is v_{dz}, the input wave has an amplitude A_r and the output has an amplitude A_0 and phase shift ϕ. The valve command is given in (8.25). At a zero crossing on the input ($t = 0$, the time base is arbitrary), (8.25) reduces to (8.26).

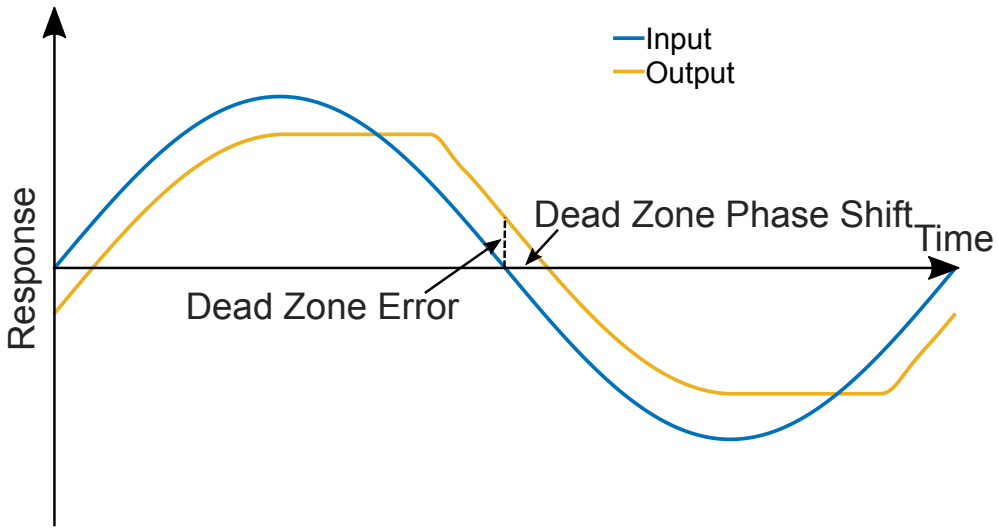

Fig. 8.5 Sine Wave Response Illustrating Parameters Used for Dead Zone Calculation.

$$v = k_{\mathrm{p}} \cdot (A_{\mathrm{r}} \sin(\omega t) - A_0 \sin(\omega t + \phi)) \tag{8.25}$$

$$v = -k_{\mathrm{p}} A_0 \sin\phi \tag{8.26}$$

In other words, the dead zone can be inferred from the amplitude of the output and the phase shift. Making the substitution $A_0 = A_{\mathrm{r}}|H|$ gives (8.27).

$$v = -k_{\mathrm{p}} A_{\mathrm{r}} |H| \sin\phi \tag{8.27}$$

The mean dead zone v_{dz0} is given by (8.28), the mean valve command over an entire cycle. The positive and negative dead zones are derived from (8.27) and (8.28) and are given in (8.29) and (8.30).

$$v_{\mathrm{dz0}} = k_{\mathrm{p}} x_0 \tag{8.28}$$

$$v_{\mathrm{p}} = v_{\mathrm{dz0}} + v \tag{8.29}$$

$$v_{\mathrm{n}} = v_{\mathrm{dz0}} - v \tag{8.30}$$

The estimates (8.29) and (8.30) become inaccurate at higher frequenciess, because the phase shift, due to the second order system, adds to the dead zone. Therefore the lowest frequency possible should be used for identifying the dead zone, or at least a frequency where $\beta < 0$, since this means there is an 'excess' phase shift due to the dead zone.

All Frequency (Global) Model

The all frequency model coefficients are calculated by fitting the complex amplitude to Eq. (8.23) and Eq. (8.24). The fitting is done by linear least squares using rearranged versions of Eq. (8.23) and Eq. (8.24). The linear least squares solution is shown in (8.31).

$$\begin{bmatrix} j\omega_1 H_1 & H_1 - 1 \\ j\omega_2 H_2 & H_2 - 1 \\ \vdots & \\ j\omega_n H_2 & H_n - 1 \end{bmatrix} \begin{bmatrix} C \\ \beta \end{bmatrix} = \begin{matrix} \omega_1^2 H_1 \\ \omega_1^2 H_2 \\ \vdots \\ \omega_n^2 H_n \end{matrix} \tag{8.31}$$

Solving (8.31) generally causes β and C to have non-zero imaginary parts. Therefore, the regression is separated into real and imaginary parts, to produce a $2n \times 2$ regression matrix and a $2n \times 1$ fitting vector.

8.3.3 State Space Model

The response of the system is modelled using a state space formulation (8.32). The quantity a_{int} is the "internal acceleration" - the estimated acceleration that is actually exerted on the ram taking into account the operating region.

$$\begin{bmatrix} \dot{x} \\ \ddot{x} \end{bmatrix} = \begin{bmatrix} 0 & 1 \\ 0 & -C(\nu) \end{bmatrix} \begin{bmatrix} x \\ \dot{x} \end{bmatrix} + \begin{bmatrix} 0 \\ a_{\text{int}}(\tilde{\beta}(\nu), a_0(\nu)) \end{bmatrix} \tag{8.32}$$

The dynamic model parameters $\tilde{\beta}$, C and a_0 are selected according to the raw valve command ν and Table 8.3. The raw valve command ν is calculated using $\nu = k_{\text{p}} \cdot (r - x)$, where r is the input waveform and x is the ram displacement and k_{p} is the proportional gain of the controller.

Table 8.3 Dynamic Model Parameters.

Command Range	C	$\tilde{\beta}$	a_0
$v \geq v_{\text{dzp}}$	C_{p}	$\tilde{\beta}_{\text{p}}$	$a_{0\text{p}}$
$v \leq v_{\text{dzn}}$	C_{n}	$\tilde{\beta}_{\text{n}}$	$a_{0\text{n}}$
$v_{\text{dzp}} > v > 0$	C_{dzp}	0	0
$v_{\text{dzn}} < v < 0$	C_{dzn}	0	0
$v = 0$	$\frac{1}{2}\left(C_{\text{dzp}} + C_{\text{dzn}}\right)$	0	0

The internal acceleration a_{int} is calculated from the raw valve command using the valve command specific values of $\tilde{\beta}$, C, and a_0. The full model of the internal acceleration a_{int} is given in (8.33).

$$a_{\text{int}} = \begin{cases} 100\tilde{\beta}_{\text{p}} - a_{0\text{p}} & \text{if } v \geq 100 \\ \tilde{\beta}_{\text{p}} v - a_{0\text{p}} & \text{if } v_{\text{dzp}} \leq v < 100 \\ 0 & \text{if } v_{\text{dzn}} < v < v_{\text{dzp}} \\ \tilde{\beta}_{\text{n}} v - a_{0\text{n}} & \text{if } -100 < v \leq v_{\text{dzn}} \\ -100\tilde{\beta}_{\text{n}} - a_{0\text{n}} & \text{if } v \leq -100 \end{cases} \tag{8.33}$$

In the dead zone, the state space model (8.32) produces a simplified response, given in (8.34). A limitation of this model is the dynamic parameters $\tilde{g}_{\text{v}}$ and $\tilde{r}_{\text{vh}}$ that make up C are likely to change when the ram is within its dead zone, so a formulation solely dependent on a constant C and initial conditions will not produce a fully accurate response.

$$x(t) = x(0^-) + \frac{x'(0^-)}{C} \cdot (1 - \exp(-Ct)) \tag{8.34}$$

8.4 Experimental Results

8.4.1 Preliminary Experiments

Valve Command and Speed Response

Initial experiments were performed on Ram 1 to confirm the accuracy of the minimal model. The experiments were performed on Ram 1 attached to the machine but with no end effector load. Fig. 8.6 shows the resulting steady state response. The waveform used was a 0.1 Hz square wave with equation $r(t) = 0.46 + 0.04\,\text{square}(0.1t)$. The frequency of 0.1 Hz was chosen to ensure the hydraulic arm settled into position quickly enough that the square wave can be interpreted as a series of step responses. Fig. 8.6 confirms the speed nearly becomes

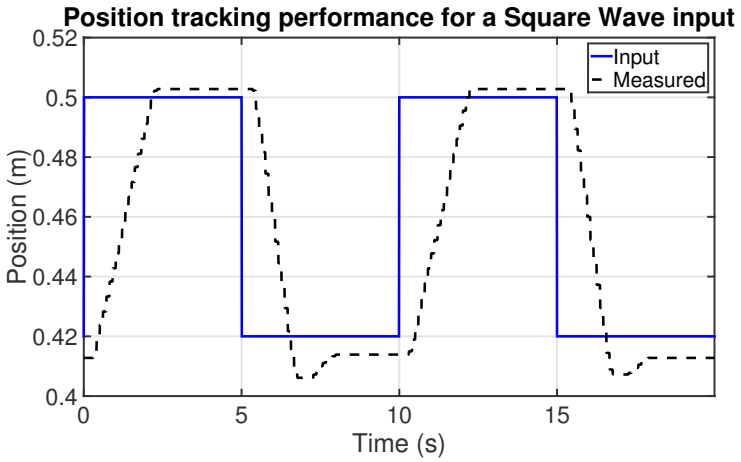

Fig. 8.6 Square wave response of Ram 1 at 0.1 Hz.

constant during the rise and fall times of the ram. Fig. 8.7 shows the relationship between valve saturation and speed. If it assumed that the flow rate is the same at $v = 100$ and $v = -100$ and the speed ratio is directly proportional to the ratio of the ram areas. Table 8.4 summarises the maximum speed data for extension and retraction.

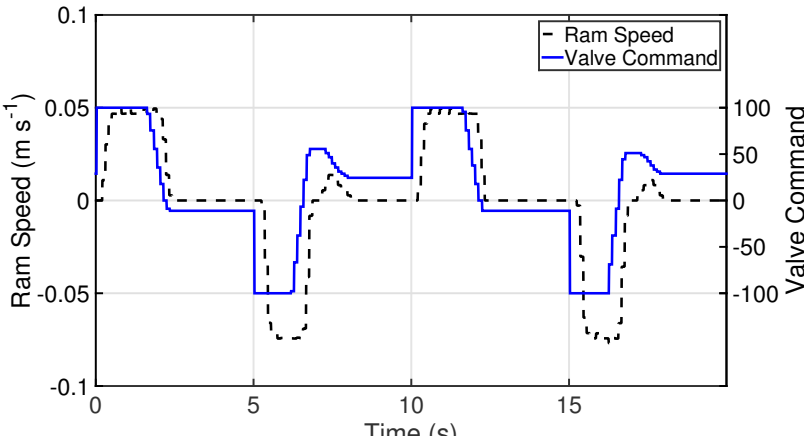

Fig. 8.7 Ram 1 speed response and valve command for square wave at 0.1 Hz.

Table 8.4 Square Wave Damping and Resonance Characteristics using Equation (8.15).

Valve Command	Absolute Speed (m s^{-1})
Extension ($v = 100$)	0.04672
Retraction ($v = -100$)	0.07420
Area Ratio	1.588

An interesting note is that for a given non-zero $\tilde{g}_v$ the ratio of $\tilde{\beta}$ between the positive and negative v should be the same as the ratio as the ram areas, i.e. $\frac{A_p}{A_n} = \frac{\tilde{\beta}_p}{\tilde{\beta}_n}$.

Identification of C, $\tilde{\beta}$ and a_0

Table 8.5 shows the values C and $\tilde{\beta}$ from (8.15) as determined by the measured data. The asymmetry between the extension and retraction behaviour of the valves during extension and retraction is notable but is directly attributable to the difference in areas between the rams.

Table 8.5 Square Wave Damping and Resonance Characteristics using Equation (8.15).

Valve Command	C (s^{-1})	$\tilde{\beta}$ ($m s^{-2}$)	a_0 ($N kg^{-1}$)	v_{dz}
$v \geq v_{dzp}$	2.559	0.001860	0.05141	27.64
$v \leq v_{dzn}$	1.105	0.001439	-0.01804	-12.54
$v_{dzp} > v > v_{dzn}$	2.559	0	0	0

The ratio $\frac{\tilde{\beta}_p}{\tilde{\beta}_n}$ is equal to 1.293, compared to 1.588 from speed ratio. The speed ratio assumes constant $\tilde{g}_v$, which is not guaranteed, so it is not surprising that the ratios of the values are not equal. Still, their relative closeness helps confirm the physical basis for the minimal model.

Confirmation of Identified Dead Zone

The v_{dzn} and v_{dzp} parameters represent the identified dead zone effects that give the best match for the set of all the negative and positive valve commands respectively. Their accuracy can be checked by comparing against a grid search of v_{dzn} and v_{dzp}. Table 8.6 shows the results. It is shown that a grid search can produce more accurate results than the calculated values. However, analysis of the results in the time domain is also required to work out the effect of the errors, as the error metrics in Table 8.6 are sensitive to time delays during changing signals.

Table 8.6 Summary of RMS Errors between Measured Output and Models.

Source	v_{dzn}	v_{dzp}	RMS Error (m)
No Dead Zone	0	0	0.01204
Identified	-12.54	27.64	0.00372
Grid Search	-22	29	0.00329

The grid search v_{dzn} and v_{dzp} have an RMS error that is about 13 % less than the identified v_{dzn} and v_{dzp}. The cause is that the grid search dead zones allow slightly better tacking of

the response during the rise and fall of the output. Fig. 8.8 shows a comparison of the square wave results. Both the identified v_{dz} and the grid search v_{dz} follow the measured output closely. The grid search v_{dz} has slightly better tracking during rises and falls of the output, reducing the RMS error. However the small difference suggests the identified dead zones are still accurate and usable for modelling purposes.

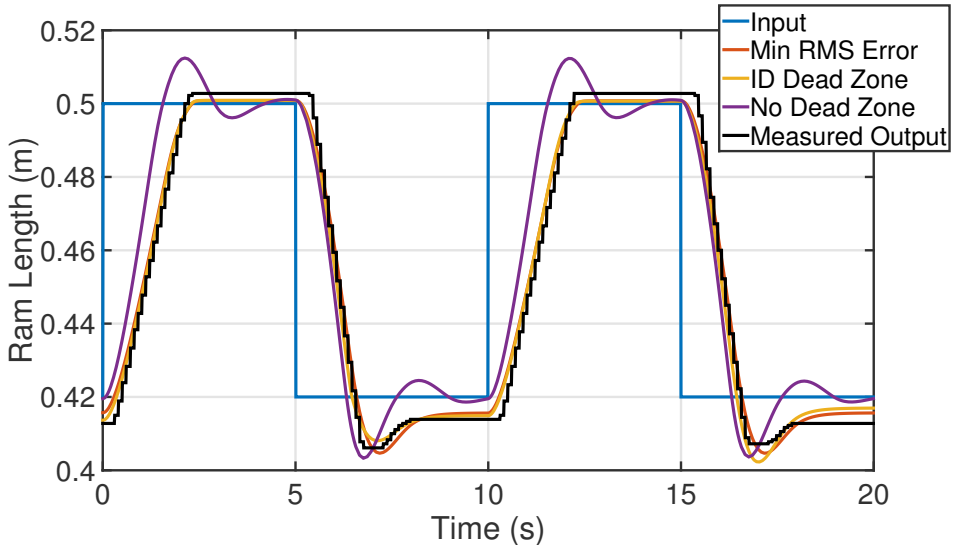

Fig. 8.8 Square wave response at 0.1 Hz with models.

8.4.2 Sine Wave on Ram 1

Ram 1 of the hydraulic test system was tested with a sine wave $r(t) = 0.46 + 0.04\sin(2\pi ft)$. The ram was tested in a horizontal position so that gravity does not affect the measurements. The test frequencies (f) used ranged from 0.025 Hz to 1 Hz. Frequencies above 1 Hz were not used as at the input amplitude used the required slew rate was too high for the ram to follow. Fig. 8.9 shows the response of the entire experiment. Fig. 8.9 shows that the response reaches a peak and decreases, and shows the response is broadly similar to an under-damped second order response.

The first approximation is to fit a sine wave to the input and output, based on the coefficients of the 2nd order transfer function. The results are shown in Table 8.7. The negative $\tilde{\beta}$ and C at frequencies below 0.1 Hz is due to the phase angle being 'too large' for the amplitude. The negative damping at frequencies above 0.5 Hz is due to the phase delay becoming greater than 180°. The dead zones are calculated from the mean error and the low frequency phase shift. The mean error gives the 'centre point' of the dead zone, and the phase shift gives the offset of the dead zone. The dead zone estimates become less accurate

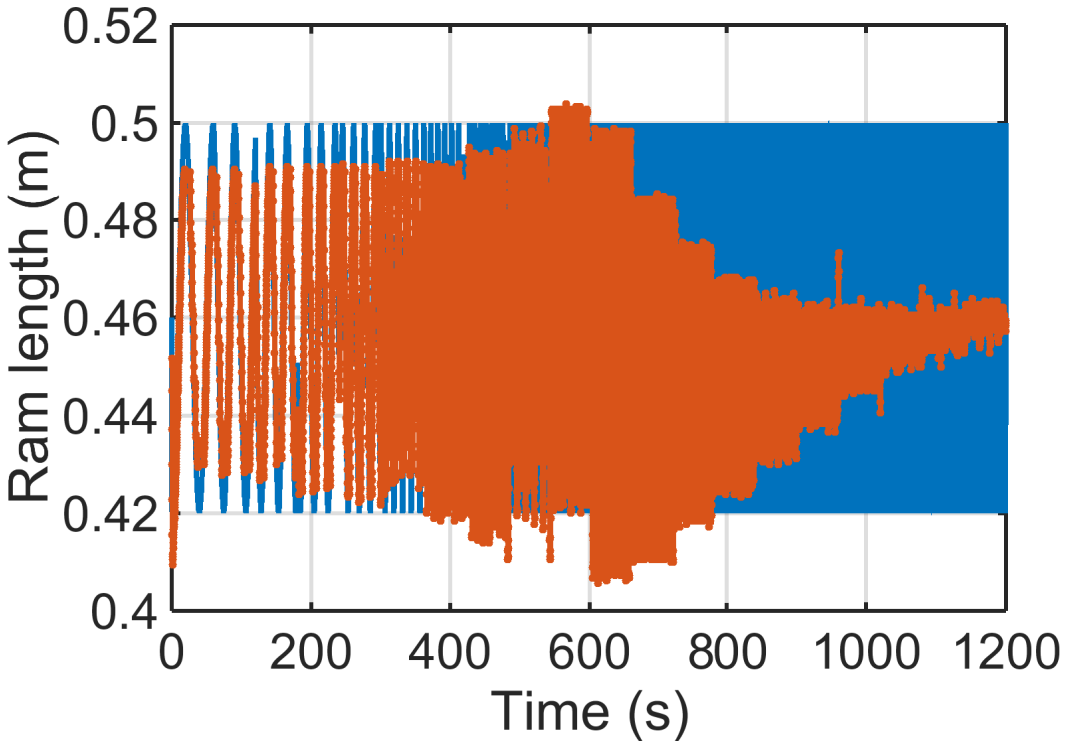

Fig. 8.9 Sine wave sweep response.

at higher frequencies, as the extra phase shift, due to the system dynamics, contributes to the dead zone calculated this way. Therefore the lowest frequency dead zone figures are used for the global model. The dead zone damping is estimated by taking the waveform within the calculated dead zone, fitting a sine wave to it and using the resulting damping. If phasor style calculations are being used, the damping will come out as a purely imaginary number. This is expected, as a complex damping represents an exponential decay, which will show up as a complex phasor gain.

Table 8.7 Sine Wave Fit Results.

Frequency (Hz)	C	$\tilde{\beta}$	v_{dzp}	v_{dzn}	C_{dz}
0.0250	−0.4499	−0.000 051 29	44.86	−49.20	6.366
0.0315	−0.7143	−0.000 104 4	42.86	−51.71	5.053
0.0400	−0.9541	−0.000 176 7	42.92	−52.35	3.979
0.0500	−2.914	−0.000 661 9	42.92	−58.29	3.183
0.0630	−6.143	−0.001 650	46.29	−62.08	2.526
0.0800	−9.462	−0.003 187	48.00	−61.95	1.989
0.100	4.185	0.001 694	49.10	−72.84	1.592
0.125	3.104	0.001 463	58.76	−76.32	1.273
0.160	3.380	0.001 688	76.00	−86.96	0.9947
0.200	2.482	0.001 322	86.44	−119.57	0.7958
0.250	2.140	0.001 007	113.54	−176.75	0.6366
0.315	1.849	0.000 808 4	108.23	−206.32	0.5053
0.400	1.530	0.000 801 8	70.46	−178.40	0.3979
0.500	0.9386	0.000 904 9	13.73	−122.80	0.3183
0.630	−0.091 77	0.001 109	−43.22	−53.56	0.2526
0.800	−2.171	0.001 561	39.51	−119.71	0.1989
1.00	−6.806	0.002 540	107.32	−156.56	0.1592
1.25	−40.07	0.009 046	142.33	−176.53	0.1273
Global	1.598	0.000 812 9	44.86	−49.20	6.366

Fig. 8.10 shows the magnitude response, and Fig. 8.11 shows the phase response to the sine wave input. There are several approximations shown: a matching of sine waves, the integral method, the integral method at all frequencies, and the results from the square wave. Table 8.8 gives the meanings of the graph annotations in the magnitude results (Fig. 8.10) and the phase results (Fig. 8.11).

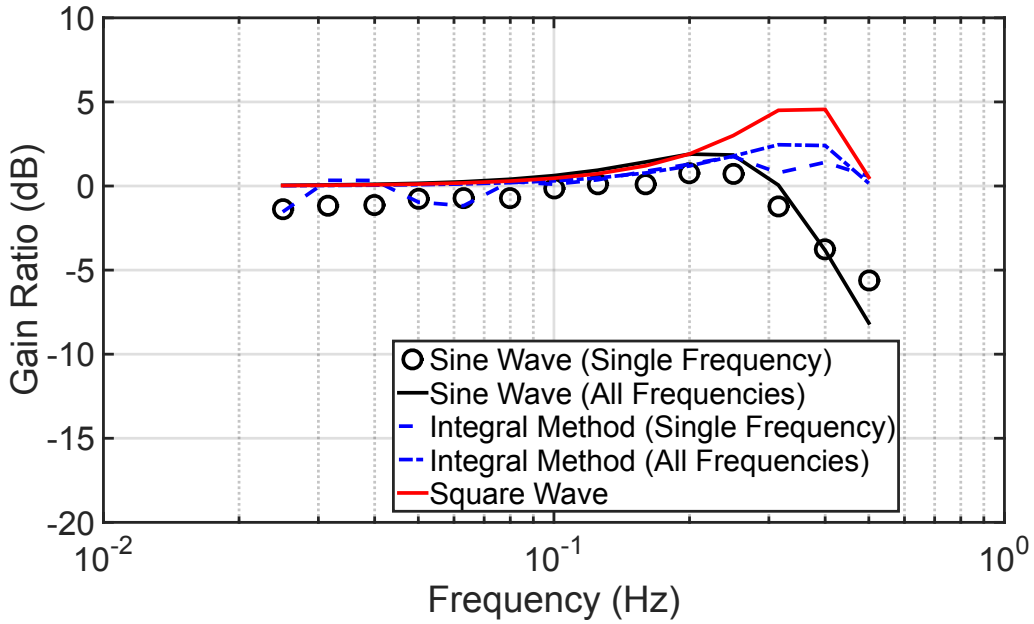

Fig. 8.10 Bode plot of response magnitude.

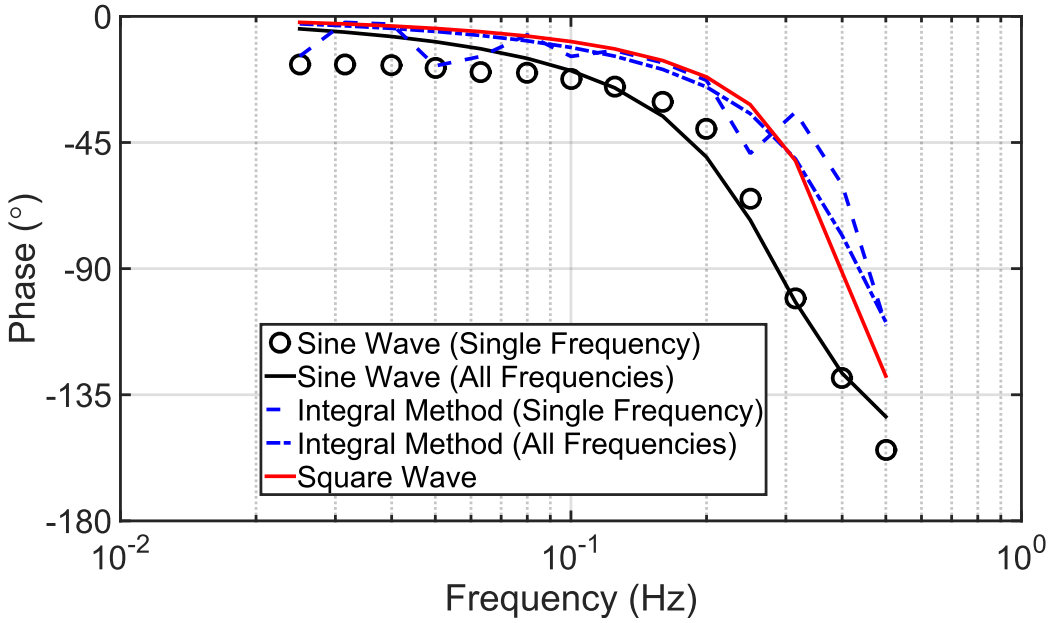

Fig. 8.11 Bode plot of response phase.

Table 8.8 Dynamic Model Parameters Explanation.

Label	**Explanation**
Sine Wave (Single Frequency)	Best sine wave fit at each test frequency, without any constraints on identified parameter values.
Sine Wave (All Frequencies)	Best transfer function fit to all of the sine wave single frequency magnitudes and phases.
Integral Method	Best integral method fit at each frequency.
Integral Method (All Frequencies)	Best integral method fit at all frequencies. Derived by fitting a 2nd order transfer function to the integral method single frequency magnitudes and phases.

The low frequency data is still usable for curve fitting for Fig. 8.10 and Fig. 8.11, as the phase delay is under 180°, but the data that implies a phase delay greater than 180° is omitted as it no longer conforms to a 2nd order system. The presence of β or C being negative is due to interactions between the response magnitude and the phase angle. The transfer function has the property that $\beta < 0$ if $\cos\phi > |H|$ and that $C < 0$ if $\sin\phi > 0$. Table 8.9 shows the comparison between $|H|$ and $\cos\phi$. It can be clearly seen that $\beta < 0$ is caused by having $\cos\phi > |H|$ and that $C < 0$ is due to $\sin\phi > 0$. Table 8.9 shows the magnitude $|H|$ and the information about phase angles. The regions where $\beta < 0$ corresponds exactly to where $\cos\phi > |H|$, and the regions where $C < 0$ corresponds to where $\sin\phi > 0$ as expected.

Table 8.9 Sine Wave Fit Results.

Frequency (Hz)	$\lvert H\rvert$	ϕ (°)	$\cos\phi$	$\sin\phi$
0.0250	0.8532	−17.09	0.9558	−0.2939
0.0315	0.8734	−17.10	0.9553	−0.2956
0.0400	0.8762	−17.32	0.9547	−0.2977
0.0500	0.9146	−18.44	0.9487	−0.3163
0.0630	0.9191	−19.80	0.9409	−0.3387
0.0800	0.9209	−20.10	0.9391	−0.3436
0.100	0.9818	−22.40	0.9245	−0.3811
0.125	1.0133	−24.97	0.9065	−0.4221
0.160	1.0121	−30.61	0.8606	−0.5092
0.200	1.0911	−40.07	0.7652	−0.6438
0.250	1.0867	−65.11	0.4208	−0.9071
0.315	0.8686	−100.58	−0.1836	−0.9830
0.400	0.6484	−128.95	−0.6287	−0.7777
0.500	0.5237	−154.74	−0.9044	−0.4269
0.630	0.3947	−181.85	−0.9995	0.0323
0.800	0.2847	−209.84	−0.8674	0.4976
1.00	0.1960	−235.57	−0.5655	0.8248
1.25	0.1146	−265.37	−0.0808	0.9967

The response magnitude $|H|$, $\cos\phi$ and $\sin\phi$ are shown in Fig. 8.12 to demonstrate the correspondence between the signs of β, C and the phase angle.

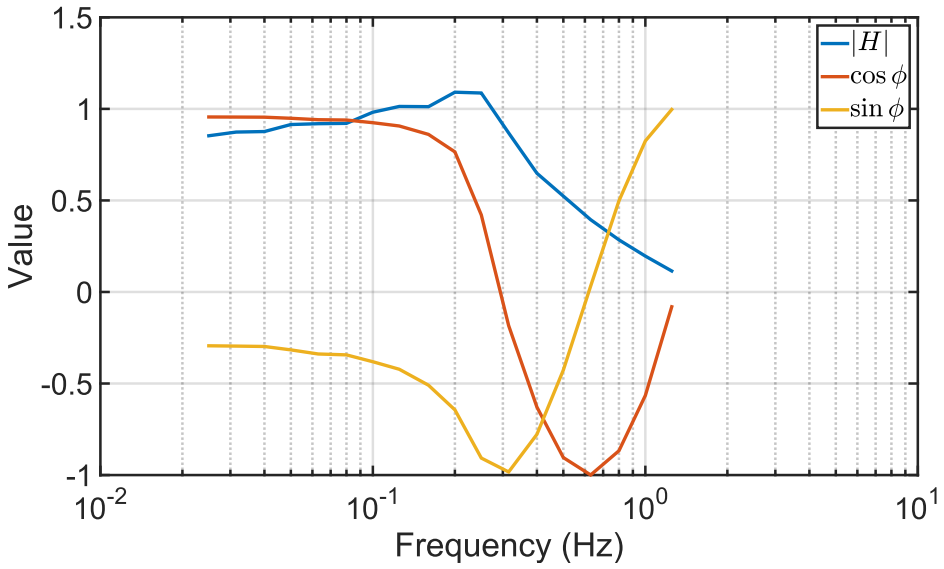

Fig. 8.12 Comparison of gain $|H|$ and $\cos\phi$.

Table 8.10 summarises the accuracy of the simulations relative to the measured data.

Table 8.10 Model Simulation Error Results.

	RMS Error (m)				**Mean Error** (m)			
Frequency (Hz)	Square Wave	Dual β	Single β	Sine Wave	Square Wave	Dual β	Single β	Sine Wave
0.0250	0.00445	0.00214	0.00285	0.00779	−0.00178	0.00130	−0.00132	0.00054
0.0315	0.00402	0.00289	0.00252	0.00735	−0.00129	0.00182	−0.00076	0.00110
0.0400	0.00361	0.00272	0.00209	0.00688	−0.00129	0.00185	−0.00068	0.00118
0.0500	0.00359	0.00420	0.00261	0.00663	−0.00063	0.00254	0.00006	0.00192
0.0630	0.00401	0.00465	0.00318	0.00669	−0.00067	0.00251	0.00011	0.00197
0.0800	0.00395	0.00447	0.00330	0.00644	−0.00099	0.00221	−0.00012	0.00174
0.100	0.00513	0.00671	0.00471	0.00634	0.00004	0.00333	0.00112	0.00297
0.125	0.00526	0.00701	0.00547	0.00611	−0.00059	0.00231	0.00032	0.00220
0.160	0.00331	0.00464	0.00420	0.00737	−0.00106	0.00131	−0.00049	0.00137
0.200	0.00327	0.00739	0.00613	0.00999	0.00171	0.00355	0.00159	0.00414
0.250	0.00496	0.01185	0.01038	0.01099	0.00155	0.00531	0.00442	0.00790
0.315	0.00835	0.01592	0.01441	0.01340	0.00490	0.00798	0.00772	0.01226
0.400	0.00658	0.01544	0.01379	0.01376	0.00380	0.00842	0.00832	0.01349
0.500	0.01442	0.01402	0.01370	0.01452	0.01337	0.00780	0.00774	0.01363
0.630	0.01039	0.01306	0.01284	0.01368	0.00730	0.00699	0.00799	0.01210
0.800	0.01072	0.01017	0.00950	0.01183	0.00854	0.00455	0.00538	0.00999
1.00	0.01021	0.00702	0.00662	0.00823	0.00849	0.00032	0.00111	0.00630
1.25	0.00736	0.00488	0.00487	0.00507	0.00607	−0.00069	−0.00126	0.00349

Fig. 8.13, Fig. 8.14 and Fig. 8.15 show the time domain responses for sine waves of frequencies 0.025 Hz, 0.2 Hz and 0.4 Hz respectively. The linear sine wave response was obtained using `lsim` in Matlab, and the non-linear responses were obtained using a standard state space model that was used with Matlab's `ode45` solver.

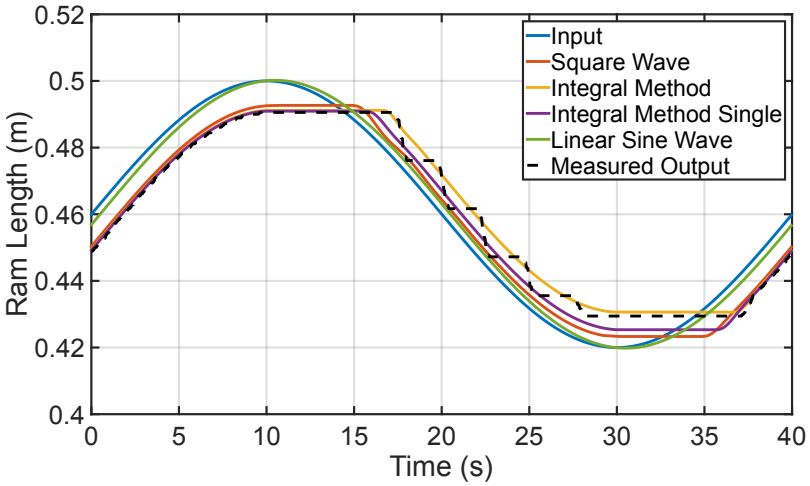

Fig. 8.13 Sine wave response at 0.025 Hz.

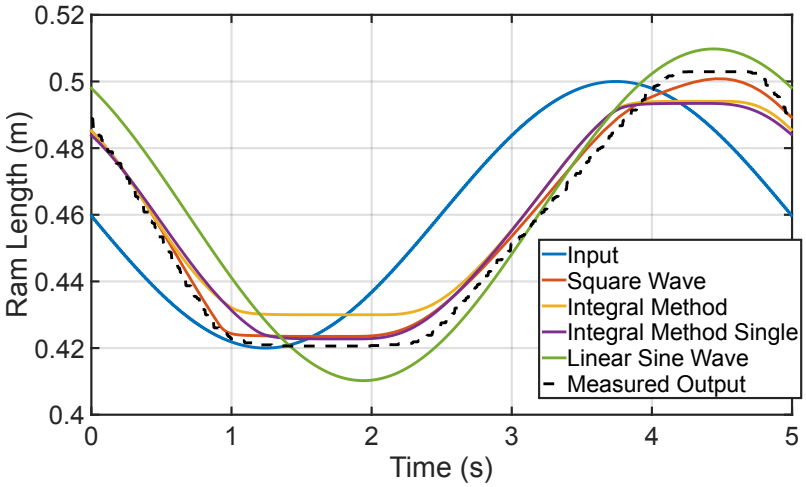

Fig. 8.14 Sine wave response at 0.2 Hz.

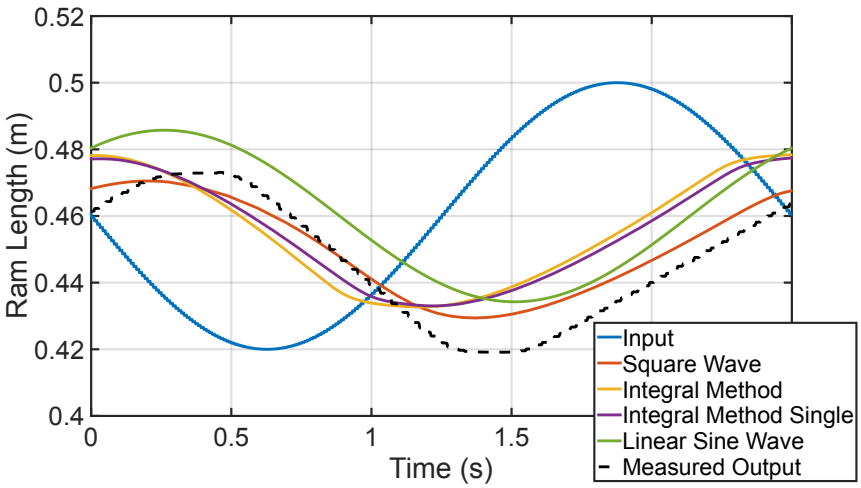

Fig. 8.15 Sine wave response at 0.4 Hz.

8.4.3 Square Wave Response Results

The square wave results were obtained using 0.1 Hz square waves. The square waves had an amplitude of 0.04 m. The rams were driven in the approximate centre of their range of movement. The offset, amplitude, maximum and minimum lengths are given in Table 8.11. The amplitude and offset for Ram 1's square wave testing is the same as Ram 1's sine wave testing.

Table 8.11 Hydraulic Lab System Specifications.

Part	**Offset** m	**Amplitude** m	**Maximum** m	**Minimum** m
Ram 1	0.46	0.04	0.50	0.42
Ram 2	0.46	0.04	0.50	0.42
Ram 3	0.5925	0.04	0.6325	0.5525

Ram 1

Ram 1 was operated under various conditions of load, as shown in Table 8.12. The data from the 'Ram Only' has been used for comparison with the results obtained from the sine wave experiment in Section 8.4.2.

Table 8.13, Table 8.14, Table 8.15, Table 8.16, Table 8.17 and Table 8.18 show the results for Ram 1. The loads go up to 45 kg as loads larger than that caused the other rams in the machine to be overloaded. It is notable there is good agreement between the median dynamic parameters and the single mean cycle parameters. It also shows that using the mean of multiple cycles is an effective method of obtaining stable dynamic parameters.

Table 8.12 Ram 1 Results Summary.

Ram Load	Ram Load Model	Results Table
Ram Only	Constant	8.13
No Load	Constant	8.14
9 kg	Constant	8.15
20 kg	Constant	8.16
30 kg	Constant	8.17
45 kg	Constant	8.18

Table 8.13 Ram 1 Summary with Ram Only.

	Positive Valve Command				Negative Valve Command			
Percentile	C	$\tilde{\beta}$	v_{dz}	v_{dz}	C	β	v_{dz}	v_{dz}
5	2.122	0.001598	29.08	0.04688	1.149	0.001485	-14.49	-0.02450
10	2.143	0.001614	29.15	0.04746	1.195	0.001504	-14.42	-0.02420
50	2.442	0.001797	30.80	0.05602	1.347	0.001614	-12.11	-0.01953
90	2.583	0.001983	34.03	0.06635	1.485	0.001713	-12.02	-0.01887
95	2.590	0.002022	34.48	0.06973	1.522	0.001747	-12.01	-0.01876
Mean	2.395	0.001787	30.96	0.05547	1.349	0.001605	-12.88	-0.02069
Std. Dev.	0.182	0.000148	1.91	0.00726	0.104	0.000076	1.14	0.00218
Single Mean Cycle	2.338	0.001746	31.00	0.05411	1.349	0.001603	-12.86	-0.02061
All Cycles	2.027	0.001647	29.50	0.04859	1.134	0.001470	-12.46	-0.01833

Table 8.14 Ram 1 Summary with No External Load.

	Positive Valve Command				Negative Valve Command			
Percentile	C	$\tilde{\beta}$	v_{dz}	v_{dz}	C	β	v_{dz}	v_{dz}
5	1.925	0.001376	31.13	0.04284	1.613	0.001552	-12.15	-0.02104
10	1.929	0.001382	31.13	0.04342	1.642	0.001575	-12.12	-0.02074
50	2.006	0.001453	33.73	0.04904	1.731	0.001656	-9.98	-0.01705
90	2.589	0.001950	36.34	0.07043	1.941	0.001783	-9.79	-0.01569
95	2.635	0.002005	36.43	0.07305	1.974	0.001794	-9.75	-0.01551
Mean	2.164	0.001590	33.69	0.05395	1.769	0.001770	-10.71	-0.01790
Std. Dev.	0.282	0.000241	2.03	0.01119	0.112	0.000076	1.12	0.00215
Single Mean Cycle	2.140	0.001567	33.67	0.05276	1.765	0.001666	-10.69	-0.01780
All Cycles	1.464	0.001259	31.46	0.03959	1.553	0.001542	-10.31	-0.01591

Table 8.15 Ram 1 Summary with 9 kg External Load.

	Positive Valve Command				Negative Valve Command			
Percentile	C	$\tilde{\beta}$	v_{dz}	v_{dz}	C	β	v_{dz}	v_{dz}
5	2.484	0.001854	34.26	0.06392	1.707	0.001628	-13.82	-0.02819
10	2.485	0.001856	34.27	0.06402	1.738	0.001649	-12.58	-0.02502
50	2.908	0.002181	34.52	0.07485	1.834	0.001737	-8.56	-0.01477
90	3.629	0.002715	36.17	0.09793	2.081	0.001988	-7.31	-0.01243
95	3.769	0.002810	36.22	0.10138	2.117	0.002041	-7.30	-0.01241
Mean	2.967	0.002214	35.04	0.07775	1.881	0.001774	-9.03	-0.01623
Std. Dev.	0.422	0.000318	0.89	0.01276	0.127	0.000127	2.21	0.00531
Single Mean Cycle	2.900	0.002164	35.03	0.07581	1.880	0.001770	-9.03	-0.01599
All Cycles	2.498	0.001941	34.77	0.06752	1.349	0.001450	-7.92	-0.01149

Table 8.16 Ram 1 Summary with 20 kg External Load.

	Positive Valve Command				Negative Valve Command			
Percentile	C	$\tilde{\beta}$	v_{dz}	v_{dz}	C	β	v_{dz}	v_{dz}
5	2.193	0.001497	26.87	0.04124	1.714	0.001756	-16.16	-0.03192
10	2.221	0.001515	27.00	0.04167	1.754	0.001792	-16.11	-0.03156
50	2.382	0.001641	28.35	0.04786	1.968	0.001927	-13.90	-0.02754
90	2.724	0.001884	30.20	0.05558	2.099	0.002040	-12.39	-0.02303
95	2.739	0.001906	30.60	0.05830	2.101	0.002042	-11.80	-0.02240
Mean	2.426	0.001673	28.41	0.04759	1.943	0.001932	-14.17	-0.02738
Std. Dev.	0.191	0.000135	1.31	0.00527	0.130	0.000095	1.38	0.00311
Single Mean Cycle	2.379	0.001644	28.43	0.04675	1.947	0.001935	-14.20	-0.02748
All Cycles	2.263	0.001642	27.64	0.04540	1.506	0.001654	-13.46	-0.02226

Table 8.17 Ram 1 Summary with 30 kg External Load.

	Positive Valve Command				Negative Valve Command			
Percentile	C	$\tilde{\beta}$	v_{dz}	v_{dz}	C	β	v_{dz}	v_{dz}
5	2.198	0.001611	30.53	0.05159	1.598	0.001538	-14.20	-0.02697
10	2.222	0.001630	30.58	0.05190	1.661	0.001598	-14.17	-0.02693
50	2.407	0.001745	32.67	0.05639	1.950	0.001808	-12.87	-0.02266
90	3.070	0.002257	35.35	0.07810	2.013	0.001917	-9.69	-0.01597
95	3.166	0.002382	35.79	0.08524	2.021	0.001923	-9.67	-0.01541
Mean	2.511	0.001824	32.56	0.05963	1.889	0.001797	-12.19	-0.02204
Std. Dev.	0.326	0.000249	1.84	0.01095	0.141	0.000123	2.10	0.00480
Single Mean Cycle	2.468	0.001792	32.57	0.05838	1.891	0.001795	-12.20	-0.02190
All Cycles	1.724	0.001391	31.38	0.04366	1.363	0.001468	-11.08	-0.01626

Table 8.18 Ram 1 Summary with 45 kg External Load.

	Positive Valve Command				Negative Valve Command			
Percentile	C	$\tilde{\beta}$	v_{dz}	v_{dz}	C	β	v_{dz}	v_{dz}
5	1.948	0.001423	30.62	0.04414	1.652	0.001605	-16.13	-0.03034
10	1.952	0.001427	30.62	0.04428	1.658	0.001610	-16.12	-0.03023
50	2.416	0.001730	30.96	0.05297	1.776	0.001771	-14.25	-0.02525
90	2.576	0.002008	35.44	0.07116	1.886	0.001876	-10.69	-0.01725
95	2.590	0.002024	35.90	0.07266	1.893	0.001883	-10.07	-0.01616
Mean	2.301	0.001698	31.89	0.05444	1.768	0.001741	-13.91	-0.02442
Std. Dev.	0.283	0.000242	2.05	0.01079	0.091	0.000108	2.26	0.00530
Single Mean Cycle	2.112	0.001568	31.95	0.05009	1.778	0.001747	-13.98	-0.02441
All Cycles	2.269	0.001775	30.21	0.05362	1.247	0.001418	-12.92	-0.01832

Ram 2

Table 8.19 shows the load masses used for Ram 2. All the results were obtained with Ram 2 installed on the hydraulic test system. Ram 2 had the highest loads, so it was not able to support end effector loads greater than 30 kg, therefore no results for the highest masses are shown.

Table 8.19 Ram 2 Results Summary.

Ram Load	Ram Load Model	Results Table
No Load	Constant	8.20
9 kg	Constant	8.21
20 kg	Constant	8.22
30 kg	Constant	8.23

Table 8.20 Ram 2 Summary with No External Load.

	Positive Valve Command				Negative Valve Command			
Percentile	C	$\tilde{\beta}$	v_{dz}	v_{dz}	C	β	v_{dz}	v_{dz}
5	4.851	0.003692	23.80	0.08820	6.743	0.006673	-19.63	-0.1542
10	4.853	0.003693	23.83	0.08850	6.763	0.006790	-19.61	-0.1521
50	4.907	0.003720	24.97	0.09298	7.251	0.007587	-18.20	-0.1382
90	4.984	0.003805	25.86	0.09688	7.557	0.007903	-16.07	-0.1115
95	4.987	0.003809	26.06	0.09696	7.606	0.007914	-15.75	-0.1051
Mean	4.915	0.003737	24.84	0.09284	7.207	0.007487	-18.00	-0.1350
Std. Dev.	0.053	0.000044	0.76	0.00328	0.305	0.000426	1.43	0.0151
Single Mean Cycle	4.910	0.003733	24.84	0.09272	7.153	0.007389	-18.00	-0.1330
All Cycles	3.808	0.002739	25.38	0.06954	2.433	0.001258	-20.72	-0.0261

Table 8.21 Ram 2 Summary with 9 kg Load.

	Positive Valve Command				Negative Valve Command			
Percentile	C	$\tilde{\beta}$	v_{dz}	v_{dz}	C	β	v_{dz}	v_{dz}
5	4.498	0.002850	10.94	0.03117	5.689	0.005685	-18.50	-0.1119
10	4.507	0.002857	11.12	0.03177	5.702	0.005723	-18.49	-0.1114
50	4.547	0.002887	12.99	0.03764	5.869	0.005894	-17.39	-0.1031
90	4.576	0.002911	13.77	0.03981	6.038	0.006062	-16.05	-0.0927
95	4.582	0.002912	13.82	0.03998	6.066	0.006063	-15.71	-0.0913
Mean	4.545	0.002885	12.75	0.03680	5.855	0.005908	-17.38	-0.1027
Std. Dev.	0.027	0.000020	1.03	0.00314	0.130	0.000139	0.92	0.0068
Single Mean Cycle	4.550	0.002889	12.75	0.03684	5.851	0.005902	-17.38	-0.1026
All Cycles	3.136	0.001831	13.76	0.02520	3.667	0.003155	-18.22	-0.0575

Table 8.22 Ram 2 Summary with 20 kg Load.

	Positive Valve Command				Negative Valve Command			
Percentile	C	$\tilde{\beta}$	v_{dz}	v_{dz}	C	β	v_{dz}	v_{dz}
5	3.760	0.002326	-2.110	-0.006731	3.904	0.003608	-23.12	-0.10674
10	3.794	0.002351	-1.982	-0.006317	3.921	0.003662	-22.58	-0.10328
50	4.371	0.002913	-0.644	-0.002054	4.154	0.004056	-21.21	-0.08360
90	4.712	0.003190	2.041	0.004961	4.564	0.004611	-19.27	-0.07323
95	4.734	0.003191	2.152	0.005311	4.604	0.004616	-19.21	-0.07006
Mean	4.291	0.002824	-0.265	-0.001270	4.209	0.004107	-20.93	-0.08614
Std. Dev.	0.409	0.000389	1.640	0.004604	0.259	0.000367	1.23	0.01090
Single Mean Cycle	4.518	0.003006	-0.363	-0.001091	4.137	0.003997	-20.96	-0.08378
All Cycles	2.655	0.001606	2.520	0.004048	3.425	0.003282	-21.59	-0.07087

Table 8.23 Ram 2 Summary with 30 kg Load.

	Positive Valve Command				Negative Valve Command			
Percentile	C	$\tilde{\beta}$	v_{dz}	v_{dz}	C	β	v_{dz}	v_{dz}
5	4.164	0.003598	-12.30	-0.04887	1.037	0.001533	-23.57	-0.06586
10	4.223	0.003659	-12.14	-0.04842	1.074	0.001535	-23.54	-0.05970
50	4.775	0.004022	-10.69	-0.04290	1.515	0.001875	-21.84	-0.04014
90	4.976	0.004151	-10.16	-0.03961	2.779	0.002664	-20.41	-0.03177
95	4.984	0.004167	-10.08	-0.03932	3.150	0.002883	-20.19	-0.03096
Mean	4.702	0.003975	-10.90	-0.04331	1.639	0.001936	-21.97	-0.04264
Std. Dev.	0.294	0.000189	0.76	0.00331	0.671	0.000436	1.24	0.01061
Single Mean Cycle	4.713	0.003980	-11.07	-0.04405	1.403	0.001765	-21.31	-0.03762
All Cycles	4.192	0.003545	-9.63	-0.03412	1.275	0.001690	-21.87	-0.03696

Ram 3

Ram 3 was tested with the same end effector loads as Rams 1 and 2. It was possible to run experiments on Ram 3 with loads of up to 65 kg, the maximum weight that was available. The results for Ram 3 show good agreement between the mean cycle dynamic parameters and the single cycle parameters.

Table 8.24 Ram 3 Results Summary.

Ram Load	Ram Load Model	Results Table
No Load	Constant	8.25
9 kg	Constant	8.26
20 kg	Constant	8.27
30 kg	Constant	8.28
45 kg	Constant	8.29
65 kg	Constant	8.30

Table 8.25 Ram 3 Summary with No External Load.

	Positive Valve Command				Negative Valve Command			
Percentile	C	$\tilde{\beta}$	v_{dz}	v_{dz}	C	β	v_{dz}	v_{dz}
5	4.611	0.003501	26.16	0.09300	5.330	0.005584	-21.04	-0.1249
10	4.616	0.003502	26.28	0.09303	5.363	0.005603	-20.92	-0.1239
50	4.747	0.003565	26.74	0.09542	5.608	0.005890	-19.73	-0.1175
90	4.817	0.003688	28.05	0.10283	5.758	0.006095	-19.14	-0.1092
95	4.839	0.003704	28.22	0.10299	5.780	0.006114	-19.04	-0.1075
Mean	4.719	0.003579	27.03	0.09677	5.579	0.005877	-19.94	-0.1171
Std. Dev.	0.079	0.000071	0.72	0.00399	0.149	0.000193	0.71	0.0055
Single Mean Cycle	4.716	0.003575	27.04	0.09666	5.561	0.005837	-19.94	-0.1164
All Cycles	3.752	0.002712	27.55	0.07469	3.917	0.003521	-20.45	-0.0720

Table 8.26 Ram 3 Summary with 9 kg Load.

	Positive Valve Command				Negative Valve Command			
Percentile	C	$\tilde{\beta}$	v_{dz}	v_{dz}	C	β	v_{dz}	v_{dz}
5	5.197	0.003825	23.28	0.09071	3.699	0.003900	-27.11	-0.11036
10	5.212	0.003842	23.39	0.09095	3.706	0.003903	-26.97	-0.10907
50	5.340	0.003969	24.06	0.09586	3.763	0.003931	-26.28	-0.10272
90	5.381	0.004053	25.23	0.10224	3.876	0.004057	-24.47	-0.09766
95	5.383	0.004055	25.40	0.10298	3.877	0.004072	-24.21	-0.09740
Mean	5.317	0.003963	24.21	0.09596	3.779	0.003957	-25.98	-0.10281
Std. Dev.	0.067	0.000082	0.71	0.00435	0.071	0.000062	0.92	0.00413
Single Mean Cycle	5.321	0.003964	24.21	0.09596	3.777	0.003955	-25.98	-0.10276
All Cycles	3.882	0.002693	24.77	0.06670	2.909	0.002544	-26.84	-0.06826

Table 8.27 Ram 3 Summary with 20 kg Load.

	Positive Valve Command				Negative Valve Command			
Percentile	C	$\tilde{\beta}$	v_{dz}	v_{dz}	C	β	v_{dz}	v_{dz}
5	6.428	0.006241	20.14	0.1259	4.835	0.005391	-27.09	-0.1460
10	6.447	0.006247	20.15	0.1268	5.036	0.005465	-26.28	-0.1459
50	6.533	0.006387	20.99	0.1343	5.695	0.005943	-23.03	-0.1398
90	6.769	0.006546	21.81	0.1426	6.023	0.006197	-22.12	-0.1286
95	6.807	0.006593	21.82	0.1438	6.031	0.006202	-21.90	-0.1276
Mean	6.577	0.006376	21.05	0.1343	5.644	0.005892	-23.55	-0.1385
Std. Dev.	0.123	0.000116	0.72	0.0061	0.382	0.000283	1.60	0.0067
Single Mean Cycle	6.575	0.006373	21.05	0.1342	5.637	0.005890	-23.55	-0.1387
All Cycles	3.829	0.003024	21.76	0.0658	2.410	0.001552	-25.94	-0.0403

Table 8.28 Ram 3 Summary with 30 kg Load.

	Positive Valve Command				Negative Valve Command			
Percentile	C	$\tilde{\beta}$	v_{dz}	v_{dz}	C	β	v_{dz}	v_{dz}
5	6.869	0.007140	9.65	0.06893	5.601	0.005788	-24.56	-0.1517
10	6.878	0.007163	10.31	0.07398	5.605	0.005801	-24.25	-0.1500
50	7.038	0.007411	13.26	0.09948	5.871	0.006107	-22.98	-0.1381
90	7.478	0.007828	16.01	0.12222	6.015	0.006212	-21.10	-0.1272
95	7.623	0.007903	16.81	0.12869	6.033	0.006227	-20.79	-0.1271
Mean	7.092	0.007452	13.19	0.09851	5.831	0.006028	-22.88	-0.1380
Std. Dev.	0.236	0.000260	2.06	0.01731	0.170	0.000177	1.14	0.0086
Single Mean Cycle	7.099	0.007458	13.19	0.09833	5.823	0.006016	-22.88	-0.1377
All Cycles	1.968	0.000769	18.38	0.01414	2.962	0.002249	-24.28	-0.0546

Table 8.29 Ram 3 Summary with 45 kg Load.

	Positive Valve Command				Negative Valve Command			
Percentile	C	$\tilde{\beta}$	v_{dz}	v_{dz}	C	β	v_{dz}	v_{dz}
5	7.531	0.008333	-1.493	-0.01252	5.792	0.005714	-23.03	-0.1341
10	7.543	0.008349	-1.488	-0.01246	5.824	0.005716	-23.02	-0.1338
50	7.619	0.008547	1.832	0.01566	6.003	0.005837	-22.13	-0.1308
90	7.822	0.008783	3.718	0.03266	6.152	0.005988	-20.03	-0.1161
95	7.839	0.008788	4.055	0.03563	6.179	0.006002	-19.70	-0.1150
Mean	7.653	0.008552	1.352	0.01185	5.989	0.005849	-21.84	-0.1277
Std. Dev.	0.112	0.000176	2.017	0.01742	0.120	0.000102	1.16	0.0070
Single Mean Cycle	7.657	0.008553	1.352	0.01156	5.994	0.005853	-21.84	-0.1278
All Cycles	2.189	0.000993	5.786	0.00574	3.257	0.002632	-23.12	-0.0608

Table 8.30 Ram 3 Summary with 65 kg Load.

	Positive Valve Command				Negative Valve Command			
Percentile	C	$\tilde{\beta}$	v_{dz}	v_{dz}	C	β	v_{dz}	v_{dz}
5	8.241	0.009802	-4.092	-0.04039	5.668	0.005210	-20.83	-0.1167
10	8.259	0.009807	-3.906	-0.03848	5.721	0.005268	-20.82	-0.1156
50	8.498	0.009949	-2.519	-0.02549	5.994	0.005480	-19.73	-0.1087
90	8.879	0.010560	-1.104	-0.01139	6.136	0.005599	-19.70	-0.1066
95	8.927	0.010577	-0.993	-0.01045	6.138	0.005610	-19.69	-0.1065
Mean	8.551	0.010107	-2.453	-0.02455	5.971	0.005463	-20.09	-0.1097
Std. Dev.	0.237	0.000325	1.109	0.01061	0.155	0.000124	0.53	0.0035
Single Mean Cycle	8.573	0.010137	-2.455	-0.02489	5.967	0.005462	-20.09	-0.1097
All Cycles	3.221	0.002197	-0.827	-0.00182	5.027	0.004441	-20.36	-0.0904

8.4.4 Load Detection

The responses of Rams 1, 2 and 3 were measured while the hydraulic machine was subject to various external loads, ranging from none to 65 kg. The 'mean of all cycles' C, β and v_{dz} are used for the analysis in this section. For these results a constant force was assumed. The force was assigned an arbitrary value of 1 N, with v_{dz} being allowed to scale to give the best fit to the observed data. Table 8.31, Table 8.32, and Table 8.33 show the dynamic parameters used for the load detection characterisation.

Table 8.31 Ram 1 Load Detection Summary.

	Positive Valve Command			**Negative Valve Command**		
Load	C	$\tilde{\beta}$	v_{dz}	C	β	v_{dz}
Ram Only	2.338	0.001746	31.00	1.349	0.001603	-12.86
No Load	2.140	0.001567	33.67	1.765	0.001666	-10.69
9 kg	2.900	0.002164	35.03	1.880	0.001770	-9.03
20 kg	2.379	0.001644	28.43	1.947	0.001935	-14.20
30 kg	2.468	0.001792	32.57	1.891	0.001795	-12.20
45 kg	2.112	0.001568	31.95	1.778	0.001747	-13.98

Table 8.32 Ram 2 Load Detection Summary.

	Positive Valve Command			**Negative Valve Command**		
Load	C	$\tilde{\beta}$	v_{dz}	C	β	v_{dz}
No Load	4.910	0.003733	24.84	7.153	0.007389	-18.00
9 kg	4.550	0.002889	12.75	5.851	0.005902	-17.38
20 kg	4.518	0.003006	-0.36	4.137	0.003997	-20.96
30 kg	4.713	0.003980	-11.07	1.403	0.001765	-21.31

Table 8.33 Ram 3 Load Detection Summary.

	Positive Valve Command			**Negative Valve Command**		
Load	C	$\tilde{\beta}$	v_{dz}	C	β	v_{dz}
No Load	4.716	0.003575	27.04	5.561	0.005837	-19.94
9 kg	5.321	0.003964	24.21	3.777	0.003955	-25.98
20 kg	6.575	0.006373	21.05	5.637	0.005890	-23.55
30 kg	7.099	0.007458	13.19	5.823	0.006016	-22.88
45 kg	7.657	0.008553	1.35	5.994	0.005853	-21.84
65 kg	8.573	0.010137	-2.46	5.967	0.005462	-20.09

The effect of the load force on Ram 1's, 2's and 3's dead zones are shown in Fig. 8.16, Fig. 8.17 and Fig. 8.18 respectively.

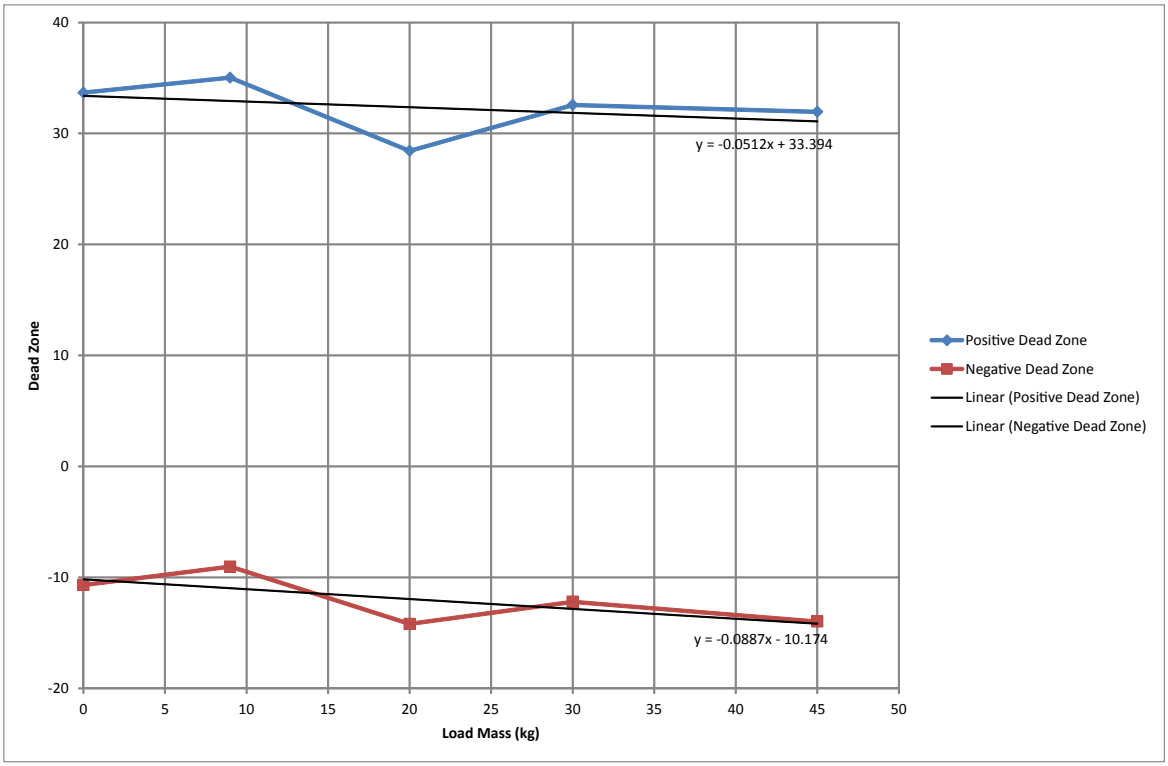

Fig. 8.16 Ram 1 dead zone with Constant Force.

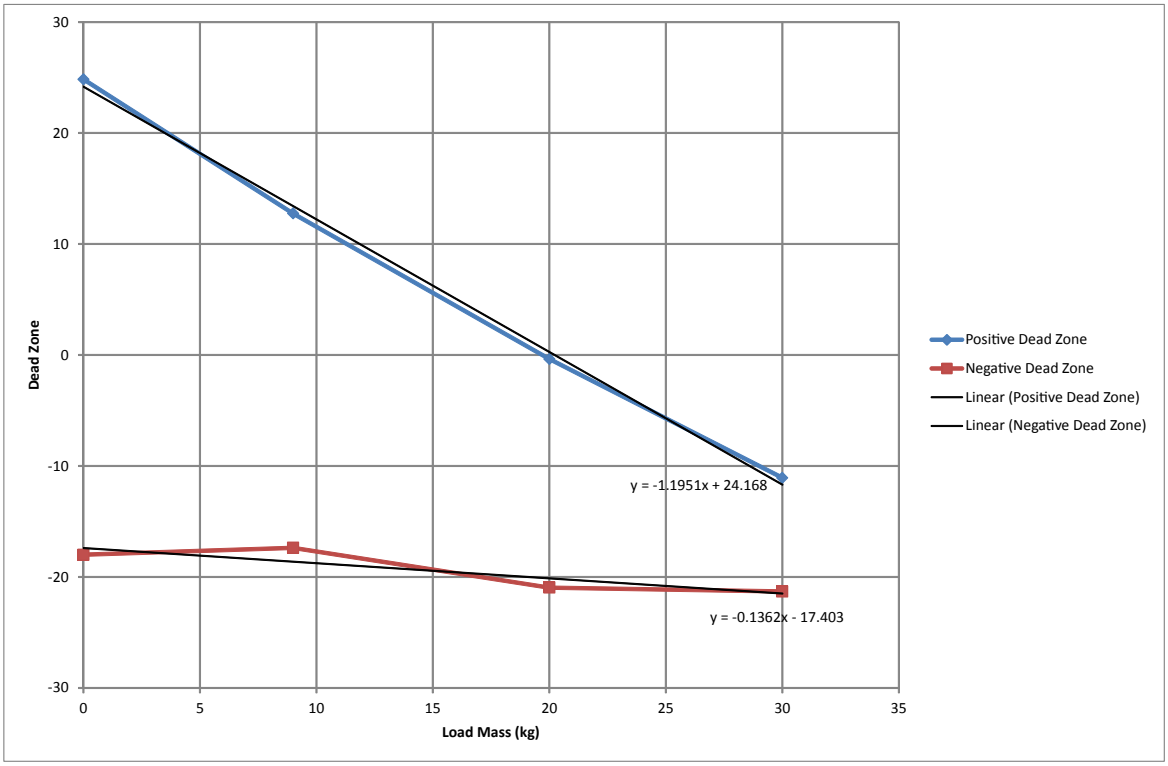

Fig. 8.17 Ram 2 dead zone with Constant Force.

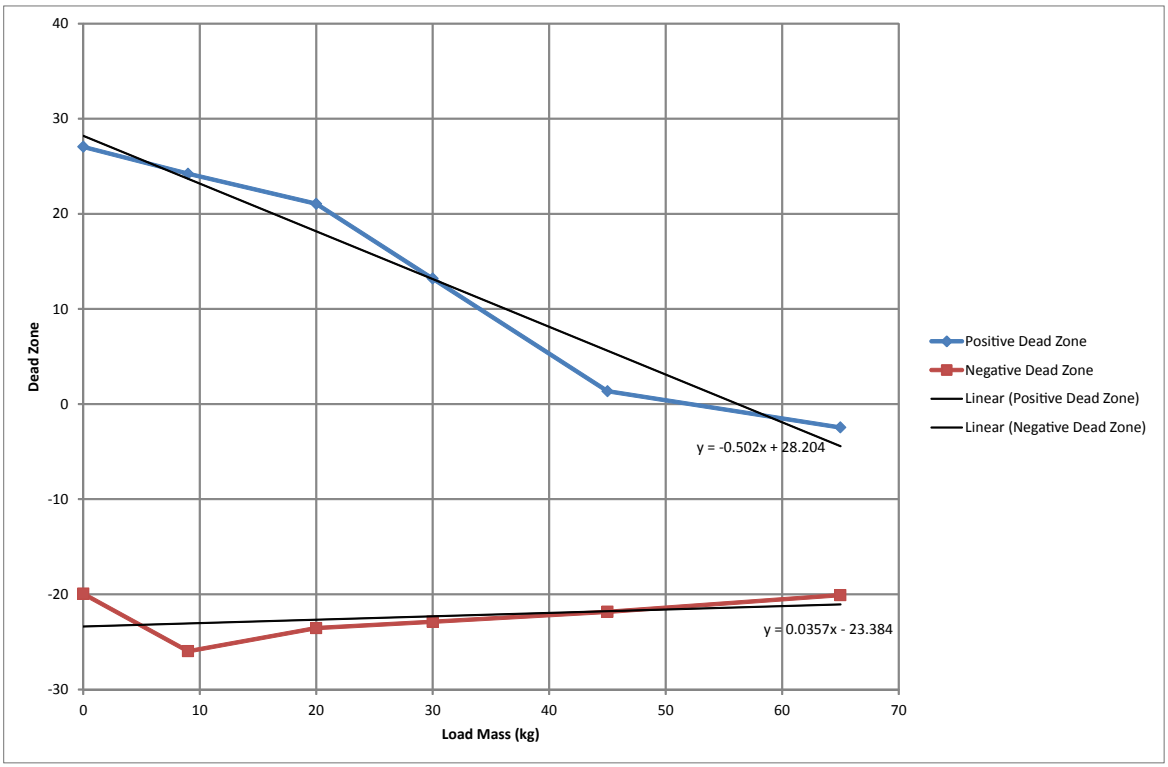

Fig. 8.18 Ram 3 dead zone with Constant Force.

8.5 Summary

The minimal modelling method produced good results for identifying the linear region of the hydraulic test system, and modelling the response of the hydraulic test system in its linear region. In particular, the minimal modelling is scalable to a full size hydraulic machine, which makes the research in this chapter useful for implementing teleoperation on a full-size harvester. The ability to identify the linear region of a non-linear actuator is a useful result, as if the non-linear region is known, the model can be changed for different operating regions. The linear dynamics are captured because the hydraulic system is designed to have a linear response in its region of normal operation. While the hydraulic test system does have significant non-linearities, this analysis is useful for quantifying the non-linearities and determining areas for improvement. Unlike Lichtsinder's study, the goal of the research in this chapter is identification of the linear region, not friction compensation. However, Lichtsinder's friction representation and its effect on amplitude and phase are applicable to the system identification, in particular the effect of the phase shift becoming constant at low frequencies. Two proofs have been given for the validity of the identified parameters: the $|H|-\cos\phi < 0$ and $\sin\phi > 0$ inequalities. These inequalities provide an explicit basis for evaluating the validity of the identified solution.

The system identification using the square wave is useful, because experiments using square waves are quicker to perform than experiments using sine waves. Though the sine wave analysis is more time consuming to perform, the sine wave analysis is useful because it shows non-linearities easily. The stability of the system identification can be improved using a singular value decomposition on the free vectors. In particular, orthogonalising the free vectors and eliminating redundancies reduces instabilities in the solver variables, due to the reduced interplay between the free variables in the solution. The disadvantage of using the SVD is that it is difficult to assign physical meaning to the singular vectors. Instead, a modified decomposition, such as the CUR decomposition could be used. The linear system identification is not capable of describing variable friction in the dead zone. This limitation can be overcome using a specific dead zone model, with a variable damping dependent on the friction.

Load detection is possible as an extension of the system identification. The system identification detects the dead zone as an offset. Fig. 8.17 and Fig. 8.18 shows the dead zone is affected by the load force, even if the load force is assumed constant. The load force can be assumed constant because the loads on Rams 1 and 2 have an offset due to gravity. The load has no effect on Ram 1's dead zones since Ram 1 only needs to bear the inertial load. There is no clear trend between the end effector load and any of Ram 1's dynamic parameters. This can also be expected, because the valve control command controls speed rather than torque, so if the rams were 'perfect' velocity actuators, the inertial parameters would not be affected by load at all.

The main limitation of the minimal modelling identification method is that the effect of un-modelled parts of the system can be unpredictable. The unpredictability comes from two sources: model limitations and system behaviour. The minimal model presented does not account for system pressure. While this configuration fits well with the actual system, the load detection ends up lumped with the dead zone, whereas if pressure measurements were available, the dead zone and load force could be separated.

The minimal modelling based system identification has worked well for the hydraulic arm. In particular, the validity of the identification has been proved by performing the experiment with both sine waves and square waves. Future work can go in several different directions. On the basis of the work in this chapter, servo valves that control ram speed directly are preferred. However, while they control one source of dynamics and dead zone, the effects of end effector load still remain, and this will provide the basis for the use of this minimal modelling technique on an upgraded hydraulic arm.

This chapter shows that the combination of a minimal model and reasonable assumptions about the normal operating range of the electro-hydraulic valves allows an accurate approxi-

mation of the response despite lacking detailed information about the internal state of the system, such as on a retro fitted full size forestry harvester. The physically derived minimal model is able to accurately model the response of a hydraulic ram to both a square wave input and sine wave inputs. The minimal model shows limitations in the sensing framework. In particular, the lack of ram pressure measurements means certain forces such as stiction cannot be observed, as it builds up and the exact values of the transfer characteristics of the hydraulic valves cannot be known in real time. However, this work shows that because a significant proportion of the operation of the valves was within a linear region this was not a significant barrier. Future work includes characterising the system with multiple rams working together and adding compensation for the proportional valves dead zone. The effect of the results of this paper on the dead zone compensation algorithm will be considered in future research.

Chapter 9

Conclusions and Future Work

9.1 Conclusions

Forestry harvesting presents a challenging environment for robotics development. The research in this thesis is aimed primarily at being able to retrofit existing machines for teleoperation, as most forestry harvesting machines in use in New Zealand are based off modified excavators. The use of ROS as a control system framework has produced several encouraging results, in particular the ability to control a hydraulic machine autonomously. This was despite the hydraulic test system not being set up as a servo mechanism, which corresponds to full size forestry harvesters not being set up as servo mechanisms. The research also demonstrated that ROS's architecture is inherently compatible with teleoperation, so teleoperation of a full sized harvester should be possible using the methods developed for the hydraulic test system. The use of ROS in this thesis also provided the basis for using ROS for the Stick Insect project, which started approximately one year after this research.

The original target machine of the research was Trinder's ClimbMax harvester. The ClimbMax uses an Opto 22 PAC, which is why a similar PAC was used in this research. While teleoperation has not been implemented on the ClimbMax, the use of the same PAC in the laboratory has produced a system that is suitable for retrofit to the ClimbMax. The research provided opportunities for testing minimal modelling, in particular grey-box minimal modelling, where known dynamics are put into a form where the effect of unobservable dynamics can be lumped with observable dynamics. This approach is particularly useful for retrofits, where a detailed system design may not be available. Minimal modelling has been found useful for non-linear systems with friction, as the minimal models in this thesis were able to relate the coefficients into a linear time variant form. The minimal model was useful in simulation as it allowed development of a state space model, with non-linearities incorporated by altering the state space model coefficients. The data driven modelling confirmed that

the minimal modelling for the Phantom Omni arm is an accurate approximation for the dynamics. It also confirmed that a pseudo random binary signal and data driven modelling is not necessarily required to obtain a frequency response, as similar results were obtained using sinusoidal steady state responses.

The integral method of identifying minimal model coefficients was found to be robust, particularly if the initial condition polynomial vectors were orthogonalised, so that ill conditioning due to correlations between the initial conditions was eliminated. While this could be done analytically using orthogonal polynomials such as Legendre polynomials, use of orthogonalisation methods such as the SVD or QR decompositions was found to be adequate. Doing this also improved the ability to find numerically stable solutions for the piecewise linear models, where the initial condition vectors became linearly independent from any 'global' initial conditions of offsets. This eliminated a source of instability from interactions between initial conditions and the solver variable vectors. The research included usage of haptic feedback in forestry harvesting, which has not been tried before. The experiments included using a Phantom Omni to control the position of the hydraulic arm. The short time delay of the laboratory system meant the haptic feedback was stable, but since the teleoperation is internet based, the haptic feedback has the potential to become unstable due to uncertain time delays. A simple method to provide stability is to turn the haptic feedback off, but methods of stabilisation using a more sophisticated mathematical approach were investigated. The research came up with coefficient bounds, that in future work can be used to check if the combinations of PD control gains and time delay are stable. Since these are known to the control system and can be measured in real time, the work can be extended to real time measurement of stability.

A novel minimal modelling methodology using the 'α-invariant' for identifying and simulating non-linear damping behaviour has been developed and shown on a Phantom Omni haptic feedback arm. The results show the α-invariant non-linear model outperforms a linear model, demonstrating the energy formulation can capture non-linear damping and resonant frequency behaviour. Overall, the research in this thesis makes useful contributions to teleoperation of forestry harvesting, through minimal modelling, haptic feedback and non-linear damping studies. One of the main limitations of the minimal modelling identification method in non linear systems with stochastic behaviours is that the effect of un-modelled parts of the system on the linear approximation can be unpredictable. For example, in the case of the load detection experiments, the valve dead zone offset on the hydraulic test system was also affected by friction, whereas if pressure measurements were available, the dead zone and load force could be separated. The ability to identify the linear region of a non-linear actuator is a useful result, as it gives a region for where the model can be changed

for different operating regions. In the case of the hydraulic test system, the linear dynamics are captured because the hydraulic system is designed to have a linear response in its region of 'normal' operation. Two proofs have been given for the validity of the identified linear model parameters based on the relationship between the linear response amplitude and phase shift. These inequalities provide an explicit basis for evaluating the validity of the identified linear minimal model solution.

9.2 Future Work

This research shows there is plenty of scope for future work. In particular, the continuing rapid drop in the price of computing power will make it easier to implement autonomous control. The autonomous control used by ROS was not directly suitable for use with the hydraulic system, so path planning algorithms that can work with ram lengths directly will make ROS more useful for ram operated machines. The ram control itself can be improved with improved valve control, in particular servo valves. Using servo valves is also beneficial as they can be used with existing machinery.

Future work includes deploying the control system on a small excavator once the communications and control methods are proven on the hydraulic test system. If the trials on the small excavator are successful, the control will be deployed on a larger excavator for field testing on a forestry harvesting site. A project to retrofit a John Deere 909 has been carried out using ROS-based remote control, and future work includes implementing the autonomous teleoperation on the John Deere 909. The ROS based control system is suitable for interfacing to the ClimbMax control system. Future work includes testing the ROS control system on the ClimbMax. This will eliminate the hazard to an operator that is required to be present in the ClimbMax on a steep slope.

The Stick Insect uses real time sensing for trees using a laser scanner. Real time tree scanning is incorporated into the steep country harvester's control system, so that it can detect trees in real time in the field. While haptic feedback has potential for enhancing situational awareness, haptic devices are mechanical devices with dynamics that contribute to the system's behaviour. Because of this, a system with haptic feedback can become sensitive to time delays and if this is not properly managed the system can become unstable. It is recommended that haptic feedback be controlled by the user so that any instabilities can be eliminated by the user without having to resort to emergency measures.

Some research questions that are still to be addressed are the types of invariants that can be used to characterise friction. The α-invariant can be used to characterise sine waves,

but there is the possibility for future research in developing more generalised invariants for characterising friction.

References

[1] J. Billingsley, V. Arto, and M. Dunn, "Robotics in Agriculture and Forestry." 2007.

[2] M. MacDonncadha, *Japanese Forestry and Forest Harvesting Techniques: With emphasis on the potential use of Japanese harvesting techniques on steep & sensitive sites in Ireland*. No. March, 1997.

[3] T. Nishino, "Forestry Principles in Japan," in *Encyclopedia of Life Support Systems*, 2000.

[4] I. Ota, "The Economic Situation of Small-Scale Forestry in Japan," in *Economic Sustainability of Small Scale Forestry*, pp. 29–41, European Forest Institute, 2001.

[5] New Zealand Ministry of Primary Industries, "International Trade - Agricultural and Forestry Exports from New Zealand." Aug. 2012.

[6] New Zealand Forestry Owners Association, "New Zealand Plantation Forest Industry - Facts & Figures 2010/2011," 2011.

[7] Occupational Safety and Health Service, *Approved Code of Practice for Safety and Health in Forest Operations*. 1999.

[8] D. Amishev, T. Evanson, and K. Raymond, "Felling and Bunching on Steep Terrain - A Review of the Literature," *FFR Technical Note*, vol. 1, no. 7, pp. 1–10, 2009.

[9] K. Raymond, "Innovative Harvesting Solutions: A Step Change," *New Zealand Journal Of Forestry*, vol. 55, pp. 4–9, Nov. 2010.

[10] T. Evanson and D. Amishev, "A New Method for Bunching Trees on Steep Terrain," *FFR Technical Note*, vol. 2, no. 5, pp. 1–9, 2009.

[11] K. M. Bayne and R. J. Parker, "The introduction of robotics for New Zealand forestry operations: Forest sector employee perceptions and implications," *Technology in Society*, vol. 34, pp. 138–148, May 2012.

[12] T. Evanson and D. Amishev, "Productivity Impacts of Bunching for Hauler Extraction," *FFR Technical Note*, pp. 1–9, 2009.

[13] K. Raymond, "Innovation To Increase Profitability Of Steep Terrain Harvesting In New Zealand," *New Zealand Journal Of Forestry*, vol. 57, pp. 19–23, Aug. 2012.

[14] Forest Owners Association, "New Zealand Plantation Forest Industry: Facts and Figures 2012/2013," p. 44, 2013.

[15] R. Parker, "Robotics for Steep Country Tree Felling," *FFR Technical Note*, vol. 2, no. 1, pp. 1–6, 2009.

[16] T. Evanson, "Valmet 445 EXL Self-levelling Feller Buncher," *FFR Harvesting Technical Note*, vol. 3, no. 8, pp. 1–9, 2011.

[17] New Zealand Forestry Owners Association, "New Zealand Forestry Bulletin, Autumn 2012," *New Zealand Forestry Bulletin*, pp. 1–8, Apr. 2012.

[18] C. V. Meaclem, L. Shao, R. Parker, S. Gutschmidt, C. E. Hann, B. J. E. Milne, and X. Chen, "Sensor guided biped felling machine for steep terrain harvesting," in *Automation Science and Engineering (CASE), 2014 IEEE International Conference on*, (Taipei), pp. 984–989, IEEE, 2014.

[19] T. Evanson and D. Amishev, "A Steep Slope Excavator Feller Buncher," *FFR Technical Note*, vol. 3, no. 2, pp. 1–8, 2010.

[20] X. Chen, "Mobile Robotics in Agriculture and Horticulture," 2012.

[21] B. Boyle, R. McMaster, and J. Nixon, "Concept evaluation trials of teleoperation system for control of an underwater robotic arm by graphical simulation techniques," *Transactions of the Institute of Measurement and Control*, vol. 17, pp. 242–250, Jan. 1995.

[22] J. G. Balchen, "Model Based Teleoperation of Untethered Underwater Vehicles with Manipulators," *Modeling, Identification and Control*, vol. 17, no. 1, pp. 37–45, 1996.

[23] Q. Lin and C. Kuo, "Assisting the teleoperation of an unmanned underwater vehicle using a synthetic subsea scenario," *Presence*, vol. 8, pp. 520–530, Oct. 1999.

[24] T. Hirabayashi, J. Akizono, T. Yamamoto, H. Sakai, and H. Yano, "Teleoperation of construction machines with haptic information for underwater applications," *Automation in Construction*, no. 15, pp. 563–570, 2006.

[25] B. P. DeJong, E. L. Faulring, J. E. Colgate, M. a. Peshkin, H. Kang, Y. S. Park, and T. F. Ewing, "Lessons learned from a novel teleoperation testbed," *Industrial Robot: An International Journal*, vol. 33, no. 3, pp. 187–193, 2006.

[26] L. Basa, L. Basanez, and R. Surrez, "Teleoperation," pp. 449–468, 2009.

[27] E. Duff, C. Caris, A. Bonchis, K. Taylor, C. Gunn, and M. Adcock, "The Development of a Telerobotic Rock Breaker," 2009.

[28] T. Hellström, P. Lärkeryd, T. Nordfjell, and O. Ringdahl, "Autonomous Forest Machines - Past, Present and Future," vol. 4, no. 1, pp. 1–17, 2008.

[29] O. Ringdahl, *Automation in Forestry - Development of Unmanned Forwarders*. PhD thesis, UmeåUniversity, Sweden, May 2011.

[30] Komatsu, "KOMATSU: Autonomous Haulage System - Komatsu's Pioneering Technology Deployed at Rio Tinto Mine in Australia," 2012.

[31] D. W. Hainsworth, "Teleoperation User Interfaces for Mining Robotics," *Autonomous Robots*, no. 11, pp. 19–28, 2001.

[32] N. Murakami, A. Ito, J. D. Will, M. Steffen, K. Inoue, K. Kita, and S. Miyaura, "Development of a teleoperation system for agricultural vehicles," *Computers and Electronics in Agriculture*, vol. 63, no. 1, pp. 81–88, 2008.

[33] A. Robotics, J. Billingsley, D. Oetomo, and J. Reid, "Agricultural Robotics," *IEEE Robotics & Automation Magazine*, p. 19, Dec. 2009.

[34] Army UAS CoE Staff, "U. S. Army Roadmap for Unmanned Aircraft Systems 2010-2035." U. S. Army UAS Center of Excellence (ATZQ-CDI-C), Bldg 5000, Lucky Star Street, Fort Rucker, Alabama, 36362-5101, 2010.

[35] P. Pounds, R. Mahony, and P. Corke, "Modelling and control of a large quadrotor robot," *Control Engineering Practice*, vol. 18, pp. 691–699, July 2010.

[36] T. Hellström, "Intelligent vehicles in forestry," 2005.

[37] E. Duff, K. Usher, K. Taylor, and C. Caris, "Web-Based Tele-Robotics Revisited," 2007.

[38] M. Brace and C. Hargrave, "Automating the Mine," *Earthmatters*, pp. 12–15, Mar. 2009.

[39] D. T. Lawton, M. Schoppers, and E. D. DiSabatino, "Interactive Model-Based Vision Systems for Telerobotic Vehicles." Aug. 1989.

[40] T. Fong and C. Thorpe, "Vehicle Teleoperation Interfaces," *Autonomous Robots*, no. 11, pp. 9–18, 2001.

[41] M. Brander, D. Eriksson, and B. Lögfren, "Automation of knuckleboom work can increase productivity," *Skogforsk Results*, Apr. 2004.

[42] S. Westerberg, I. R. Manchester, U. Mettin, P. L. Hera, and A. Shiriaev, "Virtual Environment Teleoperation of a Hydraulic Forestry Crane," 2008.

[43] B. Osafo-Yeboah and X. Jiang, "Usability evaluation of a haptically controlled backhoe excavator simulation," *IIE Annual Conference.Proceedings*, pp. 961–966, 2009.

[44] L. F. van der Zee, *Design of a haptic controller for excavators*. Master's thesis, Department of Electrical Engineering, University of Stellenbosch, 2009.

[45] C. Gunn and D. Zhu, "Haptic Tele-operation of Industrial Equipment," *Proceedings - APCHI-ERGOFUTURE 2010*, p. 6, 2010.

[46] A. Hansson and M. Servin, "Semi-autonomous shared control of large-scale manipulator arms," *Control Engineering Practice*, vol. 18, pp. 1069–1076, Sept. 2010.

[47] H. Hayn and D. Schwarzmann, "A haptically enhanced operational concept for a hydraulic excavator," in *Advances in Haptics* (M. H. Zadeh, ed.), ch. 10, pp. 199–220, Intech, 2010.

[48] J. Yoon and A. Manurung, "Development of an intuitive user interface for a hydraulic backhoe," *Automation in Construction*, vol. 19, pp. 779–790, Oct. 2010.

[49] L. Ljung, "Perspectives on system identification," *Annual Reviews in Control*, vol. 34, no. 1, pp. 1–12, 2010.

[50] S. Tafazoli, P. Lawrence, and S. Salcudean, "Identification of inertial and friction parameters for excavator arms," *IEEE Transactions on Robotics and Automation*, vol. 15, no. 5, pp. 966–971, 1999.

[51] T. Hellström, "Forestry in Sweden Automation in Sweden," pp. 1–7, 2009.

[52] I. Bergkvist, B. Nordén, and H. Lundström, "Innovative Unmanned Harvester System," *Skogforsk Results*, Feb. 2006.

[53] M. Emde, P. Krahwinkler, and J. Rossmann, "Sensor Fusion in Forestry," *GPS World*, vol. 48, pp. 30–32, July 2012.

[54] Triton Logging, "Triton Logging Website," 2012.

[55] D. Zhu, T. Gedeon, and K. Taylor, ""Moving to the centre": A gaze-driven remote camera control for teleoperation," *Interacting with Computers*, vol. 23, pp. 85–95, Jan. 2011.

[56] H. Hu, L. Yu, P. W. Tsui, and Q. Zhou, "Internet-based robotic systems for teleoperation," *Assembly Automation*, vol. 21, no. 2, pp. 143–151, 2001.

[57] A. J. Álvares and J. a. C. E. Ferreira, "WebTurning: Teleoperation of a CNC turning center through the Internet," *Journal of Materials Processing Technology*, vol. 179, pp. 251–259, Oct. 2006.

[58] F. Guerrero, "Wireless robot teleoperation via internet using IPv6 over a bluetooth personal area network Teleoperación inalámbrica de un robot vía internet utilizando IPv6 sobre una red de área personal bluetooth," pp. 172–184, 2010.

[59] Y. Yokokohji, T. Imaida, and Y. Iida, "Bilateral Teleoperation: Towards Fine Manipulation with Large Time Delay," vol. 1, 2000.

[60] P. F. Hokayem and M. W. Spong, "Bilateral teleoperation:An historical survey," *Automatica*, no. 42, pp. 2035–2057, 2006.

[61] E. Slawiñski, J. F. J. F. J. F. Postigo, V. Mut, and E. Slawinski, "Bilateral teleoperation through the Internet," *Robotics and Autonomous Systems*, vol. 55, pp. 205–215, Mar. 2007.

[62] E. Slawiñski, V. A. Mut, E. Slawinski, and J. F. Postigo, "Teleoperation of Mobile Robots With Time-Varying Delay," *IEEE Transactions On Robotics*, vol. 23, pp. 1071–1082, Oct. 2007.

[63] N. Chopra, P. Berestesky, and M. W. Spong, "Bilateral Teleoperation Over Unreliable Communication Networks," *IEEE Transactions On Control Systems Technology*, vol. 16, no. 2, pp. 304–313, 2008.

[64] E. A. Thompson, E. Harmison, R. Carper, R. Martin, and J. Isaacs, "Robot teleoperation featuring commercially available wireless network cards," *Journal of Network and Computer Applications*, vol. 29, no. 1, pp. 11–24, 2006.

[65] N. Y. Chong, T. Kotoku, K. Ohba, K. Komoriya, K. Tanie, J. Oaki, H. Hashimoto, F. Ozaki, K. Maeda, and N. Matsuhira, "A Collaborative Multi-Site Teleoperation Over an ISDN," *Mechatronics*, vol. 13, pp. 957–979, Oct. 2003.

[66] J. Y. C. Chen and J. E. Thropp, "Review of Low Frame Rate Effects on Human Performance," *Systems, Man and Cybernetics, Part A: Systems and Humans, IEEE Transactions on*, vol. 37, no. 6, pp. 1063–1076, 2007.

[67] T. B. Sheridan, "Teleoperation, Telerobotics And Telepresence: A Progress Report," *Control Engineering Practice*, vol. 3, no. 2, pp. 205–214, 1995.

[68] K. R. Ferguson, "Past and Future Challenges In Developing Remote Systems Technology," Argonne National Laboratory, 1978.

[69] D. Kim, J. Kim, K. Lee, C. Park, J. Song, and D. Kang, "Excavator tele-operation system using a human arm," *Automation in Construction*, vol. 18, pp. 173–182, Mar. 2009.

[70] A. Ghanbari, H. Abdi, B. Horan, S. Nahavandi, X. Chen, and W. Wang, "Haptic Guidance for Microrobotic Intracellular Injection," in *Proceedings of the 2010 3rd IEEE RAS & EMBS*, 2010.

[71] A. Aziminejad, M. Tavakoli, R. V. Patel, and M. Moallem, "Transparent Time-Delayed Bilateral Teleoperation Using Wave Variables," *Control Systems Technology, {IEEE} Transactions on*, vol. 16, pp. 548–555, May 2008.

[72] M. Alise, R. G. Roberts, D. W. Repperger, C. A. Moore, and S. Tosunoglu, "On Extending the Wave Variable Method to Multiple-DOF Teleoperation Systems," *Mechatronics, {IEEE/ASME} Transactions on*, vol. 14, pp. 55–63, Feb. 2009.

[73] G. Mingde, Z. Dingxuan, F. Shizhu, W. Hailong, and H. Yamada, "Force Feedback Model of Electro-hydraulic Servo Tele-Operation Robot Based on Velocity Control," in *Robotics, Automation and Mechatronics, 2008 IEEE Conference on*, pp. 912–915, 2008.

[74] G. Mingde, Y. Bin, and H. Cheng-hao, "Improved force feedback model based on position/velocity control of teleoperation system," in *Proceedings ofthe 2009 IEEE International Conference on Mechatronics and Automation*, pp. 660–664, 2009.

[75] S.-O. Chang and A. M. Okamura, "Impedance-reflecting teleoperation with a real-time evolving neural network controller," in *Intelligent Robots and Systems, 2004. (IROS 2004). Proceedings. 2004 IEEE/RSJ International Conference on*, vol. 3, pp. 2241–2246 vol.3, 2004.

[76] K. Hashtrudi-Zaad and S. E. Salcudean, "Adaptive transparent impedance reflecting teleoperation," in *Robotics and Automation, 1996. Proceedings., 1996 IEEE International Conference on*, vol. 2, pp. 1369–1374 vol.2, 1996.

[77] N. Marcassus, A. Chriette, and M. Gautier, "Theoretical and experimental overview of bilateral teleoperation control laws," in *Control and Automation, 2006. MED '06. 14th Mediterranean Conference on*, pp. 1–6, 2006.

[78] A. M. Tahmasebi, B. Taati, F. Mobasser, and K. Hashtrudi-Zaad, "Dynamic Parameter Identification and Analysis of a PHANToM TM Haptic Device," in *Proceedings of the 2005 IEEE Conference on Control Applications*, pp. 1251–1256, 2005.

[79] B. Taati, A. M. Tahmasebi, and K. Hashtrudi-Zaad, "Experimental Identification and Analysis of the Dynamics of a PHANToM Premium 1.5A Haptic Device," *Presence*, vol. 17, no. 4, pp. 327–343, 2008.

[80] A. Calanca, L. M. Capisani, A. Ferrara, and L. Magnani, "MIMO closed loop identification of an industrial robot," *IEEE Transactions on Control Systems Technology*, vol. 19, no. 5, pp. 1214–1224, 2011.

[81] L. Marton and B. Lantos, "Control of robotic systems with unknown friction and payload," *IEEE Transactions on Control Systems Technology*, vol. 19, no. 6, pp. 1534–1539, 2011.

[82] M. Gautier, A. Janot, and P. O. Vandanjon, "A new closed-loop output error method for parameter identification of robot dynamics," *IEEE Transactions on Control Systems Technology*, vol. 21, no. 2, pp. 428–444, 2013.

[83] Y.-Y. Chen, P.-Y. Huang, and J.-Y. Yen, "Frequency-Domain Identification Algorithms for Servo Systems With Friction," *IEEE Transactions on Control Systems Technology*, vol. 10, no. 5, pp. 654–665, 2002.

[84] C. E. Hann, J. G. Chase, M. F. Ypma, J. Elfring, N. M. Nor, P. Lawrence, and G. M. Shaw, "The Impact of Parameter Identification Methods on Drug Therapy Control in an Intensive Care Unit," *The Open Medical Informatics Journal*, vol. 2, pp. 92–104, 2008.

[85] K. T. Moorhead, S. Paeme, J. G. Chase, P. Kolh, L. Pierard, C. E. Hann, P. C. Dauby, and T. Desaive, "A simplified model for mitral valve dynamics.," *Computer methods and programs in biomedicine*, vol. 109, pp. 190–6, Feb. 2013.

[86] C. E. Hann, M. Snowdon, A. Rao, O. Winn, N. Wongvanich, and X. Chen, "Minimal modelling approach to describe turbulent rocket roll dynamics in a vertical wind tunnel," *Proceedings of the Institution of Mechanical Engineers, Part G: Journal of Aerospace Engineering*, vol. 226, pp. 1042–1060, Dec. 2011.

[87] N. Wongvanich, "Non linear electromechanical cart characterization using minimal modeling approach," in *2013 Control Conference (ECC)*, (Zurich, Switzerland), pp. 2927–2932, 2013.

[88] A. San-Millan and V. Feliu, "A Fast Online Estimator of the Two Main Vibration Modes of Flexible Structures From Biased and Noisy Measurements," *IEEE/ASME Transactions on Mechatronics*, no. 99, pp. 1–12, 2014.

[89] A. M. Okamura, "Methods for haptic feedback in teleoperated robot-assisted surgery.," *The Industrial Robot*, vol. 31, pp. 499–508, Dec. 2004.

[90] S.-G. Kim and M. Sitti, "Task-based and stable telenanomanipulation in a nanoscale virtual environment," *Automation Science and Engineering, IEEE Transactions on*, vol. 3, no. 3, pp. 240–247, 2006.

[91] E. Naerum, J. Cornell, and O. J. Elle, "Wavelet Networks for Estimation of Coupled Friction in Robotic Manipulators," in *Proceedings of the 2008 IEEE International Conference on Robotics and Automation*, (Pasadena, CA), pp. 862–867, 2008.

[92] E. Naerum, J. Cornell, and O. J. Elle, "Contact Force Estimation for Backdrivable Robotic Manipulators with Coupled Friction," in *Proccedings of the 2008 IEEE/RSJ International Conference on Intelligent Robots and Systems*, (Nice, France), pp. 22–26, 2008.

[93] H. Hayn and D. Schwarzmann, "Control Concept for a Hydraulic Mobile Machine Using a Haptic Operating Device," in *Advances in Computer-Human Interactions, 2009. ACHI '09. Second International Conferences on*, pp. 348–353, 2009.

[94] S. E. Salcudean, K. Hashtrudi-Zaad, S. Tafazoli, S. P. DiMaio, C. Reboulet, and C. Reboulett, "Bilateral matched impedance teleoperation with application to excavator control," in *Proceedings of the 1998 IEEE International Conference on Robotics & Automation*, (Leuven, Belgium), pp. 133–139, 1999.

[95] Y. H. Zweiri, L. D. Seneviratne, and K. Althoefer, "Parameter Estimation for Excavator Arm Using Generalized Newton Method," *IEEE Transactions On Robotics*, vol. 20, no. 4, pp. 762–767, 2004.

[96] Y. H. Zweiri, "Identification schemes for unmanned excavator arm parameters," *International Journal of Automation and Computing*, vol. 5, pp. 185–192, May 2008.

[97] Y. Liu, M. S. Hasan, and H.-N. Yu, "Modelling and remote control of an excavator," *International Journal of Automation and Computing*, vol. 7, pp. 349–358, Aug. 2010.

[98] C. E. Hann, M. Snowdon, A. Rao, R. Tang, A. Korevaar, G. Skinner, A. Keall, X. Q. Chen, and J. G. Chase, "Rocket Roll Dynamics and Disturbance – Minimal modelling and system identification." http://ir.canterbury.ac.nz/handle/10092/5105, 2010.

[99] P. Gómez and F. a. Uribe, "The numerical Laplace transform: An accurate technique for analyzing electromagnetic transients on power system devices," *International Journal of Electrical Power & Energy Systems*, vol. 31, pp. 116–123, Feb. 2009.

[100] V. Kryzhniy, "High-resolution exponential analysis via regularized numerical inversion of Laplace transforms," *Journal of Computational Physics*, vol. 199, pp. 618–630, Sept. 2004.

[101] F. Arinos de Almeida Barbuto, "Performance of Numerical Inversion of Laplace Transforms," *Journal of Advanced Engineering Software*, vol. 13, no. 3, pp. 148–155, 1991.

[102] D. Feygin, "Kinematics and Dynamics of Phantom (TM) model 1.5 Haptic Interface," tech. rep., 2001.

[103] M. C. Cavasoglu, D. Feygin, and F. Tendick, "A Critical Study of the Mechanical and Electrical Properties of the PHANToM Haptic Interface and Improvements for High-Performance Control," *Presence*, vol. 11, no. 6, pp. 555–569, 2002.

[104] B. Armstrong-Hélouvry, P. Dupont, and C. C. De Wit, "A survey of models, analysis tools and compensation methods for the control of machines with friction," *Automatica*, vol. 30, pp. 1083–1138, July 1994.

[105] M. Rahmat, N. H. Sunar, S. N. S. Salim, M. S. Z. Abidin, A. A. M. Fauzi, and Z. H. Ismail, "Review on Modeling and Controller Design," *International Journal on Smart Sensing and Intelligent Systems*, vol. 4, no. 4, pp. 630–661, 2011.

[106] E. Berger, "Friction modeling for dynamic system simulation," *Applied Mechanics Reviews*, vol. 55, no. 6, pp. 535–577, 2002.

[107] V. Van Geffen, "A study of friction models and friction compensation," tech. rep., Technische Universiteit Eindhoven, Eindhoven, 2009.

[108] K. Osman, A. Fauzdi, M. F. Rahmat, N. Mustafa, M. A. Azman, and K. Suzumori, "System Identification Model for an Intelligent Pneumatic Actuator (IPA) System," in *IEEE/RSJ International Conference on Intelligent Robots and Systems (IROS)*, pp. 628–633, 2012.

[109] B. Boulet, L. Daneshmend, V. Hayward, and C. Nemri, "System Identification and Modelling of a High Performance Hydraulic Actuator," tech. rep., McGill University, Montreal.

[110] B. Shapiro, J. Kissel, N. Mavalvala, K. Strain, and K. Youcef-toumi, "Limitations of Underactuated Modal Damping for Multistage Vibration Isolation Systems," *IEEE/ASME Transactions on Mechatronics*, no. 99, pp. 1–12, 2014.

[111] B. Na, H. Choi, and K. Kong, "Design of a Direct-Driven Linear Actuator," *IEEE/ASME Transactions on Mechatronics*, no. 99, pp. 1–10, 2014.

[112] R. J. Anderson and M. W. Spong, "Bilateral Control of Teleoperators with Time Delay," *IEEE Transactions on Automatic Control*, vol. 34, pp. 494–501, May 1989.

[113] G. Niemeyer and J.-J. E. Slotine, "Stable Adaptive Teleoperation," *IEEE Journal Of Oceanic Engineering*, vol. 16, pp. 152–162, Jan. 1991.

[114] G. Niemeyer and J. Slotine, "Designing force reflecting teleoperators with large time delays to appear as virtual tools," *Robotics and Automation, 1997. Proceedings., 1997 IEEE International Conference on*, vol. 3, no. April, pp. 2212–2218, 1997.

[115] J.-H. Ryu, J. Artigas, and C. Preusche, "A passive bilateral control scheme for a teleoperator with time-varying communication delay," *Mechatronics*, vol. 20, pp. 812–823, Oct. 2010.

[116] M. Dyck, A. Jazayeri, and M. Tavakoli, "Is the human operator in a teleoperation system passive?," in *2013 World Haptics Conference (WHC)*, no. 2, (Daejeon), pp. 683–688, IEEE, Apr. 2013.

[117] N. Chopra, M. W. Spong, and R. Lozano, "Synchronization of bilateral teleoperators with time delay," *Automatica*, vol. 44, pp. 2142–2148, Aug. 2008.

[118] A. Jazayeri and M. Tavakoli, "Revisiting Llewellyn's absolute stability criterion for bilateral teleoperation systems under non-passive operator or environment," in *2012 IEEE/RSJ International Conference on Intelligent Robots and Systems*, pp. 70–75, IEEE, Oct. 2012.

[119] A. Jazayeri, M. Dyck, and M. Tavakoli, "Stability analysis of teleoperation systems under strictly passive and non-passive operator," in *2013 World Haptics Conference (WHC)*, pp. 695–700, IEEE, Apr. 2013.

[120] K. Hashtrudi-Zaad, *Design, Implementation and Evaluation of Stable Bilateral Teleoperation Control Architectures for Enhanced Telepresence*. Phd thesis, University of British Columbia, 2000.

[121] K. Hashtrudi-Zaad and S. E. Salcudean, "Analysis and evaluation of stability and performance robustness for teleoperation control architectures," in *Robotics and Automation, 2000. Proceedings. ICRA '00. IEEE International Conference on*, vol. 4, pp. 3107–3113 vol.4, 2000.

[122] S. Tafazoli, S. E. Salcudean, K. Hashtrudi-Zaad, and P. D. Lawrence, "Impedance control of a teleoperated excavator," *Control Systems Technology, IEEE Transactions on*, vol. 10, no. 3, pp. 355–367, 2002.

[123] D. Lawrence, "Stability and transparency in bilateral teleoperation," *IEEE Transactions on Robotics and Automation*, vol. 9, no. 5, pp. 624–637, 1993.

[124] J. E. Colgate, "Robust Impedance Shaping Teleoperation," *IEEE Transactions on Robotics and Automation*, vol. 9, no. 4, pp. 374–384, 1993.

[125] R. Adams and B. Hannaford, "Stable haptic interaction with virtual environments," *IEEE Transactions on Robotics and Automation*, vol. 15, pp. 465–474, June 1999.

[126] "ROS Main Website." http://www.ros.org/.

[127] "Dane Powell's ROS Phantom Library."

[128] R. C. Dorf and R. H. Bishop, *Modern Control Systems*. 12th ed., 2011.

[129] J.-J. E. Slotine and W. Li, *Applied Nonlinear Control*. 1991.

[130] D. A. van der Schaft, *L2-Gain and Passivity Techniques in Nonlinear Control*. 1996.

[131] "SW2URDF Plugin Webpage."

[132] C. Cruz-Valverde, O. a. Dominguez-Ramirez, E. R. Ponce-de Leon-Sanchez, I. Trejo-Mota, and G. Sepulveda-Cervantes, "Kinematic and Dynamic Modeling of the PHANToM Premium 1.0 Haptic Device: Experimental Validation," in *2010 IEEE Electronics, Robotics and Automotive Mechanics Conference*, pp. 494–501, IEEE Computer Society, Sept. 2010.

[133] S. Hodgson, M. Tavakoli, M. T. Pham, and A. Leleve, "Nonlinear Discontinuous Dynamics Averaging and PWM-Based Sliding Control of Solenoid-Valve Pneumatic Actuators," *IEEE/ASME Transactions on Mechatronics*, no. 99, pp. 1–13, 2014.

[134] T. Sansanayuth, I. Nilkhamhang, and K. Tungpimolrat, "Teleoperation with Inverse Dynamics Control for PHANToM Omni Haptic Device," in *SICE Annual Conference 2012*, pp. 2121–2126, SICE, 2012.

[135] A. Mohammadi, *Disturbance Observer Design for Robotic and Telerobotic Systems*. PhD thesis, University of Alberta, 2011.

[136] S.-m. Kim, "Lumped Element Modeling of a Flexible Manipulator System," *IEEE/ASME Transactions on Mechatronics*, no. 99, pp. 1–8, 2014.

[137] R. Bellman, H. Kagiwada, and R. Kalaba, "Quasilinearization, System Identification and Prediction," *International Journal of Engineering Science*, vol. 3, pp. 327–334, 1965.

[138] Hydraforce, "SP08-47CL Electro-Proportional Valves - Directional Control Datasheet," 2014.

[139] Hydraforce, "EPFR50-S35 Pressure Compensator with Internal Load-Sense Datasheet," 2014.

[140] A. Lichtsinder and P. Gutman, "Quasi-linear analytical approach to stick – slip friction in the frequency domain," *International Journal of Robust and Nonlinear Control*, no. June 2013, pp. 2891–2908, 2013.

Appendix A

Submitted Publications

Milne, Bart; Hann, Chris; Chen, XiaoQi; "Minimal Modelling of a Hydraulic System Using Square Waves". Journal article submitted for review to ASME Journal of Applied Mechanics in September 2015.

Milne, Bart; Hann, Chris; Chen, XiaoQi; "The Alpha-Invariant: An Energy Based non-Linear Minimal Damping Model for Robotic Joints with Friction". Journal article submitted for review to ASME Journal of Computational and Nonlinear Dynamics in October 2015.

Milne, Bartholomew James Estall; Liu, Yingyi; Meaclem, Christopher Vincent; Chen, XiaoQi; Hann, Christopher Eric; Parker, Richard; "Development and Testing of a Minimal Model for a Pressure Compensated Hydraulic Cylinder Control System". Conference paper submitted to IEEE ROBIO 2015, December 6-9 2015, Zhuhai, China.

Milne, B.J.E.; Beelen, H.P.G.J.; Merks, R.W.H.; Weiland, S.; Chen, X.Q.; Hann, C.E.; Parker, R.J., "Verification of sinusoidal steady state system identification of a Phantom Omni haptic device using data driven modeling," *Automation, Robotics and Applications (ICARA), 2015 6th International Conference on*, pp.283-288, 17-19 Feb. 2015. DOI: 10.1109/ICARA.2015.7081161

Milne, Bart; Chen, XiaoQi; Hann, Chris; Parker, Richard, "Robotisation of forestry harvesting in New Zealand - An overview," *Control and Automation (ICCA), 2013 10th IEEE International Conference on*, pp.1609-1614, 12-14 June 2013. DOI: 10.1109/ICCA.2013.6564913

Milne, B.; Buchanan, G.; Paulin, S.; XiaoQi Chen; Hann, C.; Geldenhuis, A.; Parker, R., "Robotic arm kinematics and bilateral haptic feedback over an ethernet communications link," *Automation Science and Engineering (CASE), 2013 IEEE International Conference on*, pp.960-965, 17-20 Aug. 2013. DOI: 10.1109/CoASE.2013.6654005

Milne, B.; Chen, X.; Hann, C.; Parker, R.; Milliken, P. (2013). Design and Development of Teleoperation for Forest Machines: An Overview. In M. Habib, & J. Davim (Eds.)

Engineering Creative Design in Robotics and Mechatronics (pp. 186-207). Hershey, PA: Engineering Science Reference. doi:10.4018/978-1-4666-4225-6.ch012

Appendix B

Hydraulic System Kinematics Drawings

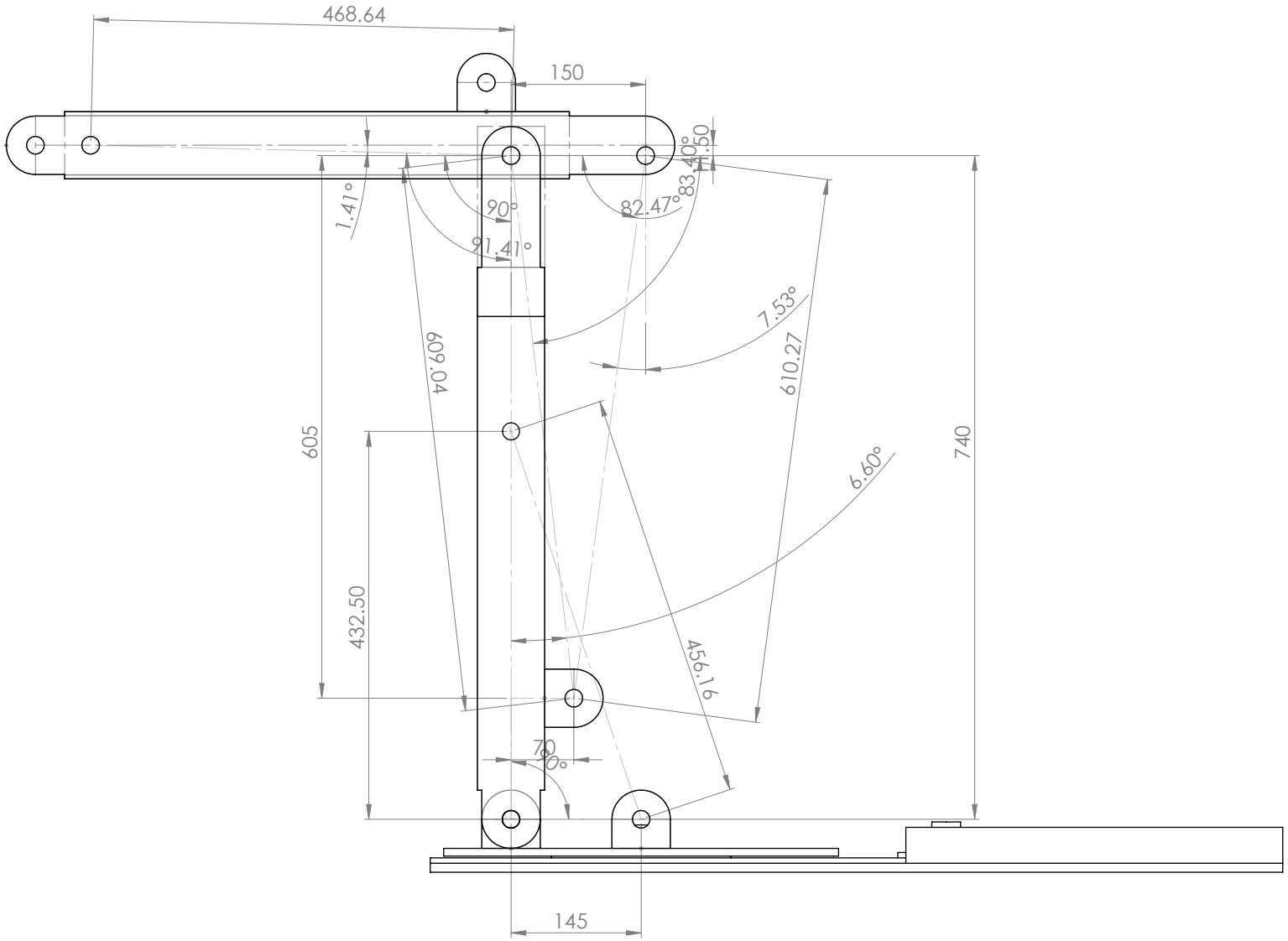

UNLESS OTHERWISE SPECIFIED: DIMENSIONS ARE IN MILLIMETERS SURFACE FINISH: TOLERANCES: LINEAR: ANGULAR:		FINISH:		DEBUR AND BREAK SHARP EDGES	DO NOT SCALE DRAWING	REVISION
	NAME	SIGNATURE	DATE		TITLE: HYDRAULIC TEST SYSTEM	
DRAWN	BJEM		JAN '13			
CHK'D						
APPV'D						
MFG						
Q.A				MATERIAL:	DWG NO. hydraulic_kinematics	A3
				WEIGHT:	SCALE:1:20	SHEET 1 OF 2

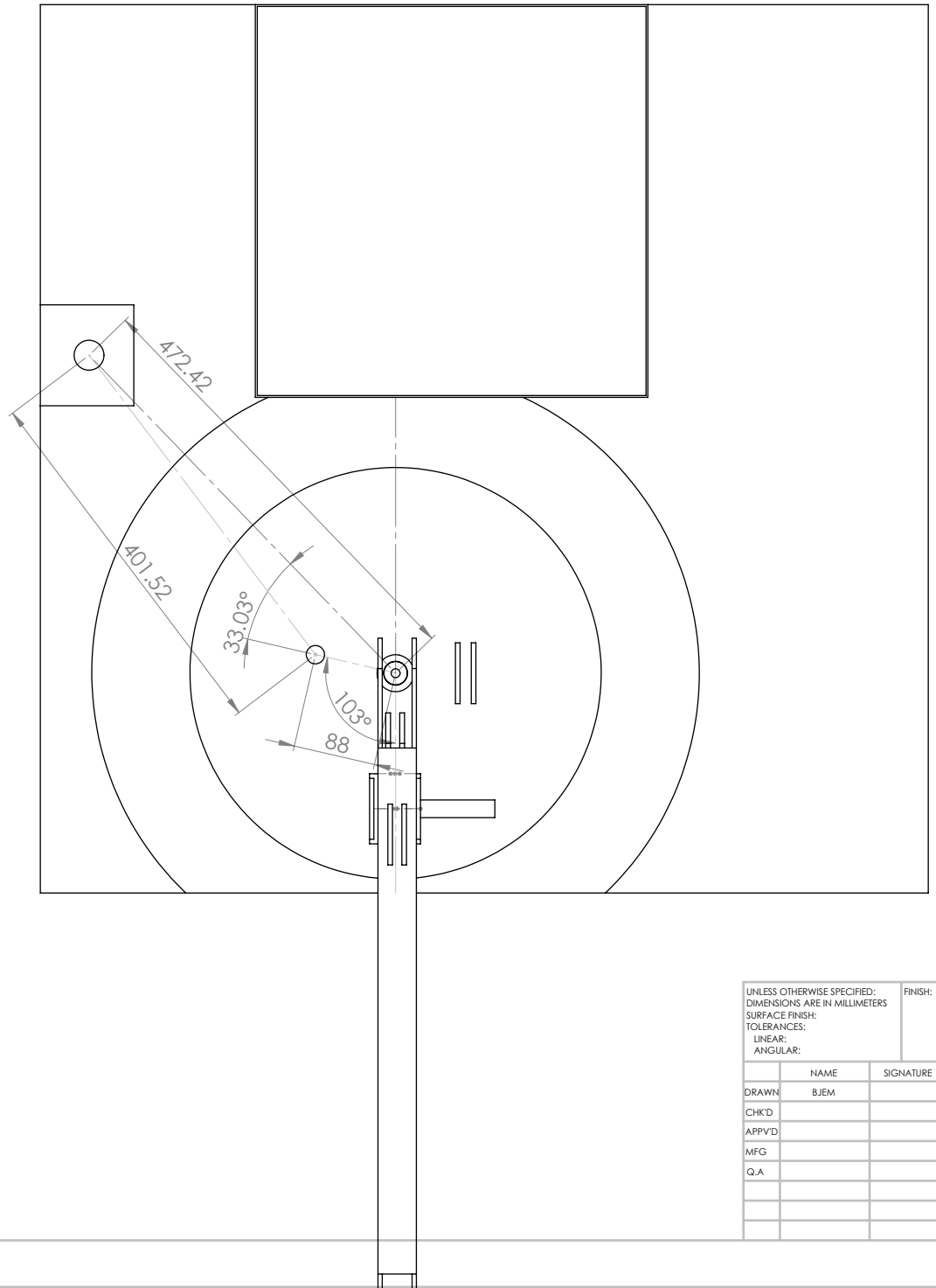

UNLESS OTHERWISE SPECIFIED: DIMENSIONS ARE IN MILLIMETERS SURFACE FINISH: TOLERANCES: LINEAR: ANGULAR:	FINISH:		DEBUR AND BREAK SHARP EDGES	DO NOT SCALE DRAWING	REVISION	
	NAME	SIGNATURE	DATE	TITLE: HYDRAULIC TEST SYSTEM		
DRAWN	BJEM		JAN '13			
CHK'D						
APPV'D						
MFG						
Q.A				MATERIAL:	DWG NO. hydraulic_kinematics	A3
				WEIGHT:	SCALE:1:20	SHEET 2 OF 2

Appendix C

Algorithm for Calculating Torque Angle

The torque angle is calculated according to a standard formula that gives the torque angle in terms of a triangle formed by the ram itself, the fixed base length and the moving arm length, as shown in Fig. C.1. The quantities in Fig. C.1 are defined in Table C.1.

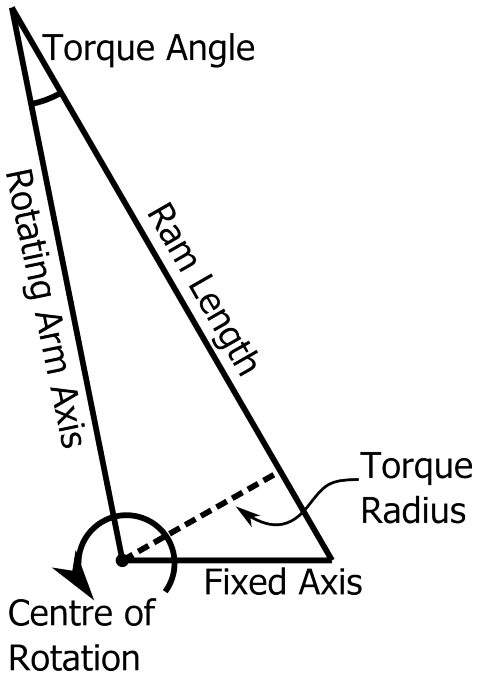

Fig. C.1 Ram Driven Rotational Joint with Torque Angle and Radius Highlighted

The torque will be at a maximum when the torque radius is either equal to α depending on which is physically possible given the relative values of α and β and the range of lengths of the ram. The torque is given in (C.1).

$$\tau = Fr \tag{C.1}$$

Table C.1 Definitions for Fig. C.1

Quantity	Variable Symbol
Fixed Axis	α
Rotating Arm Axis	β
Torque Angle	ϕ
Torque Radius	r
Ram Length	x
Ram Force	F

The value of the torque radius r is computed using (C.2).

$$r = \beta \sin\phi \tag{C.2}$$

The torque angle ϕ is computed using the cosine rule. The cosine of ϕ is shown in (C.3).

$$\cos\phi = \frac{\beta^2 - \alpha^2 + x^2}{2x\beta} \tag{C.3}$$

The actual quantity that is needed is $\sin\phi$. This can be obtained by using the standard trigonometric formula $\sin\phi = \sqrt{1-\cos^2\phi}$. The result is shown in (C.4).

$$\sin\phi = \sqrt{1 - \left(\frac{\beta^2 - \alpha^2 + x^2}{2x\beta}\right)^2} \tag{C.4}$$

The torque radius will be at a maximum when $\sin\phi$ is at a maximum, or when $\left(\frac{\beta^2-\alpha^2+x^2}{2x\beta}\right)^2$ is at a minimum. This occurs when $x = \sqrt{\alpha^2 - \beta^2}$ if $\alpha \geq \beta$ or when the derivative of $\frac{\beta^2-\alpha^2+x^2}{2x\beta}$ is zero.

$$\begin{aligned} \frac{d}{dx}\left(\frac{\beta^2 - \alpha^2 + x^2}{2x\beta}\right) &= 0 \\ \frac{d}{dx}\left(\frac{\beta^2 - \alpha^2}{2x\beta} + \frac{x}{2\beta}\right) &= 0 \\ \frac{\alpha^2 - \beta^2}{x^2} + 1 &= 0 \end{aligned} \tag{C.5}$$

Equation (C.5) has the solution $x = \sqrt{\beta^2 - \alpha^2}$. Or, an overall formulation consists of $x = \sqrt{|\alpha^2 - \beta^2|}$.

C.1 Alternative Formulation

An alternative formulation is shown in (C.6), where $\gamma = \frac{\beta^2 - \alpha^2}{2\beta}$ and $\delta = 2\beta$. The alternative form is highlighted because it is more algebraically concise to calculate.

$$\sin\phi = \sqrt{1 - \left(\frac{\gamma}{x} + \frac{x}{\delta}\right)^2} \tag{C.6}$$

It can be shown that the maximum torque occurs when $x = \sqrt{-\gamma\delta}$.
The maximum value of $\sin\phi$ is given in (C.7) for $x = \sqrt{-\gamma\delta}$.

$$\begin{aligned} \sin\phi &= \sqrt{1 - \left(\frac{\gamma}{x} + \frac{x}{\delta}\right)^2} \\ \sin\phi &= \sqrt{1 - \left(\frac{\gamma\delta + x^2}{\delta x}\right)^2} \\ \sin\phi &= 1 \end{aligned} \tag{C.7}$$

If γ and δ are both positive, then a different solution needs to be found. This can be found using the derivative.

$$\begin{aligned} \frac{d}{dx}\left(\frac{\gamma}{x} + \frac{x}{\delta}\right) &= 0 \\ -\frac{\gamma}{x^2} + \frac{1}{\delta} &= 0 \\ x &= \sqrt{\gamma\delta} \end{aligned} \tag{C.8}$$

So in effect, $x = \sqrt{|\gamma\delta|}$ will always be a solution.

Appendix D

Proof of Sine of Inverse Cosine Rule

$$y = \sqrt{1 - \left(\frac{\alpha}{x} - \frac{x}{\beta}\right)^2} \tag{D.1}$$

$$y = \sqrt{1 - u^2} \tag{D.2}$$

$$\begin{aligned} \frac{dy}{dx} &= \frac{dy}{du} \cdot \frac{du}{dx} \\ &= -\frac{u}{y} \cdot \frac{du}{dx} \end{aligned} \tag{D.3}$$

Assuming $y \neq 0$ (reasonable in all our circumstances), the maximum of y is when $\frac{du}{dx} = 0$ or when $u = 0$. We will use $u = 0$ since requiring $\frac{du}{dx} = 0$ will result in an imaginary answer.

$$\begin{aligned} \frac{\alpha}{x} - \frac{x}{\beta} &= 0 \\ x^2 - \alpha\beta &= 0 \\ x &= \sqrt{\alpha\beta} \end{aligned} \tag{D.4}$$

Consider the range of variance of y. We want to find where $y > \varepsilon_0$.

$$\begin{aligned}
\sqrt{1-\left(\frac{\alpha}{x}-\frac{x}{\beta}\right)^2} &\geq \varepsilon_0 \\
1-\left(\frac{\alpha}{x}-\frac{x}{\beta}\right)^2 &\geq \varepsilon_0^2 \\
\left(\frac{\alpha}{x}-\frac{x}{\beta}\right)^2 &\geq 1-\varepsilon_0^2 \\
\frac{\alpha}{x}-\frac{x}{\beta} &\geq \sqrt{1-\varepsilon_0^2} \\
\alpha\beta - x^2 &\geq x\sqrt{1-\varepsilon_0^2} \\
x^2 - x\beta\sqrt{1-\varepsilon_0^2} - \alpha\beta &\neq 0
\end{aligned} \tag{D.5}$$

$$\Delta = \beta^2 \cdot (1-\varepsilon_0^2) + 4\alpha\beta \tag{D.6}$$

$$\begin{aligned}
x &= \frac{\beta\sqrt{1-\varepsilon_0^2} \pm \sqrt{\beta^2 \cdot (1-\varepsilon_0^2) + 4\alpha\beta}}{2} \\
&= \beta \cdot \frac{\sqrt{1-\varepsilon_0^2} \pm \sqrt{1-\varepsilon_0^2 + 4\frac{\alpha}{\beta}}}{2}
\end{aligned} \tag{D.7}$$

Consider $\kappa = 1-\varepsilon_0$.

$$\begin{aligned}
x &\approx \beta \cdot \frac{\sqrt{1-(1-\kappa)^2} \pm \sqrt{1-(1-\kappa)^2 + 4\frac{\alpha}{\beta}}}{2} \\
&\approx \beta \cdot \frac{\sqrt{2\kappa-\kappa^2} \pm \sqrt{2\kappa-\kappa^2 + 4\frac{\alpha}{\beta}}}{2} \\
&\approx \beta \cdot \frac{\sqrt{2\kappa} \pm \sqrt{2\kappa + 4\frac{\alpha}{\beta}}}{2}
\end{aligned} \tag{D.8}$$

Appendix E

Analysis of Variance of Minimal Modelling Solution with Offsets

$$\ddot{x} + C\dot{x} + \beta x = \beta r \tag{E.1}$$

$$x = A_1 \cos(\omega t) + A_2 \sin(\omega t) \tag{E.2}$$

$$r = A_\mathrm{r} \sin(\omega t) \tag{E.3}$$

$$-\omega^2 \cdot (A_1 \cos(\omega t) + A_2 \sin(\omega t)) + \omega C \cdot (-A_1 \sin(\omega t) + A_2 \cos(\omega t)) + \beta \cdot (A_1 \cos(\omega t) + A_2 \sin(\omega t)) = \beta A_\mathrm{r} \sin \tag{E.4}$$

$\cos(\omega t)$ coefficients:

$$\omega C A_2 + \beta A_1 = \omega^2 A_1 \tag{E.5}$$

$\sin(\omega t)$ coefficients:

$$-\omega C A_1 + \beta \cdot (A_2 - A_\mathrm{r}) = \omega^2 A_2 \tag{E.6}$$

$$\begin{bmatrix} \omega A_2 & A_1 \\ -\omega A_1 & A_2 - A_\mathrm{r} \end{bmatrix} \begin{bmatrix} C \\ \beta \end{bmatrix} = \begin{bmatrix} \omega^2 A_1 \\ \omega^2 A_2 \end{bmatrix} \tag{E.7}$$

$$\Delta = \omega \cdot (A_1^2 + A2 \cdot (A_2 - A_\mathrm{r})) \tag{E.8}$$

$$\begin{bmatrix} C \\ \beta \end{bmatrix} = \frac{1}{A_1^2 + A_2 \cdot (A_2 - A_\mathrm{r})} \begin{bmatrix} A_2 - A_\mathrm{r} & -A_1 \\ \omega A_1 & \omega A_2 \end{bmatrix} \begin{bmatrix} \omega A_1 \\ \omega A_2 \end{bmatrix} \tag{E.9}$$

$$\beta = \frac{\omega^2 \cdot (A_1^2 + A_2^2)}{A_1^2 + A_2 \cdot (A_2 - A_\mathrm{r})} \tag{E.10}$$

$$\beta = \frac{\omega^2 A_0^2}{A_0^2 - A_\mathrm{r} A_2} \tag{E.11}$$

Appendix F

Correlation Between Time Monomials

We investigate the correlation between different monomials of the form t^n between $t = 0$ and $t = T$. This is important as polynomials are generally highly correlated, and this correlation reduces the numerical stability of an integral method solution when offsets and initial conditions are taken into account. The expected value of a polynomial $\frac{t^n}{n!}$ between $t = 0$ and $t = T$ is given in (F.1). The factorial division is present because it is assumed the time monomial of order n is obtained by repeated integration.

$$\begin{aligned} \mathrm{E}(t^n) &= \frac{1}{T}\int_0^t \frac{t^n}{n!}\,dt \\ &= \frac{T^n}{(n+1)!} \end{aligned} \tag{F.1}$$

Another important quantity is the expected value of the squared monomial, given in (F.2).

$$\mathrm{E}\left[\left(\frac{t^n}{n!}\right)^2\right] = \frac{T^{2n}}{(2n+1)\cdot(n!)^2} \tag{F.2}$$

Another important quantity is the expected value of the product of two monomials, given in (F.3).

$$\mathrm{E}\left(\frac{t^m}{m!}\cdot\frac{t^n}{n!}\right) = \frac{T^{m+n}}{(m+n+1)\cdot m!\cdot n!} \tag{F.3}$$

The variance is calculated according to (F.4).

$$\begin{aligned}\operatorname{Var}\left(\frac{t^n}{n!}\right) &= \mathrm{E}\left[\left(\frac{t^n}{n!}\right)^2\right] - \left[\mathrm{E}\left(\frac{t^n}{n!}\right)\right]^2 \\ &= \frac{T^{2n}}{(2n+1)(n!)^2} - \frac{T^{2n}}{(n+1)^2\cdot(n!)^2} \\ &= \frac{T^{2n}}{(n!)^2}\cdot\left(\frac{(n+1)^2-2n-1}{(2n+1)\cdot(n+1)^2}\right) \\ &= \frac{T^{2n}}{(n!)^2}\cdot\left(\frac{n^2}{(2n+1)\cdot(n+1)^2}\right)\end{aligned} \tag{F.4}$$

The variance allows the calculation of the standard deviation, given in (F.5).

$$\operatorname{Std}(t^n) = \frac{T^n}{n!}\cdot\left(\frac{n}{\sqrt{2n+1}\cdot(n+1)}\right) \tag{F.5}$$

The covariance is calculated in (F.6).

$$\begin{aligned}\operatorname{Cov}(t^m,t^n) &= \mathrm{E}\left(\frac{t^{m+n}}{m!\cdot n!}\right) - \mathrm{E}\left(\frac{t^m}{m!}\right)\mathrm{E}\left(\frac{t^n}{n!}\right) \\ &= \frac{T^{m+n}}{(m+n+1)\cdot m!\cdot n!} - \frac{T^{m+n}}{(m+1)(n+1)\cdot m!\cdot n!} \\ &= \frac{T^{m+n}}{m!\cdot n!}\cdot\frac{mn}{(m+1)(n+1)(m+n+1)}\end{aligned} \tag{F.6}$$

Once the standard deviation and covariance is known, the correlation can be calculated as in (F.7).

$$\operatorname{corr}(t^m,t^n) = \frac{\sqrt{(2m+1)(2n+1)}}{m+n+1} \tag{F.7}$$

Table F.1 gives symbolic correlations between t^m and t^n monomials on the interval $[0,T]$.

Table F.1 Correlation between different t^m and t^n monomials.

	0	**1**	**2**	**3**
0	1	$\frac{\sqrt{3}}{2}$	$\frac{\sqrt{5}}{3}$	$\frac{\sqrt{7}}{4}$
1		1	$\frac{\sqrt{15}}{4}$	$\frac{\sqrt{21}}{5}$
2			1	$\frac{\sqrt{35}}{6}$

Table F.2 gives numerical correlations between t^m and t^n monomials on the interval $[0,T]$.

Table F.2 Numerical (four significant figure) correlation coefficients between different t^m and t^n monomials.

	0	**1**	**2**	**3**
0	1	0.8660	0.7454	0.6614
1		1	0.9682	0.9165
2			1	0.9860

The correlation of *any* polynomial t^n with t^{n-k} goes to 1 with increasing n, as shown below in (F.8).

$$\begin{aligned}
\lim_{n\to\infty} \operatorname{corr}(t^n, t^{n-k}) &= \lim_{n\to\infty} \frac{\sqrt{(2n+1)(2n+1-2k)}}{2n+1-k} \\
&= \lim_{n\to\infty} \frac{\sqrt{(2n+1)^2 - 2(2n+1)k}}{2n+1-k} \\
&= \lim_{n\to\infty} \frac{\sqrt{\left(2+\frac{1}{n}\right)^2 - \left(\frac{4}{n}+\frac{2}{n^2}\right)k}}{2+\frac{1-k}{n}} \\
&= 1
\end{aligned} \tag{F.8}$$